UNIVERSITY OF BIRMINGHAM

EFFECTS OF MIXING REGIMES AND INERT SOLID SUSPENSION ON SEWAGE SLUDGE ANAEROBIC DIGESTION PERFORMANCE THROUGH EXPERIMENTAL STUDY AND CFD MODELLING

by

JOSÉ CARLOS NOGUEIRA FILHO

A thesis submitted to the

University of Birmingham

for the degree of

DOCTOR OF PHILOSOPHY

School of Civil Engineering
College of Engineering and Physical Sciences
The University of Birmingham
April 2019

Abstract

Anaerobic digestion is a widespread technology that is used to treat sewage sludge from wastewater. Mixing has been proven to be a key element for a well-performed digester but it is a power-intensive operation whose quantitative contributions to the system's energy-efficient balance in different designs is not well understood. In order to cut costs, operators try to keep mixing to minimum levels where biogas production is not adversely affected. However, sewage sludge inherently contains inert dense particles, such as grit, that cannot be biodegraded and tend to accumulate at the bottom of the digester.

For the first time, the impact of inert particle suspensions on biogas production was evaluated at a range of mixing speeds and particle loadings in mechanically-mixed, laboratory-scale digesters. Five digesters were operated for a total period of five months at different speeds and particle loadings whilst digestion stability, biogas production and treatment quality were monitored. Digesters were fed with real sewage sludge samples six days a week. Computational fluid dynamics models were used to assess the liquid-solid flow characteristics.

It has been shown that inert particles in suspension at highly-intensive mixing detrimentally affects anaerobic digestion performance and biogas yields. Low-speed mixing does not suspend inert particles but the digesters are not affected by their presence. Short-term, highly-intensive intermittent mixing, along with continuous low intensive mixing, resulted in particle suspension, stable digestion and biogas production; this being the best energy-efficient mixing regime. Computational fluid dynamics has successfully simulated sedimentation behaviour as well as particle solid distribution and cloud height within the liquid column. The liquid flow patterns change with increased particle loadings.

To my parents, who always gave me unconditional love and support.

Acknowledgements

Firstly, I would like to thank my supervisor, Professor Nigel Cassidy for his great insights, support, guidance and efforts to make this thesis possible. I am also very thankful for the contributions of Professor John Bridgeman for the opportunity and trust along the journey. I am gratefully thankful to *Conselho Nacional de Desenvolvimento Científico e Tecnológico* (CNPq), who sponsored this research (reference number - 207510/2014-8). Without this 4-year scholarship, this work would have not been possible. Thanks to Severn Trent Water for allowing me to collect the samples used in the experimental work and the University's BlueBear high performance computing facility, for their fundamental support.

A PhD is a long and complex journey, and I am deeply grateful to all those who helped me throughout this period of my life. Thanks to my family, who were always present when I needed them the most, especially to my parents, Zeca e Vaninha, who dedicated their entire life to provide the best environment and education for their children. Thanks to my brother and sisters, Kikao, Kaka e Quel for their unconditional support, it has been truly valuable. I would like to thank Vale, my partner for life, soulmate and future wife, for all your love, emotional support and care. You changed my life in a way I would have never imagined!

To all those friends who made this journey easier, I am profoundly grateful to have you in my life. John, Mayra, Jacob, Ievita, Tarso, Victor, Samara and Vitor, Fernando, Pedrinho and Pedrao, and all others that are not listed. Thank you my dear 'cult' friends, in special to Petros, who have always believed and supported my life choices. Grateful thanks to all those friends and colleagues who participated of my life throughout this journey and share the best moments of the past 4 years.

Last, but not least, thanks to Mark Carter for his long term commitments and assistance in the lab and to Allen Bowden for helping with VFAs analysis. Thanks to David Parker for granting me assess to the PEPT equipment and L Windows-Yule. Especially thanks to Ana Maria Portela, who helped me walk on my own feet with regards to CFD. To all the great scientists and teachers in this world who guide human development for making a better world, my deep appreciation.

This work would have been much more difficult without you.

Contents

List of Figures

List of Tables

Abbreviations

AD	Anaerobic digestion
AWA	Area-weighted-average
BH	Bed height
CARPT	Computer automated radioactive particle tracking
CBP	Cumulative biogas production
CFD	Computational fluid dynamics
CH	Cloud height
CHP	Combined and heat power
CMC	Carboxymethyl cellulose
CBP	Cumulative biogas production
COD	Chemical oxygen demand
CSTR	Continuous stirred tank reactors
D1, 2, 3 and 4	Digesters (four geometrically identical, lab-scale tanks)
DFV	Daily feeding volume
DI	Deionised water
DNS	Direct numerical simulation
Exp1 & 2	Experimental periods one and two
FS	Fixed solids
FID	Flame ionization detection
FISH	Fluorescence in situ hybridisation
FVM	Finite volume method
GCI	Grid convergence index
GC	Gas chromatography
GD	Glass digester
HRT	Hydraulic retention time
IWA	International water association
KE	Kinetic energy
LDV	Laser Doppler velocimetry
LCFA	long chain fatty acids
LES	Large eddy simulation
mM	Millimolar
MRF	Multiple reference frame
MSW	Municipal solid waste
OLR	Organic loading rate
P1, 2, 3 and 4	Phases of the experiment

PBT	Pitched blade turbine
PEPT	Positron emission particle tracking
PIV	Particle image velocimetry
PSD	Particle size distribution
qPCR	Quantitative polymerase chain reaction
RANS	Reynolds-averaged Navier-Stokes
RNG	Renormalized group
RPM or rpm	Rotation per minute
RSM	Reynolds stress model
RT	Retention time
sCOD	soluble chemical oxygen demand
SD	Standard deviation
SG	Sliding grid
SMP	Specific methane production
SRT	Solids retention time
SST	Shear stress transport
STW	Sewage treatment works
TKE	Turbulent kinetic energy
TS	Total solids
UDF	User defined function
UK	United Kingdom
UN	United Nations
URF	Under-relaxation factor
USC	Unsuspended solid criterion
USEPA	United States Environmental Protection Agency
V	Volume
VFA	Volatile fatty acids
VOF	Volume of fluids
VS	Volatile solids
VWA	Volume-weighted-average
WWTP	Wastewater Treatment Plant

Nomenclature

Symbols

b	baffle width (mm)
C	clearance (distance from impeller's radial centreline to tank's bottom) (mm)
C_D	drag coefficient (-)
C_1, C_2, C_μ	constants from turbulence equations
c_b	baffle's gap from the bottom (mm)
D	impeller diameter (mm)
d or d_p	particle diameter (mm)
F, $\vec{F}$	external body force (N)
G_k	generation of turbulent kinetic energy
g	gravitational acceleration (m/s^2)
g_w	baffle's gap from the wall (mm)
H	liquid height (mm)
h, *h*	impeller width, density function (mm, -)
h_b	baffle's height (mm)
K	consistency index ($Pa.s^n$)
K_{ls} or K_{sl}	interphase momentum exchange coefficient (-)
k	turbulent kinetic energy (J/kg or m^2/s^2)
k_s	Metzner and Otto constant (-)
m	mass (kg)
$\dot{m}$	mass transfer
N, *N*	rotational speed, number of cells in domain (rpm, -)
n	power-law or flow index (-)
N_{js}	minimum speed for just suspension (rpm)
N_{ss}	speed for sufficient suspension (rpm)
P	power (W)
p	static pressure share by all phases (Pa)
p	apparent order (-)
$r_{21,\ 32}$	refinement factor (-)
Re	Reynolds number (-)
Re_s	relative Reynolds number (-)
Re_{PL}	particle's Reynolds number (-)
S	Zwietering's constant (-)
S_m, S_q	Mass source term
S_k, S_ε	Turbulent source terms
X	Zwietering's concentration (mass of particle / mass of liquid) (%)
T	tank diameter, torque (mm, N.m)
t	time (s)
t_b	baffle's thickness (mm)
t_i	impeller thickness (mm)
U_z, U_r, U_t	axial, radial and tangential velocity components (m/s)
u, v, w	velocities in the x, y and z directions
V	volume (l or m^3)
V_{sp}	sample's volume (ml)

v/v	volume per volume (%)
vf	volume fraction
v_s	sphere's free fall velocity (m/s)
w	weight (g)
x, y, z	directions in the Cartesian coordinate system
Y	drag correction factor
Ø	nominal diameter (mm)
$\angle$	angle (º degree)
$\bar{\bar{I}}$	identity tensor
∇	differential operator given in Cartesian coordinates

Greek letters

α	impeller pitched angle (º)
α, α_{ls}	volume fraction, local volume fraction (-)
α_{Ns}	normalised volume fraction
α_{s_ave}	average volume fraction in the tank
δ_{ij}	Kronecker delta
ε	turbulence dissipation rate (m^2/s^3)
$\varepsilon_{21,\,32}$	error
η	Kolmogorov's length scale (mm)
η_c	Casson's parameter
η_∞	viscosity of the Newtonian plateau at high shear rates (Pa.s or $N.s/m^2$)
λ	bulk viscosity
μ	fluid molecular or dynamic viscosity (Pa.s or $N.s/m^2$)
$\mu_a=\mu_{la}$	apparent or local viscosity (Pa.s or $N.s/m^2$)
u_η	Kolmogorov's velocity scale
μ_t	turbulent eddy viscosity
ρ	density (kg/m^3)
$\sigma_k, \sigma_\varepsilon$	turbulent empirical constants
τ, τ_0	shear stress, initial yield stress (N)
$\bar{\bar{\tau}}$	stress-strain tensor
τ_η	Kolmogorov's time scale (s)
$\dot{\gamma}$	shear rate (s^{-1})
$\overline{\overline{S_{ij}}}$	mean rate of strain (-)
υ	kinematic viscosity (m^2/s)
φ	any scalar quantity or variable of interest
ω	specific turbulent dissipation rate (s^{-1})

Subscripts

B	buoyancy
D	drag
G	gravitational
L	lift
T	turbulent
i	class and cell index

j	class index
p & q	p^{th} & q^{th} phases
l	liquid phase
s	solid phase
sp	sample
td	turbulent dispersion
vm	virtual mass

CHAPTER 1 INTRODUCTION

In the UK, there are about 9000 wastewater treatment facilities returning over 10 billion litres of treated wastewater to the environment every day. In 2010-11, wastewater treatment resulted in approximately 1.5 million tons of dry solids as sewage sludge being produced as the by-product of treatment processes (WaterUK, 2012). These numbers are only expected to grow as population increases and the implementation of more stringent legislation requires higher controls on wastewater quality before being returned to the environment.

Sewage sludge is rich in pathogens and putrescible matter and needs to be stabilised prior to disposal. Sludge can be stabilised chemically, thermally or biologically. The resulting product of biological stabilisation can be used on agricultural land as bio-fertiliser and is the most common route for the disposal of sewage sludge in the UK. In fact, 71% of sludge disposal in the UK consists of land application, thus reducing the need for mineral fertilisers (WaterUK, 2012). Biological stabilisation consists of the biodegradation of organic matter and the destruction of pathogens. Anaerobic digestion is an effective route for stabilising sewage sludge and provides opportunities for the recovery of energy, contributing to the circular economy and promoting a more sustainable solution for sludge management.

Mesophilic anaerobic digestion consists of mixing sludge with anaerobic bacteria that break down the organic matter into more stable compounds and produces a methane-rich biogas as a by-product. Biogas is considered a renewable energy fuel that is harnessed in combined heat and power (CHP) units. The energy recovered can then be used to supply the wastewater treatment plant energy demands.

Sewage sludge is rich in organic matter that is consumed by the microorganisms and transformed into biogas. Sludge inherently contains all sorts of organic and inorganic material that cannot be biodegraded in the anaerobic digestion process, including hair, gravels, animal shells, stones and grit. Before entering the digesters, sludge is normally passed through screening equipment designed to separate particles of a certain size and density from the sludge and stop them from entering the digesters. Unavoidably, particles smaller than the screen size will be carried within the sludge inside the digesters. These undesirable particles tend to settle down and accumulate, which may be inconvenient, as with time they will cause operational problems of the digesters.

Mixing AD has been proven to be essential in order to maintain digestion stability by promoting a homogenous solution throughout the digester in terms of temperature, substrate availability, dispersing toxins and avoiding stratification and sedimentation of the solid particles. However, mixing is an energy-intensive process that accounts for up to 20%

of the operational costs (Bridgeman, 2012). As designers and operators of AD plants look for better methods and practices to decrease costs and mitigate the environmental impacts of the process; decreasing the energy consumption in terms of mixing power seems to be a reasonable option for reducing costs. The ideal mixing regime would, therefore, reduce mixing energy input without compromising biogas production. A conflict arises when dense particle sedimentation is considered, as it is known to be a mixing intensive process (Paul et al., 2004).

Despite the advancements in the understanding of mixing regimes and its role on biogas production (Kariyama et al., 2018), little is known about the impacts of inert particles suspension and/or sedimentation on the digestion performance. In order to understand how to avoid sedimentation, it is important to consider the flow patterns in a digester, which are determined by sludge rheology, particle properties and ultimately, the mixing regimes. In recent years, computational fluid dynamics (CFD) have been systematically applied to the understanding of flow patterns in anaerobic digesters and stirred tanks for solid suspension in the chemical industry. However, there are clear limitations to the work when tackling solid suspension in anaerobic digesters.

Considering the above and as shown later in chapters 2 and 3, there appears to be a knowledge gap in how the presence of inert dense solid particles, in suspension or not, might affect AD performance both in terms of sludge treatment quality and energy recovery from the biogas produced. Additionally, to the knowledge of this author, no scientific work published on CFD models of stirred tanks of AD systems has considered the multi-phase nature of poly-dispersed inert particles suspension.

1.1. Research Relevance

The research presented in this thesis focuses on the experimental and numerical analysis of mechanically mixed anaerobic digesters in order to better understand the effects of inert particles on digestion performance, biogas production and mixing power. Experimental work on laboratory-scale sewage sludge digesters was undertaken in order to determine the impact of solid sedimentation and suspension, under different particle loadings and mixing regimes, on the overall energy efficiency of the system. CFD modelling was used to understand the flow patterns of the laboratory digester and was validated using particle imagine velocimetry (PIV).

1.2. Layout of this Thesis

Following this introduction (Chapter 1), the principles of anaerobic digestion biochemistry and mixing along with a literature review is provided in Chapter 2. The fluid mechanics theory and a CFD literature review on stirred tanks, focusing on the suspension of solid

particles and anaerobic digesters, are presented in Chapter 3. The established objectives set to achieve the aims of this research are both stated in Chapter 4. Chapter 5 provides the materials and methods used in the AD experimental work. The key findings of the experimental investigation are given in Chapter 6 with the methodology, results and validations of the CFD simulations presented in Chapter 7. A general discussion on the experimental and computational results and their implications are provided in Chapter 8. Finally, the main conclusions and recommendations for future research are given in Chapter 9.

CHAPTER 2 ANAEROBIC DIGESTION

This chapter presents the fundamental principles of anaerobic digestion with a focus on wastewater sludge treatment. In section 2.1, a short overview is provided about the use of anaerobic digestion (AD) in wastewater treatment plants, the current industrial challenges and future perspectives. Section 2.2 presents the main biochemical stages and reactions of AD. In section 2.3, the main operational and monitoring parameters of an AD plant are described whilst section 2.4 presents the concept of AD mixing systems, their principal characteristics and a literature review highlighting the importance and impact of mixing on AD processes. Finally, a brief summary and discussion on the current knowledge gaps in the published literature are provided in section 2.5.

2.1 Anaerobic Digestion Overview

Sewage sludge is the by-product of a wastewater treatment plant (WWTP) and consists of a high-viscosity fluid (water) with a high solids content (typically 3 to 6%) (IWA Publishing, 2007). It is rich in pathogenic microorganisms, biodegradable organics, nutrients and contaminants and needs further treatment (or stabilisation) before disposal. Disposal consists of the transportation of stabilised sludge from the WWTP to landfills, incinerators or agricultural applications (IWA Publishing, 2007). The volume of sludge must be reduced prior to disposal due to the high transportation costs. Sludge management can account for up to 60% of the WWTP operational costs (UN-Habitat, 2008, IWA Publishing, 2007). Stabilisation prior disposal is essential in order to avoid contamination of the environment and reduce transportation-related costs. Common treatment routes include biological, chemical or thermal stabilisation. Biological treatment can be aerobic or anaerobic with both methods consisting of biodegrading or digesting part of the organic fraction, thus reducing its solids content.

Anaerobic digestion (AD) consists of the controlled biodegradation of the organic fraction contained in the sludge and is a natural biochemical process where anaerobic bacteria/archaea grow in the absence of free molecular oxygen. They degrade (digest) organic compounds breaking them down into smaller and more stable molecules whilst producing biogas as an end product. The biogas is mainly composed by 60-70% methane (CH_4) and 30-40% carbon dioxide (CO_2), two known greenhouse gases. The methane-rich biogas produced from AD can be used to run combined heat and power plants (CHP), resulting in the co-generation of electricity and heat, which can be used in the WWTP or be exported elsewhere generating revenue. AD has three main benefits:

1) Stabilising the sludge – to reduce pathogens and putrescible organics to safe levels before disposal;
2) Reducing the sludge volume - by breaking down part of the complex organic fraction via biodegradation (or digestion), which is then transformed into biogas; and
3) Recovering energy from organic waste – the use of the methane-rich gas as an renewable energy source to produce electricity or heat, thus reducing sludge management costs;

Methane is 21 times more impacting as a greenhouse gas when compared to carbon dioxide, thus requiring stricter controls in order to mitigate its impact on climate change (Appels et al., 2008). Therefore, more sustainable routes for managing methane emission sources have been part of governmental agenda around the world in recent years. Policies such as green certificates and increased feed-in tariffs for AD-related renewable energy have advanced AD technologies and promoted its application/adoption at industrial levels. In Europe, the number of biogas plants fed with all types of biomass rose from 6,227 to 17,439 between 2009 and 2016 with an installed total electricity capacity of 63 TWh (Bioenergy Europe, 2018). There are 345 sewage sludge biogas plants in the UK (out of a total of 2,601), mostly as centralised sites to cover of the 6000 sewage works.

AD-based renewable energy has advantages over other sources, such as photovoltaic and wind, in that it can provide a stable and continuous supplied energy source that is flexible enough to use as electricity, heat or fuel in vehicles. It is also easy to transport and store. Additionally, the by-product of the AD process can be used as bio-fertiliser in agricultural fields, contributing to the circular economy and, therefore, decreasing the amount of waste incinerated or landfilled. However, the Bioenergy Europe (2018) statistical report shows that the annual growth of biogas plants has declined from 69% to 1%. This sharp decline is attributed to recent changes in legislation with governments across Europe now cutting subsidises for renewable energy. Social pressure with regards to the intensive land use for so-called ‘energy crops’ has played a major role in the legislation change, which of course, also affects the AD plants that treat sewage sludge. Therefore, there is a pressing socio-economic need to make AD plants more cost-efficient and without the need of subsidies.

2.2 Biochemistry of AD

Although complex, the microbiology of anaerobic digesters is well understood with the breakdown of organic compounds occurring in three key phases: hydrolysis, acidogenesis

and methanogenesis. Note that some authors consider acetogenesis as an intermediary phase occurring in-between acidogenesis and methanogenesis (Van Lier et al., 2008, Gerardi, 2003). A general illustration of these stages is shown in figure 2.1. For biochemical modelling purposes, the process can be separated into even more stages (Myint et al., 2007).

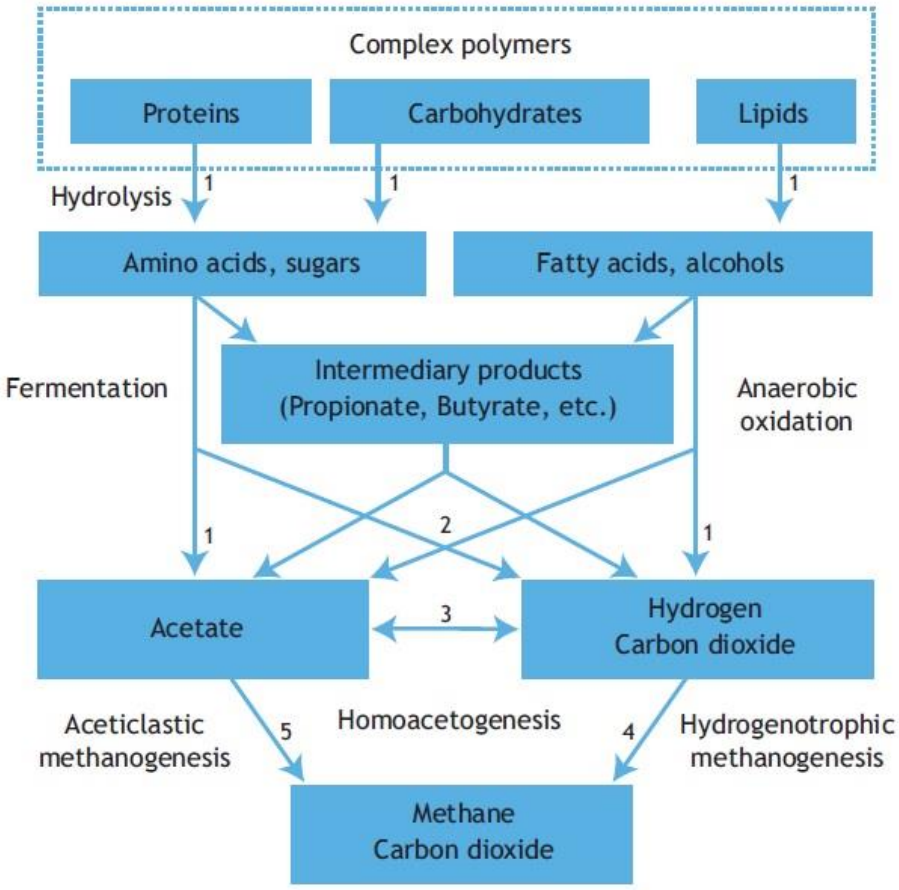

Figure 2.1: General representation of anaerobic digestion processes. Numbers indicate the bacteria group. 1. Hydrolytic and fermentative, 2. Acetogenic, 3.Homo-acetogenic, 4. Hydrogentrophic methanogens, 5. Aceticlastic methanogens (Van Lier et al., 2008).

In hydrolysis, insoluble organic matter and high molecular weight compounds (e.g. carbohydrates, proteins and lipids) are broken down into smaller compounds (such as amino acids and sugars). This step occurs due to the excretion of enzymes from obligate or facultative anaerobes (Van Lier et al., 2008). For some slurries, hydrolysis is a rate-limiting step due to the duration of the degradation. To enhance the digester performance, thermal, chemical or mechanical pre-treatments can be applied (Park et al., 2005).

The next stage called acidogenesis is the further degradation of the now simplest compounds. Sugars, long-chain fatty acids (LCFA) and amino acids are assimilated into the bacteria cells and fermented or oxidized to smaller organic compounds such acetate (volatile fat acids – VFA), hydrogen and carbon dioxide. Higher organic acids are also

formed, e.g. propionate, butyrate and alcohols. Acidogens have a quick growing rate and are less sensitive to environment changes (Van Lier et al., 2008).

The higher-order organic compounds resulting from acidogenesis are then further broken down to acetate, hydrogen and carbon dioxide. As a result of acetogens being obligatory hydrogen producers, their growing rate is limited by a low hydrogen partial pressure. Therefore, they are more sensitive to environmental conditions (Van Lier et al., 2008, Gerardi, 2003).

The last step of AD is the conversion of the remaining organic compounds into biogas, mainly methane and carbon dioxide. Methane is mostly formed from acetate and hydrogen, but methanogenic bacteria (referred to as methanogens, the obligate anaerobic specialised group belonging to the domain of Archaea) can also transform formate, methanol and methylamines. About 70% of the methane produced originates from acetoclastic methanogens whilst the remaining 30% derives from the hydrogenothrophic group. Note that acetoclastic methanogens have a very low growth rate of several days in contrast to a few hours (4 to 12 hours) for the hydrogenotrophic methanogens. Therefore, extreme care should be taken to avoid wash-out of methanogens, which might result in the accumulation of volatile acids and ultimately lead to AD process failure. All other organic matter must be transformed first to compounds that methanogens can use, otherwise they will remain as soluble chemical oxygen demand (sCOD) substances. The main chemical reactions are as follows (Gerardi, 2003):

$$4H_2 + CO_2 \rightarrow CH_4 + 2H_2O \quad (2.1)$$

$$CH_3COOH \rightarrow CH_4 + CO_2 \quad (2.2)$$

$$4CH_3OH \rightarrow 3CH_4 + CO_2 + 2H_2O \quad (2.3)$$

$$4HCOOH \rightarrow 3CH_4 + 3CO_2 + 2H_2O \quad (2.4)$$

The complete chain of chemical reactions for the other digestion phases is broadly available in the literature (Van Lier et al., 2008, Gerardi, 2003).

2.3 AD Operational Conditions and Monitoring Parameters

The design and operational parameters of AD tanks depend on several factors, amongst which are the type of feedstock, solid concentration, retention times, temperature, pH, and mixing systems. Control of these parameters is required for the digester to function in an optimal, energy-efficient regime. In general, operational and monitoring conditions focus on the methane-forming bacteria/archaea groups because of their rate-limiting reactions and extreme sensitivity to parameters such as temperature and pH.

2.3.1 Feed sludge

Feed sludge characteristics influence the main design and operational parameters of the AD process, such as organic loading rates (OLR), retention times, mixing regimes, volatile solids reduction and biogas composition. The solid concentration of the feed can vary widely in terms of composition and quantity. A broad range of minerals, nutrients and diverse concentrations of carbohydrates, proteins and fats are likely to be present in AD plants treating food waste or sewage sludge. The total solids (TS) concentration is generally between 15 to 22% for urban solid waste feedstock and between 3 to 6% for sewage sludge, a significant difference that needs be considered when designing the mixing system. On the other hand, the substrate from an energy-crop AD plant is normally mixed with animal manure in order to keep the total solids concentration below 10% (called co-digestion). Such feedstock might need additional micronutrients to maintain a high biogas yield rate. In WWTPs, the TS of the feed sludge varies rapidly over time, thus constant monitoring is crucial in order to maintain a good balance between retention times, organic loading rates and biogas production. Additionally, retention times are also affected by the withdrawal of supernatant and grit removal (which must be removed in order to ensure adequate control of the process (Gerardi, 2003)).

2.3.2 Retention times and organic loading rate – OLR

Layers along the liquid column having different solid concentrations can occur in AD tanks if no or poor mixing is provided. In this case, the dense solid fraction settles down to the lower regions of the tank whilst the upper region contains the dissolved and suspended organic and inorganic materials (i.e. volatile fatty acids, sulphur, nitrogen and phosphorous), forming the so-called supernatant. Solid and hydraulic retention times (SRT and HRT, respectively) are the average time solids and liquid stay in the tank. Where no recirculation of the supernatant occurs and homogenous suspension exists, they are considered the same. The rate of biogas yields is directly linked to the retention times (RT), which reflects the time bacteria need to reproduce and digest the organic matter. Short RTs might lead to the wash-out of bacteria whilst longer SRTs are advantageous up to a certain limit. This is because longer SRTs allow more time for the degradation of long and difficult to degrade molecules, such as lignin and cellulose, thus enchaining the solid's conversation into biogas. For AD plants that mainly deal with such compounds, the SRT can be as long as 100 days or more whereas retention times for sewage sludge AD lies between 12 and 20 days.

The organic loading rate (OLR) is a measure of the degradable fraction added to the tank per unit of volume and time and is normally given in terms of kilograms of volatile solid

(VS) per cubic meter per day (kgVS/m³/day). Values may vary widely (0.5-7.2 kgVS/m³/day) according to the operating temperature, mixing mode and solids composition (Noutsopoulos et al., 2013, Gerardi, 2003). In wastewater treatment plants, sludge is normally “degrited” to avoid inert solid particles entering the tank and thickened to increase the degradable TS concentration before feeding. However, it is not always possible to keep TS concentrations constant and the feeding volume might be adjusted so that a constant OLR is achieved.

2.3.3 Temperature

Anaerobic digestion can be performed over a large range of temperatures (4-60°C), and the process is categorised into three groups: psychrophilic (4-20°C) mesophilic (30-40°C) and thermophilic (50-60°C) digestion. Psychrophilic is not appropriate for industrial applications because of its slow bio-activity rate and is normally found in small-scale applications and only at ambient temperatures, such as septic tanks and lagoons. The higher operating temperatures required by thermophilic AD plants make its use more common when a surplus of heat is available, thus avoiding heat losses and increased energy efficiency. Thermophilic AD can operate at higher organic loading rates, shorter retention times and result in higher pathogen destruction. The mesophilic range predominates in industrial applications, especially in sewage sludge plants, because of the balance between low heating energy and high biogas yields. Additionally, anaerobic mesophilic bacteria are more abundant in nature when compared to psychrophilic and thermophilic (Gerardi, 2003).

The operating temperature of an AD plant will determine which groups of microorganisms will prevail in the process. Fluctuations in temperature can benefit some groups yet have adverse effects on others. Each group have their own ideal temperature range. In general, earlier stage processes (hydrolysis and acidogenesis) experience less adverse effects due to temperature changes whilst late-stage processes (acetogenesis and methanogenesis) will strongly suffer from temperature fluctuations. Therefore, once the operating temperature is set, it should be kept constant throughout the tank otherwise the predominant microorganism groups can vanish (even with small temperature variations). This is especially true for the most sensitive methane-forming bacteria. In case of subtle or frequent temperature changes, intermediate products (i.e. organic alcohols and short change volatile acids) can accumulate and cause digestion inhibition, ultimately leading to process failure. Failure can occur within temperature fluctuations of 1°C/day and, therefore, AD systems should be kept to within 0.6°C/day (Appels et al., 2008).

Mixing plays a crucial role in maintaining a homogeneous temperature across the whole tank, thus preventing temperature gradients and isolated areas of temperature variation (Gerardi, 2003).

2.3.4 pH

Anaerobic digestion occurs as a result of the chemical chain reaction described in section 2.2 and as with temperature, each stage of this process has its own ideal range for pH. Acid-forming bacteria can thrive with acceptable enzymatic activity when pH is above 5.0, whilst fermentative bacteria function well in the range between 4.0 to 8.5. Methanogens, however, do not survive when pH below 6.2. In order to avoid the accumulation of volatile acids due to a predominance of acidogens, pH should be kept ideally between 6.8 and 7.2 for a well-performing reactor (Gerardi, 2003).

pH is directly linked to alkalinity, which is represented in terms of a balance between carbon dioxide, ammonia and carbonate ion concentrations, and is defined as the buffer capacity to quick changes in pH. Low alkalinity concentration is linked to (i) organic acid accumulation due to low levels of methanogenic conversion to methane, (ii) high loads of organic acids entering the digester (iii) methanogen wash-out due to low retention times and (iv) the presence of methanogen inhibitors. As such, monitoring the levels of alkalinity is a good proxy indication of process stability - low concentrations indicate that pH is likely to rapidly drop to unsafe levels whilst high concentrations indicate that the process is well-buffered, thus stable.

2.3.5 Toxicity

Anaerobic digestion is subjected to a broad range of organic and inorganic substances that are toxic and inhibitory to microbiological activities under certain concentrations. As a result of inhibition, volatile fatty acids (VFAs) accumulation, low methane yields and a drop in pH can all be noted (Sindall, 2014). Depending on the nature of exposure to these inhibitory substances, bacterial may adapt by repairing damaged enzyme systems or by the preferential growth of bacterial populations capable of developing the enzymes needed to degrade inhibitors. The acclimation ability of digesters will, therefore, depend on the rate that inhibitors enter and spread into the tank (concentration) as well as the consistency of the exposure time (chronic exposure) (Gerardi, 2003). Gerardi (2003) suggests that three common types of toxicity result from direct exposure to concentrations of ammonia, hydrogen sulphide and heavy metals above specific limit levels. Table 2.1 shows a list of inorganic substances and their toxic concentration limits.

Table 2.1: Toxic concentration limits for inorganic substances (Gerardi, 2003).

Waste	Concentration (mg/l) in Influent to Digester
Ammonia	1500
Arsenic	1.6
Boron	2
Cadmium	0.02
Chromium (Cr^{6+})	5–50
Chromium (Cr^{3+})	50–500
Copper	1–10
Cyanide	4
Iron	5
Magnesium	1000
Sodium	3500
Sulfide	50
Zinc	5–20

High ammonia concentrations are a common cause of inhibition in anaerobic sludge digestion, despite it being beneficial to the process below concentrations of about 200 mg/l. Ammonia may be transferred to, or produced in, the anaerobic digestion process, mainly due to the degradation of nitrogen organic compounds (i.e. proteins, amino acids, urea). In the range between 200 and 1500 mg/l, no adverse effects may be noted.

As seen in the previous sections, volatile fatty acids (VFAs) are both crucial for, and inhibitory to, AD systems. These low-molecular-weight, short-chain acids are precursors to methane formation and the main ones present in anaerobic digesters are shown in table 2.2, out of which acetate is largely the most recurrent (accounts for ~85% of all VFAs). Nevertheless, VFAs are also responsible for lowering pH and therefore a balance between VFAs concentrations and alkalinity is crucial for stable digestion. Higher concentrations of acetate, butyrate and propionate can be inhibitory to AD causing rapid drops in alkalinity, thus lowering pH. Propionate is the most toxic of the VFAs and may inhibit AD above concentrations of 5mg/l in its unionised from (Gerardi, 2003). A typical stable and well-operated anaerobic digester has a total VFAs concentration below 500mg/l, whilst concentrations above 2,000 mg/l might be inhibitory (Labatut and Gooch, 2012).

Table 2.2: VFAs often found in anaerobic digesters (Gerardi, 2003).

Volatile Acid	Number of Carbon Units	Formula
Formate	1	$HCOOH$
Acetate	2	CH_3COOH
Propionate	3	CH_3CH_2COOH
Butyrate	4	$CH_3(CH_2)_2COOH$
Valeric acid	5	$CH_3(CH_2)_3COOH$
Isovaleric acid	5	$(CH_3)_2CHCH_2COOH$
Caproic acid	6	$CH_3(CH_2)_4COOH$

2.3.6 Soluble chemical oxygen demand – sCOD

According to Van Lier et al. (2008), chemical oxygen demand (COD) is the most commonly used parameter to represent the level of contaminants in wastewater. COD is a measure of the suspended and dissolved organic matter that will consume oxygen (in the oxidation process). It is determined from the equivalent mass of oxygen consumed by dichromate in a solution with wastewater or sludge at 150°C (given in mg O_2/l) (Van Lier et al., 2008). Soluble COD (or sCOD) contains only the very small suspended and/or dissolved organic matter fraction that is readily available for transformation into biogas. sCOD concentrations are, therefore, lower than COD (Geerdink et al., 2017), but can be used either as a measure of the stability of the fermentation or the environmental contamination potential of the digestate (e.g., if used as bio-fertiliser in food crops) (Rubal et al., 2012).

2.4 Anaerobic Digestion Mixing

Although the biochemical process of AD is well-documented in the literature, the mixing characteristics of AD systems and their impact on the biological communities, biogas yields and system performance are still not well understood. Studies have confirmed that mixing is essential for maintaining physical, biological and chemical homogeneity and also to avoid grit deposition and scum formation in the digester (Lindmark et al., 2014b). It is recognised that the contact between microorganisms and the substrate is essential for optimum conversion of organic matter into biogas (Gomez et al., 2006). Nevertheless, studies have also demonstrated that intensive mixing can have neutral or unfavourable impacts on both the degradation process and the energy efficiency of the AD system (Ong et al., 2002, Ward et al., 2008, Bridgeman, 2012, Tian et al., 2013). Mixing can represent up to 20% of the operational costs of an AD system in temperate climates (Bridgeman, 2012) and according to Dachs and Rehm (2006), mixing of AD tanks from energy crops can consume up to 54% of the power of biogas plants. Therefore, research have focused on developing an improved understanding of the role of mixing on AD biochemical processes, microbiological communities, distribution of solids and inhibitors, foam/scum formation, grit accumulation and so on. Accumulation of grit is the main topic of this research and is discussed in the next chapter (section 3.1.1).

2.4.1 Type of Mixing

The natural convection processes that occur in an AD vessel due to the formation (and rising) of biogas, plus the heating system and temperature difference throughout the system, can contribute to the fluid mixing process to some degree. However, it cannot

provide sufficient levels of mixing (Appels et al., 2008) to guarantee an efficient gas production process. Therefore, other forms of maintaining AD homogeneity become necessary. There are three main types of mixing systems used in AD, mechanical mixing, biogas recirculation and sludge recirculation (Figure 2.2). Mechanical mixers, often called continuous stirred tank reactors (CSTR), make use of different combinations of propellers and agitators to impose fluid motions into the AD system. Mechanical mixing is broadly used in the AD industry and it is known as the most efficient system both in terms of energy and mixing effectivity (Wu, 2010a). Mechanical mixing has the greatest pumping to power ratio of all three mixing systems. However, if it fails, shut-down and draining of the digester must be carried out, unless the tank is inherently designed to allow for this type of maintenance. Without access for maintenance there is a risk of direct personal contact with the slurry, with a significant health hazard. Such procedures are also costly, dangerous, and require the tank to be turned off for several days, apart from the extra costs due to diverting the waste treatment somewhere else.

Recirculation of biogas is a conventional method used to mix AD and is common in Severn Trent's wastewater treatment plants. The mechanism relies on a tank-top gas collection point, pressurisation through an external compressor and reinjection of the gas in the bottom through gas nozzles. The control system setup (e.g., intermittent or continuous supply) and design (e.g., location, direction, dimensions of nozzles and draft tubes) can vary widely according to designer's and operator's needs. Nevertheless, the physical principle is the same: biogas bubbles rise due to buoyancy forcing the surrounding sludge to move way, causing momentum transfer. The advantage of gas recirculation systems is that they include externally mounted pumps and easier for general maintenance. However, the clogging of nozzles and high power requirements are negatively impacting considerations when using this method. Special care needs to be taken when designing gas recirculation mixing systems as recent research shows that the velocity field falls drastically when the same mixing power is used for higher solid concentrations, which subsequently increases the slurry's viscosity (Dapelo et al., 2015).

Another common mixing system is sludge recirculation. This technique has a similar principle to gas recirculation, but using sludge. Sludge is usually collected at the bottom of the tank and pumped back into the system through external pumps. Two mixing principals are involved; the first is the transfer of material from one side of the tank and pumped back to another point inside the system. The second is the induced fluid motion created by pressure differences at the inlet and outlet points. The displacement of the sludge collected in the inlet creates a low-pressure field which induces local fluid motion whilst the high-velocity jets at the outlet pushes the surrounding sludge creating a momentum exchange and mixing.

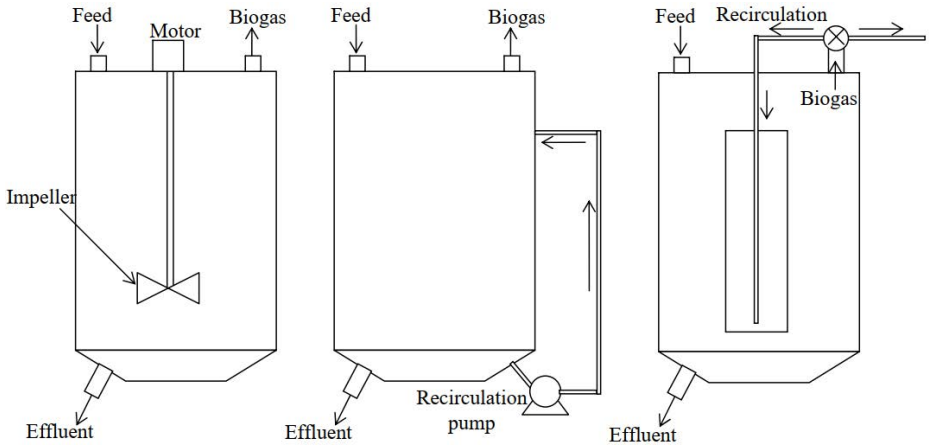

Figure 2.2: Schematic representation of mixing principles for the three main types of mixing used in AD tanks (Vesvikar, 2006).

The optimisation of mixing systems in the wastewater industry has improved, especially with the development of computational models and the increasing use of Computational Fluid Dynamics (CFD). CFD models have been applied to flocculation treatment (Bridgeman et al., 2010), aeration tanks (Karpinska and Bridgeman, 2018) and AD tanks (Meister et al., 2018, Dapelo et al., 2015, Sindall, 2014, Yu et al., 2013, Bridgeman, 2012, Wu, 2011, Wu, 2010a, Vesvikar and Al-Dahhan, 2005). In this work, combined experimental and CFD investigations on the presence and impact of dense inert particles in AD tanks are explored for the first time. The mathematical background for this CFD modelling is given in section 3.2.

2.4.2 Effects of mixing on anaerobic digestion

Mixing can be performed continuously, intermittently, vigorously or moderately. Vigorous (or intensive) mixing strongly contributes to a homogenous suspension of a broad range of solid particles but requires high power consumption. It may cause damage to mechanical parts, such as impellers and recirculation pumps, through abrasion. Moderate or minimal mixing may contribute to power savings but they increase the tendency of dense, solid particles to settle in the bottom of the digester and light materials to float to the top of the fluid column. As such, the digester's fluid becomes stratified and the degree of contact between the bacteria and substrate becomes poorer. The floatation of light and 'elongated' materials, (such as fibrous solids) may form a layer of foam/scum on the liquid surface which may block biogas release. The sedimentation of animal shells (i.e. egg and snail shells) plus grit (i.e. sand, stones) may block gas nozzles and pumps and decrease the effective volume of the tank. As a consequence, a decrease in biochemical reactions can be expected and the biogas yield may drop (Kariyama et al., 2018).

Yu et al. (2013) showed that controlled sedimentation can increase solid retention times (SRT) and that uncoupling hydraulic retention times (HRT) can be beneficial for avoiding microorganism washout in semi-continuous feeding digesters and enhancing biogas production. Benbelkacem et al. (2013) studied the effect of high concentrations of TS (22%<TS<30%) in the segregation of particles and found that at higher yield stresses, denser particles are more stable in the solution and more unlikely to settle. They also showed that a higher mixing power is required in order to achieve a more homogenous solution and elevated rates of biogas yield (due to the lower viscosity and higher yield stresses involved). Hence, there is a need to find a balance between sedimentation rates and mixing intensity to optimise the performance of any mechanically-mixed AD system.

Kaparaju et al. (2008) conducted experiments to assess three different mixing modes for thermophilic digestion (55°C) in 6-litre, mechanically-mixed cylindrical lab-scale digesters: (i) continuous, (ii) intermittent (withholding mixing for 2 hours prior to feeding/withdraw), and (iii) minimal (10 minutes prior to extraction/feeding). The tanks were semi-continuously fed with blended fresh cow manure diluted in water at a ratio of 1:1. Feeding occurred, at 12-hour intervals with volumes of 233 ml/day in order to achieve an HRT of 15 days. Feed TS and VS were 8.1 and 6.2%, respectively. The experiment was carried out for 70 days and started with inoculation of digestate from a pilot tank treating cow and pig manure. For comparison, they also investigated an 800 litre (500-litre wet volume), mechanically-mixed pilot digester operated at 54 ±1°C. The feed (TS=6.5-7.5%, VS=5-6.3%) was in a storage tank 15 minutes prior to feeding. The digester's feeding volume started at 10 l/day and increased to 25 l/day at 8 hours intervals. Continuous mixing consisted of 5 minutes on and off cycles and the mixing was completely withheld for 2 hours prior to feeding for the intermittent regime. The impeller type and speed were not specified and therefore the mixing intensity could not be evaluated. They also tested mixing intensities in 1-litre (400 ml liquid volume) serum bottles in batches at 55°C for a substrate to inoculum ratio of 10/90 and 40/60. The bottles were mixed in a shaker table for gentle (55 times per minute) and vigorous intensities (110 times per minute), whilst minimal mixing consisted of hand-shaking for 1 minute every 12 hours.

The lab-scale results revealed that minimal and intermittent mixing regimes produced 1.3% and 12.5% more methane, respectively. Errors associated with the measurements were not provided and one might conclude that the differences associated with the minimal mixing could be within the error margins. Variances might also have been associated with the constant or intermittent release of biogas from the bulk fluid due to different mixing modes (Kress et al., 2018). For the pilot-scale experiment, the intermittent mixing regime

showed an average biogas yield of 7% greater than for the continuous mixing. They reported solid stratification when intermittent mixing was in place for the lab- and pilot-scale experiments with distinct, high-solid concentrations in the bottom and top of the tank. No analysis of the power consumption was provided for the experiments, which makes a comparison between the level of the benefits brought by different mixing modes difficult.

The effects of mixing intensity showed that for a 40/60 substrate to inoculum ratio, gentle and minimal biogas production started immediately and reached a maximum methane volume of 0.21 m^3/kgVS applied. For vigorous mixing, initial methane production was delayed for 25 days and only produced a volume of 0.18 m^3/kgVS. Acetate and propionate accumulation was noted in the vigorously-mixed bottle but was rapidly consumed after switching from vigorous mixing to gentle mixing, which also improved methane yields by 36%. For the 10/90 ratio, methane production started immediately for all mixing modes but remained low for the vigorously-mixed bottle. After 73 days methane yields for the gentle, minimal and vigorous mixing modes were 0.32, 0.20 and 0.19 m^3/kgVS, respectively. They concluded that mixing modes have a direct impact on biogas and methane yields.

Hoffmann et al. (2008) investigated the effects of mixing intensity (in terms of locally applied shear forces) on digester performance, microbiological communities and their syntrophic relationship in four continuously mechanically-mixed, 4.5 litres (wet volume) digesters (unbaffled). These were mixed at 50, 250, 500 and 1,500-rpm under mesophilic conditions (34±1°C). The digesters were equipped with a 62 mm diameter axial flow impellers (Lightning A-310) and were inoculated with 100% wastewater sludge and left to rest for 24 hours before mixing started. Fresh dairy cow manure was collected twice throughout the 259-day experiment and stored at -20°C. Prior to feeding, manure was screened in a 2 mm sieve and diluted with tap water in order to achieve a desired organic loading rate (OLR). To avoid overloading, the OLR was increased from start-up in the following way: 0.6 (days 1-49), 1.0 (days 50-121), 1.7 (days 122-196), 2.5 (days 197-234), and 3.5 gVS/l (days 235-259). They inserted a trace particle in a 1 mm polypropylene sphere in the digester and tracked it using computer automated radioactive particle tracking (CARPT) for over 24 hours. From this, they were able to compute the spatially-averaged velocity gradients in conjunction with a computational CFD model. Feed and digestate were monitored for TS, VS, total VFAs, soluble chemical demand (sCOD), alkalinity and total ammonium. Biogas was analysed weekly using a gas-chromatographer. Hybridisation and fluorescent in situ hybridization (FISH) were used to determine the comparative relationship between methanogenic populations and syntrophic microbes.

Their results showed that the broad range of mixing intensities had no statistically significant effect on either biogas or methane rates/yields during steady-state conditions. The exception was at the start-up period for the highest mixing speed where lower biogas rates and total VFAs accumulations were noted. Biogas yield increased with OLR in all tanks and overall, VS increased across all tanks due to the shorter retention times. Biogas yields started to level off to a maximum value at higher OLRs. This is expected as the digesters approached maximum OLR, or maximum rates of conversion before overload was reached. Despite similar production rates, sCOD concentrations were consistently higher for the 1,500-rpm impeller speed, when compared to the 50-rpm speed, during the entire experimental period. This is not surprising as sCOD is a measure of the readily available organic matter, which includes VS. Ammonia concentrations were similar over the course of the experiments, at about 1.24 g NH4-N/l, which is near to the inhibitory level shown in table 2.1. The impact of different mixing intensities on the digestion performance and stability were, therefore, minimal. Average fluid velocity gradients varied from 3,500 to 17 s^{-1} and the maximum axial shear stresses, computed from the CARPT and CFD model for impeller speeds of 250 and 500-rpm, were 100 and 800 Pa, respectively. The maximum radial shear stresses were 900 and 1400 Pa (250 and 500-rpm), both found in the vicinity of the impeller. However, in the bulk flow region, shear stresses were much lower (and constant) at approximately 10 and 100 Pa for the radial and axial components.

It is worth noting that despite the high shear stresses, the absence of baffles makes the fluid rotate evenly around the cylindrical tank and subtle changes in the fluid direction are unlikely, thus not contributing to turbulence (i.e., the precursor of mixing and energy dissipation). As such, the velocity and shear rate gradients between two consecutive fluid layers are very low and particulates/microorganisms might just follow a defined flow path only experiencing potential flow disruption in the near-region of the impeller. This may explain the similar biogas yields produced by the different impeller speeds. Modelling of the fluid's rheological properties was not included, therefore a critical analysis of the energy dissipation in the tank, and consequently any potential damage to the microbial cells, was not possible. An analysis of the microbial population showed that mixing intensities did not have an impact on microbial abundance. However, the acetrotrophic methanogen *Methanosarcina* ssp. population predominated at high speeds whilst *Methanosaeta concilii* predominated at low mixing speeds. This is likely due to the increased availability of VFAs at high speeds, findings that are supported by Kaparaju et al. (2008).

The research implies that, despite similar methane yields, higher mixing intensities can be detrimental to some groups of bacteria, as in this case for the two archaea studied. Furthermore, they analysed the microbial flocs (or clusters) and concluded that higher mixing speeds destroyed them, but without affecting the overall digestion stability or

performance. Despite the slightly more stable digester behaviour at the highest mixing regime, the final net energy balance (i.e., power consumption versus methane yields) does not appear to justify such mixing intensities, results that are corroborated by many other researchers (Kaparaju et al., 2008, Bridgeman, 2012, Sindall, 2014, Lindmark et al., 2014a, Kariyama et al., 2018).

Sindall (2014) investigated the impact on biogas production and microbial population of four mechanically-mixed, cylindrically-baffled tanks operating at 0, 50, 100 and 200-rpm impeller speeds. The flat-bottomed tanks (diameter T=200 mm, liquid height H=180 mm, baffles' width b=5 mm, 6 litres wet volume) were equipped with one, four-bladed Rushton impeller (D=50 mm) positioned at a distance of 50 mm from the bottom of the tank. They operated under mesophilic conditions (35°C) and synthetic feed sludge was used with TS=30.5 g/l and VS=28.5 g/l. 0.1 g/l of carboxymethyl cellulose (CMC) was added to the feed to mimic the rheological properties of real sewage sludge. The digesters were fed 5 days a week with 250 ml of feed. The retention time (RT) was set to 33.6 days but there was no mention of the hydraulic or solid retention times. All tanks were mixed at 100-rpm during the start-up period (65 days) in order to ensure homogenous mixing and stable operation. TS, VS, pH, VFAs, alkalinity, biogas and methane yields were measured over the entire experimental time and microbiological communities assessed using quantitative real-time polymerase chain reaction method, or qPCR. A CFD model was used to assess the fluid flow and velocity gradients in the tanks and the results were validated and compared with particle imaging velocimetry (PIV) and positron emission particle tracking (PEPT) measurements.

The results showed that biogas production increased by ~20% when impeller speed decreased from 100 for 50-rpm and fell by more than 50% when the mixing increased to 200-rpm. Biogas production stopped completely before day 100 and 110 in the 100 and 200-rpm digesters during experiments one and two, respectively. However, relatively stable production was observed for the unmixed and 50-rpm digester in both experiments. Similar results were found for methane content in the biogas.

Stability was measured in terms of pH, VFAs concentration and Ripley's Ratio (alkalinity) and the results indicated that at high mixing speeds (i.e. 100 and 200-rpm) the digesters became unstable within days after the mixing speed was changed. They were considered completely soured after 2.3 RT. For the unmixed and the 50-rpm speed digester, instabilities started after 3 RT. In a second experiment, irreversible souring was noted at only 1.8 (200-rpm), 2.3 (unmixed) and 3 RT (100 and 50-rpm tanks) after the change in mixing. Throughout both experiments, pH dropped below 6.5 in all tanks, reaching levels below 5.5 for the higher mixing speeds, where methanogens cannot survive. VFAs

concentration also followed the same pattern and increased to nearly 100 mM in the unmixed and more mixing-intensive tanks, whilst they were considerably lower in the 50-rpm digester. TS and VS remained relatively constant for all tanks before the mixing changed whilst the unmixed and 50-rpm digesters performed better for reducing VS.

Most of the bulk flow experienced local velocity gradients below 20 s^{-1} and less than 10 s^{-1} in 20-85% of the tanks' volume. The maximum gradient of 100 s^{-1} was found near the impeller for the 200-rpm impeller speed. That is not a surprise as shear-thinning, non-Newtonian fluids tend to dissipate energy via viscous forces quicker than purely low-viscosity Newtonian fluids (such as water). In terms of mixing quality, Rushton turbines are radial impellers and are more often used to disperse gases in chemical processes (Paul et al., 2004). They generally create two recirculation loops in the tank (i.e. above and below the impeller region) to promote good mixing in the loop but keep these regions apart. Furthermore, under-dimensioned baffles contribute very little to mixing quality as was shown in the velocity plot results (Sindall, 2014), where the fluid flow is barely affected by the baffles' presence. In this sense, it is not a surprise that up to 85% of the tank's volume experienced velocity gradients less than 20 s^{-1} in the bulk region away from the impeller.

For the microbial community analysis, Sindall showed that methanogenic populations thrived better in low mixing regimes, where acetoclastic *Methanosaeta* dominated. Throughout both experiments, the population of methanogenic bacteria steadily declined over time in all tanks. The results seem to agree with previous works (Hoffmann et al., 2008, Kaparaju et al., 2008), despite the mixing intensities being substantially different amongst the published experiments. Sindall pointed out that this is not only due to the intensive mixing, thus high shear stresses, but also due to the long-term exposure of the bacteria to intermediate inhibitory metabolites produced as a result of the synthetic sludge composition.

As such, the use of synthetic sludge may help standardise the digestion parameters but may not mimic the real-life AD phenomena. The fact that all the digesters failed by the end of both experiments is an example of that. Industrial anaerobic sludge digesters may run for over 5-10 years non-stop.

Kress et al. (2018) conducted a study on a mechanically-mixed, full-scale AD plant (923 m^3 net volume) co-digesting maize silage, grass silage, slurry from pig and cattle production, horse manure and ground corn (65% from energy crops and 35% animal manure). The focus of their research was on the impact of mixing modes on nutrient distribution and power consumption. The tank was equipped with two propellers: an inclined agitator (15 kW) and a submersible mixer (13 kW). It had several sampling collection points and was also equipped with a tube viscometer. The mixing regimes investigated were 20, 10 and 2 minutes per hour but impeller speeds were not given. The experiment was carried

out in two phases: start-up (35 days or ~35% of the HRT) and a test phase (53 days). Mixing modes were applied during 7 days with two samples collected on days 4 and 7 for each period. Samples were analysed for TS, VS, pH, VFAs and alkalinity (FOS/TAC method). The TS feeding loads were 6495 ±1454 and 8513 ±837 kgTS/day, whilst volatile solids loads were 2963 ±727 and 2990 ±358 kgVS/day, for the start-up and test phases, respectively. Note that feeding OLR fluctuated around 3.53 ±0.24 kgVS/m³/day through the start-up phase according to substrate availability. The results showed that there were no significant differences in nutrient distribution at all measurement points (apart from the inlet feeding region) and no dead-zones could be identified. They reported a reduction in biogas release from the digesters as mixing time decreased, but not necessarily less biogas production. They pointed out that 15% of the produced biogas was trapped in the bulk of the liquid at a mixing time of 2 min/h, but was released after intensive mixing was provided for 4 consecutive hours. Interestingly, lower mixing modes resulted in higher non-Newtonian viscosities by the end of each experiment, which could explain the trapping of biogas in the bulk liquid. The hydrodynamic forces acting on a bubble are dependent on the bubbles' mean diameter, the fluids' viscosity and density differences between the two phases. Once biogas is released by the bacteria, one assumes that its inertia will be similar to that of the bacteria carried by the fluid flow. If mixing intensity is low, the inertia of the whole fluid flow is lower. Based on Newton's inertia law, bubbles will then keep their low inertia unless some force is applied (e.g. more mixing energy). For higher viscosities, the resistance of the bubbles to the flow increases, thus more biogas is trapped in the bulk flow and released as soon as more intensive mixing is provided. This phenomenon might only be observed in large-scale digesters because of the dimensions involved (Kowalczyk et al., 2013) and further investigation on the long-term impact on biogas yields and digestion stability is recommended.

Despite the 15% biogas accumulation observed for the shorter mixing times, power savings of 85% were achieved when compared to the longer mixing times. The results of this work corroborate the idea that anaerobic digesters can operate at lower mixing modes in order to save power without significant detrimental effects on biogas production and treatment quality.

A recent review paper published by Kariyama et al. (2018) supports the argument that net energy production efficiency can be optimised with low to moderate, as well as intermittent, mixing. Kariyama et al. (2018) reviewed several works on lab-, pilot- and industrial-scale digesters and summarised that mixing has a range of impacts on microorganisms, scum & foam formation, VFAs, overall efficiency of the mixing modes and HRT/SRT. They highlighted the importance of understanding the dynamics of each AD

when defining mixing systems but provide evidence that higher mixing intensities are likely to be energy-inefficient and have a neutral influence on biogas production or effluent treatment quality.

2.5 Summary and Knowledge Gaps

This chapter has presented a brief introduction and review of the relevant literature relating to anaerobic digestion technology, principles and mixing practices in mechanically stirred tanks.

It has stressed that mixing in AD tanks is essential in order to achieve high biogas production and that it becomes difficult to make a definitive conclusion of the impact that mixing modes and intensities have on the overall anaerobic digestion process. This is mainly due to the diversity in digesters sizes, designs and operational status, mixing types, modes and intensities, plus the broad variability of the feedstock characteristics. However, general conclusions can be drawn:

- High mixing intensities have shown to have either negative or neutral effects on biogas production and effluent treatment quality,

- Low and moderate mixing intensities can keep the AD process stable with relatively good biogas production rates and organic matter reduction,

- Minimal or no mixing seems to have an adverse effect on laboratory-scale AD experiments but has yet to be investigated at the industrial scale.

- There appears to be a lack of research with regards to investigating the sedimentation of dense, non-biodegradable solid particles within mechanically mixed AD systems.

CHAPTER 3 MIXING AND COMPUTATIONAL FLUID DYNAMICS (CFD)

This chapter provides details about the mixing systems used in AD tanks and the mathematical modelling used to mimic the experimental AD tank. Section one gives a brief overview of the importance and types of mixing in AD tanks and highlights the problem of sedimentation of dense, inert solids encountered in many AD plants. Section two presents the relevant mathematical background information used to build the CFD model as well as the rheological models most commonly used to describe sewage sludge. A focused literature review relating to solid suspension in stirred tanks in general, as well as single- and multi-phase, non-Newtonian CFD models used to represent AD tanks in laboratory and industrial scales, is presented in section 3.3. Lastly, section 3.4 provides a summary with insights into the knowledge gaps for this research.

3.1 Mixing in AD tanks – Background and Context

Mixing is needed when two or more substances are brought together and a homogeneous solution is desired throughout the container. The homogeneity 'parameter' can be of any process variable such as temperature, phase and/or concentration (physical), mass transfer and/or reaction (chemical and biological) (Paul et al., 2004). Homogeneity brought by mixing disperses toxins, therefore turning their effects less concentrated and harmful to the microbiological community (Lindmark et al., 2014b). This helps stabilise methane-forming bacteria which are the most sensitive to small changes in temperature and pH.

AD mixing is necessary to maintain the contact between the biomass and bacteria which is of considerable relevance for effective sludge stabilisation. The metabolic activity of acetate- and methane-forming bacteria requires close contact (Gerardi, 2003, USEPA, 1976) and appropriate mixing may guarantee that no dead zones and/or short-circuiting will exist at any point in the digester. The sedimentation of solid particles and the build-up of scum layers can also be avoided by mixing (Ganidi et al., 2009, USEPA, 1976). Studies of industrial equipment showed that inefficient mixing could lead to a reduction of the working volume of anaerobic digester by up to 70%, which can compromise digestion treatment efficiency (Monteith and & Stephenson, 1981, Wood and Tchobanoglous, 1975).

3.1.1 Solid particle sedimentation in AD tanks

As discussed in the previous chapter, the proper mixing and homogenisation of solid particles are vital for an efficient AD process. Having a thorough understanding of the behaviour of the bulk sludge with different total solids concentration (and their distribution throughout the tank) is very important in order to achieve optimal system operation and

avoid recirculation or dead zones (Lindmark et al., 2014b). The complexity of such systems varies widely and depends not only on the concentration of the solid particles but also on the type of waste, particle shape and size, mixing system, tank design, and so on.

Some studies have focused on the distribution and suspension of the solids component contained in the bulk of the sludge (Yu et al., 2013, Lemmer et al., 2013, Yu et al., 2011, Lant and Hartley, 2007) but they all refer to the solid particles as components that will biodegrade and therefore generate biogas through anaerobic digestion. None of these studies, however, consider the dense inert solid particles that build up in the bottom of the tank over time and, as such, do not contribute to biogas production. The loss of effective working volume due to the presence of inert particles sedimentation and accumulation will affect the overall AD process efficiency. The working conditions to which the tank was designed for (such as retention time, organic load and mixing system), will no longer be applicable because of the physical change in the tanks' geometry. Furthermore, digestion can be affected by microorganism wash-out due to shorter retention times, blockage of the heating systems and gas nozzles. Lastly, biogas production might decrease or even stop completely due to these process changes. This phenomenon has been overlooked during the years of AD technology development and particularly with the development of computational models. Only one recent study has addressed the sedimentation of inert solid particles (Klimento et al., 2004).

The build-up of inert solid particles, or sediment, results from the settling of materials having a density difference. Despite the lack of reporting in the literature, most anaerobic tanks face the problem of inert solids sedimentation to some degree. A Severn Trent Ltd internal document showed that digesters that have operated for over five years accumulate significant amounts of sediment which can occupy as much as 11.2% of the volume of the tank. Klimento et al. (2004) reported that their waste activated sludge anaerobic digester accumulated approximately 2 metres of sediment in the tank every four years. In both cases, the mixing energy was within the recommended range (5–8 W/m³) and that screening or de-gritting systems were in operation at the site (USEPA, 1976).

Dense solid suspension, on the other hand, has been thoroughly investigated because of its applicability to the chemical industry. Achieving a balance between mixing energy and dense solid suspension/dispersion throughout a vessel is essential for optimising the chemical reactions and energy efficiency (Paul et al., 2004). Parameters such as complete or uniform suspension, cloud height, off-bottom suspension and minimum speed for just suspension (N_{js}) are the most commonly used parameters for designing and operating a stirred tank containing dense solid particles. N_{js} is defined as the minimum impeller speed where no particles stay stationary at the bottom for longer than 1-2 seconds.

The N_{js} was proposed by Zwietering (1958) and has been used as one of the most crucial parameters for operating a liquid-solid stirred tank (Paul et al., 2004). Many authors have been adapting the Zwietering correlation parameter to find a better fit to specific processes and obtain improved predictions of the N_{js}. This has included new empirical formulations as well as numerical models (Ayranci and Kresta, 2014, Tamburini et al., 2012). Zwietering empirically correlated the main parameters of different Newtonian liquids in a monodispersed-solid stirred tank system in the following way (Zwietering, 1958):

$$N_{js} = S\upsilon^{0.1}\left[\frac{g\,(\rho_s - \rho_l)}{\rho_l}\right]^{0.45} X^{0.13} d_p^{0.2} D^{-0.85} \qquad 3.1$$

where $\mathrm{D}, d_p, \rho_s, \rho_l, \upsilon$ and g are the impeller diameter, particle diameter, solid particle and liquid densities, fluid kinematic viscosity and gravitational acceleration constant, respectively. S is the Zwietering constant and is dependent of the impeller type as well as the impeller diameter to liquid height rate (D/T) and C/T rate (C = impeller distance from the bottom). X is the Zwietering's concentration given by the mass of particle per mass of liquid in percentage. The Zwietering correlation fails to provide an exact N_{js} in many Newtonian and non-Newtonian cases (Tamburini et al., 2012, Fangary et al., 2002). It also does not account for non-Newtonian behaviour and poly-dispersed liquid-solid mixtures. Nevertheless, it provides a good approximation for most processes and is still used as the starting point for designing stirred tanks. Equation 3.1 has been used in this work to estimate the N_{js} for the minimum particle loading investigated, considering the average viscosity (see section 3.2.2).

3.2 Computational Modelling

The development of computational fluid dynamics (CFD) dates back to the end of the1940s, but its boom era is associated with the increase of computational power processing in the last three decades. CFD combines the mathematical descriptions of thermo-fluid mechanics and numerical processing to solve complex industrial problems. The capacity of process optimisation and technological development using CFD triggered the growth of several, paid and free, coding packages (e.g., Ansys® Fluent and OpenFOAM®, respectively). Fluent is a licensed software vastly used across all disciplines, from micro-fluids and blood vein studies to wind and nuclear power plants design. Its diverse use and commercial purpose make if one of the most complete CFD software available to date. The literature shows that is the most used software to simulate stirred tanks and multi-phase flow (see section 3.3). Nevertheless, open-source codes such as OpenFOAM have advantages such as generally lower costs and the ability to manipulate the source code in

order to create new solvers or functionality for specific, and often, new applications. Its main limitations are the lack of a friendly graphical user interface and insufficient details in the programmer's guides, frequently making the progress slow and costly time-wise. Despite the constant upgrades and market dominance of licensed software, open-source code usage and applications have significantly increased in the past decade.

These traditional CFD methods use the finite volume method (FVM) to discretise the domain (grid-based) to solve a set of algebraic equations. They are currently the most used numerical simulation method for solving fluid dynamic engineering problems and have demonstrated to be exceedingly robust and versatile. Nevertheless, the use of alternative methods, such as the smoothing particle hydrodynamics (SPH) has been growing in popularity over the past few years across a wide range of engineering fields. SPH is a meshfree, fully Lagrangian formulation that accounts for individual particle's motion in an open space. It was originally developed for astrophysical research in the late 1970s, but since earlier 1990s have been applied to CFD simulations (Nikolic and Frawley, 2016). The principle of the SPH method relies on the interaction of set of particles within a determined range, controlled by a weight or smoothing function. The discretisation of the Navier-Stokes equations is based on discrete particles, where fluid pressure is derived from the local density, whilst the velocity field and other quantities are calculated from the pressure and density (Liu and Liu, 2010). The continuity equation does not need to be solved because the mass balance is explicitly determined from defined particles with specified masses. Despite its growing application for solving multi-phase flows in stirred tanks, the SPH turbulence predictions and computational costs are still inferior compared to grid-based methods (Nikolic and Frawley, 2016). Regardless of the method, all the approaches mentioned are based on the fundamental theory of fluid mechanics, which are presented in this section, with focus on the FVM method.

3.2.1 Governing equations

The Navier-Stokes set of equations are used to describe the motion of any viscous fluid along with the continuity equation so that velocity and pressure fields can be found. For the continuity equation, it assumes that the mass of the fluid in a given control volume remains constant at all times, the so-called the *continuum hypothesis* (Pope, 2000). At a molecular level, a fluid "particle" or "element" is considered as the smallest volume in the system, or an "infinitesimal". There are two common methods to describe the motion of "infinitesimal" elements. In the first, element(s) are followed along a trajectory in the system and the velocity field is derived from the path over time. This is called the Lagrangian field approach. In the second, the properties of the elements are computed in a fixed grid and

the velocity field is derived for each point as if the particles are passing by (Pope, 2000). This is called the Eulerian approach and is the method adopted here for all phases (more details are given in chapter 7). As an analogy, the Lagrangian description is like sitting on a train while the Eulerian approach is more like sitting on a bench outside, watching the train pass by.

The computational fluid dynamics (CFD) model presented here is based on the finite volume method (FVM) which discretises the modelling domain in a finite number, but large amounts, of smaller control volumes, or cells, where the governing equations are solved (ANSYS Inc., 2013). As such, the continuity equation in the Cartesian coordinate system is given as:

$$\frac{\partial \rho}{\partial t} + \frac{\partial (\rho u)}{\partial x} + \frac{\partial (\rho v)}{\partial y} + \frac{\partial (\rho w)}{\partial z} = S_m \qquad 3.2$$

where ρ, t are density and time, and u, v and w are the velocities in the x, y and z directions, respectively. S_m is a source term that in multiphase modelling, accounts for the mass transfer between phases as well as phase transformation (e.g., vaporisation). Assuming an incompressible fluid flow and no mass exchange within the system, equation 3.2 in vector notation becomes:

$$\nabla \cdot \vec{u} = 0 \qquad 3.3$$

where $\vec{u}$ is the velocity. As for the mass, the momentum applied to any "element" must be conserved in each cell of the domain. The momentum equation is described by:

$$\frac{\partial}{\partial t}(\rho \vec{u}) + \nabla \cdot (\rho \vec{u}\vec{u}) = -\nabla \mathrm{p} + \nabla \cdot \bar{\bar{\tau}} + \rho \vec{g} + \vec{F} \qquad 3.4$$

where p is the static pressure, $\bar{\bar{\tau}}$ is the stress-strain tensor, and $\vec{g}$ and $\vec{F}$ are the gravitational and external body forces. In a multi-phase model, the force $\vec{F}$ accounts for the lift and drag forces acting between phases, among others (see 7.1.4 for further explanation). The stress tensor is given by:

$$\bar{\bar{\tau}} = \mu\left[(\nabla \vec{u} + \nabla \vec{u}^T) - {}^2/_3 \nabla \vec{u} \bar{\bar{I}}\right] \qquad 3.5$$

where μ is the fluid molecular or dynamic viscosity and $\bar{\bar{I}}$ the identity tensor. Note that for an incompressible fluid, as the one assumed here, eq. 3.5 becomes:

$$\bar{\bar{\tau}} = \mu(\nabla \vec{u} + \nabla \vec{u}^T) \qquad 3.6$$

The tensor in parentheses is called the rate-of-strain and its magnitude is called the shear rate ($\dot{\gamma}$) (Chhabra, 2007, Morrison, 2001, Pope, 2000). In Ansys Fluent, the shear rate is written in terms of the second invariant of the rate-of-strain tensor, $\overline{\overline{S_{ij}}}$, derived from the partial derivatives of the Eulerian velocity field, given by (ANSYS Inc., 2013):

$$\overline{\overline{S_{ij}}} = \frac{1}{2}\left(\frac{\partial u_j}{\partial x_i} + \frac{\partial u_i}{\partial x_j}\right) \quad 3.7$$

$$\dot{\gamma} = \sqrt{\overline{\overline{S_{ij}}} : \overline{\overline{S_{ij}}}} \quad 3.8$$

From equations 3.6 and 3.8, the shear stress becomes dependent only on the fluid shear rate and the fluid's molecular viscosity (μ) as follows:

$$\tau = \mu\dot{\gamma} \quad 3.9$$

For Newtonian fluids, the viscosity is constant and the shear stress is a function only of the shear rate ($\tau(\dot{\gamma})$). For any other case (where the viscosity changes with the shear rate) further constrains apply, which is discussed in the next section.

3.2.2 Fluid rheology and sludge behaviour

For any velocity gradient between two consecutive viscous fluid layers, there will be shearing forces acting on the fluids. These forces are responsible for dispersing the motion induced by the mixing device and are called shear stresses. Shear stress (τ) is complex and depends on the fluid viscosity and velocity gradient, which in turn depends on the impeller's geometry and its rotational velocity. All these variables relate to turbulence levels to some extent (Paul et al., 2004).

A Newtonian fluid is characterised by a linear relationship between the shear stress and shear rate ($\dot{\gamma}$) which means that the viscosity (μ) is constant under any condition the fluid is submitted to, varying only with temperature and pressure (Morrison, 2001). Thus, the shear stress is related to the shear rate for incompressible and isotropic Newtonian fluids by equation 3.9. Shear rate is therefore defined as the velocity difference between two adjacent layers of a fluid and is expressed in terms of partial derivatives of the Eulerian velocity field (eq. 3.8).

For any other condition where a dependency between the shear rates and shear stresses occur, the fluid is said non-Newtonian and its study is called rheology. According to Skelland (1967), there are mainly three categories of non-Newtonian fluids: (i) time-dependent, (ii) time-independent and (iii) viscoelastic fluids – all three can happen concomitantly. Category (i) represents liquids where the viscosity might increase or decrease, and then might return, or not, to its previous state, depending on the duration of the shearing. The viscosity in (ii) and (iii) depends on the instantaneous local shear rate and dominates most of the rheological fluids. Fluids falling in categories (ii) and (iii) can be either pseudo-plastic (shear-thinning) or dilatant (shear-thickening), which means that the viscosity will decrease or increase, respectively, when the shear rate increases.

Due to the non-linear dependency of shear rate for non-Newtonian fluids, a local or apparent viscosity (μ_a) is defined by:

$$\mu_a = \frac{\tau}{\dot{\gamma}} \quad 3.10$$

Models have been developed that better describe non-Newtonian fluid's behaviour where the viscosity is a function of shear rate ($\mu_a(\dot{\gamma})$). A more detail description of the models presented below is available in (Paul et al., 2004, Chhabra, 2007). The simplest and most commonly used is the power-law or Ostwald model:

$$\tau = K\dot{\gamma}^n \quad 3.11$$

where K is a measure of the average viscosity of the fluid called consistency index and n is a measure of the deviation of the fluid from a Newtonian, named power-law index or flow index.

Equation 3.11 can describe three different scenarios. For n=1, the viscosity is constant (Newtonian fluid). For 0<n<1 the fluid assumes shear-thinning properties and for n>1, the fluid is said as shear-thickening. By replacing Eq. 3.11 into Eq. 3.10, the apparent viscosity can be described as:

$$\mu_a = K\dot{\gamma}^{n-1} \quad 3.12$$

When the fluid exhibits an initial resistance to flow after being subjected to a shear strain, a term called the initial yield stress (τ_0) is added to the right-hand side of eq. 3.11 for shear-thinning (refered to as the Herschel-Bulkley plastic model) or shear-thickening fluids which obey the same rules. For n=1, equation 3.13 reduces to eq. 3.14 and is called the Bingham plastic model:

$$\tau = \tau_0 + K\dot{\gamma}^n \quad 3.13$$

$$\tau = \tau_0 + K\dot{\gamma} \quad 3.14$$

Other models used to describe the non-Newtonian behaviour of sludge are the Casson model (eq. 3.15) and the Sisko model (eq. 3.16).

$$\tau^{1/2} = {\tau_0}^{1/2} + (\eta_c\dot{\gamma})^{1/2} \quad 3.15$$

$$\tau = \eta_\infty\dot{\gamma} + K\dot{\gamma}^n \quad 3.16$$

where η_c is the Casson's parameter and η_∞ the viscosity of the Newtonian plateau at high shear rates. Other models are available in the literature (Chhabra, 2007, Morrison, 2001), however, the ones presented here can describe the majority of sewage sludge behaviours and cover the model used in this work. A schematic representation of non-Newtonian fluid behaviour is summarised in figure 3.1.

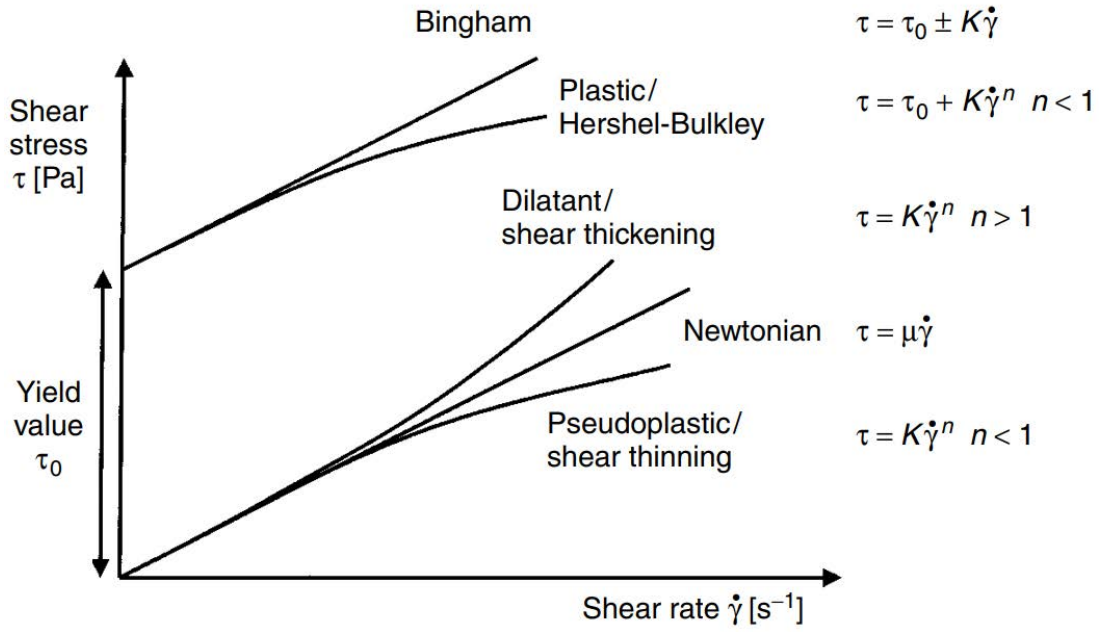

Figure 3.1 : Graphical representation for Newtonian and non-Newtonian fluids flow curves (Paul et al., 2004)

Sewage sludge can behave as a Newtonian or non-Newtonian fluid, depending mainly on the total solid (TS) concentration (Baroutian et al., 2013, Eshtiaghi et al., 2013, Baudez et al., 2011). Researchers agree that below 2.5%, TS viscosity is constant and above this limit the fluid assumes a pseudo-plastic behaviour (Malczewska, 2009). Additionally, high TS concentration might imply that the sludge will not only behave as a shear-thinning fluid but also present a yield stress, which increases for higher TS concentration (Pevere et al., 2006, Spinosa and Lotito, 2003, Forster, 2002, Sanin 2002).

By computationally solving the momentum equations for each cell in the domain, the local and average shear rate can be computed. However, under very low shear rates, non-Newtonian fluids present a nearly constant viscosity, known as the upper plateau limit (figure 3.2-region-A), which in the specific case of this work is associated with the power-law model (eq. 3.12) (Olatunji, 2016). This is a consequence of dynamic molecular/particulate entanglements, where the rate of the molecule's and particulate's entanglement is equal or higher than the shear rate, thus resulting in a constant entanglement rate and high constant value of viscosity. As the shear rate increases (figure 3.2, region-B), the rate between new entanglements and disentanglements decreases until a point where the shear rate is so high that re-entanglements can no longer keep up with disentanglements. This is known as the power-law fluid behaviour. At this point, disentanglements are constant, entanglements are not occurring and the viscosity will not depend on shear rate anymore (figure 3.2, region-C). This state is called the lower plateau limit at infinite shear rate (Olatunji, 2016). The power law model of fluid behaviour does not always give the full range of shear rates where viscosity can vary. As such, viscosity values

outside these limits might generate deviations from the real rheological behaviour of the fluid medium (Cortada-Garcia et al., 2018). For modelling purposes, therefore, defining the upper and lower limits of the fluid viscosity behaviour become necessary.

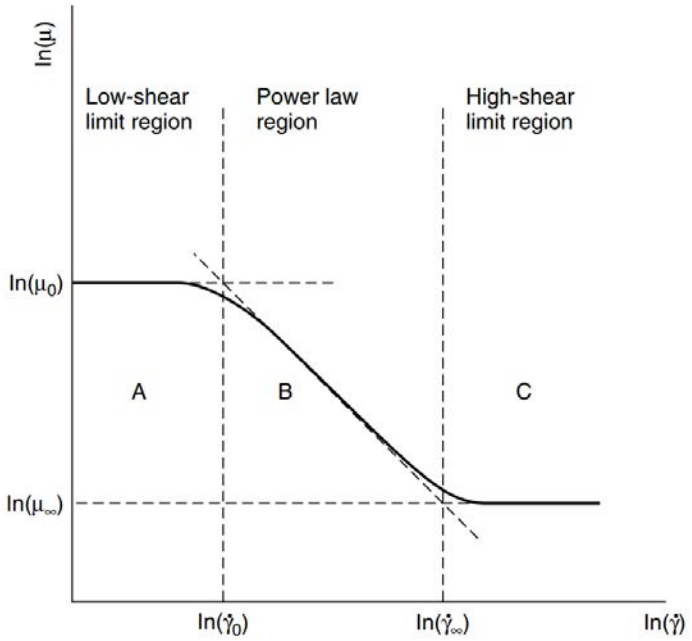

Figure 3.2: Viscosity as a function of the shear rate for shear-thinning fluid (Paul et al., 2004).

An empirical formulation for the average shear rate, based on the impeller's rotational speed (N) in cylindrical stirred tanks has been proposed by Metzner and Otto (1957). Although shear rate varies significantly with increasing distance from the tip of the impeller region, (where the fluid velocities present the highest values and gradients, especially for non-Newtonian fluids), the following equation can be applied for power-law fluids:

$$\dot{\gamma}_{ave} = k_s N \qquad 3.17$$

where k_s is a dimensionless empirical constant and depends on the impeller's geometry. According to Katoh and Yoshida (2009) $k_s = 11.0$ for pitched-blade turbines (PBT). Alternative correlations have been proposed to describe the average shear rate's behaviour to other rheological fluid properties (Campesi et al., 2009, Calderbank and Moo-Young, 1959). In order to make eq. 3.17 independent from experimental measurements, Kelly and Gigas (2003) used CFD to compute the average shear rate on PBT and hydrofoil impellers in the transitional flow regime (Reynolds numbers: 25–400) under a range of shear conditions (0.1–1000 s^{-1}). They found that $\dot{\gamma}_{ave}$ increases not only with increasing impeller rotational speed (as proposed by Metzner and Otto (1957)) but also with decreasing flow index (n) and discharge angle. They proposed a k_s=64.3 for transitional fluid flow. The equation proposed by (Metzner and Otto, 1957) has been successfully used for scaling up stirrer tanks (Wu, 2012).

3.2.3 Turbulence in mixing tanks

Turbulence is generally defined in terms of the dimensionless Reynolds Number (Re), which represents the ratio of inertial forces to viscous forces acting on the fluid. For stirred tanks, Re is given by (Paul et al., 2004):

$$Re = \frac{\rho N D^2}{\mu} \tag{3.18}$$

where ρ is the fluid's density, N rotational speed, D is the impeller diameter, μ is the dynamic viscosity of the fluid. For general applications in stirred tanks, a Re<10 shows laminar behaviour while a Re>10^4 is considered fully turbulent. The flow regimes that fall between these limits are in the transitional flow. However, these assumptions are considered for Newtonian fluids only (Paul et al., 2004, Metzner and Otto, 1957). Considering the rheological properties of sludge, and applying the apparent viscosity equation (eq. 3.12) to eq. 3.18, the Reynolds Number is now given by:

$$Re = \frac{\rho N D^2}{\mu_a} \tag{3.19}$$

Substituting eq. 3.17 into eq. 3.12, and considering only the average shear rate in the impeller region, the apparent viscosity becomes:

$$\mu_a = K(k_s N)^{n-1} \tag{3.20}$$

Substituting eq. 3.20 into eq. 3.19, the resulting impeller Reynolds number for stirred tanks mixing non-Newtonian fluids becomes (Paul et al., 2004):

$$Re = \frac{\rho N^{2-n} D^2}{K\, k_s{}^{n-1}} \tag{3.21}$$

Turbulence is well known to be the main driver of mixing and drastically affects processes such as mass and heat transfer, chemical and biological reactions, gas/liquid/solid dispersion and solids suspension. Several textbooks deal with the understanding of turbulence, its application in mixing devices and its role in modelling (Kresta, 2016, Versteeg and Malalasekera, 2007, Paul et al., 2004, Pope, 2000). Turbulence has been the topic of many scientific works since CFD became popular approximately two decades ago (Tamburini et al., 2014, Coughtrie et al., 2013, Gohel et al., 2012, Wu, 2011, Venneker et al., 2010, Aubin et al., 2004). Therefore, this thesis limits the discussion on turbulence modelling to only that which is relevant to the work presented.

Turbulence is a chaotic fluid motion characterised by sudden changes in velocity and pressure and is considered a very complicated manifestation of the physical principles that rule laminar flows (Pope, 2000). A fully turbulent flow happens when the inertial forces dominate over viscous forces. It is characterised by several structural elements such as

vortices, ejections and eddies. The scale of turbulence varies from kilometres (e.g., in the atmosphere) down to micrometres at the smallest scale of motion, e.g., in stirred tanks. The mechanism that drives turbulent mixing is based on the concepts of dispersion, diffusion and convection, where the energy is spread out throughout the domain (Paul et al., 2004). Given the non-deterministic nature of turbulent flows, it is necessary to establish some structure over time so that it can be resolved by means of mathematical modelling. As such, it becomes relevant to introduce the concepts of length and time scales. A common method used to describe the velocity field in a turbulent flow is based on the fact that the instantaneous velocity fluctuates around a mean value and is normally distributed (Paul et al., 2004). Despite the clear unsteady state of turbulent flows, it is assumed steady on average and hence statistical formulations can be applied. Using averaged velocities to describe turbulence implies a loss of detail but gives a broadly-accepted overall picture of the flow field. This concept is further described in the next section.

Mixing can be divided into three main stages: macro-, meso-, and micromixing (Paul et al., 2004). Macromixing refers to the largest scales of motion in the fluid, such as convection due to temperature gradients. For a stirred tank, a characteristic length for macromixing is the dimensions of the vessel. The microscale represents the mixing at the smallest scale of motion where viscous energy dissipation dominates up to the molecular level. The smallest length scale at which turbulent flows occur is called the Kolmogorov scale (eq. 3.22). Kolmogorov turbulent scales also include time (eq. 3.23) and velocity (eq. 3.24) effects. The energy transfer through momentum exchange from the largest, anisotropic scale to the smallest, isotropic scale of turbulence defines the mesomixing. The concept of turbulent eddies helps to understand the turbulent dissipation process and mixing categories (figure 3.3). The process in which big eddies (highest energy) dissipate into smaller and smaller eddies (lowest energy) up to the smallest length scale, η, is called energy cascade (Pope, 2000) and is illustrated in figure 3.3. The Kolmogorov turbulent scales are given by:

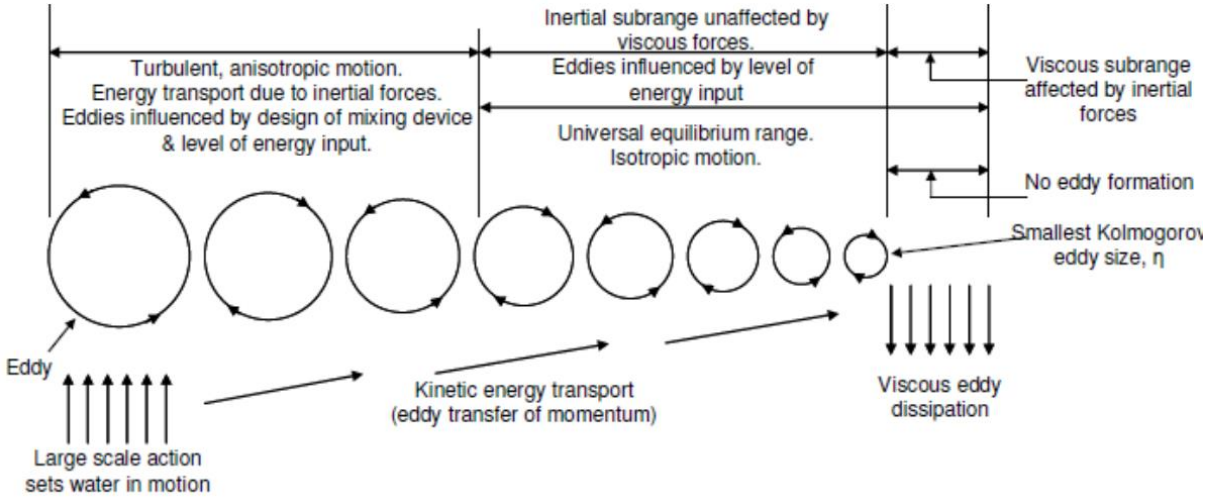

Figure 3.3: Idealised visualisation of the energy cascade for turbulent behaviour. By Sindall (2014) adapted from Stanley and Smith (1995).

$$\eta = \left(\frac{\upsilon^3}{\varepsilon}\right)^{1/4} \tag{3.22}$$

$$\tau_\eta = \left(\frac{\upsilon}{\varepsilon}\right)^{1/2} \tag{3.23}$$

$$u_\eta = (\varepsilon\upsilon)^{1/4} \tag{3.24}$$

where υ is the kinematic viscosity, ε is the turbulence dissipation rate and η, τ_η and u_η are the Kolmogorov length, time and velocity scales respectively.

The relationship between turbulence and solid suspension are based on the drag and lift forces (F_D, F_L) exerted from the liquid to the solid particles (Kresta, 2016, Ayranci et al., 2012). Fletcher and Brown (2009) and Ljungqvist and Rasmuson (2001) showed that lift forces have negligible effects on fluid-solid momentum exchange when $\rho_s/\rho_l > 2$, which is the case in this work. Their results are reinforced in the Ansys Fluent theory guide (ANSYS Inc., 2013). Therefore, drag can be considered as the main force acting on the particle and the particle will be in suspension when this force is balanced with the gravitational (F_G) and buoyancy (F_B) forces. Solids pick-up from the bottom is caused by the mean flow and turbulent eddies coming from the bulk flow and generated by the impeller. This is influenced by the geometry of the tank and the impeller, as well as the presence of baffles and the geometrical relationship of these features such D/T and C/T (where D is the vessel diameter, T the liquid height and C the clearance, or the distance of the impeller from the bottom).

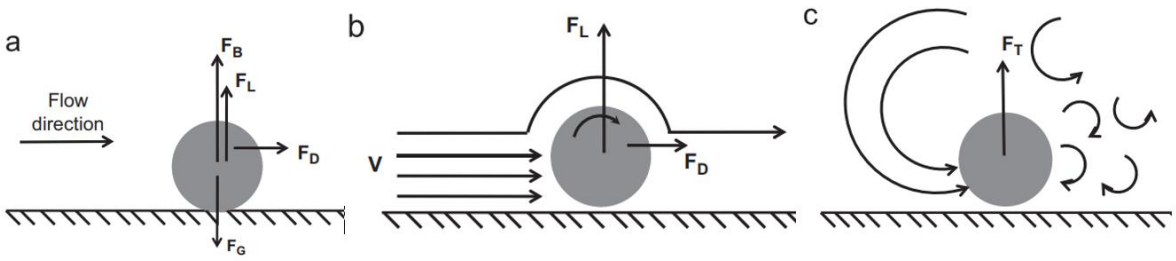

Figure 3.4: Effect of mean velocity and turbulence on a particle on a flat plate. (a) The forces effective on the particle. (b) Mean velocity isolated from turbulence. (c) Turbulent eddies isolated from the mean flow. Adapted from (Ayranci et al., 2012).

3.2.4 Turbulent fluid modelling using CFD

Computational Fluid dynamics models use numerical algorithms to iteratively solve the governing equations in given discretised control volumes and the flow field is built up by interpolating the quantities among neighbour cells in the whole domain. In order to do that, several steps must be followed, such as applying simplifications, selecting the equations to be solved, discretisation of the domain, defining boundary conditions, solving the chosen governing equations, validation of the models and flow visualisation. These steps are further described in chapter 7.

In order to solve the Navier-Stokes equations, the number of unknown variables must match the number of equations. Equations 3.3 and 3.4 together with 3.7 and 3.9 provide a closed set of equations, hence a solution can be found for the Eulerian velocity and pressure fields. However, due to the high number of length scales involved in turbulent flows, an exact numerical solution becomes very expensive computationally. Models have been developed to give a high-precision solution for turbulent flows, such as direct numerical simulation (DNS). DNS is extremely computationally intensive due to the need for grid cells as small as the smallest length scale and require transient simulation with adequate temporal resolutions (Versteeg and Malalasekera, 2007). The large eddy simulation (LES) has proven to be applicable to stirred tanks and requires much less computational power. LES directly solves the large eddies in the flow and uses low-pass filtering, or time- and spatial-averaging of the Navier-Stokes equations, to resolve the smaller turbulent eddies, which are the most computationally intensive. The drawbacks of LES is that finer grids are required for high Reynolds numbers and it is still much more computationally intensive than alternatives such as the Reynold averaged Navier-Stokes equations (RANS) approach (Versteeg and Malalasekera, 2007).

As a practical solution, the modelling of stirred tanks has been predominantly used the simpler, but useful, turbulent models based on the RANS equations. All references to CFD simulation for stirred tanks presented throughout this thesis are based on the RANS model, unless otherwise stated. The RANS models are based on the statistical averaged-

velocities around the mean flow, plus a fluctuating component. In mathematical terms, the mean velocity is given as:

$$u = \bar{u} + u' \tag{3.25}$$

where $\bar{u}$ is the mean velocity of the fluid and u' is the fluctuating velocity component. This concept can be extended to any scalar quantity φ:

$$\varphi = \bar{\varphi} + \varphi' \tag{3.26}$$

Integrating eq. 3.25 over a given time interval Δt, results in the time-average instantaneous velocity becoming the mean velocity whilst the instantaneous fluctuating component is zero. However, the product of two consecutive velocity components are not always zero. Applying this technique to the governing equations results in:

$$\nabla \cdot \bar{\vec{u}} = 0 \tag{3.27}$$

and

$$\rho \frac{\partial \bar{u}_\iota}{\partial t} + \rho \bar{u}_\jmath \left(\frac{\partial \bar{u}_\iota}{\partial x_j} \right) = -\frac{\partial \bar{\mathrm{p}}}{\partial x_i} + \frac{\partial}{\partial x_i} \left(\mu \frac{\partial \bar{u}_\iota}{\partial x_j} - \overline{u'_\iota u'_\jmath} \right) \tag{3.28}$$

where the additional term $\overline{u'_\iota u'_\jmath}$ is known as the Reynolds stress. The new set of equations are called the Reynold averaged Navier-Stokes equations (RANS) (Versteeg and Malalasekera, 2007).

3.2.5 Two-equation models of turbulence

The two most commonly used turbulence models for modelling stirred tanks and mechanically-mixed anaerobic digesters are the standard and the realisable k-ε models. The k-ε models are based on the Boussinesq hypothesis, which postulated that the deviatoric Reynolds stress is proportional to the eddy viscosity or mean rate of strain. This concept is analogous to the relationship between the shear stress and rate of strain, in which momentum is transferred in a Newtonian fluid. The Reynolds stress term is thus given as:

$$-\overline{u'_\iota u'_\jmath} = 2\mu_t \overline{\overline{s_{\iota\jmath}}} - \frac{2}{3} k \delta_{ij} \tag{3.29}$$

where μ_t and k are the turbulent eddy viscosity and kinetic energy, respectively. $\overline{\overline{s_{\iota\jmath}}}$ is the mean rate of strain given by eq. 3.6.

3.2.5.1 The standard k-ε model

The standard k-ε model is the most popular and includes two additional transport equations: one for the turbulent kinetic energy, k, and another one for the turbulence dissipation rate, ε. This is a robust model with good convergence rates and provides decent

results for fully turbulent flows. However, it performs poorly for adverse pressure gradients (ANSYS Inc., 2013). k and ε are calculated from:

$$\frac{\partial}{\partial t}(\rho k) + \frac{\partial}{\partial x_i}(\rho k u_i) = \frac{\partial}{\partial x_i}\left[\left(\mu + \frac{\mu_t}{\sigma_k}\right)\frac{\partial k}{\partial x_i}\right] + G_k - \rho\varepsilon + S_k \quad 3.30$$

$$\frac{\partial}{\partial t}(\rho \varepsilon) + \frac{\partial}{\partial x_i}(\rho \varepsilon u_i) = \frac{\partial}{\partial x_i}\left[\left(\mu + \frac{\mu_t}{\sigma_\varepsilon}\right)\frac{\partial \varepsilon}{\partial x_i}\right] + C_1\frac{\varepsilon}{k}G_k - C_2\frac{\varepsilon^2}{k}\rho + S_\varepsilon \quad 3.31$$

where $\sigma_k, \sigma_\varepsilon, C_1$ and C_2 are empirical constants with standard values of 1.0, 1.3, 1.44, and 1.92, respectively, and S_k and S_ε are source terms. G_k is the generation of turbulent kinetic energy and is a function of the turbulent eddy viscosity μ_t in the following way:

$$G_k = \mu_t\left(\frac{\partial u_i}{\partial x_j} + \frac{\partial u_j}{\partial x_i}\right)\frac{\partial u_j}{\partial x_i} \quad 3.32$$

$$\mu_t = \rho C_\mu \frac{k^2}{\varepsilon} \quad 3.33$$

where C_μ=0.09.

3.2.5.2 The realisable k-ε model

The realisable k-ε model followed on from the standard k-ε and calculates μ_t and the dissipation rate from the exact equation for the transport of the mean-squared vorticity fluctuation (ANSYS Inc., 2013):

$$\rho\frac{\partial \varepsilon}{\partial t} + \rho\frac{\partial}{\partial x_i}(\varepsilon u_i) = \frac{\partial}{\partial x_j}\left[\left(\mu + \frac{\mu_t}{\sigma_\varepsilon}\right)\frac{\partial \varepsilon}{\partial x_j}\right] + \rho C_1 S_\varepsilon - \rho C_2\frac{\varepsilon^2}{k + \sqrt{\varepsilon \upsilon}} + S_\varepsilon \quad 3.34$$

$$C_1 = max\left[0.43, \frac{\eta_{k\varepsilon}}{\eta_{k\varepsilon} + 5}\right] \quad 3.35$$

$$\eta_{k\varepsilon} = \frac{k}{\varepsilon}\sqrt{2S_{ij}S_{ji}} \quad 3.36$$

where C_2=1.9, σ_ε=1.2. The motivation for its development came from the fact that for highly strained flows, some negative normal Reynolds stresses appear in the standard k-ε model, making the results unphysical. Deriving C_μ from the local strain rate prevents the negative Reynolds stresses terms occurring and makes the turbulent flow physics more consistent with reality. The realisable k-ε model better predicts the spreading rate of round jets, such as those from impellers in mixing tanks (ANSYS Inc., 2013, Paul et al., 2004). The main drawback of this model is the production of non-physical turbulent viscosities when used

without care with rotating reference frames. Nevertheless, this model has been successfully used in recent works for modelling non-Newtonian fluid mixing (Sindall, 2014, Bridgeman, 2012, Wu, 2011).

3.3 Literature Review of CFD Models Applied to Solid Suspension and AD Tanks

3.3.1 CFD applied to stirred tanks and solid suspension

Tamburini and his colleagues published a series of papers between 2009 and 2014 where they investigated solid suspension in fully baffled (four symmetrically-positioned baffles), mechanically-mixed, cylindrical, flat-bottomed tanks using CFD. All simulations were carried out using the Ansys CFX numerical code. Particles started at rest in the bottom of the tank with water (Newtonian) as the carrier, or fluid, phase (Tamburini et al., 2014, Tamburini et al., 2013, Tamburini et al., 2012, Tamburini et al., 2011, Tamburini et al., 2009). In Tamburini et al. (2009) they studied the transient suspension of silica particles in the range of 212-250 μm diameter (ρ_s=2580 kg/m³) mixed in water with a six-blade Rhuston turbine (D=T/2). The tank had a diameter of T=0.19m, liquid height H=1.5T, baffle width b=T/10, and an impeller clearance of only C=0.0017m, in order to create a single recirculation loop. The CFD was initiated with all the particles lying on the bottom of the tank (forming a 'bed'), and only deals with one particle loading (9.6% v/v). With an impeller speed of 380-rpm, the Reynolds number was ~57,000, resulting in a fully turbulent flow regime. The CFD model used the Eulerian-Eulerian approach for the multi-phase flow, the RANS "homogenous" k-ε turbulence model, the transient sliding grid (SG) for modelling impeller rotation and a modified version of Gidaspow drag model, according to the local volumetric fraction. They compared their CFD results with experimental visualisations during the formation of the suspension and up to 50 revolutions of the impeller, when complete suspension was assumed to be achieved. They concluded that the drag inter-phase force impacts on both solid distribution and suspension through liquid-particle and particle-particle momentum exchange. They implemented an independent algorithm to avoid an unrealistic maximum volume fraction packing limit. The results showed good agreement with the experimental work, although no advanced techniques for measuring particle distribution, such as positron-emission particle-tracking (PEPT) or laser Doppler velocimetry (LDV) were used. As such, specific details of the solid distribution could only be extracted from the CFD model.

They have used similar configurations for all of their more recent work (Tamburini et al., 2011, Tamburini et al., 2012, Tamburini et al., 2013, Tamburini et al., 2014). The main differences were: T=H=0.19m (apart from (Tamburini et al., 2013), where T=H=0.29m), C=T/3, particle loadings of ~6-12% v/v, particle sizes of 212-710 μm (always

monodispersed) and slightly different particle densities (2,470 to 2,500 kg/m³). They investigated different turbulence and drag models, always using RANS-based turbulence models, sliding grid (SG) and/or multiple reference frame (MRF) models for the rotational reference frame (see section 7.1.1 for details),

In Tamburini et al. (2011), the focus was on the prediction of suspension curves, i.e. solid suspension concentration for different mixing speeds. They concluded that a turbulent free-stream is strictly linked to the drag force, especially for larger particles. As soon they considered drag inter-phase force modelling (e.g., by choosing a suitable drag model), neither particle size nor particle loading seems to affect the quality of the predictions. Grid refinement and rotational frame modelling changes (SG and MRF) give negligible differences to the prediction of the suspension curves.

In Tamburini et al. (2012), they investigated and compared several methods for predicting the impeller speed for just suspension (N_{js}) with the specific purpose of finding the most appropriate method for validating CFD models. They developed, and proposed, a new method for designing stirring based on the impeller speed for sufficient suspension, N_{ss}. N_{ss} is based on their proposed unsuspended solids criterion (USC), a CFD-based method that can be used to judge whether any control volume (cell) in the domain should be considered as suspended or not. They concluded that only two of the CFD-based methods correlated N_{js} well with the original work of Zwietering. Most of the methods underestimated N_{js} to some extent and produced misleading results under different particle sizes and loading. They finally highlight that above N_{js}, increasing mixing speed, thus energy consumption, does not achieve equivalent gains in particle suspension in the fluid volume.

In their most recent work, Tamburini et al. (2014) investigated the influence of drag and turbulence models on solid suspension, using similar systems to their previous research. A modified drag modelling approach proposed by Gidaspow (1994) was used to account for particle-particle interaction and homogenous and asymmetric k-ε turbulence models were tested for four cases: (i) two phases sharing the same k-ε, (ii) k-ε calculated for each phase individually, (iii) fluctuation of the solid phase computed in terms of the liquid phase turbulent terms, and (iv) turbulence terms accounting only for liquid phase fluctuations and neglected for the solid phase. They concluded that the inclusion of extra modelling effects are only applicable in specific cases. The most commonly used, and simpler models (which do not include such effects for drag and turbulence), give the best overall multi-phase flow field predictions over the range of complete and incomplete solid suspensions. Overall, Tamburini and his colleagues' work have provided a significant contribution to the field of solid suspension in stirred tanks. However, it only deals with a

limited range of particle sizes and a specific carrier fluid (water). Furthermore, the research only considers a Rushton impeller, a design that does not contribute to solid suspension but gas dispersion instead (Paul et al., 2004). Nevertheless, the modelling principles are applicable for any type of mixing system where fluid-solid interactions are present in the range of the Reynolds number investigated, i.e. turbulence.

Liu and Barigou (2013) validated their lab-scale, monodispersed and fully-baffled stirred tank CFD model using PEPT. The flat-based, cylindrical vessel (T=H=0.288 m, C=T/4, b=0.1T) was equipped with a 6-blade, 45° pitched turbine, mixing two solid particle sizes individually (d_p~1 and 3 mm, ρ_s=2,485 kg/m³) in water, whose density was adjusted to 1,150 kg/m³ to make the particle tracer neutrally buoyant. Particle loadings varied between 0 and 20% by weight (w/w, or 0-10.4% v/v). They adopted an Eulerian-Eulerian approach together with MRF and the standard *k*-ε turbulence model for the multi-phase CFD simulations. The lift and virtual mass forces were neglected whilst the Coriolis and centrifugal forces were considered. Also, they attempted to include particle-particle interaction force without success, therefore it was neglected. They used the drag force model proposed by Gidaspow (1994). The two-phase velocity field results showed excellent agreement between the experimental data and computational model throughout the tank, apart from at the base where the solid concentration was overestimated (for $N < N_{js}$). They also highlighted that the highest total slip velocities (i.e., the difference between the fluid and particle velocities in the same spatial position) occur near the impeller. The largest slip velocity differences are in the axial direction, which is minimised at $2N_{js}$. At $2N_{js}$, the solid homogeneity reaches 90% of the tank, but at a price of seven times more power consumption. Smaller solid particles are more homogenously distributed than the bigger particles at N_{js}, but negligible differences can be noted as the impeller speed increases. They pointed out that particle loadings up to 10% w/w (5.2% v/v) had no effects on the liquid's velocity field. Above this threshold, the fluid-phase velocity decreases, mainly in the axial component close to the impeller and the walls. Despite these advances, their work deals with only one type of impeller, one particle size at a time, only large particles (d_p~1 and 3 mm) and one Newtonian fluid. Furthermore, there are no gaps between the baffles and the lateral & bottom walls, which might have a significant impact on the energy consumption of the mixer and, to a lesser extent, in the flow field and for the solid suspension (Paul et al., 2004).

Wadnerkar et al. (2016) investigated a broad range of particle loadings in a flat-bottomed, cylindrical tank. The fully baffled, lab-scale tank had the following dimensions:

T=H=0.288 m, C=T/4, b=T/10. The mixing device consisted of a 6-blade, 45°-pitched turbine, top-mounted and with a diameter of D=T/2. The liquid phase had a viscosity of μ=0.0001 Pa.s and a density of ρ_l=1,150 kg/m³. They investigated four particle loadings, i.e. 5.2, 10.6, 20 and 40% w/w for particle size d_p=0.003 m and density ρ_s=2,585 kg/m³. They tested several turbulence models including zero- (mixing length), one- (Spalart-Allmaras) and two-equation (k-ε, k-ω, and their variants) approaches, the Reynolds stress model (RSM) and the large eddy simulation LES. They investigated three different restitution coefficients (i.e., the degree of energy conserved during particle-particle interaction): 0.9 (default), 0.95 and 0.99. Their main conclusion was that, despite minimal differences, a 0.95 restitution coefficient is the most appropriate for solid distribution in the entire tank, whilst 0.90 and 0.99, over-predicts the solid concentration at the tank's bottom and in the impeller region, respectively. All coefficients over-predict solid concentration in the top of the tank. Of all the turbulence models investigated, the RSM approach predicted the flow fields with the highest degree of accuracy but requires much higher computational power. The standard k-ε approach showed the best performance in terms of computational cost and prediction of axial and radial solid distribution. The realisable k-ε produced very similar results. The k-ε RNG showed over-prediction in the region above the impeller and under-prediction below it (both by one order of magnitude difference) whilst predictions with k-ω models deteriorated further in the same regions. They also showed that turbulent dispersion force modelling has a negligible effect at high particle loadings but significantly improves predictions under low particle loadings. From the drag models studied, the Syamlal-O'Brain (ANSYS Inc., 2013) model provided the best solid distribution overall, but still over-predicated solid concentration in the region above the impeller. However, the geometrical extent of this over-prediction region was smaller than that of the other models. Their studies focused on one impeller type, a single Newtonian fluid mixing one big, monodispersed particle size (when compared to the other studies previously discussed) and only for the impeller speed at N_{js}. Therefore, their recommendations are not necessarily valid for smaller particles, impeller speeds under or above N_{js}, or for non-Newtonian fluids. The also used baffles with no gaps from the walls (lateral and bottom), which goes against best practice design for solid suspension in baffled-stirred tanks (Paul et al., 2004).

From the current published literature, it is clear that stirred tanks are overwhelmingly modelled using the k-ε RANS turbulence models and the results are generally in good agreement with experimental data. Researchers have also investigated different fluid-solid interaction forces, such as drag and turbulent dispersion, which presented contradictory results and therefore no general conclusion can be drawn. It is evident that there is a lack

of research on the CFD-based modelling of mixing in non-Newtonian, solid suspension stirred tanks, especially for poly-dispersed systems.

3.3.2 Non-Newtonian fluid and fluid-solid mixing

One of the few works that has investigated solid suspension in non-Newtonian stirred tanks was carried in by Fangary et al. (2002), who used the positron-emission particle tracking (PEPT) for the first time to determine the particle distribution, spatial occupancy, velocity distribution and N_{js} in a monodispersed liquid-solid mixture. The flat-bottomed cylindrical tank had a diameter of T=0.290 m and an impeller of D=0.6T with a clearance C=T/3. Two hydrofoil impellers (A410 and A320) were investigated having an upwards pumping mode. No information about the liquid height was provided. They used a power-law model to describe the highly viscous, non-Newtonian behaviour of two mixtures of carboxymethyl cellulose (CMC) at 0.70 and 0.85 % w/w. They calculated the average shear rate using eq. 3.17 (55-128.3 s^{-1}) and the Reynolds number using eq. 3.21 (329-1962). One particle size (d_p=8 mm) and two particles densities (1200 and 1400 kg/m³) were investigated under particle loadings of 0.83 and 4.17% v/v for the less denser particles and 0.71-3.57% v/v for the more denser ones. The results showed that both mean particle velocity and circulation reduce as particle loading increases. When complete suspension is achieved, particle concentration was higher in the bulk central region resulting in an inhomogeneous particle distribution. They highlight that the Zwietering's correlation fails by a large margin to predict the N_{js}, probably due to the large particle size and rheological properties of the fluid modelled. Despite this pioneering research, important information such as liquid height, axial solid distribution and cloud height are missing, plus upwards pumping does not contribute to solid suspension. The authors did not provide any information on the specific determination of the viscosity dependence on the shear rate, other than empirical calculations, and no limits were established, thus making a hydrodynamic analysis of the fluid-solid impossible.

3.3.3 Stirred tank of AD tanks

In the past two decades, several authors have investigated laboratory and industrial scale AD tanks with the help of CFD models. Vesvikar and Al-Dahhan (2005) built a CFD model of a gas mixing digester (V=7.2 litres) with a draft tube using water and air for the liquid and gas phases. They studied several tank designs and flow rates and validated their model against experimental data, which showed a good agreement for the velocity field, recirculation and stagnation zones, but not for the velocity magnitudes. They concluded that a wider draft tube and a conical-shaped bottom to the tank improve the velocity field in

the outer region, decreasing dead-zones and improving mixing. The mismatch in velocity magnitude is likely to be because the experimental velocity measurements used sludge at TS=5% (non-Newtonian fluid) whilst the CFD models used the properties of water (Newtonian fluid). Furthermore, they used a standard k-ε model for the liquid phase and zero-equation mixing length turbulence models. Despite the liquid phase being reasonable predicted by the turbulence model, the gas phase is unlikely to be represented by a single velocity scale (ANSYS Inc., 2013).

Wu and Chen (2008) implemented a single-phase, non-Newtonian, power-law model to investigate gas mixing in pilot-scale AD tanks (1-5 m³) using CFD. They used the standard k-ε approach for modelling turbulence and the model was validated against experimental velocity measurements using CMC at concentrations of 0.1, 0.2, 0.3 and 0.4% w/w to mimic the rheological behaviour of sludge. Water and sludge at TS=2.5 % were simulated under inlet velocities of 2 and 5 m/s. They concluded that the non-Newtonian behaviour of liquid manure increases with TS and that the power input per unit volume increases logarithmically with scaling-up. There were clear differences between mixing water and non-Newtonian fluid, where velocities are under-estimated near the walls. This is likely to be due to the incorrect definition of the shear rate and viscosity limits. For example, it is known that slurry at TS=2.5% behaves as a Newtonian fluid, but was modelled as a non-Newtonian fluid with shear-rate limits of 226–702 s^{-1}. As highlighted by Cortada-Garcia et al. (2018), the highest viscosity gradients in non-Newtonian fluids simulated with CMC occur in the range between ~0.1 to 100 s^{-1} where, after that, viscosity changes are almost negligible. They also concluded that increasing inlet velocity only improves the mixing zone, with little impact in dead-zones. No details of the grid or independence tests are provided.

Wu (2010b) was one of the first authors to model a full-scale anaerobic digester (4888 m³) to determine the most efficient mixing mode (i.e., either upwards or downwards pumping). CFD was used to assess the flow patterns of an egg-shaped, mechanically-mixed tank (with a draft tube) rotating in the range of 400 and 750-rpm for water and power-law based non-Newtonian fluids. The Reynolds number varied widely, from 717 for the highest viscous fluid (at 450-rpm mixing speed) to 1.95×10^6 for water and 750-rpm, covering a broad range of transitional to fully turbulent flows (these were modelled using realisable k-ε). Mixing power was the only validation method, thus the CFD velocity fields cannot be compared. Furthermore, there were substantial differences between the experimental and simulated power number (up to 42.4%), which the authors attributed to the small MRF region due to physical restrictions associated with the draft tube. In addition, the boundary layer might have not been properly resolved, which is a drawback of the RANS turbulence models.

The author concluded that the egg-shaped AD tank mixing upwards from a draft tube is more efficient than downwards. He noted that the flow patterns for Newtonian and non-Newtonian fluids are similar and that mixing energy increases exponentially whilst the average velocity increases linearly as impeller speed increases. In addition, the research showed that mixing is 43.8-49.7% more efficient for mechanical methods than for slurry recirculation, as well as for an egg-shaped verses cylindrical tanks.

Bridgeman (2012) used a 6-litre, cylindrical vessel mixed by two 6-blade, Rushton turbines rotating in the range of 20-200-rpm. Bridgeman used the rheological characteristics of dairy cattle manure provided by Achkari-Begdouri and Goodrich (1992), and previously used by (Wu and Chen, 2008, Wu, 2010b), as it was considered similar to the non-Newtonian behaviour of sewage sludge. The main dimensions of the tank were: T=0.160m, H=0.305m, D=0.070, and C_{imp1}=0.0475 and C_{imp2}=0.1975, where imp1/imp2, are for impeller one and two. Bridgeman investigated the standard, realisable and RNG k-ε models as well as the standard k-ω and RSM models, totalling 5 turbulence models. The MRF approach was used to simulate the impeller's rotation whilst the SG model was discounted because of its high processing costs. No-slip conditions were applied to the walls and free-slip was assumed in the top surface (open liquid). All standard convergence monitoring residuals were set to $1x10^{-5}$ and mixing power was used to validate the model. The grid convergence index (GCI) test proposed by (Roache, 1998) was applied with three different grid densities. RSM was found the most suitable turbulence model for this type of reactor whilst the realisable k-ε was recommended when considering the computational costs involved. Despite simulating highly viscous fluids and low mixing speeds, no details of the Reynolds number was provided. Laminar flow could better represented the flow regimes, especially for higher TS concentrations and lower impeller speeds, indicating that the use of turbulence models would be unnecessary (Liu, 2014). An assessment of the stagnant zones (defined as regions experiencing mean velocities less than 5% of the maximum velocity magnitude) indicated a second order polynomial relationship with total solids (TS). A reduction in the mean velocity followed by an increase in stagnant zones was noted as TS increased. Mixing speed did not appear to have any impact on biogas yield, despite only having a short-term digestion (i.e., 11-days), where common AD sewage sludge retention time is ~15-days. Nevertheless, Bridgeman was one of the first authors to link biogas production and mechanical mixing using CFD.

Craig et al. (2013) studied rheological behaviour changes of sewage sludge (raw and digestate) in a full-scale, draft tube anaerobic digester (V=1250 m³) powered by a

rotating triple-helix-blade impeller at 500-rpm. The MRF treatment along with the shear stress transport (SST) k-ω turbulence model was applied. No-slip conditions were applied to the walls and free-slip was assumed in the top surface (open liquid). The liquid-gas interface was initially tested using the volume-of-fluids (VOF) model in 2D. Despite jet formation on the exit of the impeller towards the open-"air", the return to the liquid surface into the fluid volume showed unrealistic physical interaction in the 2D model. A complete 3D VOF modelling was considered computationally too expensive and, therefore, was not attempted. The convergence residuals of the governing equation terms were set as $1x10^{-3}$, apart from ω, which was set as $5x10^{-3}$. The grid convergence index (GCI) test proposed by (Roache, 1998) was applied with three different grid densities but only for water. They used the Herschel-Bulkley non-Newtonian model with various indexes to represent the viscosity change as sludge was digested and compared the results to water.

The results showed that despite the power consumption per unit volume did not vary significantly for water and raw sludge (9.92 and 10.40 W/m³, respectively), the velocity fields and magnitude varied considerably (0.3 and 0.03 m/s, respectively), mainly in the bulk and bottom regions of the tank. The velocity distribution in the raw sludge and digestate was also considerable, but smaller differences were seen through the bulk and bottom regions of the tank. It is interesting to note that despite the symmetry of the tank, the velocity fields are not symmetrical, indicating a non-convergent simulation. Residuals of 10^{-3} are generally too large to consider solution convergence.

Dapelo et al. (2015) used an Eulerian-Lagrangian approach to simulate a lab-scale, gas-mixed anaerobic digester (V=4 litres) mixing sewage sludge mimicked by three CMC solutions in water (i.e. 2, 4 and 8 g/l), under three flow rates, (2.05, 5.30 and 8.63 ml/s) and bubble sizes varying from 7.01 and 13.8 mm. The model was validated using the particle image velocimetry (PIV) technique for the averaged-velocity field and GCI test was applied for grid independence test. The authors used the open-source CFD code OpenFOAM and the Launder-Gibson (Gibson and Launder, 2006) model to account for turbulence, despite no information on the Reynolds numbers range being given. Considering the highly viscous fluid investigated, and the low velocities of the rising bubbles (maximum 0.04 m/s from the PIV measurements for the less viscous fluid), it is likely that the flow regime is in the laminar region, therefore making the use of turbulence models inappropriate.

Overall, the results of the velocity magnitude, flow pattern and vorticity positions agree between the measurements and simulations. However, the CFD model under-predicts velocity magnitudes near the bubbles' column and in the bulk flow, especially near the bottom. It also over-predicts velocities at the upper region close to the top surface of the fluid column. They attribute these divergences to the large cell size in the central region and

the sudden expansion of the bubbles, introduced into the system as pointwise elements. The velocity over-prediction is attributed to the no-slip boundary condition at the top surface, which leads to the loss of momentum transfer because of the inhibition of water hump dispersion, a phenomenon that is evident in the experimental measurements. The CFD-computed average shear rates presented in the regions near the bubble column strongly disagree with the PIV measurements and to a lesser extent, in the bulk flow. The disagreement was attributed to the same factors but while the shear rate range varied from 100 to 500 s^{-1}, and the average shear rate is in the range between 0.1 and 1 s^{-1}. No information on local shear rate was provided, but as previously discussed, the range of CMC solutions where the viscosity is highly dependent on the local shear rate is below 100 s^{-1}. Therefore, the disagreements between the CFD results and measured values are likely to be due to the modelled shear rate range.

In one of the most recent works Meister et al. (2018) investigated the flow field in one conical-bottomed, cylindrical AD tank (4888 m³) and one egg-shaped tank (2,500 m³). The conical-bottomed tank used a helical impeller, similar to that presented by (Wu, 2010b), and a 4-blades, 45°-pitched turbine, both pumping upwards. For the egg-shaped tank only a helical impeller was used but for tanks the mixing devices are centred within the tanks. The egg-shaped tank also accounted for sludge recirculation pumping with the inlet on the top of the tank and outlet in the bottom. They simulated Newtonian (water) and power-law, non-Newtonian fluids with TS concentrations varying from 2.5 to 12.1%, as in Achkari-Begdouri and Goodrich (1992). MRF treatment was used for the rotational region and speeds were set to 840 and 600-rpm for the PBT and helical impellers, respectively. The mass flow rate for the liquid recirculation was 36.124 kg/s and the egg-shaped tanks were investigated with solely pumped recirculation, solely mechanical mixing and then both together. No-slip conditions were set for all walls, including the impellers, whilst shear-free symmetry boundary conditions were prescribed for the top surface. Two turbulence models were investigated: realisable k-ε and standard k-ω. Again no information on the Reynolds numbers was provided, despite the much higher rotational speeds. The GCI test was used for grid independence for three mesh densities.

The results for the velocity field in the cylindrical tank shows a relatively constant velocity of 1 m/s inside the entire draft tube and lateral walls, whilst it was halved for the bulk region. No significant differences in the velocity field are noticed between impellers, apart from a slight shift in the position of the vortices towards the tank's bottom for the helical impeller. They did not define the most suitable turbulence models because of the lack of model validation, which was based on the work of Wu (2010b). Their decision to use the realisable k-ε model for all other simulations was based on previous works (Sindall, 2014,

Bridgeman, 2012, Wu, 2011). They then compared the velocity fields produced by pumped recirculation, mechanical mixing and both together for TS=2.5%. They conclude that combined mixing provides the best homogenous mixing properties and the highest velocity magnitudes throughout the whole tank. The combined system breaks the symmetrical mixing seen in mechanical devices, whilst decreasing the presence of dead zones to nearly zero, which represents 26.39% of the bulk region with velocity magnitudes lower than 0.01 m/s. They further analysed mixing modes for the egg-shaped tank for increasing TS concentrations and conclude that mixing quality deteriorates as TS increases, especially in the bulk region at distances away from the draft tube and lateral walls. No details about either the power consumption or the biogas yields are given. Therefore, no conclusions can be made on the energy balance. Furthermore, the use of rheological data from dairy cattle slurry has been consistently used in the literature to represent the non-Newtonian behaviour of sewage sludge but it does not hold for every case. Eshtiaghi et al. (2013) highlight that sewage sludge's rheological characteristics highly depend on the treatment type for solid concentrations in the range of 3%<TS<10%. Additionally, sludge can behave as a thixotropic colloidal fluid at high shear rates and as a polymer at low shear rate. Seyssiecq et al. (2003) draw special attention to the shear rate range used to characterise sewage sludge, which can vary from 0.01 up to 4000 s^{-1} for a broad range of TS concentration. Therefore, caution should be taken when modelling rheology in CFD codes as it is clear that viscosity has a strong impact on the nature of the velocity fields and energy dissipation through turbulent mixing.

3.4 Summary and knowledge gaps

This chapter has presented the published research relating to the main mixing methods used for AD tanks and why it is important. Mechanical, gas and liquid recirculation mixing systems have been investigated for a range of configurations and across several designs, sizes, mixing modes and viscosities. The chapter also highlights the lack of published information regarding the sedimentation of inert dense solid particles, a phenomenon that can impact on the overall energy efficiency of the process in terms of sludge treatment quality, biogas production and mixing energy. It is also shown that turbulence plays a crucial role in mixing, especially for a homogeneous distribution of temperature and pH, as well as suspension of dense particles. The chaotic nature of turbulence and its relationship with the fluids' viscous properties (in terms of the energy dissipation from the largest to the smallest scales of motion) led the development of several mathematical formulations for industrial mixing and solid suspension. Suspension of dense

particles in stirred vessels occurs mainly through the momentum exchange between the carrier and solid phases as a consequence of the drag force in turbulent flows.

The literature review showed that CFD has been broadly used to simulate stirred tanks, both for solid suspension and anaerobic digesters. Most of the research relates to solid suspensions that deal with mono-dispersed particles of small sizes (<1mm), Newtonian fluids and high mixing speeds. One study addressed mono-dispersed solid suspensions in non-Newtonian fluids but, so far, no published papers have dealt with either poly-dispersed particles or CFD modelling. This is a clear gap in our understanding of such systems.

CFD works performed in AD tanks are focused mainly on the understanding (and optimisation) of the mixing system looking for better homogeneity for less mixing energy. Single- and multi-phase models involving all manner of mixing types and tank designs have been investigated. However, no research considers the influence and presence of inert particles in the flow patterns and velocity fields. Again, another limitation in the wider understanding of AD processes.

Finally, it would appear that there have been limited studies linking biogas production with CFD models in the literature. From what has been published, the research indicates that increasing mixing intensities has no (or little) effect on biogas yields. This may, or may not, be entirely correct and there is a need for more research to investigate the validity of this hypothesis.

CHAPTER 4 AIMS AND OBJECTIVES

The aim of this project is to investigate an energy-efficient mixing regime designed to avoid the sedimentation of inert solids in a mechanically-mixed anaerobic sludge digester. The intention is to find a balance between mixing energy and biogas yield such that the energy input is minimised without imposing a negative impact on biogas production.

In order to achieve this aim, the following objectives have been set:

- Characterise sewage sludge and sediment particle distribution of samples from full-scale anaerobic digestion tanks.

- Quantify the impact of inert particle loadings, sedimentation and/or suspension on sludge treatment quality and biogas yields in laboratory-scale, mechanically-mixed digesters.

- Assess the flow fields and sedimentation/suspension of sewage sludge solid particles inside a laboratory-scale anaerobic digester under different mixing scenarios through CFD simulations and physical experiments.

- Determine the minimum mixing intensity required to keep organic and inorganic particulates in homogeneous suspension throughout the digester.

- Monitor biogas yields and methane content during a range of mixing conditions and assess the parameters that increase biogas yield with the highest calorific value.

The outcomes of the research were intended to be three-fold;

- To define appropriate, high-efficiency mixing regimes that can be translated from the laboratory scale through to real-word industrial anaerobic digesters.

- To establish and validate new approaches for the physical and computational modelling of mechanically-mixed anaerobic sludge digesters that include particle sedimentation effects.

- To investigate and quantify the performance of digesters in order to inform the future design of AD processes in wastewater treatment plants in the UK and globally.

CHAPTER 5 MATERIAL AND METHODS

This chapter provides information on the material and methods used in the laboratory-scale anaerobic digestion (AD) experimental work. Section 5.1 describes the laboratory setup for the AD experiment whilst the characterisation of the sewage sludge and inert solid particles taken from real sediments found in industrial AD tanks is described in section 5.2 and 5.3. These two sections provide the physical parameter information used to model the fluid flow of the tank with computational fluid dynamics (CFD) methods. Finally, in section 5.4, the methods used to control and monitor the AD process, determine the quality of the sludge treatment and measure the biogas yield are explained.

5.1 Semi-continuous Laboratory-scale Anaerobic Digestion Experiments

5.1.1 AD lab-scale experimental setup

To investigate the impact of mixing regimes and inert solid sedimentation in the AD tanks, a total of five lab-scale digesters were utilised. Four identical, 6-litre tanks (named D1, D2, D3 and D4 hereafter) were used to investigate the different AD mixing/process parameters whilst one, 5-litre (named GD) glass digester was used as the control tank (i.e., a tank where no parameters were changed from beginning to the end of the experiment). The GD control tank had a 1-litre headspace for gas holdup and was equipped with a top-mounted, double, 6-blade Rushton turbine positioned at a distance of ~1/5 and ~4/5 from the bottom of the total liquid height of the tank. It was heated at 37±1°C from the tank's flat-bottom by an electrical resistance heating pad (see figure 5.1). The other four identical D-tanks had a liquid capacity of 6 litres each and ~1.73 litres of head space for gas holdup. The D-tanks are an adapted version from a previous project (Sindall, 2015) and follow the design guidebook for stirred tank solid suspensions (Paul et al., 2004). They are equipped with one symmetric 4-pitched-blade turbine (PBT) centred positioned at a distance of 1/3 of the height of the tank from the flat-bottom. The rotation direction (clockwise) was chosen to impose a down-flow pumping regime, hence contributing to the solid suspension behaviour. They were heated by means of a water bath tank kept at 37±1°C. The water bath tank was equipped with a Grant® thermostatic circulator Y38-VFPK, which includes built-in temperature control. A mercury thermometer (±0.1°C) was placed in the corner with the poorest mixing region and used as a second temperature control (see figure 5.2 and 5.3). Constant temperature monitoring inside the tank was performed by placing a mercury thermometer inside the tanks through the feeding hole (see figures 5.1-a and 5.2). As such, no biogas could leak and negligible amounts of oxygen were transferred into the sludge

inside the digesters. The impeller speed was kept unchanged and no inert particles were added inside the tank for the control digester (GD) throughout the entire experimental time.

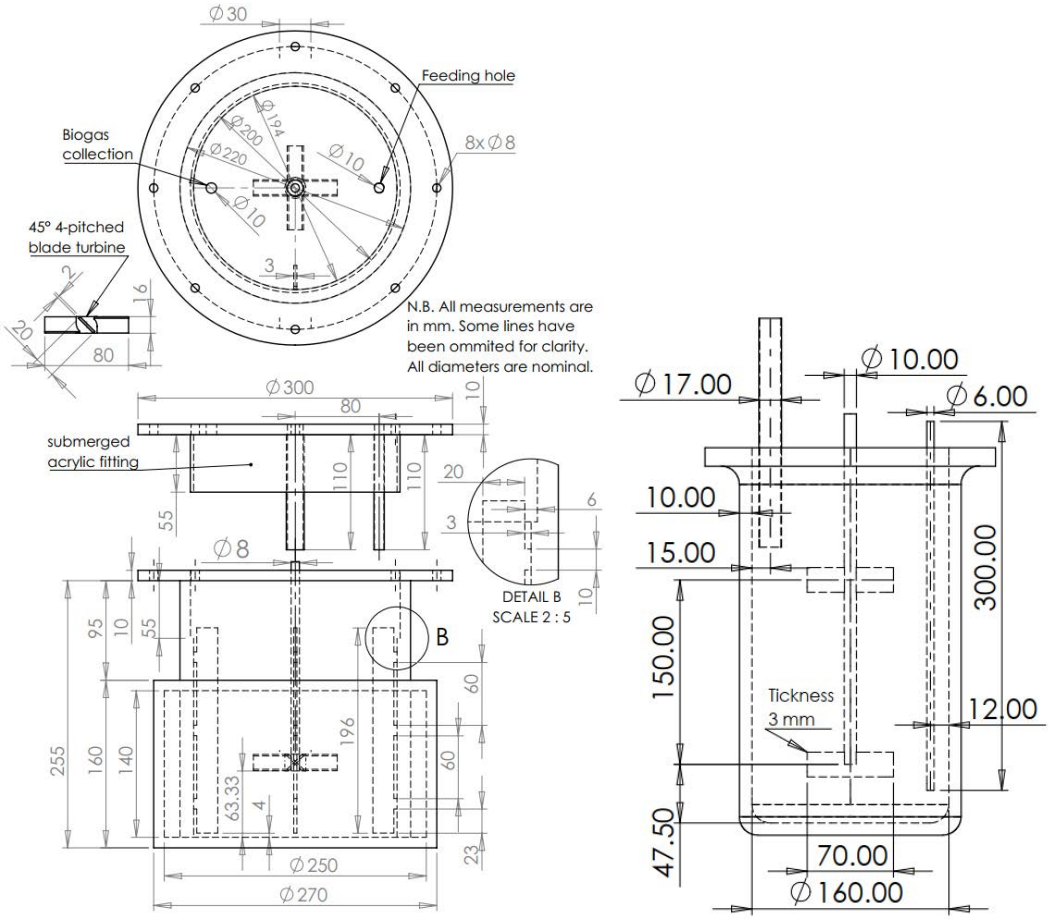

Figure 5.1: Detailed schematic view of four identical D-tanks and (b) the GD digester. Figures are not scaled and photographs of the digester are provided in figures 5.2 and 5.3.

The laboratory work consisted of two main parts: (i) sewage sludge and inert sediment characterisation, and (ii) semi-continuously fed anaerobic sludge digestion. In (i), inert means that the particles are non-biodegradable and, therefore, do not contribute to biogas production (see section 6.1.1 for details). In the first part (i), sewage sludge was characterised in terms of total, volatile and fixed solids (abbreviated as TS, VS and FS, respectively) (sections 5.2, 5.4.1.1 and 6.1) and its rheological behaviour (sections 5.2.2 and 7.1.5), whilst the inert sediment found in industrial tanks was characterised in terms of the particle size distribution (PSD) and its density (sections 5.3 and 6.1.3). In the second part, (ii), mid-term anaerobic digestion of real sewage sludge samples were investigated in the laboratory in order to find the impact on sludge treatment and biogas yields in the presence of inert particles under different mixing regimes. The investigation methodologies are presented in this chapter and the results in chapter 6.

For the main experimental work of part (ii), two similar experiments were carried out but with different time scales. The timeline for the experimental setup can be seen in table 5.1. The first experiment (Exp1) was carried out for 63 days (10th October to 12th December 2017) while the second experiment (Exp2) continued for 90 days (24th January to 24th April 2018). Both experiments were divided into four phases. In phase 1 (P1), 14 days were allowed for inoculation and a steep increase of the organic loading rate (OLR) (section 5.1.2). During the acclimation (second phase - P2), constant feeding was carried with no other changes in order to stabilise digestion and biogas production (section 5.1.3). Mixing speed was kept at 100-rpm in all tanks during P1 and P2. In the third phase (P3), impeller's speeds in D1, D2 and D3 were changed to 200, 400 and 600-rpm, respectively, whilst kept unaltered in D4 and GD (e.i. 100-rpm). Finally, in phase 4 (P4), sand particles were added only into the D tanks and mixing speeds were kept as in P3.

The mixing regime during P4 of Exp2 was modified in D3, following the final results from Exp1 and partial results of Exp2 (see chapter 6 for results and discussion). Constant mixing at 600-rpm during P4 was changed to continuous mixing but with long, low-intensity and short, high-intensity intermittent mixing regimes in the end of day 58. From day 59 onwards, the impeller speed was kept at 100-rpm for most of the time during the day and only increased to 600-rpm for five minutes prior, and during, the feeding process, totalling a maximum of 15 minutes high-intensity mixing per day (see table 5.1).

The control digester (GD) experimental setup incorporated the same changes as for all tanks during the P1 (inoculation) and P2 (acclimation) stages. For the rest of the experiments, the setup conditions of P2 were maintained (i.e. the same feeding rate as for all other tanks, but neither mixing speed changes (P3) nor inert solid particles additions (P4) were applied. These conditions were intended to control the interference of unmonitored parameters on the digestion and biogas stability in the D tanks (e.g., intoxication by high ammonia concentrations or heavy metals) thus preventing, as much as possible, potential misinterpretation of the experimental results. The geometrical differences between the tanks D and GD were considered to have a negligible effect on the digestion performance. The double impeller of the GD tank provides sufficient mixing at 100-rpm, enough to maintain a homogenous substrate availability and temperature distribution. Despite no specific tests were carried out to initially test this assumption, it became evident throughout the experiments that these considerations hold valid (see results in Chapter 6).

Table 5.1: Experimental setup timeline and a detailed description of the four phases.

Phases	P1-Inocculation	P2-Acclimation		P3-Speed change		P4- 5% v/v sand particles added over the first 4 weeks			
Experiment	Exp1&2	Exp1	Exp2	Exp1	Exp2	Exp1	Exp2		
Time	Day 1-14 (14 days)	Day 15-29 (15 days)	Day 15-36 (22 days)	Day 30-35 (6 days)	Day 37-50 (14 days)	Day 36-63 (28 days)	Day 51-58 (7 days)	Day 59-90* (33 days)	
	Speed (RPM)								Sloppy sand particles addition (vol/vol)
Mixing mode	continuous	continuous		continuous		continuous	continuous	interm. D3	
D1 - PBT	100	100		200		200	200	200	+ 5% v/v / week
D2 - PBT	100	100		400		400	400	400	+ 5% v/v / week
D3 - PBT	100	100		600		600	600	**100/600***	+ 5% v/v / week
D4 - PBT	100	100		100		100	100	100	+ 5% v/v / week
GD - Rushton	**100**	**100**		**100**		**100**	**100**	**100**	**no particles added**

*from day 59 onwards in Exp2, D3 was operated at a continuous, but long, low-intensity (100-rpm) and short, high-intensity (600-rpm) intermittent mixing regime. The impeller speed was only increased for a maximum of 15 minutes, prior and during the feeding process.

Experimental phases 1 and 2 (P1 and P2, detailed in sections 5.1.2 and 5.1.3) where designed to inoculate and stabilise the digesters with a steep increase in the organic loading ratio (OLR) so that the microorganisms present could adjust to the new system and avoid wash-out (Gerardi, 2003). The third phase (P3) was designed to investigate the short-term impact of different mixing intensities on biogas yields and sludge treatment quality prior to adding the inert particles in all D-tanks in phase 4 (P4). Whilst the impeller speed in the control digester and in D4 were kept unchanged during all phases, the D1, D2 and D3 tanks experienced a speed change so that the inert particles for phase 4 could be partially or totally suspended. The speed change was designed in accordance with the system's geometry and liquid/solid physical properties (Paul et al., 2004). The tank with the highest impeller speed, D3, was chosen so that the minimum speed for 'just suspension' (referred to as the 'N_{js}' – see section 3.1.2 in chapter 3 for details) was achieved for the minimum particle loading, i.e. 5% v/v (Zwietering, 1958). For D1 and D2, however, intermediary mixing intensities were set so that a broad range of mixing regimes could be investigated (table 5.1). The Zwietering correlation method was preferred for its simplicity and broad use amongst researchers. The N_{js} is defined as the minimum impeller speed in which no particles remain stationary in the bottom of the tank for longer than 1 or 2 seconds and is defined by a series of correlated parameters for a given stirred tank (eq. 3.1).

The fourth experimental phase (P4) investigated the impact of different mixing regimes on solids suspension/sedimentation, sludge treatment and biogas yield/quality. It consisted of additions of 5% v/v (volume/volume) sand particles every week for four consecutive weeks, totalling 20% v/v by the end of the fourth week. Sand particle sizes were selected to mimic the inert particles found in the industrial tanks' sediment due to their similar density, easy and cheap availability. They were separated according to the particle size distribution (PSD) characteristic of industrial sediment (see section 5.3.2 and 6.1.3). The end of the first experiment coincided with the end of the 4th week of sand particle addition, resulting in little time for evaluating the effect of inert particles accumulation on the

quality parameters (see section 5.4). Therefore, Exp2 was designed with a longer experimental time allowing two extra weeks after the last particle addition.

5.1.2. Inoculation strategy

All tanks were inoculated with 100% fresh digestate from Finham Sewage Treatment Work's (STW) operating AD tanks. Table 5.2 gives a complete view of the feeding strategy throughout the entire experimental time. Feeding was increased during the first 14 days, starting with 30% of the designed daily feeding volume (DFV) from day 1 to day 4. From day 5 to 8, and then from day 9 to 14, the DFV was increased to 62.5% and 75% of the designed volume, respectively. After 14 days, all tanks were fed according to the designed solid retention time (SRT) until the end of the experiments (see sections 5.1.3 and 6.1.2 for more details).

Table 5.2: Digesters' feeding characteristics.

Averages of each phase		Daily Feeding Volume (ml)				Solid Retention Time (days)			Organic Loading Rate (kgVS/m³/day)		
		D design	D real	GD design	GD real	D/GD design	D real	GD real	D/GD design	D real ± SD*	GD real ± SD*
Exp. 1	Phase 1	increase up to 400.00	195.00	increase up to 333.33	162.86	N/A	N/A	N/A	increase up to 2.50	1.11 ±0.40	1.11 ±0.40
	Phase 2	400.00	342.86	333.33	285.43	15.0	17.5	17.5	2.50	2.01 ±0.15	2.01 ±0.15
	Phase 3									1.25 ±0.40	1.25 ±0.39
	Phase 4						15.5			2.43 ±1.02	2.09 ±0.78
Exp. 2	Phase 1	increase up to 400.00	195.00	increase up to 333.33	162.86	N/A	N/A	N/A	increase up to 2.50	1.18 ±0.48	1.19 ±0.48
	Phase 2	400.00	341.33	333.33	284.16	15.0	17.6	17.6	2.50	1.65 ±0.23	1.65 ±0.23
	Phase 3									1.75 ±0.27	1.75 ±0.27
	Phase 4						**15.0**			**1.85 ±0.40**	**1.56 ±0.23**

5.1.3 Feeding strategy

The digesters were fed daily from Monday to Saturday (6 times a week). Before feeding, the sludge was screened through a 3.5 mm sieve to avoid introducing long fibrous rags and bigger particles, which can adhere to the impellers or clog the baffles. The feed sludge was brought to room temperature via a water bath and then fed to the tanks. The designed solid retention time (SRT) for all tanks was based on the actual SRT used in the full-scale digesters where the samples were collected (~15 days). This way, the lab-scale process could be compared to the full-scale treatment process based on weekly sampling. SRT is the expected time the solid phase stays inside the digester, whereas the hydraulic retention time (HRT) is the expected time the liquid is held in the tank. Note that the meaning of solids used here is only those contained in the bulk of the sludge (see section 5.4.1.1), which can stay in suspension with little or no mixing. In AD plants that neither withdraw nor recycle the supernatant, SRT and HRT are the same, which is the case of Finham STW AD tanks.

According to Severn Trent's AD operational practice and the literature (Noutsopoulos et al., 2013, Bolzonella et al., 2002), the feeding system is designed to operate with a total solid (TS) of 5.0-6.5 g/l. Based on this figure, the OLR is calculated in terms of the average volatile solids (VS) present, ideally kept at a constant rate of 2.5 kgVS/m³/day. Previous measurements showed that the VS percentage of TS is approximately 75%, a value that was confirmed later by the end of Exp1 and Exp2 and the literature (IWA Publishing, 2007). However, due to the unpredictable nature of the wastewater upstream, it is not always possible to maintain total control of the system. In laboratory scale AD experiments, the variation of the TS throughout the experimental period plays a significant role on sludge treatment quality in terms of VS and chemical oxygen demand (COD) reductions (Li et al., 2018). Despite these challenges, it is important to note the use of real sludge in laboratory experiments in order to have a more realistic understanding of the industrial process. These aspects are discussed in more details in section 6.1.1 of chapter 6.

With a constant daily feeding volume of 400 ml, a solid retention time (SRT) of 15-days and a 75% proportion of organic matter in a 50 g/l total solid feed, the OLR can be calculated from:

$$OLR = \frac{VS.V_{feed}}{V_{tank}} = \frac{0.75.TS.V_{feed}}{V_{tank}} \quad 5.1$$

Two (Watson Marlow Model 313S) peristaltic pumps were used in the feeding process and after the inoculation phase (P1) (see table 5.1), the daily volume of sludge fed was set at a constant rate of 400±5 ml for the four D digesters and 333±5 ml for the GD 'control' digester, such that OLR=2.5kgVS/m³.

Initially, the feeding hose (10mm Ø) was tightly connected to the intake hole (see Figure 5.2) and the digestate taken from the lab-scale AD tanks. The hose, when filled up with digestate, was then inserted in a 500ml volumetric cylinder containing the feed and pumped into the AD tanks. After feeding, the intake holes were blocked with rubber bungs to avoid contact/transfer with any gases from outside. In order to maintain a constant volume of 6 and 5 litres for D and GD tanks, respectively, a weekly level control was performed in all digesters.

5.2 Feed and Digestate Sludge Characterization

5.2.1 On-site sludge sampling

Unless otherwise stated, 'sludge' in the context of the experiments refers to mixtures of thickened feed sludge from primary, secondary and industrial sludge sources collected

every Tuesday morning in the Severn Trent Finham STW, Coventry, UK. Sampling points in the pumping house were used for feed sludge and digestate collection from the pump that was active at the time of collection. In order to have fresh and non-contaminated digestate, the tap was left open for 1 minute or more before collecting samples. The exact period of this 'purging' interval depended on the daily environmental temperature so that fresh digestate at around ~37°C could be sampled.

Sludge samples were immediately brought back to the laboratory after collection and stored in the fridge at 4°C, as according to the Standard Methods (Eaton et al., 2005). Digestate samples were stored in the incubator at 37°C.

5.2.2 Sludge rheology measurements

Monitoring of the feed and digestate sludge viscosity was carried out at least once a week using a Couette viscometer Fann Model 35. This co-axial viscometer is filled with a known volume of fluid and the test fluid contains the annular space (shear gap) between the outer cylinder and the bob. The outer cylinder, rotating at a known speed, causes a viscous drag on the bob, creating a torque. The bob is coupled to a high-precision spring, which translates the torque to an analogue display. The instrument calibration was checked using standard liquids (User Guide, 2016). A 350ml cup was filled with feed or digestate sludge samples and brought to 37.0 ± 1.0°C before the viscosity measurements. The level marks were aligned and readings recorded for the six measurement speeds: 600, 300, 200, 100, 6 and 3 rpm. Using the conversion factors provided by the manufacturer (Fann Instrument, 2016), the speeds and readings were converted to shear rate and shear stress, respectively. The viscosity curve was then produced for each sample by dividing the shear stress by the shear rate (see figure 7.4).

5.2.3 Mimicking the rheology of the sewage sludge

Carboxymethyl cellulose (CMC) is known to accurately reproduce the rheological behaviour of sewage sludge at a total solids concentration above 2.5%, the threshold point where sludge will start behaving as a non-Newtonian shear-thinning fluid (Sindall, 2015, Dapelo et al., 2015, Malczewska, 2009, Wu and Chen, 2008). It is a common chemical used in several industrial processes, mostly in the food industry, to "thicken" a liquid solution. It is broadly used to mimic the rheological properties of slurries in order to validate CFD models.

It was found that a CMC solution at a concentration of 4g/l was capable of reproducing the fresh feed sludge for a TS concentration of 5.54% at 37°C, which is in the designed TS concentration and operating temperature range that Severn Trent Water use

to run their industrial AD tanks (results are presented in chapter 7, section 7.1.5). The solution was prepared one day before each experiment by mixing tap water with the addition of 1 gram of the CMC powder per hour. The impeller mixing speed was set at a specific rate to avoid introducing air in the liquid solution and was left mixing overnight at low speed for up to three hours before the measurements were started, when mixing was then turned off. The solution was also used to assess the velocity field in the particle image velocimetry (PIV) and the solid suspension experiments, the methodologies for which are given in chapter 7.

A TA Instruments Discovery Hybrid Rheometer 2 (HR2) was used to assess the rheological properties of the CMC4 solution at 20°C (the same temperature at which all experiments were carried out) before each test. The HR2 has a heated plate for temperature control and provides a shear rate range from $1x10^{-3}$ up to 5000 s^{-1}. The range at which the CMC4 solution viscosity depends on shear rate was found to be 0.7-1500 s^{-1}. Above and below these limits the viscosity becomes constant. The 60 mm diameter, steel Peltier cone plate (∠2.005°), rotating for 80 shear rate increases over 120 seconds, was used for all measurements.

5.3 Solid particles characterisation

5.3.1 On-site sediment sampling

Inert sediment samples were collected while the AD tank was isolated for cleaning and maintenance at Severn Trent's Toton STW in Nottingham, UK. The sediment was pumped out of the tanks' bottom after the liquid phase was drained and separated into two parts after further dewatering; i.e, the (i) rag and (ii) grit parts. Three sediment samples were collected from different points and times on the grit pile and brought to the laboratory for characterisation.

5.3.2 Particle size distribution (PSD) and density tests

The PSD and density tests were performed according to the British Standard method for soil characterisation (BS1777:P2:1990: 9.2 and 9.3, respectively) (Head, 2006). The particles of interest were the inert solids, which do not biodegrade and therefore have no potential for biogas transformation. As such, their accumulation is detrimental to the AD process. Because these particles were collected straight after an ongoing AD process, biodegradable material was present within the samples. Therefore, the samples were heated at 550°C for 1 hour, dried in the dissector until they reached room temperature and weighted so that only the non-biodegradable material was analysed (Eaton et al., 2005).

This process was repeated when variations in weight exceeded 4% between two consecutive measurements.

5.4 Process Control and Quality Monitoring of the Sludge Treatment Processes and Biogas Yield

5.4.1 Sludge treatment quality parameters

5.4.1.1 Total, volatile and fixed solids measurements

Total, volatile and fixed solids (referred in their short form of TS, VS and FS hereafter) were measured in triplicates twice a week, i.e. Tuesdays (sampling day) and Fridays based on the Standard Methods (2540 B and E) (Eaton et al., 2005). Nickel tins were washed, heated to 550°C and then placed into dissectors until cooled to room temperature. Tins were then weighed (w_1) to the nearest millesimal (in grams - 0.001 g), filled with 50±1 ml samples and then dried overnight at 103°C before being placed in the dissector to cool down to room temperature. They were then weighed (w_2) and placed back in the oven for another hour before being cooled in the dissector and weighed. This procedure continued until the weight difference was less than 4% between two consecutive measurements (two times were normally enough). The same procedure was used for VS and FS. Once the weight losses were stabilised, samples were placed in the furnace at 550°C for one hour and weighed (w_3). TS and VS concentrations were then calculated, based on the following equations:

$$TS = \frac{w_2 - w_1}{V_{sp}} x1000\ (g/l) \qquad 5.2$$

$$VS = \frac{w_3 - w_2}{V_{sp}} x1000\ (g/l) \qquad 5.3$$

where TS and VS (in grams – g) are the total and volatile solids concentrations, respectively, and V_{sp} is the sample's volume in ml. The FS concentration is the difference between TS and VS.

5.4.1.2 pH monitoring

A Mettler Toledo FiveEasy Plus bench pH meter was used to measure the samples' pH on a daily basis. A 3-point calibration (4.01, 7.00 and 10.01 pH standard solutions) was performed three times a week. The pH sensor was stored in 0.1 M HCl solution and rinsed with deionized water (DI) before any measurement/calibration step. To avoid the

accumulation of organic compounds in the membrane/diaphragm (e.g. proteins, grease) the electrode was soaked in acetone for 5 minutes as often as necessary and rinsed with deionized water.

5.4.1.3 Soluble chemical oxygen demand (sCOD) methodology

For the sCOD, 50±1 ml of sludge and digestate samples from each tank were centrifuged at 10,000-rpm for 10 minutes and then filtered using a Whatman grade GF/C filter through vacuum pumping (Kim et al., 2006). Samples were then diluted according to table 5.3 and processed according to the Hach method 8000 (Hach, 2015). 2 ml of the diluted samples were mixed in duplicates and left to digest for 2 hours at 150°C using a Hach DRB 200 digital reactor block. After 2 hours, the vials were taken from the heating block, but only after the temperature had dropped to 120°C. Samples were then mixed and left to cool down to room temperature in a water bath before readings were taken (DR 890 portable colourimeter) and recorded.

Table 5.3: Soluble chemical oxygen demand analysis.

Soluble Chemical Oxygen Demand - sCOD (mg/L O_2)				
	Dilution factor	Average	Minimun	Maximum
Feed	10	4220	2580	5950
D1	2	1401	870	2005
D2	10	4514	890	11790
D3	10	3179	900	8635
D4	2	1026	760	1256
GD	2	1390	1202	1755
Fresh Dig.	2	1054	820	1225

5.4.1.4 Volatile fatty acids - VFAs

For the VFAs measurements, 1.5 ml from the sCOD samples were further filtered using sterile Pall® Acrodisc® 0.2 µm syringe filters and stored at -20°C until the samples could be analysed (Eaton et al., 2005). On the day of the VFAs measurements, samples were unfrozen in a 4°C fridge, and then 0.5 ml were pipetted into 2 ml vials. A proprietary mixture of six free fatty acids, i.e. acetic, propionic, butyric, iso-butyric, valeric, iso-valeric acids at 1000 g/l in water, was used to prepare a solution for the 4-point calibration curve over the concentration range of 10–1200 g/l (Sigma-Aldrich). 20 µl of the internal standard butanediol at a concentration of 1,000 ppm, which has similar molecular weight as the six standard acids but is not present in the samples, was added to every sample and standards. As such, the area ratio between each individual VFA and the internal standard is kept constant, assuring an R^2>0.95 for all calibration curves. Deionised water was used to

prepare dilutions directly in the vials when necessary with a maximum dilution factor of 2. A blank was placed in-between every ten samples to avoid the build-up of acids in the column whilst a new calibration curve was measured every 30 samples so that potential deviation in between readings could be accounted for.

1µl, sampled from at a distance of 1 mm from the bottom of the vial, was analysed in a Gas-Chromatograph (GC-2010 AOC-20i auto injector-Shimadzu), equipped with flame ionization detection (GC-FID), a Topaz Liner Split/Splitless with Wool 3.5 x 5.0 x95 mm and a 30m Stabilwax-DA Capillary Column 30m; 0.25mm ID and a 0.25µm film thickness. The starting oven temperature was set at 150°C and then steeply increased to 220°C for a total duration of 15 minutes per sample. The individual VFAs concentration was then calculated from the area below the peaks. The results are shown in chapter 6, section 6.2.1.3.

5.4.2 Measurement of biogas and methane yields

A semi-continuous gas counter was used to measure the volume of biogas produced. This device works on the principle of biogas accumulation in a double, 20ml inverted 'bucket' chamber that is immersed in a 350ml liquid receptacle. When the chamber is filled with gas bubbles, the bucket turns. Every time it turns, a sensor, which is coupled to the device and connected to a computer, registers the activity. This device was designed to measure gas flow rates of 1 to 20 l/day (Pearce, 1975) and was calibrated using a Platon 5-100cm³/min flow meter. A 3-way valve was placed between the gas counter and the AD tanks in order to collect samples for methane measurements, thus minimising losses. For all measurements, the biogas was considered to be at room temperature (~21°C), assuming that enough time was allowed for the heat to transfer from the carrier tube to the counter holder.

The methane content of the biogas was measured using a portable gas detector GMI GT44 (GMI Ltd, 2016). The instrument was calibrated every day before the measurements were taken with a 1ml syringe used to insert five CH_4 air/gas mixtures: 1) 100% CH_4, 0% air 2)- 75% CH_4, 25% air 3) 50% CH_4, 50% air 4) 25% CH_4, 75% air and 5) 0% CH_4, 100% air. As shown in figure 5.2, the biogas samples for methane measurements were taken from the red, 3-way valve just before the digesters' feeding process started. As soon as the valve was opened, the needle was tightly inserted in the rubber tube connected to the valve. 1 ml of biogas was taken, inserted in the gas detector and readings were recorded.

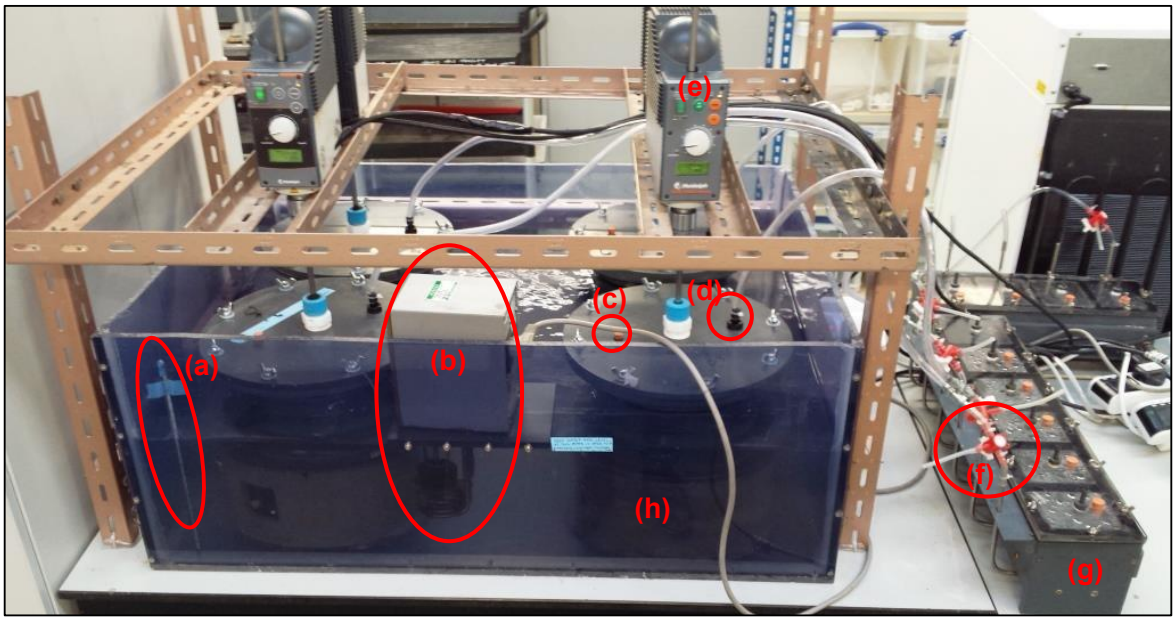

Figure 5.2: Schematic view of the experimental AD setup: (a) mercury thermometer, (b) Thermostatic / circulator, (c) feeding hole with rubber bung, (d) gas collection hole/hose, (e) head stirrer, (f) three-way valve for gas sampling, (g) gas counter, and (h) water batch tank.

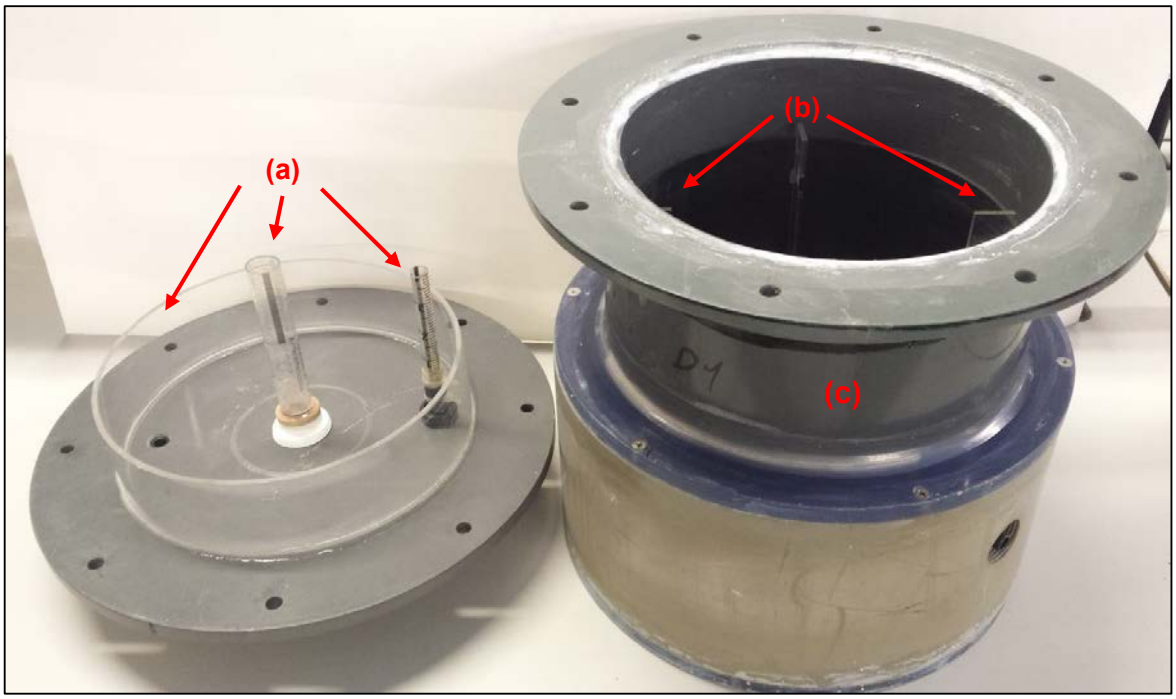

Figure 5.3: View of the D-digester used for the anaerobic digestion of sewage sludge showing the main components: (a) submerged components to avoid gas leakage, (b) baffles, and (c) cylindrical vessel.

CHAPTER 6 ANAEROBIC DIGESTION LABORATORY RESULTS

This chapter presents the results of the laboratory work that consisted of: (i) characterisation of inert sediment particles and sewage sludge (SS) from industrial anaerobic digestion tanks and (ii) semi-continuous lab-scale anaerobic sludge digestion. The results of (i) were used for the CFD model (chapter 7) and preparation of the experimental work (ii). The aim of (ii), the lab-scale AD experiments, was to investigate an energy-efficiency mixing regime required to avoid inert particles sedimentation in mechanically-mixed AD tanks, in which mixing energy and biogas yield are balanced such that energy input is minimised without detrimental impact on biogas production or sludge treatment quality. The results show that high mixing intensity, thus constant inert solid particles suspension inhibits the biogas and methane production and leads to poor sludge treatment quality, whilst low mixing regimes did not seem to have a negative impact on treatment quality and biogas production despite the accumulation of 20% v/v of inert particles in the bottom of the tank. Intermittent mixing was found to be the most energy-efficient solution for a well-stabilised AD operation. The chapter is divided into four sections. Section 6.1 provides an analysis of the variation of the feed sludge content, its physico-chemical characteristics and inert solid particles characterisation. In section 6.2, the results of the semi-continuous AD experiments and the analysed parameters used to assess the system's performance are given. Finally, the results of the rheological characteristics of sewage sludge based on the TS concentration are summarised in section 6.3, followed by the chapter's summary given in section 6.4.

6.1 Feed Sludge and Sediment Characterisation

6.1.1 Variation of sludge properties

Wastewater sludge consists of water and solids. The solid fraction is classified in three main groups: total solids (TS), volatile solids (VS) and fixed solids (FS) (Eaton et al., 2005, Von Sperling et al., 2007). TS is the sum of VS and FS, which accounts for all forms of solids present in the sludge. TS is categorised as dissolved solids (passing through a filter with a pore size smaller than 2.0 μm) and suspended solids (retained by the chosen filter). VS and FS contain both dissolved and suspended solids (see Figure 6.). The VS fraction, also called organic dry matter (ODM), represents the source from which biogas is produced. This means that all biogas produced is the result of the reduction or biodegradation of a portion of the VS fraction, whereas FS is the inorganic fraction which cannot be biodegraded. The determination methods for the solid fractions are presented in chapter 5, section 5.4.1.1.

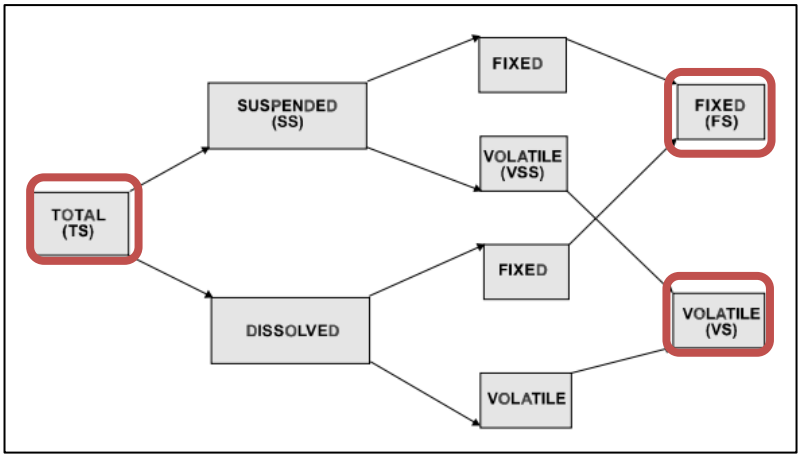

Figure 6.1: Wastewater sewage sludge solid distribution according to size and organic fraction (Von Sperling et al., 2007).

As VS contains the organic matter that can be biodegraded and converted into biogas, its variation with time is an indicator of whether the organic matter fraction is being broken down through anaerobic digestion and finally exiting the system as biogas. Alternatively, the VS can exit the system as untreated sludge contributing to higher organic load levels in the sludge's disposal fraction.

Wastewater treatment plants (WWTPs) are designed to work on a broad range of wastewater hydraulic load due to the daily or even hourly quantitative and qualitative variation of the receiving wastewater. The concentration of solids, fat and grease, chemicals, heavy metals, plastic, grit, COD levels, etc., are all subject to variations. These variations can be due to a set of factors, including the time of the day, input flow load (high or low), holidays, weather, seasons, commercial and/or industrial activities etc. The differences in load arising from a combined sewerage system when compared to a separate system are significant.

According to Severn Trent Water's guidelines, and the literature, a sewage sludge anaerobic digestion system is designed to operate at a solid retention time (SRT) of 15 days and an organic loading rate (OLR) of 2.5KgVS/m³/day. The Finham WWTP (where all sewage sludge samples were collected for this research) aims to feed the AD tanks with sludge containing between 50.00 to 65.00 g/l (or 5.0 to 6.5%) of total solids (TS). These values were the assumptions on which the experiments were based (described below, see section 5.1.1 for complete details). As will be shown later in this section, this 'sludge load' goal was not achieved in practice (certainly within the time period of the samples collected for this research). The implication of this will be discussed at the end of the chapter.

Finham WWTP treats the wastewater from the city of Coventry, UK, via a combined sewerage network. The estimated total population served is 360,100 and the urban area is 98.6 km². The two laboratory AD experiments (section 5.1.1 and summarised next) were

designed to replicate real AD processes at the site and, as such, the potential effect of rainfall on the AD feed sludge parameters was evaluated.

The two laboratory AD experiments consisted of four identical 6-litres and one 5-litre, mechanical mixed, semi-continuous anaerobic digester. Experiments 1 and 2, named Exp1 and Exp2, were inoculated with fresh digestate, fed 6 times a week (Mon-Sat) and divided into 4 phases: P1-inoculation, P2-acclimation, P3-impellers' speed change and P4-solids addition (*vide* section 5.1.1, table 5.1). They were carried out for a total period of 5 months or 123 days between October 2017 and April 2018. Exp1 started on the 10th of October and finished on the 12th of December 2017 (63 days / 9 weeks - autumn/winter). In this period, 9 fresh sewage sludge samples were collected from the Finham WWTP with the fresh digestate only used to inoculate the digesters. Exp2 started on the 24th of January and finished on 24th of April 2018 (90 days / 13 weeks - winter/spring). Due to technical problems (i.e. lack of staff and car maintenance), sample collection did not occur for the weeks of the 6th of March and the 3rd of April 2018. However, 11 fresh sludge and 10 fresh digestate samples were collected and analysed. The fresh sludge was stored in a 4°C fridge for daily feeding whilst the fresh digestate samples were used to make a comparison with the laboratory process and inoculated the digesters at the start and when needed.

Daily rainfall data was compared with feed sludge properties as a way to account for the sludge variation. The fresh sludge collected from the site was analysed for TS and VS and rainfall data was provided by the National Meteorological Library and Archive – Met Office, UK. Note that the rainfall data only includes input from direct precipitation collected using a standard rain gauge and does not include input from other precipitation effects (e.g., hail, snow, dew, fog, etc). To make a more complete statistical analysis of the feed sludge constituents, sampling should have been collected ideally every day. Considering the distance from the WWTP from the laboratory, facilities available, time for the daily tasks and sample analysis and the prohibitively high costs involved in such experiment, it was decided that the current setup (weekly) was acceptable and consistent with the literature (Liu et al., 2017).

Figure 6.2 shows the daily total rainfall precipitation as well as the feed sludge TS concentration for the experimental periods. It can be seen from Fig. 6.2 (a) and (b) that even light rainfall might have contributed to the variation of the total solids. The overall daily rainfall precipitation averages for the periods of Exp1 and Exp2 are 1.2 ±2.5 mm and 2.0 ±3.4 mm, while the overall TS concentrations are 44.23 ±12.60 g/l and 35.95 ±7.13 g/l, respectively. Note that for the rainfall precipitation periods considered, the SD is 108.5% and 70% higher than the mean of the data sets.

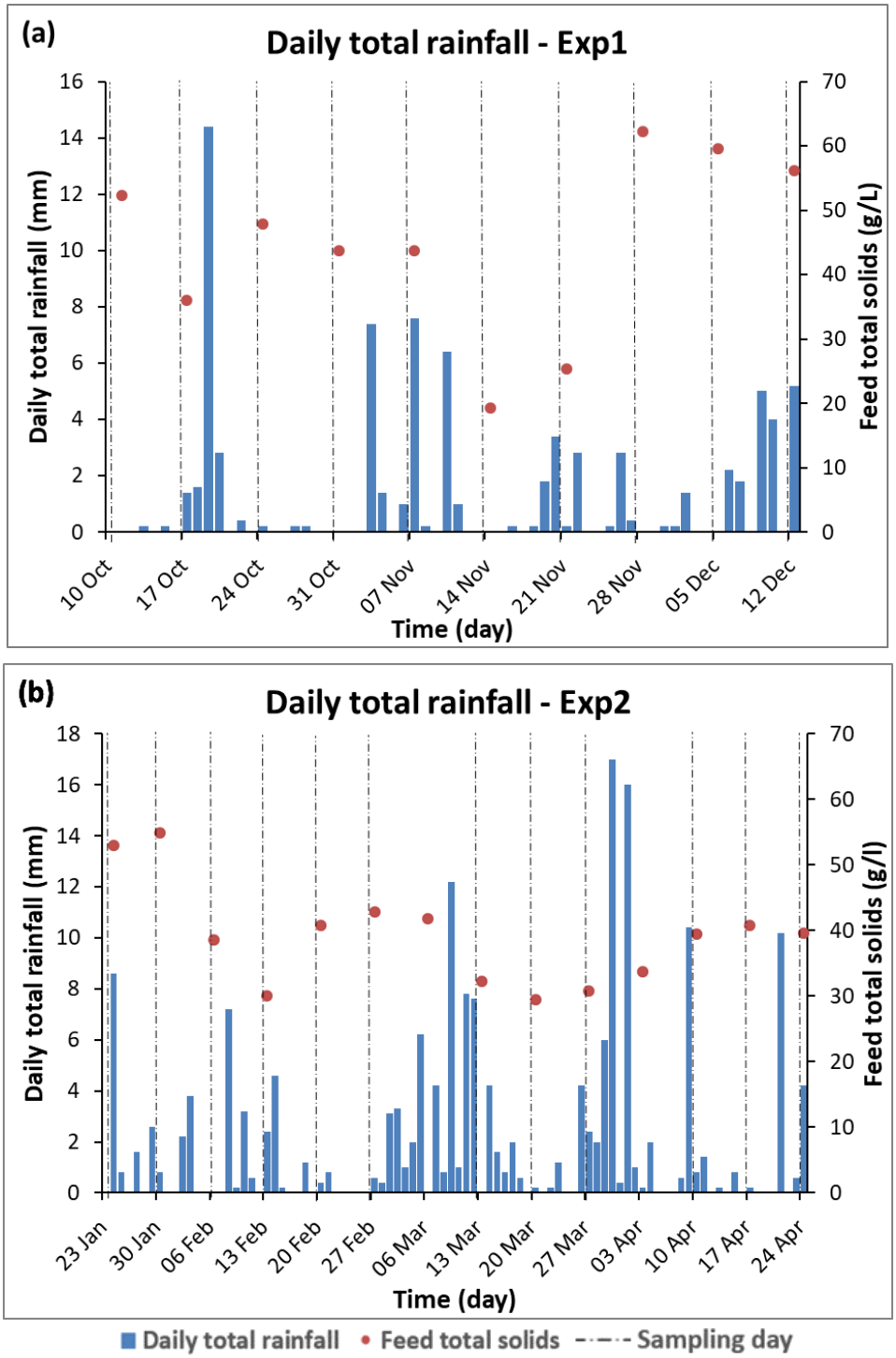

Figure 6.2: Daily total rainfall and feed TS along the entire experimental period. Vertical dashed lines indicates the sampling days (the lack of dashed lines indicates the days where no sampling happened). Note that the last samples (12/12/17 and 24/04/18) were not used in the experiment, only for the feed sludge variation analysis. Daily total rainfall precipitation provided by the National Meteorological Library and Archive – Met Office, UK.

During Exp1, all samples collected after a dry day have a TS concentration of more than 40 g/l, except for the 14th of November 2017, when the TS was the lowest of all samples (19.25 g/l) despite there being no rainfall for the two previous days. A similar pattern can be seen for Exp2, except for the 30th of January. Even with daily rainfall

precipitation of 2.6 mm, the TS concentration was 54.94 g/l, the highest TS concentration of all samples for Exp2. In general, AD feed sludge goes through pre-treatments, such as sludge thickeners, in order to increase the TS concentration and keep it as constant as possible. Nevertheless, the results show that TS concentration varied between approximately 2 to 6.2%. From this analysis, it can be seen that there is no clear trend in predicting TS from precipitation and, therefore, it is difficult to assume that rainfall precipitation can significantly influence the TS concentration of the AD tanks' feed sludge. However, it could be used, together with other relevant factors (e.g., settling tanks and thickening processes efficiency), for predicting variations in TS concentration. Such analysis is out of the scope of this research, but it is suggested for future work. Note that no sampling occurred in the weeks commencing 6th of March and 3rd of April 2018. This means that the fresh sludge samples from the previous week were stored at 4°C for two consecutive weeks before the sludge was used to feed the digesters. TS and VS were measured nevertheless.

Figure 6.3 shows the TS, VS concentrations and the percentage of VS in the TS of the feed sludge samples for Exp1 (a) and Exp2 (b). Tables 6.1 show a summary of the phases' averages followed by their standard deviation (SD) and the total averages of the feed. Phases 1, 2, 3 and 4 (see section 5.1.1) are abbreviated as P1, P2, P3 and P4, respectively. The total number of measurements for each phase are indicated in parentheses in front of each phase's name. All samples were measured twice a week (see section 5.2.1) to monitor the degradation of the stored samples and establish digestion efficiency (see section 6.2).

During Exp1, a significant variation in the feed sludge TS concentration can be seen in figure 6.3 (a) and table 6.1. To comply with Finham's best practices for the anaerobic digestion of sewage sludge, the feed should contain a TS concentration ranging from 50.00 to 65.00 g/l. However, over the entire experimental period, TS ranged from a minimum of 19.25 g/l to a maximum of 62.17 g/l, with an overall average of 44.32 ±12.60 g/l (Fig. 6.3(a)). Only 3 out of the 9 weekly samples presented a TS concentration within the aimed values. Among the phases, the smallest variation occurred in P2 (44.60 ±2.85 g/l), followed by P1 (45.65 ±6.95 g/l) and P3 (28.96 ±8.51g/l), while the greatest variation was in P4 (49.79 ±16.17 g/l). For VS, the minimum and maximum concentrations were 14.51 and 48.23 g/l respectively, while the overall average was 34.50 ±9.67g/l. For the phases' averages, the VS variations were a minimum of (P2) 34.23 ±2.65, followed by (P1) 35.96 ±5.36, (P3) 22.56 ±7.21 and a maximum of 38.72 ±12.09g/l (P4). Although significant variations for individual samples and within phases can be recognised, they are less relevant in terms of percentage VS in the TS, which ranges from 75.41 to 81.03% with an overall average of 77.94 ±1.69%. These results indicate that no matter the TS concentration, the percentage of VS in the feed sludge is relatively constant. This increases the reliability of the experiments for complying

with the designed OLR, which is calculated on the TS/VS concentration (section 5.1.3). Digestate results are discussed in subsequent sections of this chapter.

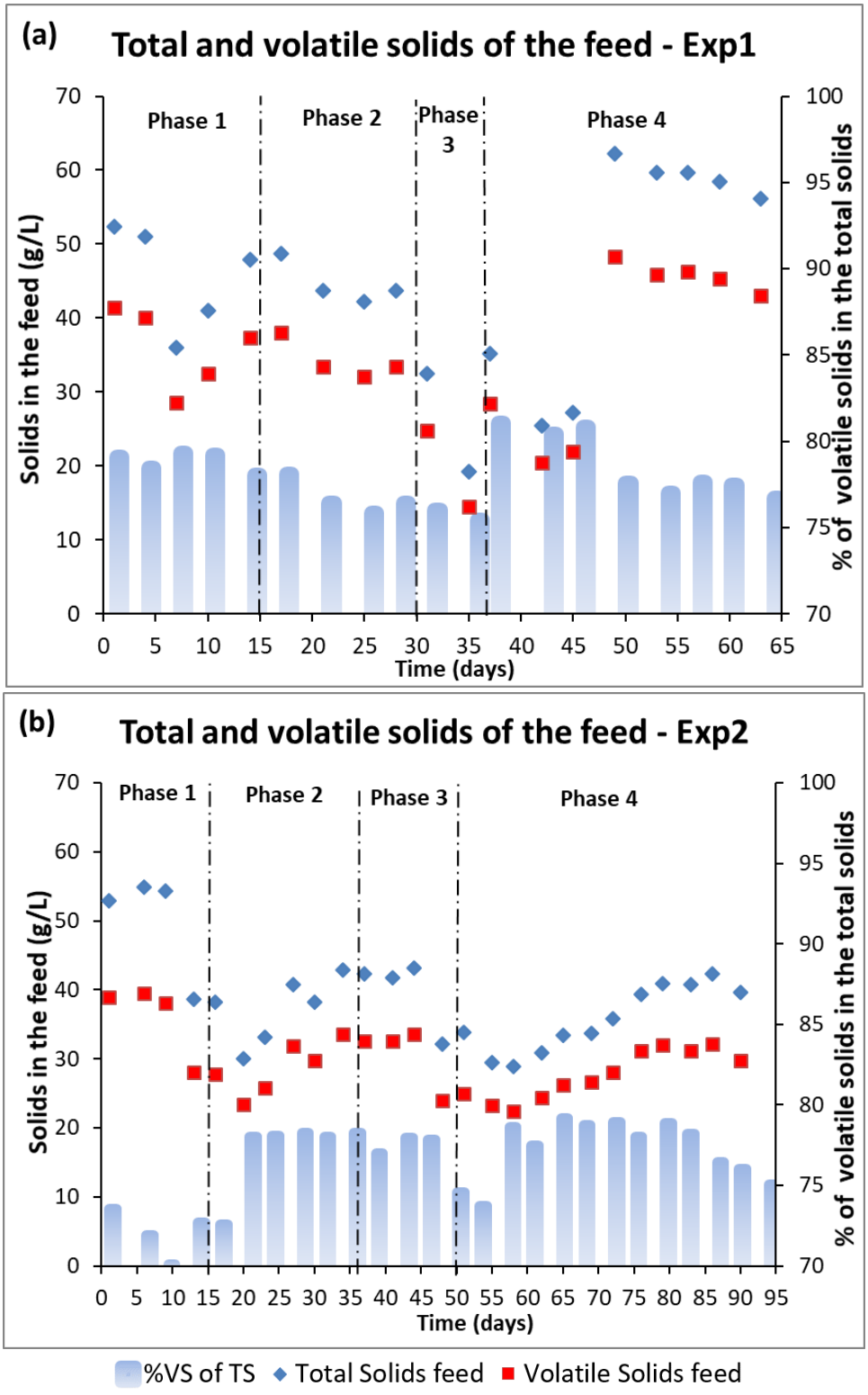

Figure 6.3: TS and VS concentrations in g/l (left vertical axis) and percentage of VS fraction in the TS (right vertical axis) over the entire experimental time. (a) Exp1 ad (b) Exp2.

Table 6.1: TS and VS averages and standard deviation for the feed sludge during each phase for experiment 1 and 2.

Experiment	Exp1		Exp2	
Phases (number of data points - Exp1, Exp2)	TS (g/L) Ave ± SD	VS (g/L) Ave ± SD	TS (g/L) Ave ± SD	VS (g/L) Ave ± SD
Phase 1 (5, 4)	45.65 ± 6.95	35.96 ± 5.36	50.22 ± 7.77	36.17 ± 5.42
Phase 2 (4, 6)	44.60 ± 2.85	34.23 ± 2.65	37.54 ± 5.08	28.70 ± 3.80
Phase 3 (3, 4)	28.96 ± 8.51	22.56 ± 7.21	39.86 ± 5.13	30.69 ± 4.47
Phase 4 (7, 12)	49.79 ± 16.17	38.73± 12.09	35.77 ± 4.71	27.68 ± 3.50
Total average	44.32 ± 12.60	34.50 ± 9.67	35.95 ± 7.13	29.98 ± 4.82

Similar patterns for Exp2 can also be recognised, although less significant variations are noted. Figure 6.3 (b) shows a minimum TS of 28.98 g/l and maximum of 54.94 g/l. The overall TS concentration average of 35.95 ±7.13g/l presented in table 6.1 indicates a smaller variation within the experimental period of 90 days. Variations within each phase are also less significant when compared to Exp1, with the smallest variation in P4 (35.77 ±4.71 g/l), followed by P2 (37.54 ±5.08 g/l) and P3 (39.86 ± 5.13 g/l), and the greatest variation in P1 (50.22 ±7.77 g/l). The smallest variation can be attributed to a greater number of samples as well as a smaller variation within the samples. Only 2 out of 11 samples in Exp2 presented a concentration within the aimed range. For the VS concentration phases' average, the respective values for the TS minimum and maximum were 22.46 g/l and 39.50 g/l, respectively. The percentage of VS present in the feed sludge ranges from 70.13 to 79.19 with an overall average of 76.47 ±2.58%. These results reiterate the hypothesis that VS content is about 75% and varies independently of TS concentrations, which is in agreement with the literature (IWA Publishing, 2007).

Figure 6.4 (a) and (b) shows a boxplot representation of the data presented in table 6.1. In both experiments, a significant variation can be noted amongst the phases within and between each experiment. Severn Trent try to control these fluctuations by increasing or decreasing the feeding volume in order to correct the OLRs. However, such practice may occasionally lead to overloads or microbial wash-outs and requires constant TS monitoring, which is not practiced. These fluctuations may have a direct impact on the efficiency of the AD process.

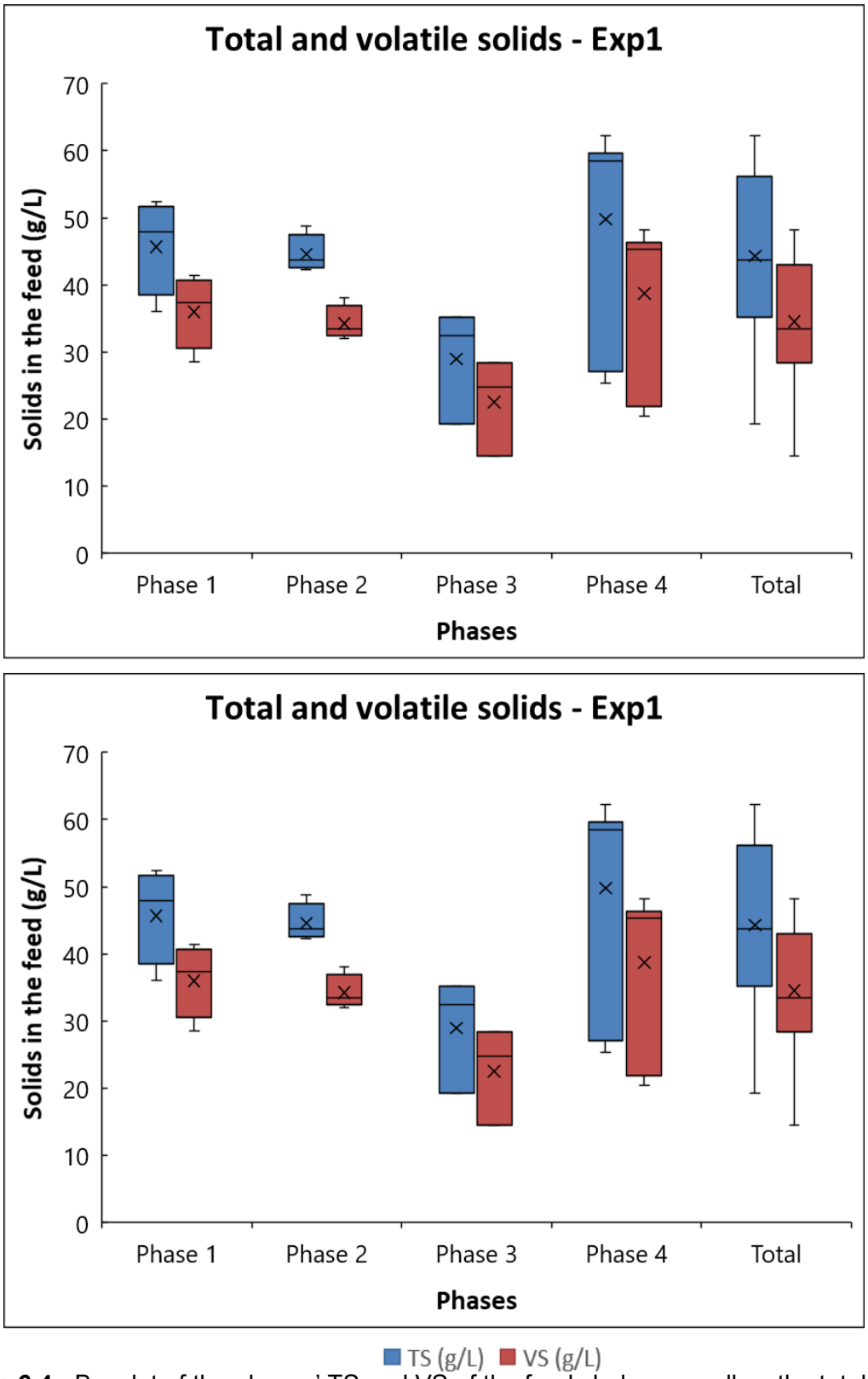

Figure 6.4: Boxplot of the phases' TS and VS of the feed sludge as well as the total for all samples in Exp1 (a) and Exp2 (b).

6.1.2 Organic loading rate - OLR

Variations in the feed sludge's total solid concentration throughout both experiments impacted on the OLR. The design of the AD experiments was based on the assumption of a minimum TS content of 50 g/l, an OLR = 2.5kgVS/m³/day, a solid retention time (SRT) of 15 days and a VS=0.75xTS (75% of the TS content is VS, (IWA Publishing, 2007)). The daily feeding volume (DFV) was calculated and kept constant because it was the only controllable parameter. The digesters were fed from Monday through Saturday. Figure 6.5 shows the DFV and the OLR for Exp1 (a) and Exp2 (b).

During the first 15 days (P1) of both experiments, the DFV was increased to achieve more stable inoculation. However, due to the TS variations, the OLR did not necessarily increase. For the D and GD tanks, respectively, the DFV during P1 was increased from 120 and 100 ml to 250 and 210 ml on day 6, then to 300 and 250 ml on day 9 and finally to 400 and 333.33 ml on day 15, when phase 2 started. The feeding volume was then kept constant throughout the rest of the experiment, although considerable variations can be seen for the OLR.

To present the OLR results, the concept of 'designed' and 'real' values are introduced. The designed values are the ones aimed at, based on the initial assumptions, whilst the real values are those achieved for each digester. Further to the initial assumptions described above (i.e. TS=50 g/l, OLR=2.5kgVS/m³/day and VS=0.75xTS), an optimum mixing regime is assumed. The optimum mixing regime consists of a 'complete mixing scenario' where the temperature, pH, food availability, sludge, inert particles, etc., are homogeneously distributed within the tank's domain (described chapter 2 and 3). In this scenario, no sedimentation or accumulation of non-biodegradable dense particles occurred at the bottom of the tanks. It assumes that all regions are well mixed and, therefore, there are no dead zones. The designed values also include daily feeding, including Sundays. On the other hand, the real values are based on the analysed real feed sludge data which takes into account variations of TS and VS, 6-days-a-week feeding (no feeding occurred on Sundays) and the creation of dead-zones caused by inert particle accumulation in phase 4. Consequently, the SRT and OLR were affected by the non-ideal conditions of the experiment.

Daily OLR variation is shown in figure 6.5, while the phases' averages are presented in table 6.2. In Exp1, the OLR of 0.83 kgVS/m³/day for the first 4 days and doubled to 1.67 on day 6. Between days 7 and 14, the OLR was below 1.62, reaching a minimum of 1.19 kgVS/m³/day on days 7 and 8. A similar pattern can be noted in Exp2, which started from an OLR=0.78 kgVS/m³/day from day 1 to day 4, increased to 1.65 from day 6 to day 8,

reached a maximum of 1.91 and decreased again for the last two days to 1.40 kgVS/m³/day before starting phase 2.

Table 6.2: Phases' average principal control parameters (DFV, SRT and OLR) illustrating the variation in feed conditions during the two experimental periods.

Averages of each phase		Daily Feeding Volume (ml)				Solid Retention Time (days)			Organic Loading Rate (kgVS/m³/day)		
		D design	D real	GD design	GD real	D/GD design	D real	GD real	D/GD design	D real ± SD*	GD real ± SD*
Exp. 1	Phase 1	increase up to 400.00	195.00	increase up to 333.33	162.86	N/A	N/A	N/A	increase up to 2.50	1.11 ±0.40	1.11 ±0.40
	Phase 2						17.5			2.01 ±0.15	2.01 ±0.15
	Phase 3	400.00	342.86	333.33	285.43	15.0		17.5	2.50	1.25 ±0.40	1.25 ±0.39
	Phase 4						15.5			2.43 ±1.02	2.09 ±0.78
Exp. 2	Phase 1	increase up to 400.00	195.00	increase up to 333.33	162.86	N/A	N/A	N/A	increase up to 2.50	1.18 ±0.48	1.19 ±0.48
	Phase 2						17.6			1.65 ±0.23	1.65 ±0.23
	Phase 3	400.00	341.33	333.33	284.16	15.0		17.6	2.50	1.75 ±0.27	1.75 ±0.27
	Phase 4						**15.0**			**1.85 ±0.40**	**1.56 ±0.23**

* SDs do not include Sundays, when OLR=0 kgVS/m³/day, whilst the averages do.

The OLR depends on the SRT, which also depends on the tank's working volume and the VS content of the TS concentration (see eq. 5.1 in section 5.1.3). During P1, P2 and P3, these parameters varied equally in the D and GD tanks for Exp1 and Exp2, but diverged in P4 due to the addition of the inert solid particles in the D tanks.

Table 6.2 shows the phases' averaged DFV, SRT and OLR for both experiments and also the standard deviation (SD) for the OLR. In order to keep the same SRT and OLR between D and GD tanks, there must be a difference in the design DFV values due to the tanks' total volume difference (6 and 5 litres, respectively). The aim during P1 was to achieve the desired DFV in a steeply changing manner, which therefore resulted in a lower average for that period. It can be seen that the real DFV average for phases P2, P3 and P4 was approximately only 85% of the designed value in both experiments. This difference is exclusively attributed to the lack of feeding on Sundays. As a result of the smaller DFV, the real SRT average was greater than the designed value during P2 and P3 in both experiments. The weekly addition of 5% v/v of inert particles inside the D tanks and its accumulation (presented in section 7.2.2, chapter 7) in P4, led to a decrease in the digesters' total working volume. At this point, weekly monitoring of the digesters' maximum level was carried out after particles were added, guaranteeing that the digesters were working at the designed capacity. Given the constant DFV and the smaller tank volume during P4 in the D tanks, the SRT of P2 and P3 decreased from 17.5 and 17.6 to 15.5 and 15.0 days in Exp1 and Exp2, respectively.

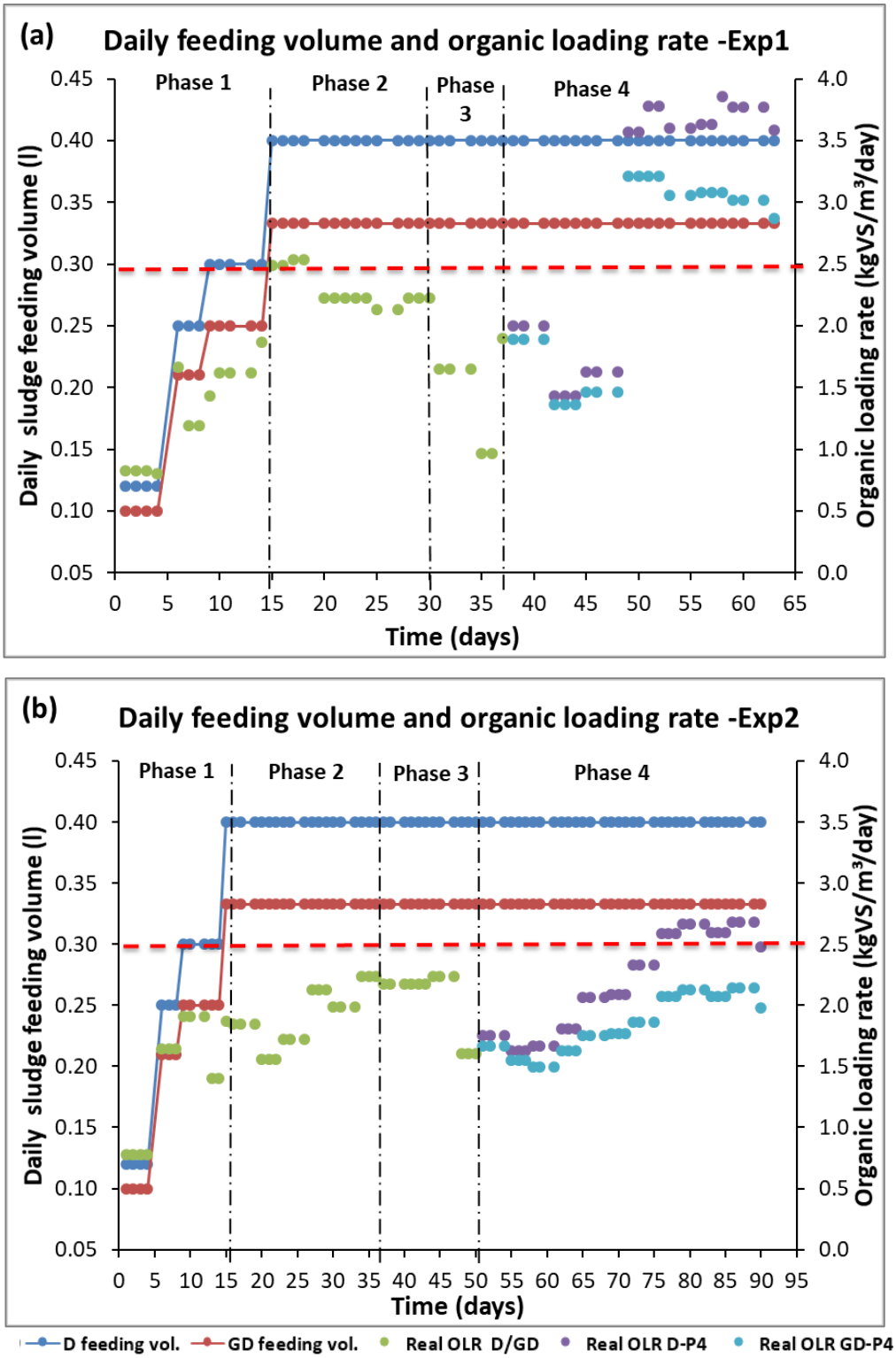

Figure 6.5: Daily sludge feeding volume in ml (left vertical axis) and OLR in kgVS/m³/day (right vertical axis) over the entire experimental period for Exp1 (a) and Exp2 (b). Red dashed horizontal line marks the designed ORL=2.50 kgVS/m³/day.

In Exp1, a small OLR variation during P2 can be noted when compared to P3 and P4. The results are shown in Figure 6.5 (a) and table 6.2. The maximum, minimum and average OLR for P2 were 2.13, 2.54 and 2.01 ±0.15 kgVS/m³/day, respectively. A sharp

drop in the TS concentration during P3 (Fig. 6.3(a)) resulted in an OLR minimum of 0.97, while the maximum and average values were 1.90 and 1.25 ±0.40 kgVS/m³/day, respectively. OLR was the same for all D and GD tanks until P3 but during P4 there were differences because of the addition of the inert solid particles. In figure 6.5, the D and GD OLRs until P3 are represented by the green circles, while in P4, the D OLR is represented by purple circles and the OLR for the control tank (GD) by light blue circles. The difference started off as a small amount relative to the 5% weekly loss of the total working volume due to the particle addition and grew to 20% throughout the next 4 weeks. Additionally, the greatest OLR variation can be noted during P4 due to the large variation in TS concentration. For this phase, the minimum, maximum and average OLRs for the D and GD tanks were 1.43 and 1.36, 3.78 and 3.22, and 2.43 ±1.02 and 2.09 ±0.78 kgVS/m³/day, respectively.

The feeding setup was the same for Exp1 and Exp2 (Fig. 6.5) yet the variations in feed sludge characteristics were clearly different (section 6.1.2). In Exp2, the steep increase in OLR during P1 started with 0.78 kgVS/m³/day until day 4. It then increased to 1.65 during days 6 to 8, then to 1.91 during days 9 to 12 from which it dropped to 1.40 kgVS/m³/day during the last 2 days before P2 started. As discussed in section 6.1.2, a smaller variation in TS concentration between the following phases in Exp2 can be also seen through the examination of the OLRs. The minimum, maximum and average OLRs for P2 were 1.56, 2.24 and 1.65 ±0.23 kgVS/m³/day, while for P3 they were 1.60, 2.24 and 1.75 ±0.27 kgVS/m³/day, respectively. Figure 6.5 (b) demonstrates the increasing divergence of OLRs for the D and GD tanks in P4 when the minimum, maximum and average OLRs were 1.63 and 1.50, 2.68 and 2.14, and 1.85 ±0.40 and 1.56 ±0.23 kgVS/m³/day, respectively.

For a daily analysis of the OLR in Exp1, it is relevant to note that until day 49, the OLR was only close to designed value on days 15 and 16 (2.49 kgVS/m³/day) and was slightly above this on days 17 and 18 (2.54 kgVS/m³/day). An abrupt increase of the OLR from day 49 to day 50 occurred due to a change in the feed's TS concentration, which resulted in the OLR more than doubling (i.e., going from 1.63 to 3.57 for the D tanks and from 1.46 to 3.21 kgVS/m³/day for the GD tank). The daily OLR remained above the designed value until the end of Exp1. For Exp2, the OLR reached or exceeded the designed value only in the last 15 days (13 of feeding), as shown in figure 6.5 (b). This meant that from day 15 until day 75, all tanks were working under their designed capacity (excluding the inoculation phase – P1). By analysing the OLR averages for every phase in both experiments, it can be noted that they were all below the designed value. These results emphasise the challenges of dealing with real sewage sludge in mid- to long-term laboratory AD experiments. The impact of the OLR variation on the AD process is provided in the following sections and discussed further in chapter 8.

6.1.3 AD inert solid particles properties

Figure 6.6 shows the results for the particle size distribution (PSD) and density (specific weight, see section 5.3 for details) of the inert particles as an average of triplicates from a random sampling of the sediments found in an industrial scale sewage sludge AD tank (Toton WWTP, Nottingham, UK). The sieve sizes were 3.350, 2.000, 1.180, 0.600, 0.425, 0.300, 0.212, 0.150, 0.075 and 0.063 mm. In order to simplify the fluid-solid and solid-solid phases' interactions in the computational fluid dynamics (CFD) models, the particles retained in each sieve were grouped into 4 sizes: 1.180, 0.600, 0.300 and 0.150 mm and a value of density assigned to each group. The 0.150 mm group contains all particles smaller than 0.300 mm. The other groups contain only particles bigger than the sieves' pore size. The density for each solid particle size was calculated and then weight-averaged by percentage for each simplified group. Table 6.3 shows the simplified particles' PSD and density results.

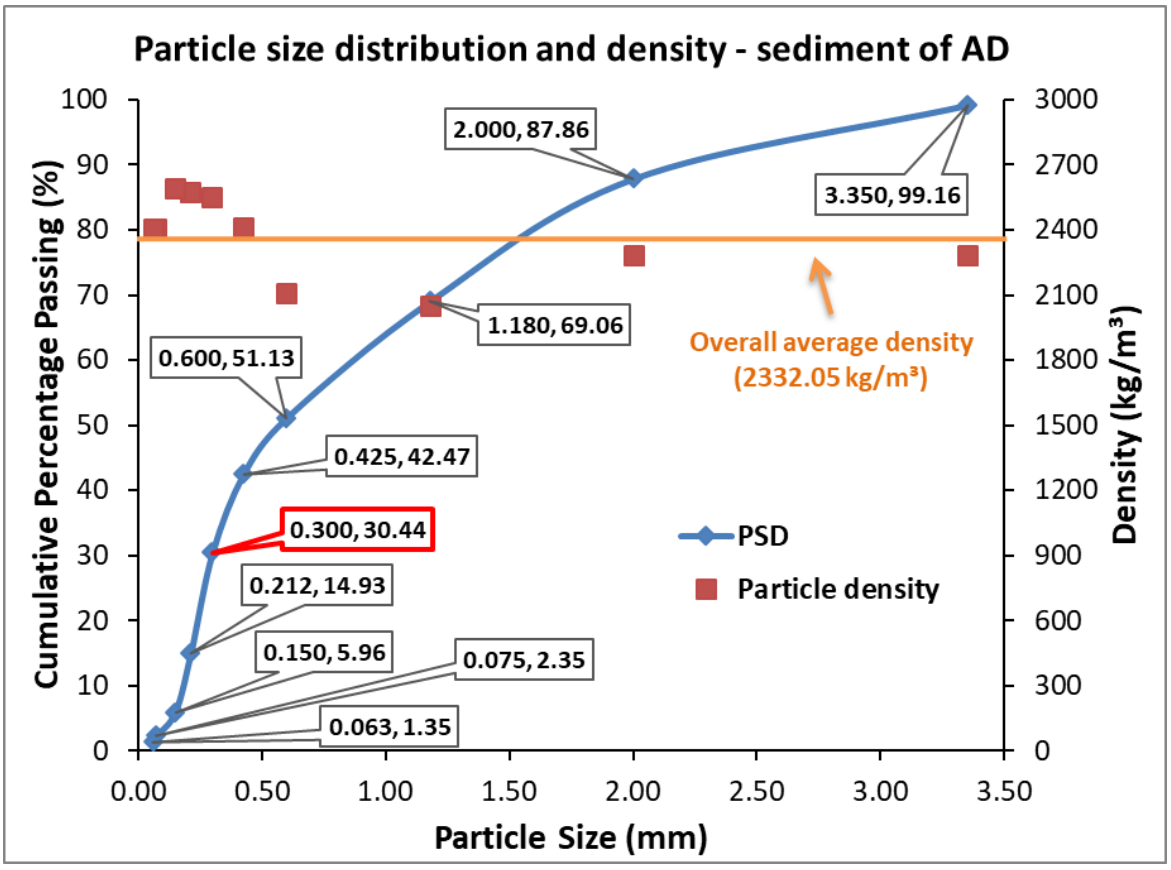

Figure 6.6: Particle size distribution (PSD) and density of each particle size group.

Figure 6.6 shows the cumulative percentage of the particles passing each sieve. The left-hand number in the boxes is the sieves' pore size whilst the number on the right-hand side is the cumulative percentage of particles passing that sieve. For example, the "0.300, 30.44" box (highlighted in red) means that 30.44% of all particles passed through

the 0.300 mm sieve. After grouping, this also represents the 0.150 mm group. 99.16% of particles in the samples passed the 3.350 mm sieve, which means that only 0.84% of the particles found in the sediment of the AD tank is bigger than 3.350 mm.

Table 6.3: Simplified particle size distribution and density of the AD sediment particles.

PSD and density - simplified		
Sieve Size (mm)	Percentage (%)	Density (Kg/m³)
1.180	30.94	2143.12
0.600	17.93	2108.01
0.300	20.69	2495.29
0.150	30.44	2545.08
	100.00	**2332.05**

The results show that the smallest particles have a higher density and that the particles in the middle range have the lowest densities. The densities of the 0.150 and 1.180 mm particles are 2590.40 kg/m³ and 2052.93 kg/m³, respectively, representing the maximum and minimum values measured. The overall average particle density is equal to 2332.05 kg/m³. In the laboratory AD experiments sand particles of density = 2650.00 kg/m³ were used to mimic the real sediment because of their low cost, inert properties, ease of procurement and similar density values. The simplified PSD was used to separate the sand particles before each 5% v/v addition into the D digesters in phase 4. The same experimental arrangements and sediment properties were used for the CFD modelling.

6.2 Anaerobic Digestion Performance

This section provides the results of the lab-scale anaerobic digestion experiments (Exp1 and Exp2) used to assess its performance. Digestion stability was assessed by analysing the pH, biogas and methane yields plus volatile fatty acids (VFAs). Sludge treatment quality was assessed through the analysis of total solids (TS), volatile solids (VS) and soluble Chemical Oxygen Demand (sCOD). The energy efficiency was assessed through an analysis of the energy balance of mixing, biogas production and the treatment efficiency of each tank in terms of sCOD. This is provided in chapter 7 and discussed in chapter 8.

During Exp1, the tanks that exhibited early failure indications, i.e., D2 and D3, were left unchanged until the end of the experiment. This was done to confirm the irreversibility of the failing process if no action was taken. Although Exp2 was first proposed as a duplicate of Exp1, it was redesigned according to the results of Exp1. Two main adaptations were carried out: (i) a longer experimental period, 90 instead of 63 days and (ii), an intermittent mixing (100/600-rpm) during phase 4 for the digester which experienced the highest mixing intensity (D3) (see section 5.1.1 for details). The reasons for the additional time were to

improve digestion stability in P2 (+6 days), investigate the short-term effect of different mixing regimes in P3 (+6 days) and evaluate the effects of intermittent mixing of the D3 tank in P4 (+12 days) (see section 5.1.1). The intermittent mixing started during P4 in D3 only after the tank showed a strong indication of likely failure (see figure 6.7 (b)). The reasons for the change (ii) during P4 was to a) help understand the role of constant high energy mixing, and consequently, inert solid particle suspension in Exp1 plus b) the effect of intermittent mixing, thus intermittent particle suspension, in Exp2, on the digesters' stability. As shown in chapter 7, the lowest mixing regime (100-rpm) does not provide enough energy to suspend most of the particles whilst the highest mixing regime (600-rpm) provides enough energy to keep them in suspension at any time.

6.2.1 Digestion stability

6.2.1.1 pH monitoring

According to the literature (Appels et al., 2008, Adekunle and Okolie, 2015), the optimal pH range for methanogenic bacteria in sewage sludge anaerobic digestion is between 6.50 and 7.50. In this pH range, methanogens are the group most sensitive to pH (and temperature) changes and should be kept within these values for better digestion stability. Rajeshwari et al. (2000) suggest that a more restricted pH range, between 6.80 and 7.20, should be maintained for an optimal operational sewage sludge digester. In these experiments, the pH's lower and upper stability limits were assessed to be 6.80 and 7.50, respectively, and any value out of this range meant that the process is likely to fail. The digesters performed well when working within this range.

pH was measured every day from Monday to Saturday, straight after the feeding process for both Exp1 and Exp2. Fig 6.7 shows the daily feed sludge and digestate pH while table 6.4 shows the average pH for each phase in both experiments. During Exp1 the pH meter stopped working in the second phase and the data between days 26 and 29 are missing, as can be seen in Fig 6.7 (a). A marked increase in the pH from day 20 until day 25 is an early indication of the pH equipment's failure, considering that all other monitoring parameters remained stable.

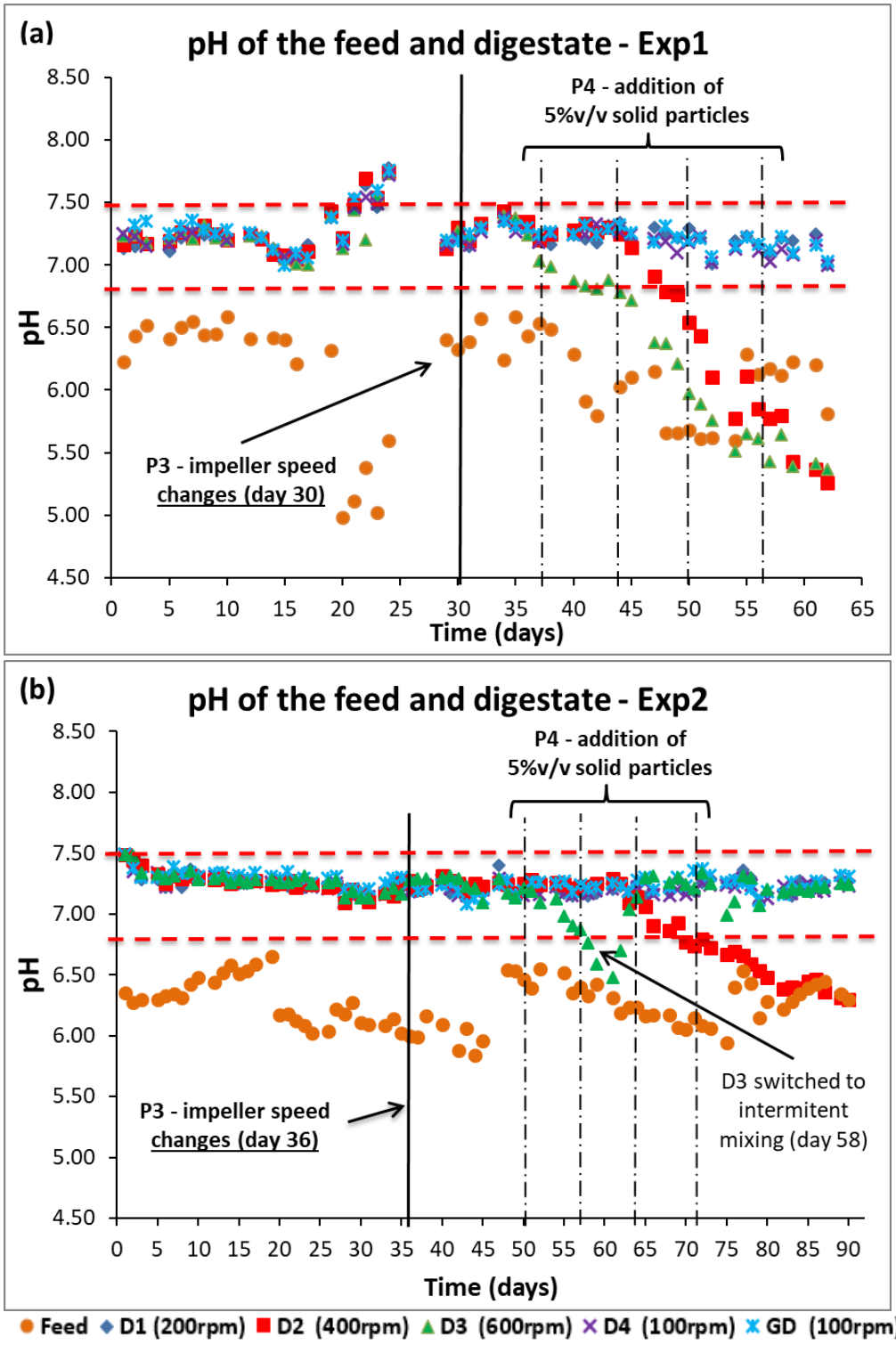

Figure 6.7: daily digestate and feed sludge pH for Exp1 (a) and Exp2 (b) for the full experimental period. In Exp2, intermittent mixing consisted of a maximum of 15 minutes high-intensity mixing (600-rpm) prior and during the feeding process, but a continuous, low-intensity mixing regime (100-rpm) during the rest of the day.

As shown in table 6.4, the average pH over all digesters was 7.22±0.06 during inoculation (P1) of Exp1. The small standard deviation (SD) indicates that variations between tanks are minimal and are attributed to having the same initial conditions (inoculation and then a sharp increase in the DFV). During phase 2 (P2) the pH started to

diverge amongst the tanks, although no process changes had been applied to the tanks, and an overall increase in pH up to day 25 can be noted in figure 6.7 (a). It can also be noted that the feed sludge pH reduced to levels not seen throughout the entire experimental period. This behaviour is also likely to be an initial indicator of the pH meter's failure, considering that no other monitoring parameters exhibited significant change. The average pH for all digestates was 7.32 ±0.24 for P2, where the high SD suggests the onset of pH sensor failure. During P3 no substantial variation was noted and the average pH values were within the proposed ideal range of 7.29 ±0.07, indicating stable operation. From figure 6.7 (a), an immediate pH decline in D3 can be noted at the start of P4. All other digesters presented constant and stable pH values up to day 45, when D2's pH also started to decrease. D3 and D2 crossed the pH minimum limit of 6.80 on day 44 and 48, respectively. From this point, they were considered 'soured' but were fed normally to investigate the variation in other process parameters. D1, D4 and GD kept pH values within the limits throughout the entire experiment and showed no sign of failure, apart from the days preceding the pH sensor breakdown.

Table 6.4: average pH values for each phase in Exp1 and Exp2.

	Phase 1 - ave ± SD		Phase 2 - ave ± SD		Phase 3 - ave ± SD		Phase 4 - ave ± SD	
	Exp1	Exp2	Exp1	Exp2	Exp1	Exp2	Exp1	Exp2
Feed	6.45 ± 0.09	6.39 ± 0.10	5.71 ± 0.62	6.22 ± 0.20	6.43 ± 0.14	6.14 ± 0.14	6.00 ± 0.03	6.28 ± 0.15
D1 (200rpm)	7.20 ± 0.05	7.32 ± 0.09	7.34 ± 0.25	7.21 ± 0.05	7.27 ± 0.07	7.20 ± 0.07	7.20 ± 0.08	7.22 ± 0.15
D2 (400rpm)	**7.21 ± 0.06**	**7.33 ± 0.08**	**7.35 ± 0.26**	**7.21 ± 0.06**	**7.33 ± 0.08**	**7.24 ± 0.04**	**6.50 ± 0.73**	**6.83 ± 0.15**
D3 (600rpm)	**7.22 ±0 .05**	**7.34 ±0 .08**	**7.27 ± 0.25**	**7.21 ± 0.06**	**7.30 ± 0.07**	**7.20 ± 0.07**	**6.16 ± 0.62**	**7.11 ± 0.21**
D4 (100rpm)	7.22 ± 0.05	7.32 ± 0.06	7.34 ± 0.23	7.21 ± 0.05	7.27 ± 0.07	7.20 ± 0.05	7.18 ± 0.03	7.20 ± 0.04
GD (100rpm)	7.27 ± 0.07	7.34 ± 0.06	7.31 ± 0.27	7.28 ± 0.05	7.28 ± 0.06	7.20 ± 0.06	7.21 ± 0.08	7.25 ± 0.06
Total digestate	7.22 ± 0.06	7.33 ± 0.07	7.32 ± 0.24	7.23 ± 0.06	7.29 ± 0.07	7.22 ± 0.06	6.85 ± 0.61	7.12 ± 0.24

From the individual digesters, the average pH for each phase can be seen in table 6.4, where a clearer picture of the mean pH value and its variations can be identified. Whilst the pH values of D2 and D3 had the same range and variation of those found in D1, D4 and GD during P1, P2 and P3, they clearly diverged in the last phase of the experiment (highlighted in red).

For Exp2, the pH results are shown in figure 6.7 (b). The first thing to note is that the two tanks that experienced the lowest mixing speeds, D4 (100-rpm) and D1 (200-rpm), and the control tank, GD (100-rpm), present a more constant value of digestates' pH throughout the entire experiment. It can also be noted that the pH values of D2 and D3 dropped below the lower limit again. As explained at the beginning of section 6.2, the experimental conditions for Exp2 were similar to Exp1 but with two main adaptations; (i) longer experimental time and (ii) intermittent mixing in D3 during part of P4 only.

As shown in figure 6.7 (b), the pH of all digesters stayed stable throughout the first 3 phases. During P4, the pH started to decrease in D3 two days after the inert particles

were added (day 50). A pH drop was also noted in D2 15 days later (day 65), i.e., one day after the tank was complete with 15% v/v of inert solid particles. D2 reached a pH of 6.77 on day 70, when it was considered soured. It is interesting to note that D2's pH drop in Exp2 was less marked when compared to Exp1, presenting less of a difference within two consecutive days and a higher final pH value (6.30 compared 5.26 at the end of Exp1). Similarly to Exp1, D2 was left unchanged until the end of Exp2 whereas D3 was changed to intermittent mixing on day 58, when the pH reached 6.76. This happened because of the lower OLR in Exp2 during P4 when compared to the same period in Exp1. This hypothesis is further explored in the next sections. By definition, the D3 tank was then considered soured and likely to fail at this point. Exp1's results showed that lower mixing regimes (D1 and D4) did not inhibit the process; results that were confirmed in Exp2. However, tanks under low mixing intensities were affected by the loss of working volume due to the accumulation the sand particles. Tanks at higher mixing intensities had particles that were partially (D2-400-rpm) or totally (D3-600-rpm) in constant suspension. These results are presented in the next chapter (chapter 7) and discussed in chapter 8.

Under suspension, the inert particles exit the system, thus avoiding sedimentation and accumulation. Therefore, in order to investigate the effects of an intermittent mixing regime, the speed of D3 was decreased to 100-rpm on day 58 and only raised to 600-rpm 5 minutes before and during feeding. The pH kept dropping until day 62, when instead of being fed with feed sludge, the tank was re-inoculated with 2 litres of fresh digestate (pH=7.17, TS=23.41 g/l). On day 63, the pH was already above the minimum threshold and kept constant until day 90.

6.2.1.2 Biogas and methane yields

The range of methane content in the biogas suggested in the literature for anaerobic digestion of sewage sludge varies from 60-70% CH_4 (Von Sperling et al., 2007, Appels et al., 2008), while other studies have shown variations between 50 and 65% CH_4 (Yang et al., 2015). Adopting less conservative range limits of 50-70% for the biogas methane content in this work, the stability of the process was considered unstable below 50% and to be of concern only when the CH_4 content dropped below 40%. Daily methane measurements were used to assess the performance of each tank and are presented below.

Figure 6.8 shows the cumulative biogas production (CBP) for the entire experimental period. Note that the D tanks have a total liquid working volume capacity of 6 litres whilst the GD tank (the control) has a 5-litre capacity. For this reason, all biogas/methane volumes presented in this section are normalised by the volume of each tank. Figure 6.8 and 6.9 (a) show biogas recording breaks in the D tanks on days 16, 20 and 35 (during P1, P2 and P3 of Exp1) and also on day 45 in D1. These breaks are a consequence the gas counter

malfunctioning (i.e. due to electricity cuts, software error and backflow water from the counter recipient to the tank in case of D3). The malfunctioning occurred on day 17 and 25 in D3. Figure 6.10 (a) also indicates that the backflow issue in D3 affected the biogas production during P2 mainly. These faults were restored as soon as possible. The biogas production discrepancies between D3 and all other tanks are attributed to gas counter malfunctioning, considering that until P4 started no other parameters (e.g. pH, methane, VFAs) indicated digestion instabilities. Methane content started to be monitored daily on day 16 of Exp1, but throughout the entire period in Exp2. During Exp2 the gas counter experienced malfunctions only once on day 44.

During Exp1 the cumulative biogas production (CBP) is shown in figure 6.8 (a), the daily biogas production in figure 6.9 (a) and the phases' average biogas production in figure 6.10 (a). These indicate a slow digestion start as a consequence of the steep increase of the OLR during P1, thus low VS availability. The average OLR during this phase was 1.11 ±0.40 kgVS/m³/day (see table 6.2 and figure 6.10 (a)), the lowest of all phases. Biogas production among the digesters in P1 is within the errors, indicating no significant differences, with an average daily biogas production of 0.74 ±0.25 $l/l_{reactor}$ (see figure 6.10 (a)).

Table 6.5: daily average biogas production for each phase, phases' average of all digesters (bottom line) and total overall average of each tank throughout the entire experimental period (right-hand-side column) for Exp1 (in litres/day).

Exp1	Phase 1		Phase 2		Phase 3		Phase 4		Total ave	
	Ave	±SD	Ave	±SD	Ave	±SD	Ave	±SD	Ave	±SD
D1 (200rpm)	0.78	0.22	1.14	0.44	0.71	0.30	1.15	0.29	**1.01**	**0.44**
D2 (400rpm)	0.75	0.20	1.15	0.46	0.69	0.27	0.44	0.18	**0.71**	**0.41**
D3 (600rpm)	0.70	0.18	0.75	0.47	0.61	0.23	0.26	0.07	**0.52**	**0.35**
D4 (100rpm)	0.76	0.24	1.16	0.46	0.72	0.31	1.18	0.25	**1.02**	**0.43**
GD (100rpm)	0.74	0.37	1.29	0.46	0.83	0.30	1.22	0.22	**1.08**	**0.47**
Digesters' total ave	**0.74**	**0.25**	**1.07**	**0.48**	**0.71**	**0.27**	**0.85**	**0.56**		

Table 6.6: daily average biogas production for each phase, phases' average of all digesters (bottom line) and total overall average of each tank throughout the entire experimental period (right-hand-side column) for Exp2 (in litres/day).

Exp2	Phase 1		Phase 2		Phase 3		Phase 4		Total ave	
	Ave	±SD	Ave	±SD	Ave	±SD	Ave	±SD	Ave	±SD
D1 (200rpm)	0.58	0.23	0.90	0.22	0.93	0.35	0.89	0.23	**0.85**	**0.27**
D2 (400rpm)	0.54	0.15	0.75	0.20	1.09	0.40	0.59	0.18	**0.70**	**0.29**
D3 (600rpm)	0.68	0.21	0.86	0.21	0.79	0.25	0.68	0.28	**0.74**	**0.25**
D4 (100rpm)	0.73	0.20	0.93	0.26	1.00	0.35	0.90	0.24	**0.90**	**0.27**
GD (100rpm)	0.70	0.18	0.86	0.29	1.21	0.32	1.03	0.26	**0.96**	**0.31**
Digesters' total ave	**0.65**	**0.20**	**0.86**	**0.24**	**1.01**	**0.36**	**0.82**	**0.28**		

In P2, when the daily feeding volume reached the designed value of 400 ml/day, average OLR increased to 2.01 ±0.15 kgVS/m³/day. This led to a daily average biogas production of 1.07 ±0.48 $l/l_{reactor}$ (see fig. 6.10 (a)). Note that due to the malfunctioning of the gas counter, D3 produced 0.75 ±0.47 $l/l_{reactor}$ of biogas whilst all other tanks were above

1.14 $l/l_{reactor}$. GD experienced a slightly higher average biogas production of 1.29 ±0.46 $l/l_{reactor}$ because it was not affected by the malfunctioning of the gas counter in this phase.

As average OLRs dropped to 1.25 ±0.40 kgVS/m³/day in P3, biogas production followed with an average of 0.71 ±0.27 $l/l_{reactor}$, the lowest production of all phases. With the gas counter issue restored in D3, biogas production among all tanks was similar and within the error range. The impeller speed change did not seem to influence the biogas production in the short term (i.e. 6 days, see table 5.1 in chapter 5).

During P4 (addition of inert particles), biogas production increased in D1 (200-rpm), D4 (100-rpm) and GD (100-rpm, control tank - no particle addition), whilst it dropped significantly in D2 (400-rpm) and D3 (600-rpm). Figure 6.8 (a) shows that until day 38, all tanks apart from D3, produced biogas at similar rates. At this point, a drop in biogas production in D2 can be noted. From day 38 onwards, D2 and D3 biogas production declined until the end of the experiment. The average real OLR in the control tank was 2.09 ±0.78 kgVS/m³/day whilst in the D tanks, it was 2.43 ±1.02 kgVS/m³/day. As previously explained, this difference is accounted by the of working volume due to the accumulation of inert particles in the bottom of the D tanks and constant maximum liquid level monitoring. In both cases, the OLR was the highest of all phases but still below the designed threshold of 2.50 kgVS/m³/day - the threshold for a stable and efficient anaerobic sewage sludge digestion (Noutsopoulos et al., 2013).

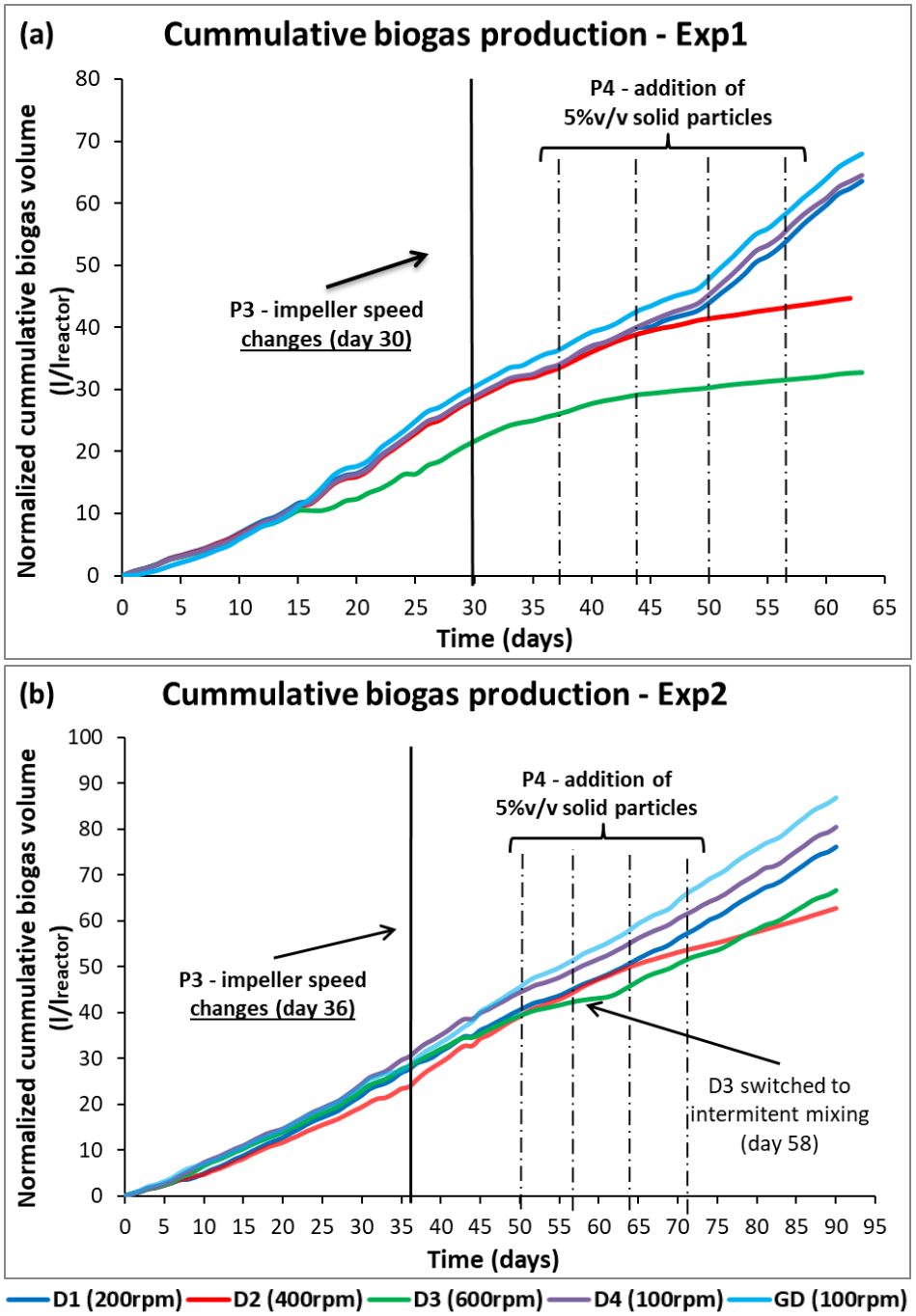

Figure 6.8: Normalized cumulative biogas production (CBP) by volume (l - litres) for Exp1 (a) and Exp2 (b). In Exp2, intermittent mixing consisted of a maximum of 15 minutes high-intensity mixing (600-rpm) prior and during the feeding process, but a continuous, low-intensity mixing regime (100-rpm) during the rest of the day.

An increase in biogas production followed by the higher OLR during this phase can be seen in D1, D4 and GD, especially after day 49, when OLR increased to 3.57 kgVS/m³/day. Although D1 and D4 had 20% less total working volume due to the accumulation of inert particles by the end of the last phase, they responded to the increased OLR well and did not show signs of overload or failure. Individually, they produced similar amounts of gas as GD during P4, whilst D2 and D3 almost ceased production by the end of the experiment (see fig. 6.8, 6.9 and 6.10 (a)). The daily biogas production averages during

P4 for D1, D4 and GD were 1.15, 1.18 and 1.22 $l/l_{reactor}$, respectively, whilst for D2 and D3 they were 0.44 and 0.26 $l/l_{reactor}$ (see table 6.5). The anaerobic digestion was affected by either a longer and more intensive mixing period and/or constant inert particle suspension. Chapter 8 presents a discussion on the causes of the AD process failure.

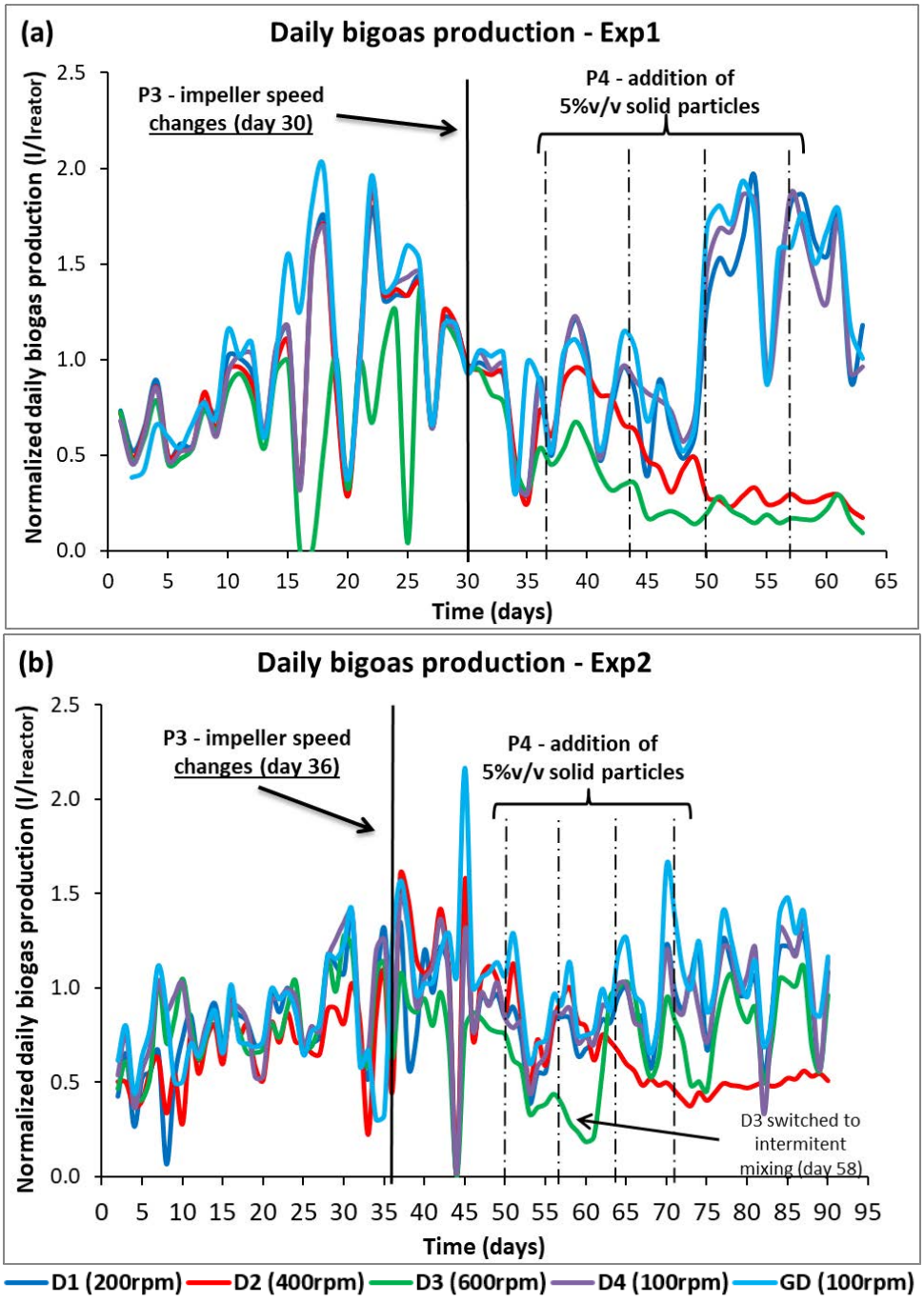

Figure 6.9: Normalized daily biogas production by volume (l - litres) for Exp1 (a) and Exp2 (b). In Exp2, intermittent mixing consisted of a maximum of 15 minutes high-intensity mixing (600-rpm) prior and during the feeding process, but a continuous, low-intensity mixing regime (100-rpm) during the rest of the day.

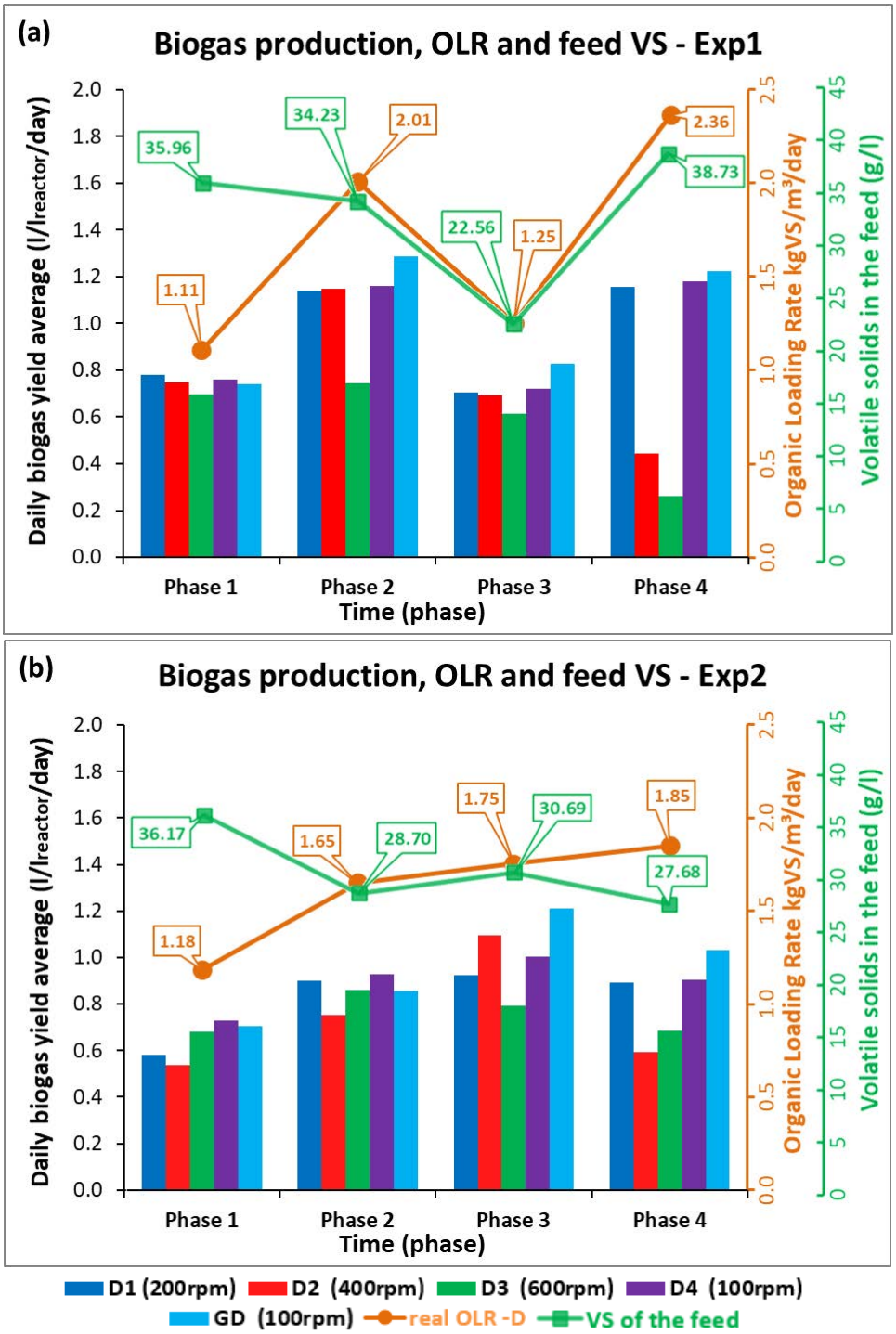

Figure 6.10: Phases' average of: (i) daily biogas production (left-hand side vertical axis), (ii) organic loading rate (inner right-hand side vertical axis - in orange) and (iii) total volatile solids in the feed sludge (outer right-hand side vertical axis – in green) for Exp1 (a) and Exp2 (b). Error bars were omitted for the sake of clarity. See tables 6.5 and 6.6 for standard deviations.

Figure 6.8 (b) indicates a more constant rate of biogas production throughout the entire experimental period of Exp2 when compared to Exp1. Figure 6.9 (b) shows the daily biogas production and figure 6.10 (b) the phases' average biogas production, OLR and VS in the feed. The steep increase in OLR from an average of 1.18 ±0.48 to 1.65 ±0.23

kgVS/m³/day from P1 to P2, resulted in an overall increase in the daily averaged biogas production from 0.65 ±0.20 to 0.86 ±0.24 $l/l_{reactor}$, respectively. Compared with Exp1, where the phase's average OLR almost doubled from P1 to P2, a moderate increase in biogas production is expected in Exp2. D1 and D2 produced less biogas than D3, D4 and GD in P1 but similar production rates can be noted in P2, shown in figure 6.10 (b). From P2 to P3, there was a small average OLR increase from 1.65 ±0.23 to 1.75 ±0.27 kgVS/m³/day. With the change in the mixing speed during P3, the daily average biogas production increased in all tanks except for D3, which dropped from 0.86 ±0.21 to 0.79 ±0.25 $l/l_{reactor}$. D1 and D4 experienced a small increase whilst D2 and GD had the highest phases' average production throughout the entire experiment, i.e., 1.09 and 1.21 $l/l_{reactor}$. From figure 6.8, 6.9 and 6.10 (b), it can be noted that biogas production in D3 declined during P3 and continued declining in P4, reaching the lowest production from day 53 until day 61. Other monitoring parameters (i.e., pH presented in section 6.2.1, CH_4 content and VFAs which are presented next) showed strong signs of failure in D3 when the impeller speed changed from 100-rpm in P2 to 600-rpm in P3 (day 36 – see figure 6.9 (b)). On day 58, the mixing mode of this digester changed to intermittent mixing in an attempt to recover digestion stability (which at this point was considered as souring with a high chance of complete failure if no action was taken). On day 62 pH, CH_4 content and VFAs were all out of the stability range so the re-inoculation of D3 was carried out. Figure 6.8 and 6.9 (b) shows a substantial drop in biogas production and its recovery after re-inoculation.

With the decline in the phases' average VS content of the feed (fig. 6.10 (b)) from P3 to P4, the average OLR decreased from 1.75 ±0.27 to 1.56 ±23 kgVS/m³/day in the control tank, GD. However, the addition of 5% v/v inert particles throughout the next 4 weeks and the withdrawal of excess slurry over the maximum liquid level led to an increase of the OLR in the D tanks to 1.85 ±0.40 kgVS/m³/day in P4. The impact of this decline in GD's OLR can be noted in figure 6.10 (b) where the daily total average biogas production dropped from 1.21 ±0.32 to 1.03 ±0.26 $l/l_{reactor}$. An overall decline in the D tanks can be also noted. Whilst D1 and D4 had only a slight drop in the daily average biogas production (from 0.93 and 1.00 to 0.89 and 0.90 $l/l_{reactor}$, respectively), D2 and D3 dropped from 1.09 and 0.79 to 0.59 and 0.68 $l/l_{reactor}$, respectively (see table 6.6 for standard deviations). Although there was an overall drop in biogas production in D3 during P4, no signs of process failure occurred after the mixing mode was changed to intermittent and re-inoculation carried out. Furthermore, similar production rates in D3 can be noted when compared to the D1, D4 and GD tanks (figures 6.8, 6.9 and 6.10 (b)). In contrast to Exp1, the decline in biogas production of D2 in Exp2 took longer. This behaviour is attributed to the lower average OLR in Exp2, when compared to Exp1, and the ideal feeding threshold of 2.5 kgVS/m³/day.

6.2.1.3 Specific methane production (SMP) during Exp1 and Exp2

Figure 6.11 shows the cumulative specific methane production (SMP) of the digesters and figure 6.12 the percentage daily methane production. In Exp1, the cumulative SMP in phases 1, 2 and 3 were very similar and followed the same production rate with slightly higher values for GD and smaller for D3, as shown in figure 6.11 (a). These differences are attributed to the gas counter issues only. Figure 6.12 (a) shows that the CH_4 content did not drop below the stability limit of 40% in any tank until P4. During P4, D3 experienced a constant drop from day 38, one day after the first addition of inert particles (5% v/v), and hit the stability limit on day 40. On day 45, D2 also start decreasing its CH_4 content, reaching the stability limit on day 50.

Figure 6.11 (a) shows the cumulative SMP decline of D3 followed by D2 during P4 for Exp1. Both digesters reached a plateau by the end of the experiment because of a decline in the overall biogas and methane production. While D1, D4 and GD finished the experiment with a cumulative SMP of 2.08, 2.22 and 2.34 l CH_4/gram $VS_{fed}/l_{reactor}$, D2 and D3 stagnated at approximately 1.45 and 0.83 l CH_4/gram $VS_{fed}/l_{reactor}$. In figure 6.13 (a), the boxplot of the CH_4 content in the biogas shows the mean percentage connected by a line across each digester throughout the entire experimental time. The maximum and minimum values are also shown. Note that the CH_4 content in D2 and D3 reached a minimum of 16 and 5%, whilst the maximum of all tanks varied between 63 and 69%. The average CH_4 content of D1, D4 and GD were very similar.

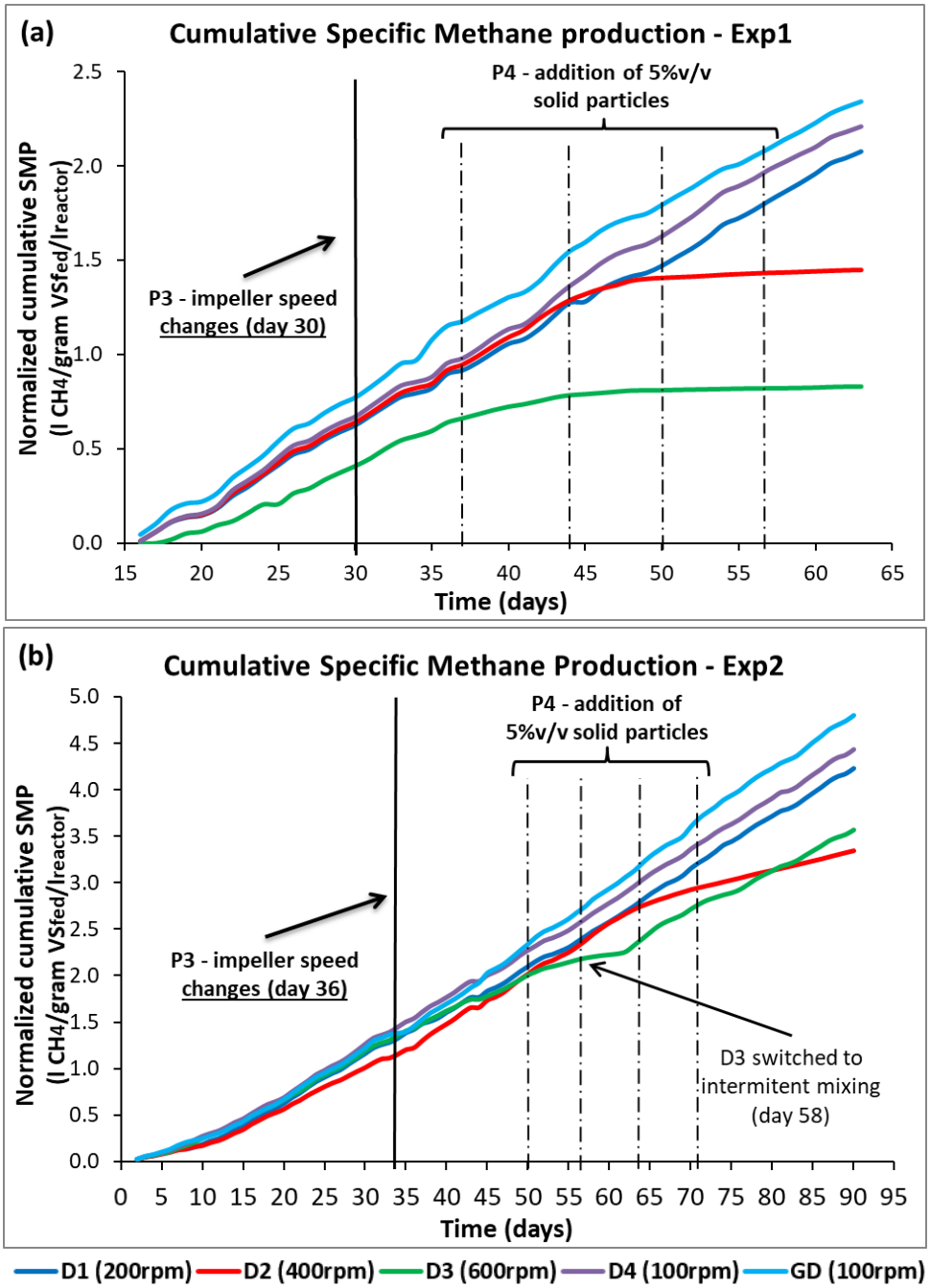

Figure 6.11: Normalized cumulative specific methane production over the entire experimental time for Exp1 (a) and Exp2(b). In Exp2, intermittent mixing consisted of a maximum of 15 minutes high-intensity mixing (600-rpm) prior and during the feeding process, but a continuous, low-intensity mixing regime (100-rpm) during the rest of the day.

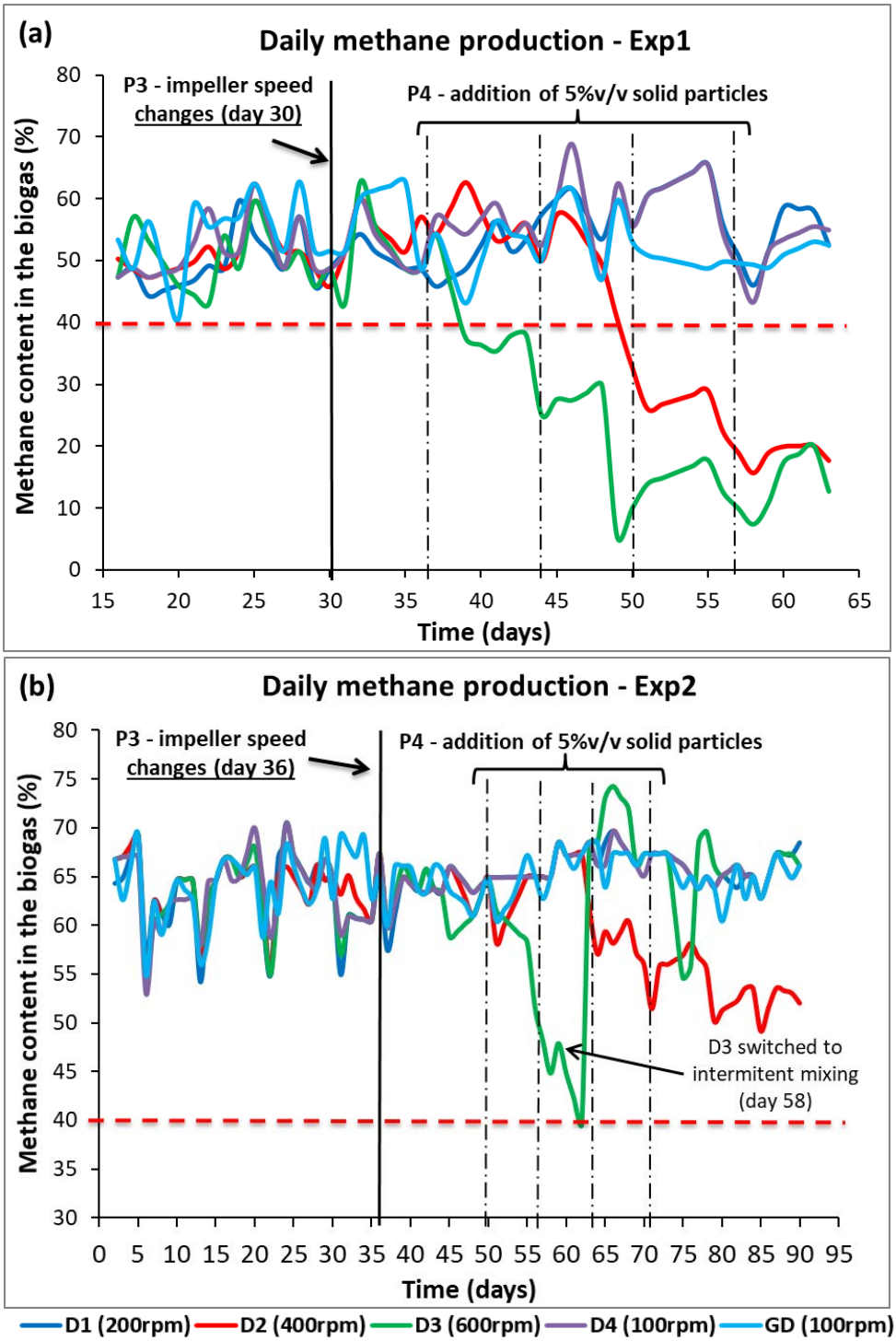

Figure 6.12: Daily methane content in the biogas for Exp1 (a) and Exp2 (b). Note that methane content for Sunday periods were averaged between the Saturday and Monday readings. In Exp2, intermittent mixing consisted of a maximum of 15 minutes high-intensity mixing (600-rpm) prior and during the feeding process, but a continuous, low-intensity mixing regime (100-rpm) during the rest of the day.

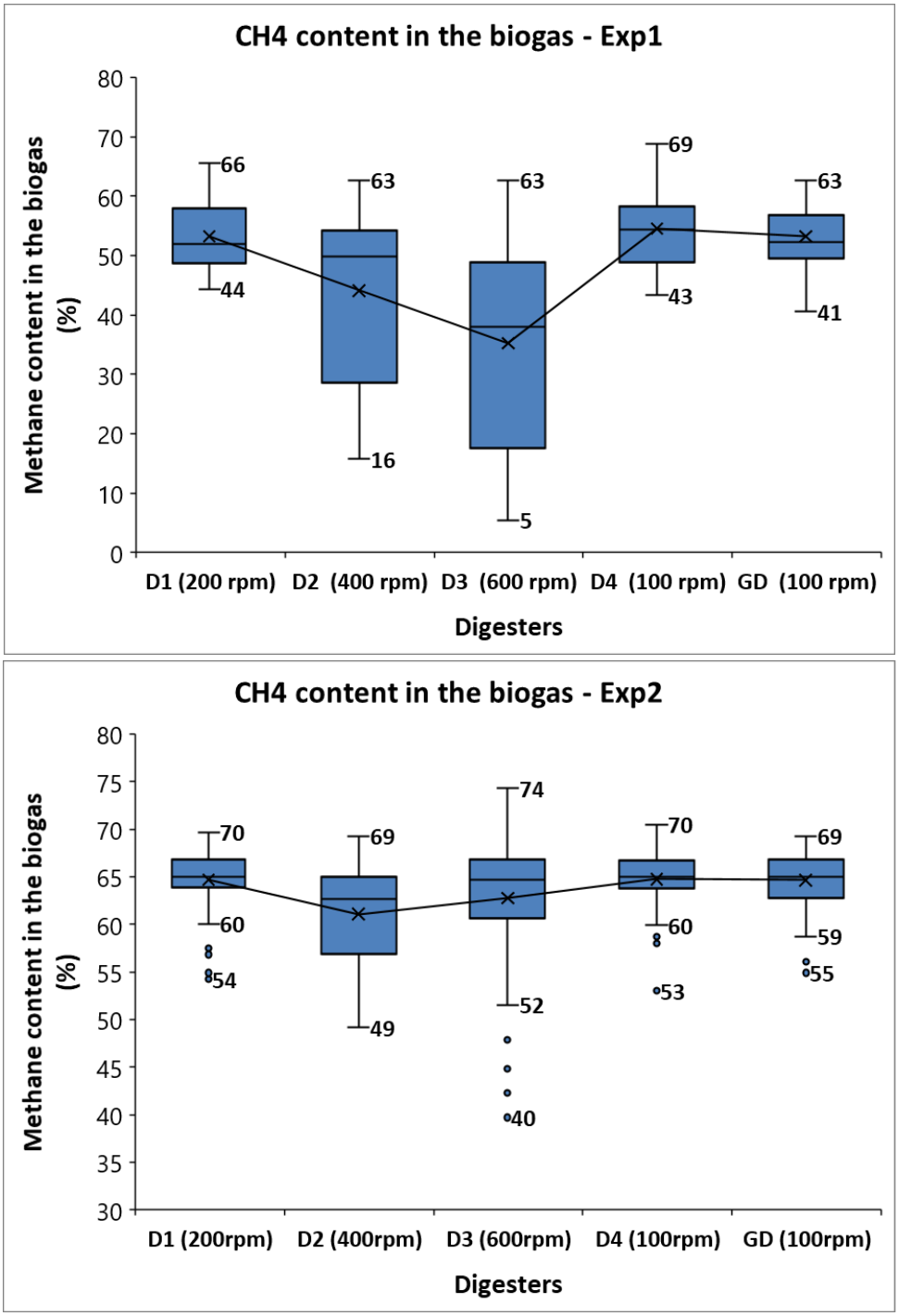

Figure 6.13: Boxplot of the methane content in the biogas throughout the entire experimental time of Exp1 (a) and Exp2 (b).

Similar plots are shown in figures 6.11, 6.12 and 6.13 (b) for Exp2. The cumulative SMP of all digesters is shown in figure 6.11 (b), which indicates a constant CH_4 concentration in all tanks from P1 to P3. On day 50, the beginning of P4, the CH_4 content in D3 was similar to all other tanks and well above the stability limit (65%) (see figure 6.12 (b)). On day 51, CH_4 concentration started to drop, reaching the limit of 40% on the 58th day, when intermittent mixing started in D3. On day 62, re-inoculation was carried out in D3. The biogas production and CH_4 content immediately grew above the stability limit reaching

similar levels to the other digesters. Note the occurrence of anomalously high CH_4 concentration between days 65 and 68 shown in figure 6.12 (b). This may have been caused by the consumption of the accumulated volatile fatty acids (VFAs – presented in the next section). The daily CH_4 content in D3 was the highest for all phases and digesters during Exp2, reaching 74.29% on day 66 (see figure 6.12 and 6.13 (b)). As a consequence, the cumulative biogas production of D2 also dropped during P4. Similarly, lower levels of CH_4 content can be seen in figure 6.12 (b). Again, this phenomenon is attributed to the constant, high-intensity mixing and the suspension of inert solid particles. Although pH and VFAs crossed the stability limits on day 70 and 69, respectively, the CH_4 concentration never dropped below 40%. In fact, it had very similar average values to all the other tanks.

It is interesting to note from figure 6.11 that the cumulative SMP in the GD tank is the highest, followed by D4 and D1. This could lead to the conclusion that the addition of inert particles and the increase of mixing speed, even if slight (D1, 200-rpm), could have had a negative effect on methane yields. This hypothesis is not discarded entirely, considering that the difference amongst the digesters seems to increase with time, especially in Exp2. However, figure 6.12 shows that the daily methane content in the biogas is relatively constant in all tanks throughout the entire experimental periods with only a few days of exceptions, as previously discussed. In fact, figure 6.13 shows substantial similarities in CH_4 percentage in the overall picture of both experiments across tanks GD, D4 and D1, especially in Exp2. It is, therefore, questionable to assume a negative impact on methane yield without further investigation.

6.2.1.4 Volatile fatty acids

Volatile fatty acids (VFAs) are broadly used as a monitoring parameter to assess anaerobic digestion stability and methanogens inhibition. pH fluctuations that concomitantly occur with low methane content and the accumulation of VFAs indicate an imbalance between the acidogenic bacteria and methanogenic archaea that could lead to process failure (Zealand et al., 2017, Xu et al., 2014, Xiao et al., 2013, Komemoto et al., 2009, Banks et al., 2008). Accumulation of VFAs are associated with high OLR, low pH, a lack of essential trace elements as well as high levels of ammonia in different types of AD feedstock (Banks and Heaven, 2013, Shi et al., 2017). Wang et al. (2009) reported detrimental specific biogas yields at a level of 900 mg/l propionic acids whilst Li et al. (2010) reported that acetic acid accumulation was the main cause of acetoclastic methanogen inhibition in wet thermophilic AD. Xiao et al. (2016) reported degradation of acetic acid at 4200 mg/l without a lag phase and the potential to degrade up to 8200 mg/l of acetic acid with stepwise acclimation. There is no common agreement on what levels of individual or total VFAs are considered limiting for the process to become irreversible. This is because of its

dependence on the buffer capacity of each system due to its alkalinity. For this work, an intermediate limit of 3000 mg/l of total VFAs accumulation was established based on the aforementioned reseach and that of Labatut and Gooch (2012). They suggested that VFA concentrations above 2000 mg/l might be inhibitory. Above this limit, the chances of recovery are minimal if no action is taken.

Figure 6.14 shows the total VFAs concentration on all digesters starting on day 25 (second phase - P2) until the end of the Exp1. The horizontal dashed red line marks the stability limit. Total VFAs concentration was kept stable, and below this limit, in all digesters until day 49, when D3 accumulated a total of 3170 mg/l. At this point, CH_4 and pH in D3 had already crossed their stability limits on days 39 and 44, respectively. Although CH_4 and pH were measured 6 times a week,VFAs were collected only once. This 10/5-days difference means that there is a delay in the response on these stability parameters as indicators of imminent failure in a concurrent fashion. D2 showed a significant increase in total VFAs concentration later on in P4 from a previous value of approximately 1000 mg/l on day 49 to 5348 mg/l on day 56. The last measurement on day 63 of Exp1 showed a high concentration of total VFAs on both D2 and D3 (approximately 10,700 and 11,600 mg/l, respectively), accounting for almost 4 times more VFAs than the stability limit. For all other digesters the levels maintained stable throughout the entire experimental period, except for D4, which presented a concentration of 3054 mg/l on day 63. Note, however, pH and CH_4 yield were within the stability limits for D4. Although D1 and GD showed no signs of instability during Exp1, as evident by VFAs, an overall increase in VFAs can be noted in the last 4 weeks of the experiment. This might have been a consequence of the increased OLR during P4 which stressed the system with an overload of biodegradable organic substrate. This may have led to an overgrowth of the fast-reproducing acidogenic and acetogenic bacteria whilst methanogens consumed all readily available acids at its maximum rate. In fact, from figures 6.8 (a), 6.11 (a) and 6.13, it is evident that biogas production increased during this period whilst methane production did not vary as prominently.

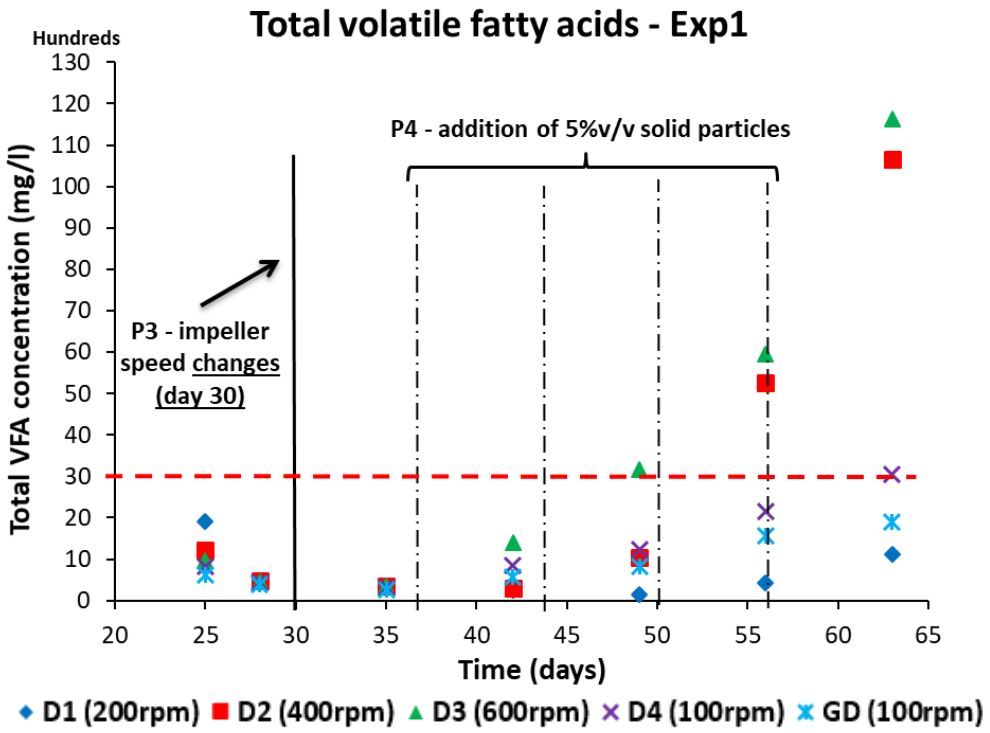

Figure 6.14: total volatile fatty acids (VFAs) in all digesters over the course of Exp1.

Figure 6.15 shows the individual VFAs measured in each tank during Exp1 (acetic, propionic, valeric, iso-valeric, butyric and iso-butyric acids). The relatively low concentration of VFAs in all tanks until day 35 is an indication of a well-balanced microbiota; i.e. acidogenic bacteria produce VFAs at the same rate as acetogenic bacteria and methanogenic archaea can consume them. With the increased OLR from day 37 onwards, all digesters experienced accumulation of mainly acetic and propionic acids.

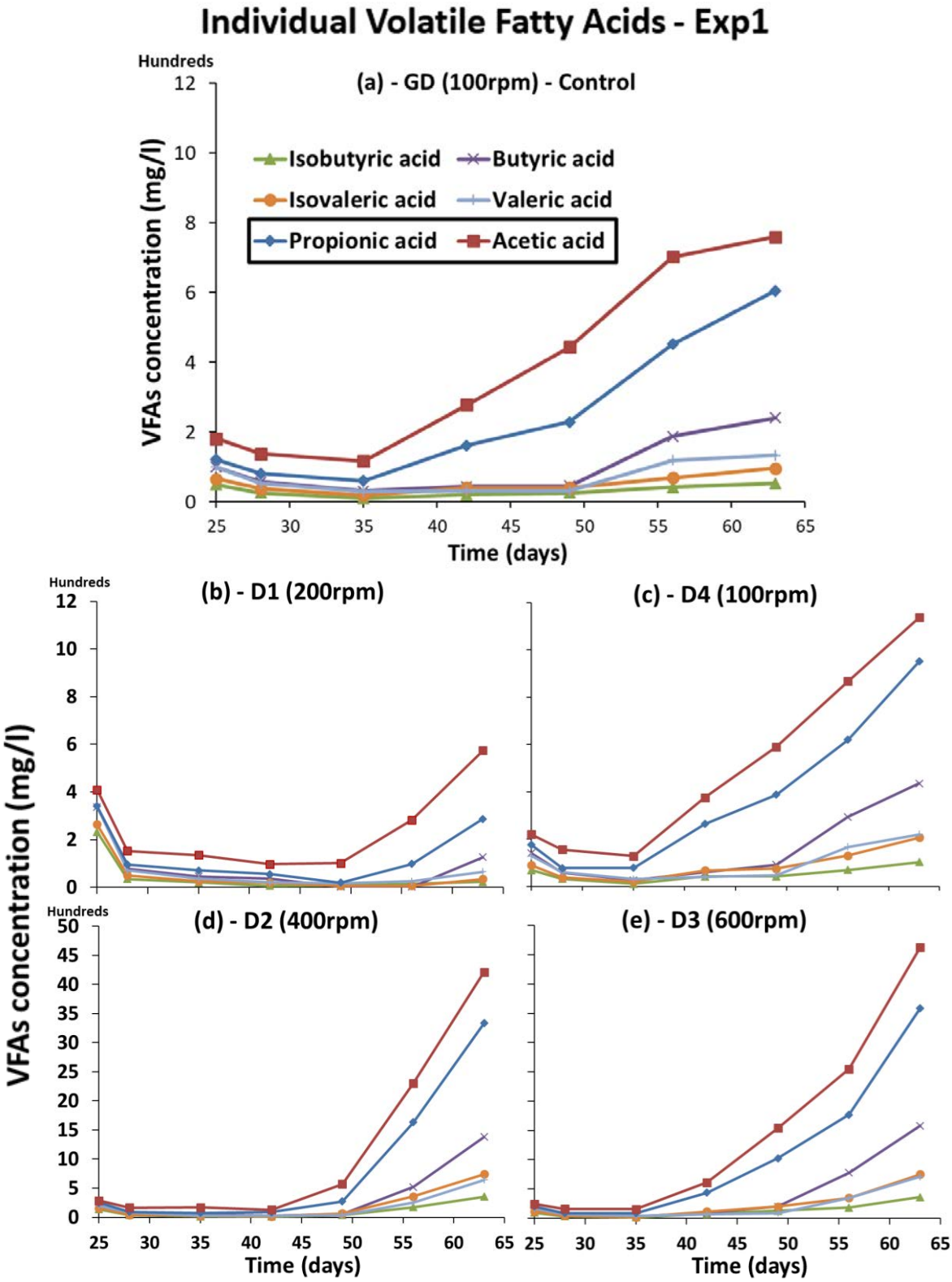

Figure 6.15: Individual volatile fatty acids (VFAs) in each digester over the course of **Exp1**: (a) GD (100-rpm), (b) D1 (200-rpm), (c) D4 (100-rpm), (d) D2 (400-rpm) and (e) D3 (600-rpm). Note that due to the difference in concentration, the scales are different.

The control (GD) and the low mixing speed tanks (D1 and D4) have experienced a less pronounced increase in acetic, propionic and butyric acids when compared to the high-intensity mixing systems, i.e., D2 and D3. By the end of Exp1, D4 presented the highest

values of 1100, 950 and 435 mg/l for these acids amongst the stable tanks. Figure 6.15 (d and e) shows the individual VFAs for D2 and D3. Acetic, propionic and butyric acids were present in higher concentrations when compared to the other acids measured. The doubling of OLR on day 49 coincided with the fast accumulation of VFAs and the addition of the inert particles. Acetic acid has always been present in higher concentration than all other acids, although propionic acid has been produced at similar rates, especially over the accumulation and instability period. By the end of Exp1 (day 63), D2 and D3 presented individual VFAs concentrations above the total threshold value. Whilst acetic acid concentrations were approximately 4220 and 4640 mg/l, propionic acid concentrations were 3335 and 3590 mg/l in D2 and D3, respectively.

Figure 6.16 shows the total VFAs over the course of Exp2 in all digesters plus the collected fresh digestate samples from Finham's WWTP. During the inoculation and acclimation phases (P1 and P2), total VFAs were very low, sometimes even below the detection range of the gas-chromatography equipment (GC). This means that all readily available VFAs were being consumed and converted into biogas very quickly. During Exp2, the steep increase in OLR, and its natural variation according to the TS fraction in the feed sludge was the only parameter altered until the end of P2. On day 40, there was a jump in VFAs concentration in all tanks. D4 experienced the highest increase, going from 0 to almost 3000 mg/l. Note that during this week, no fresh sludge sample was collected. Therefore, this large variation might have occurred because of the use of stored feed sludge over a total of two weeks (instead of normally 1 week). Although low temperature slows down biological activities and the degradation of organic matter, it does not stop it from happening. As such, VFAs might have been produced but not consumed. VFA measurement of the feed sludge was not carried out, hence no data is available to validate this hypothesis.

D1, D4 and GD tanks were kept under the stability limits at all times during Exp2. By the end of P4 (day 90), D1 and D4 showed higher total VFA concentrations (670 and 2237 mg/l, respectively) compared to the end of P2 (0 and 40 mg/l, respectively). GD went from 43 mg/l by the end of P2 to a total VFA concentration of 1313 mg/l by the end of Exp2. No other stability parameters, i.e. pH and CH_4, showed the indication of stress in these tanks over the course of Exp2. As shown in figure 6.10, the variation of OLR during P2, P3 and P4 of Exp2 was very low compared to the same phases during Exp1. Nevertheless, a similar overall increase of total VFAs in D1, D4 and GD can be noted over the course of P4. In both experiments, D4 ended with higher total VFAs whilst D1 had the lowest. The control tank was somewhere in between. Given that the only difference between D1 and D4 throughout Exp1 and Exp2 was the mixing speed, which started in P3, the impact of OLR variations should be the same in both tanks. This is because the energy input (results given in section 7.3, chapter 7) is insufficient to keep the inert solid particles in suspension, which creates a

permanent dead zone in the bottom of the tanks. Therefore, it reasonable to assume that the use of higher mixing regimes hinders biogas forming microorganisms. Analysis of the microbial population was not carried out, hence no data is available to validate this hypothesis

Similarly to Exp1, D2 and D3 experienced high VFAs fluctuations throughout the last phase of Exp2. Digestion was stable during P1, P2 and P3. During P4 no relevant change in VFAs can be noted in D3 after the first particle addition. On day 58, impeller speed in this tank was switched to intermittent mixing. On day 62, after all stability monitoring parameters crossed the threshold point, D3 was re-inoculated in an attempt to stabilise the process again. At this point, the total VFAs concentration in D3 was 3346 mg/l, pH=6.48 and biogas CH_4 content was 39.72%. On day 69, after the third 5% v/v particle addition and intermittent mixing was in place, the VFAs concentration of D3 was 1306 mg/l, whilst all measurements after the fourth and last particle addition were on the stability limit. It is interesting to note that although the VFAs concentration was high, all other control parameters were within the stability limits. Therefore, no further action was taken to mitigate the high VFAs concentration.

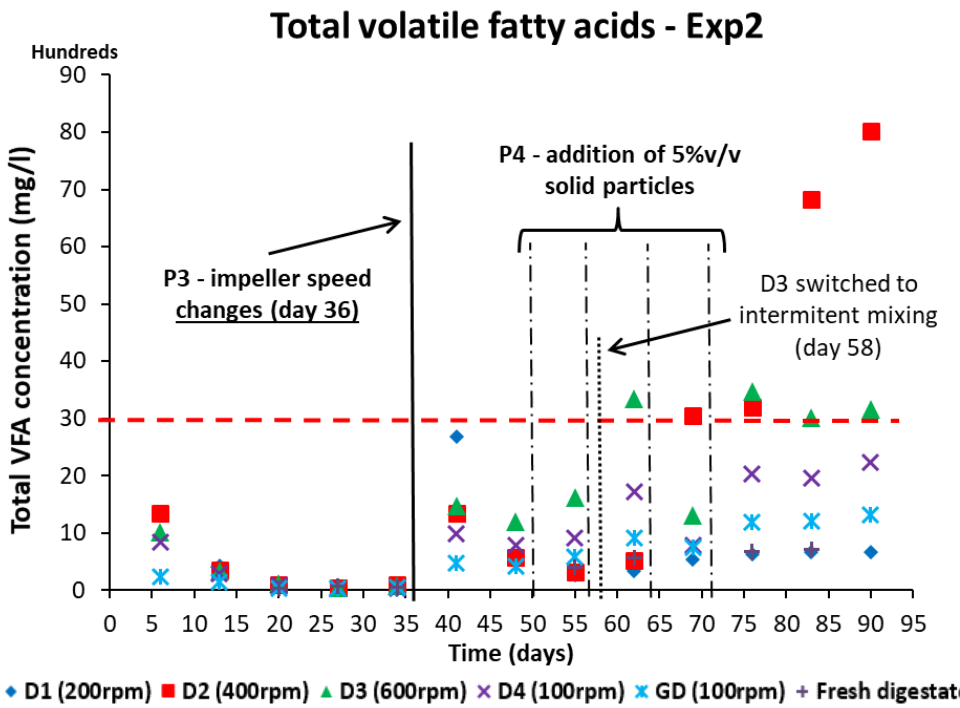

Figure 6.16: total volatile fatty acids (VFAs) in all digesters and fresh digestate over the course of Exp2. In Exp2, intermittent mixing consisted of a maximum of 15 minutes high-intensity mixing (600-rpm) prior and during the feeding process, but a continuous, low-intensity mixing regime (100-rpm) during the rest of the day.

The behaviour of D2 during Exp2 was similar to that of Exp1. A later reaction to the addition and constant suspension of inert particles is marked by a increase of VFAs in this digester after the third week of particle addition. pH and CH_4 fluctuations were earlier

warnings of an imminent failure, which started on day 65. The total VFAs crossed the stability limit on day 69, jumping from 524 mg/l on the previous measurement (day 62) to 3047 mg/l. By the end of Exp2, VFAs concentration in D2 was 8013 mg/l whilst pH was 6.30. Although biogas and CH_4 production were much lower than in all the other tanks, it did not cease (as happened in the first experiment). The results indicate that the process did not fail completely and methanogens were present. Stability could probably have been recovered by applying either intermittent mixing or smaller OLRs.

Figure 6.17 shows that amongst the individual VFAs, acetic acid has the highest concentration of all acids measured over the course of Exp2, followed by propionic acid. Butyric acid showed no significant difference when compared to the other acids. Plots (a), (b) and (c) of figure 6.17 compares the individual VFAs present in the GD, D1 and D4 tanks, respectively. By the end of Exp2, concentrations of acetic acid for the GD, D1 and D4 tanks were 796, 443 and 1236 mg/l, whilst they were 327, 137, 618 mg/l for propionic acid.

For the two higher mixing intensity tanks, D2 and D3, the accumulation of VFAs was again much higher when compared to the low mixing systems and the control digester. Figure 6.17 (d) and (e) shows the individual VFAs for the duration of Exp2 for these two tanks. The results show that until the end of P3, all tanks had similar individual VFAs concentrations. On day 55, 5 days after the 5% v/v addition of inert particles in all D tanks, the acetic acid concentration increases considerably in D3. From day 55 to day 62, acetic acid concentrations increased from 1202 to 2182 mg/l and the total VFAs concentration had crossed the stability limit of 3000 mg/l. After constant mixing was changed to intermittent and re-inoculation was carried out, a clear decrease in mainly acetic acid can be noted in D3. Although pH and CH_4 did not show signs of instability, the concentration of acetic and propionic acids were stable at high concentrations.

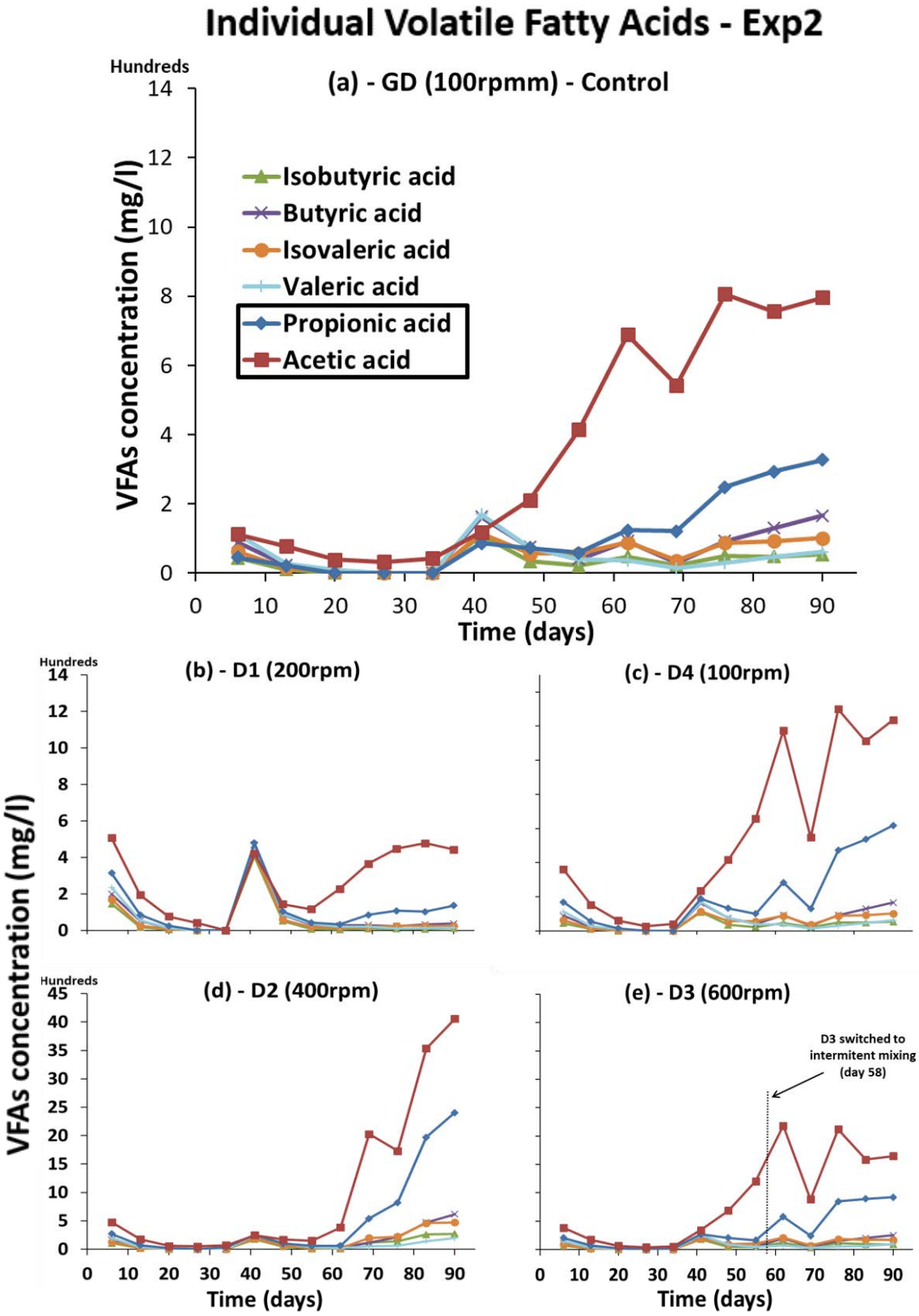

Figure 6.17: Individual volatile fatty acids (VFAs) in each digester over the course of **Exp2**: (a) GD (100-rpm), (b) D1 (200-rpm), (c) D4 (100-rpm), (d) D2 (400-rpm) and (e) D3 (600-rpm). Note that due to the difference in concentration, the scales are different. In Exp2, intermittent mixing consisted of a maximum of 15 minutes high-intensity mixing (600-rpm) prior and during the feeding process, but a continuous, low-intensity mixing regime (100-rpm) during the rest of the day.

D2, on the other hand, has demonstrated a gradual increase in VFAs along P4, especially acetic and propionic acids. Figure 6.17 (d) shows a sudden fivefold increase in acetic acid concentration from day 62 to day 69, going from 385 to 2028 mg/l. During the same period, pH dropped from 7.25 to 6.93 whilst CH_4 dropped from 67 to 57%. A slight reduction in acetic acid was evident while propionic acid continued to increase, leading to a total VFAs increase. By the end of Exp2, the acetic acid concentration was almost double than that of propionic acid at 4,055 and 2,406 mg/l, respectively. Compared to Exp1, butyric acid did not accumulate significantly in the digesters of Exp2. D2 ended Exp2 with the highest concentration of butyric acid (615 mg/l), much lower than the same tank in Exp1 (1380 mg/l). Similarly to Exp1, acetic and propionic acids were the main contributors to the inhibition of methanogenic archaea in Exp2. It is not entirely clear whether the primary source of methanogen inhibition was due to the accumulation of these acids or whether it was directly linked to the constant solid suspension and intensive mixing regimes.

As previously explained, the longer experimental time of Exp2 had the purpose of investigating the effects of (i) changing in mixing modes; (ii) adding inert solid particles and (iii) constant suspension of these particles on biogas production, CH_4 content, sludge treatment quality and energy balance. Despite the challenges faced by variations in feed sludge properties, this goal was partially achieved.

6.2.2 Sludge treatment quality

Being able to recover energy from sewage sludge is one of the advantages of AD. However, sludge stabilisation and volume reduction play a crucial role in achieving digester efficiency and compliance with disposal legislation. Therefore, the monitoring of an AD plant's treatment quality is the most important parameter needed for the control of sludge stabilisation. In order to measure treatment quality in the experimental digesters, total, volatile and fixed solids (TS, VS and FS, respectively) plus soluble chemical oxygen demand (sCOD) were assessed and the results are presented in the next sections.

6.2.2.1 *Total, volatile and fixed solids of digestate (TS, VS and FS)*

TS, VS and FS concentrations of all digestate were measured twice a week and the results of TS and VS are shown in figures 6.18 and 6.19 (a) for Exp1 and (b) for Exp2. Table 6.7 and 6.8 show the TS and VS average of each phase, as well as the total average in each digester (right-hand side column), and the average of all digesters in each phase (bottom row).

Figures 6.18, 6.19 (a) and table 6.7 show an initial constant TS and VS along the first 35 days of Exp1 with only small variations within the digesters and phases. The phases' TS and VS averages are 26.19 and 16.06, 24.21 and 15.15 and 25.15 and 17.90 g/l, for P1,

P2 and P3, respectively. These small variations mean that despite the feed's significant TS variation over the course of the three phases (see section 6.1.1), the rate of the AD biochemical reactions was not significantly affected. Considering that the designed OLR was only achieved for four days during the initial 35 days of the experiment, VS production/consumption ratios were well balanced with a good buffer capacity. This means that the system was working at full efficiency and the kinetics of all digestion phases were fully synchronised. Figure 6.19 (a) shows a drop in the VS concentration followed by an initial drop in OLR from day 35 until day 48. Digesters D1, D4 and GD seemed to respond very quickly to the doubling of OLR (1.63 to 3.78 kgVS/m³/day, which is approximately 50% more than the designed value of 2.5 kgVS/m³/day) from day 49 until the end of Exp1 (day 63). As such, OLR seems to have an immediate impact on the TS and VS. An increase in VS from day 49 until day 59 can be noted in all tanks whilst the last measurement shows a smaller VS concentration, indicating a stabilisation of the process. The biogas results provided in section 6.2.1.2 indicate that the microbial community coped well with the extra OLR, evidenced by the increased biogas yield. Despite the 20% v/v of inert solid particle addition in all D4 tanks by day 56, D1 and D4 did not present any increase in TS concentration relative to the control tank, GD. This is due to the mixing speeds of the tanks (100 and 200-rpm) not being able to provide enough energy to keep the added, dense inert particles in suspension. The particles settled in the bottom of the tank creating a dead zone.

D2 and D3 presented higher TS and VS concentrations, during P4. The increased VS concentrations indicate that the bacteria groups responsible for consuming the volatile solids are less present during P4. The overall P4 TS average for D2 and D3 were 46.21 and 80.37 g/l, more than double than that of D1, D4 and GD, which contained 24.28, 21.90 and 23.90 g/l, respectively. VS concentration was slightly higher in D2 and D3 than in D1, D4 and GD. Although the phases' average values are within the error (see table 6.7), the individual VS concentration showed in figure 6.19 has clearly been impacted by the higher mixing speeds and the addition of inert solid particles. Furthermore, the higher TS concentration (figure 6.18) indicates that the added inert particles were being withdrawn from the tank in the feeding process. It is notable that the individual and average TS concentrations in D3 are higher than in D2, indicating that a 600-rpm mixing speed (D3) provides a better solid suspension than 400-rpm (D2). A full analysis of the mixing speeds and solid suspension is presented in chapter 7.

Sludge exhibited less stability at the start of Exp2 when compared to Exp1, despite all tanks being inoculated with the same 100% fresh digestate and the parameters being kept the same until the end of P2 (day 36). During P1 and P2, TS and VS concentrations in all tanks differed significantly, as showed in figures 6.18 and 6.19 (b); however, variations within each tank were minimal, similar to those experienced in Exp1 (see table 6.8). D1

presented the lowest TS and VS concentrations, followed by D4 and D2, whilst D3 had similar TS and VS concentrations to the control tank (GD). In fact, D1 stopped producing gas on day 8 and D2 showed low biogas production in days 8, 9 and 10. Despite these TS and VS variations, the equivalent results for pH, CH_4 and VFAs showed no signs of instability. What caused these differences in the solid concentration is unclear.

Table 6.7: TS and VS digestate average concentration and standard deviation for all 5 tanks over the course of Exp1. The number of measurements is indicated in parentheses in front of the phases' number.

Exp1	Phase 1 (5)		Phase 2 (4)		Phase 3 (1)		Phase 4 (9)		Total average	
	TS (g/L)	VS (g/L)	TS (g/L)	VS (g/L)	TS (g/L)	VS (g/L)	TS (g/L)	VS (g/L)	TS (g/L)	VS (g/L)
	Ave ± SD	Ave ± SD	Ave ± SD	Ave ± SD	Ave	Ave	Ave ± SD	Ave ± SD	Ave ± SD	Ave ± SD
D1 (200rpm)	27.02 ± 2.30	15.97 ± 1.41	23.96 ± 0.32	15.09 ± 0.21	25.22	15.09	24.28 ±5.73	14.61 ± 2.43	24.98 ± 3.57	15.09 ± 1.84
D2 (400rpm)	25.68 ± 2.45	15.95 ± 1.41	23.75 ± 0.57	14.93 ± 0.41	26.47	14.83	46.21 ± 26.09	16.65 ± 4.69	35.04 ± 20.57	16.01 ± 3.28
D3 (600rpm)	25.19 ± 2.59	15.93 ± 1.45	22.46 ± 2.20	14.24 ± 1.46	24.25	14.08	80.37 ± 35.97	16.27 ± 4.08	50.70 ± 37.61	15.64 ± 3.00
D4 (100rpm)	25.96 ± 2.24	16.17 ± 1.23	24.44 ± 0.79	15.35 ± 0.55	24.49	15.12	21.90 ± 4.75	13.80 ± 3.09	23.64 ± 3.80	14.82 ± 2.39
GD (100rpm)	26.94 ± 1.45	16.28 ± 1.00	26.46 ± 0.18	16.14 ± 0.09	25.30	15.36	23.90 ± 3.30	14.65 ± 2.13	25.31 ± 2.71	14.43 ± 1.69
Total digestate*	26.19 ± 2.17	16.06 ± 1.21	24.21 ± 1.65	15.15 ± 0.91	25.15 ± 0.87	14.90 ± 0.49	39.33 ± 29.67	15.19 ± 3.44	31.94 ± 21.54	15.40 ± 2.50

Table 6.8: TS and VS digestate average concentration and standard deviation for all 5 tanks plus fresh digestate from Finham's WWTP AD tank over the course of Exp1. The number of measurements is indicated in parentheses in front of the phases' number.

Exp2	Phase 1 (4)		Phase 2 (6)		Phase 3 (4)		Phase 4 (12)		Total average	
	TS (g/L)	VS (g/L)	TS (g/L)	VS (g/L)	TS (g/L)	VS (g/L)	TS (g/L)	VS (g/L)	TS (g/L)	VS (g/L)
	Ave ± SD	Ave ± SD	Ave ± SD	Ave ± SD	Ave ± SD	Ave ± SD	Ave ± SD	Ave ± SD	Ave ± SD	Ave ± SD
D1 (200rpm)	23.88 ± 6.28	13.91 ± 3.41	15.63 ± 0.71	9.48 ± 0.48	20.75± 0.88	12.51 ± 0.28	19.57 ± 0.99	11.71 ± 0.52	19.51 ± 3.50	11.66 ± 1.91
D2 (400rpm)	26.94 ± 4.23	15.63 ± 2.26	17.88 ± 3.61	10.75 ± 1.85	32.21 ± 2.29	17.49 ± 0.85	27.94 ± 3.07	13.45 ± 1.94	26.12 ± 5.78	13.78 ± 2.83
D3 (600rpm)	30.00 ± 2.19	17.39 ± 1.10	23.23 ± 2.58	13.64 ± 1.45	30.23 ± 1.71	16.71 ± 0.56	51.59 ± 5.60	13.27 ± 1.07	38.46 ± 13.27	14.52 ± 2.03
D4 (100rpm)	25.55 ± 5.14	14.93 ± 2.72	18.62 ± 2.59	11.09 ± 1.60	24.31 ± 0.48	14.78 ± 0.40	18.31 ± 1.35	11.15 ± 0.75	20.42 ± 3.86	12.28 ± 2.18
GD (100rpm)	31.94 ± 0.92	18.03 ± 0.66	26.92 ± 2.82	15.3 ± 1.33	23.75 ± 0.43	14.44 ± 0.34	20.15 ± 1.11	12.23 ± 0.69	24.08 ± 4.64	14.17± 2.27
Fresh digestate	31.75 ± 2.10	18.19 ± 1.17	26.64 ± 1.67	15.85 ± 0.56	21.41 ± ---	13.05 ± ---	22.11 ± 1.26	13.60 ± 0.99	25.33 ± 4.20	15.14 ± 2.08
Total digestate*	27.66 ± 4.81	15.78 ± 2.56	20.48 ± 4.82	12.05 ± 2.52	26.25 ± 4.56	15.19 ± 1.87	27.51 ± 12.94	12.36 ± 1.40	25.72 ± 9.84	13.28 ± 2.50

*Total digestate average does not include fresh digestate values.

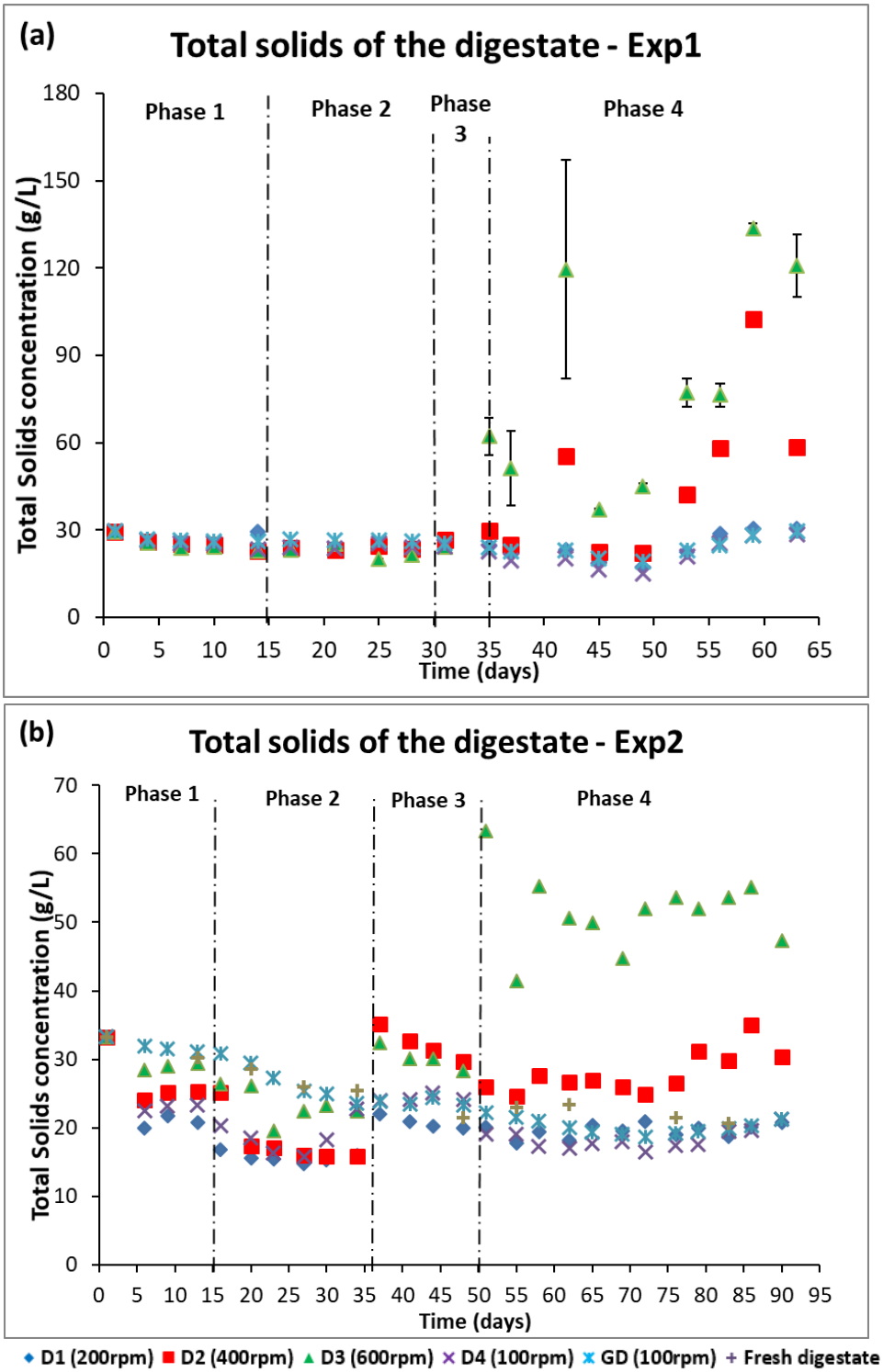

Figure 6.18: TS concentration of all 5 digesters during the entire experimental period of Exp1 (a) and Exp2 (b). Plot (b) also contains fresh digestate values from Finham's WWTP AD tank. Error bars are not visible in all samples because of their small value.

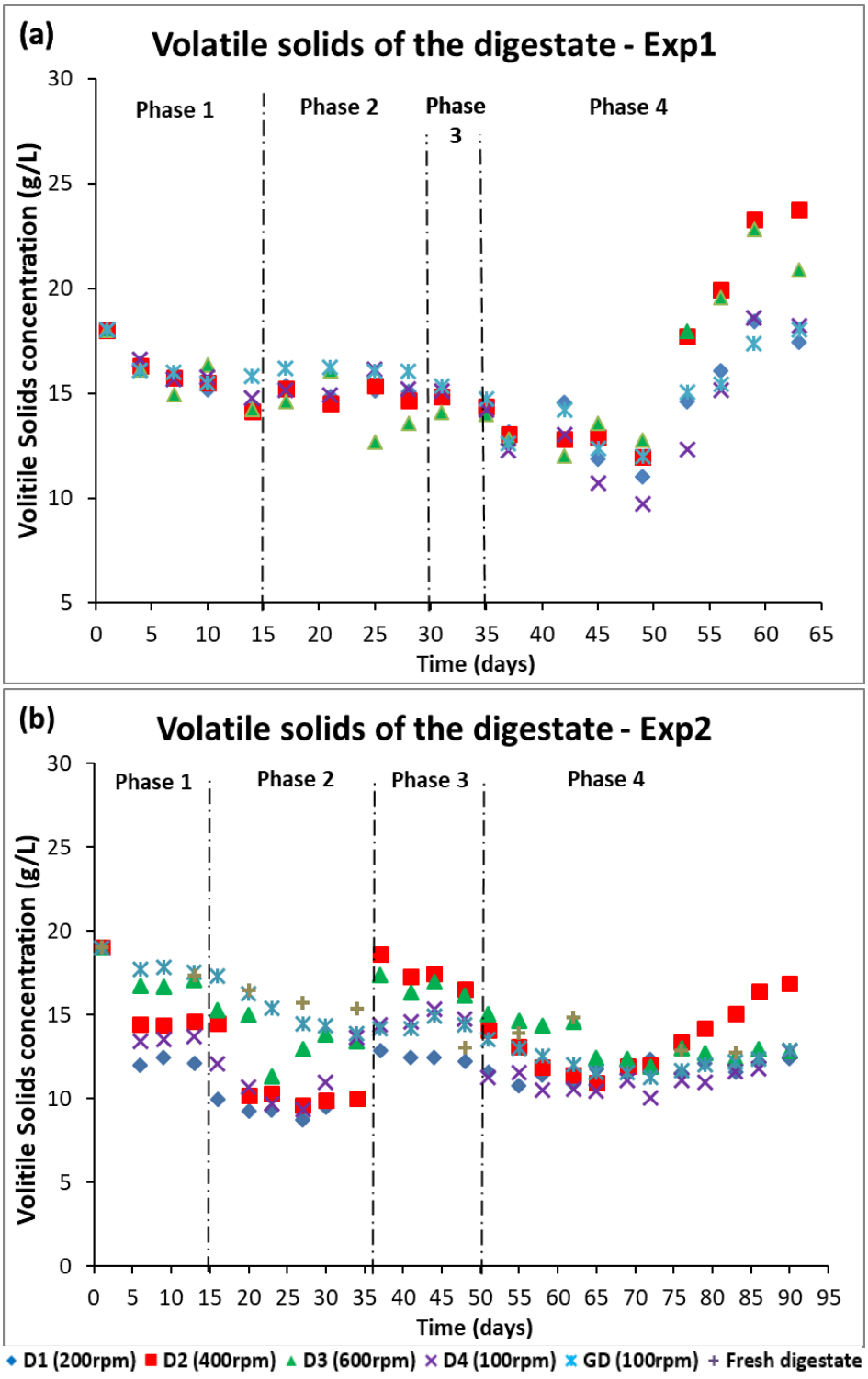

Figure 6.19: VS concentration of all 5 digesters during the entire experimental period of Exp1 (a) and Exp2 (b). Plot (b) also contains fresh digestate values from Finham's WWTP AD tank. Error bars are not visible in all samples because of its small value.

From the beginning of P3 (day 36 to 37), D2 (400-rpm) and D3 (600-rpm) experienced overflow and leaking. Sludge flowed from the tank to the gas counter through the gas hose and leaked from the stirrer's bearings. Although the OLR did not change during this transitional period, TS and VS increased significantly, from 15.87 and 22.41 g/l, to 35.13

and 32.44 g/l, for D2 and D3, respectively. These events indicate that higher mixing speeds detrimentally disturbed the AD system, probably causing foaming, which could explain the increased in TS and VS as well as the overflow and leaking in D2 and D3. Interestingly, pH and CH_4 content were not affected. VFAs increased in all tanks during P3, but within the stability limits. A fact that indicated, again, no warnings of process failure. Level control of all tanks was then carried out and any excess liquid withdrawn from the tanks. On day 38, D2 and D3 stopped leaking; therefore, it was decided to carry on the experiment without opening the tanks to check inside. As shown in figures 6.18 and 6.19 (b), TS and VS linearly decreased in D2 and D3 until the end of P3. From day 37 until the end of Exp2, D1, D4 and GD presented constant and similar solid concentrations. 20% v/v of particle addition during P4 did not seem to have any impact on TS and VS concentrations in these tanks.

In contrast to this, immediately after the first 5% v/v inert particle addition of P4 on day 50, TS concentrations in D3 increased significantly going from 28.27 to 63.34 g/l. Although higher VS concentrations in D3 can be seen in figure 6.19 for P4, they did not show a significant change until the mixing was changed from continuous to intermittent on day 58. TS, however, followed a similar pattern to Exp1, with a phase average for D2 of 27.94 g/l and 19.57, 18.31 and 20.15 g/l, respectively for the D1, D4 and GD tanks. The higher TS concentrations in D3 and D2 are attributed to the constant particle suspension due to the higher mixing energy of these systems. As seen in P4 of Exp1, the 400-rpm (D2) tank seemed to be able to keep part of the solid particles in suspension at a certain height in the tank whilst at 600-rpm, D3 seemed to keep most of the particles, if not all, suspended, thus escaping the tank while the feeding process is carried out. After intermittent mixing and re-inoculation had taken place, and towards the end of P4, D3 presented very similar VS concentrations to all other tanks, except D2. On day 76, after pH and total VFAs had crossed the stability limits, the VS concentration in D2 started to increase. The final VS concentration in D2 was 16.87 g/l, whilst the D1, D3, D4 and GD tanks were 12.43, 12.83, 12.83 and 12.89 g/l, respectively.

In summary, digesters D1 and D4 seem to show similar performances as the control digester, GD, in terms of TS and VS throughout the entire experimental periods of Exp1 and Exp2. This is despite the differences in mixing speed and the presence/accumulation of up to 20% v/v inert solid particles. Digesters D2 and D3, i.e., those with the highest mixing speeds, seem to be affected by the presence and suspension of the inert particles, which is indicated by the higher TS and VS concentrations by the end of P4. The consequence of this is discussed in chapter 8.

6.2.2.2 Soluble chemical oxygen demand (sCOD)

Soluble Chemical Oxygen Demand (sCOD) is the filtered fraction of the organic carbon in the substrate, as suspended and dissolved matter, that is readily biodegradable (Rubal et al., 2012). sCOD is one of the most straightforward and quickest measures of treatment quality from wastewater (Van Lier et al., 2008). An increase in the digestate's sCOD means either an increase in organic load or an accumulation of soluble organic matter in the sludge due to imbalances in the system.

Figure 6.20 shows the weekly monitored levels of sCOD in all digesters plus the feed sludge. sCOD levels in digesters D1, D4 and GD were under 2000 mg/l throughout Exp1, whilst D2 and D3 presented extremely high levels by the end of this experiment. sCOD levels in D2 and D3 increased slightly over the course of P3. This started first in D3 and by the end of the first week (after the addition of the 5% v/v inert solid particles) levels of sCOD had jumped from 2460 in day 35 to 7000 mg/l in day 42. sCOD increased slightly in the following two weeks, reaching 8820 mg/l on day 56, then doubled to 17160 mg/l in the last day of Exp1 (day 63). By the second inert particle addition on day 42, D2 presented slightly higher sCOD levels than D1, D4 and GD tanks (see fig. 6.20 (a)). After that, sCOD levels jumped up from 2640 to 6200 mg/l and was as high as in D3 by the end of the Exp1 (15960 mg/l).

As in Exp1, the Exp2 sCOD levels for D1, D4, GD and the fresh digestate were relatively constant over the course of the entire experimental period (figure 6.20 (b)). The minimum sCOD concentration for these tanks during Exp2 was 760 mg/l in D4 on day 27 whilst the maximum was 2005 mg/l in D1 on day 41. Until day 34, D2 and D3 presented similar levels to other tanks. sCOD levels in D2 and D3 then increased from 1420 and 1650 on day 34 to 3660 and 3740 mg/l on day 41, respectively. The next measurement during P3 took place on day 48 and showed that sCOD in D2 did not vary whilst it increased to 5820 mg/l in D3. It is unclear if this increase was caused by the change in mixing speed or because of foaming and leaking in the tank. sCOD concentrations in D3 continued increasing until day 62 when it dropped from 8635 to 2135 mg/l on day 69 after re-inoculation and intermittent mixing had taken place. On the other hand, sCOD in D2 slightly decreased from day 41 until day 62, following the same pattern as for VS. After that, sCOD levels only increased in D2 until the end of Exp2, presenting a final value of 11790 mg/l. D3 ended the experiment with similar sCOD levels to that of the other tanks (figure 6.20 (b)). This indicates that a) short-term high-intensity mixing does not affect anaerobic sludge treatment quality and b) constant high-intensity mixing detrimentally affects not only the sludge treatment quality but also the AD process stability and inhibits the methane forming microorganisms.

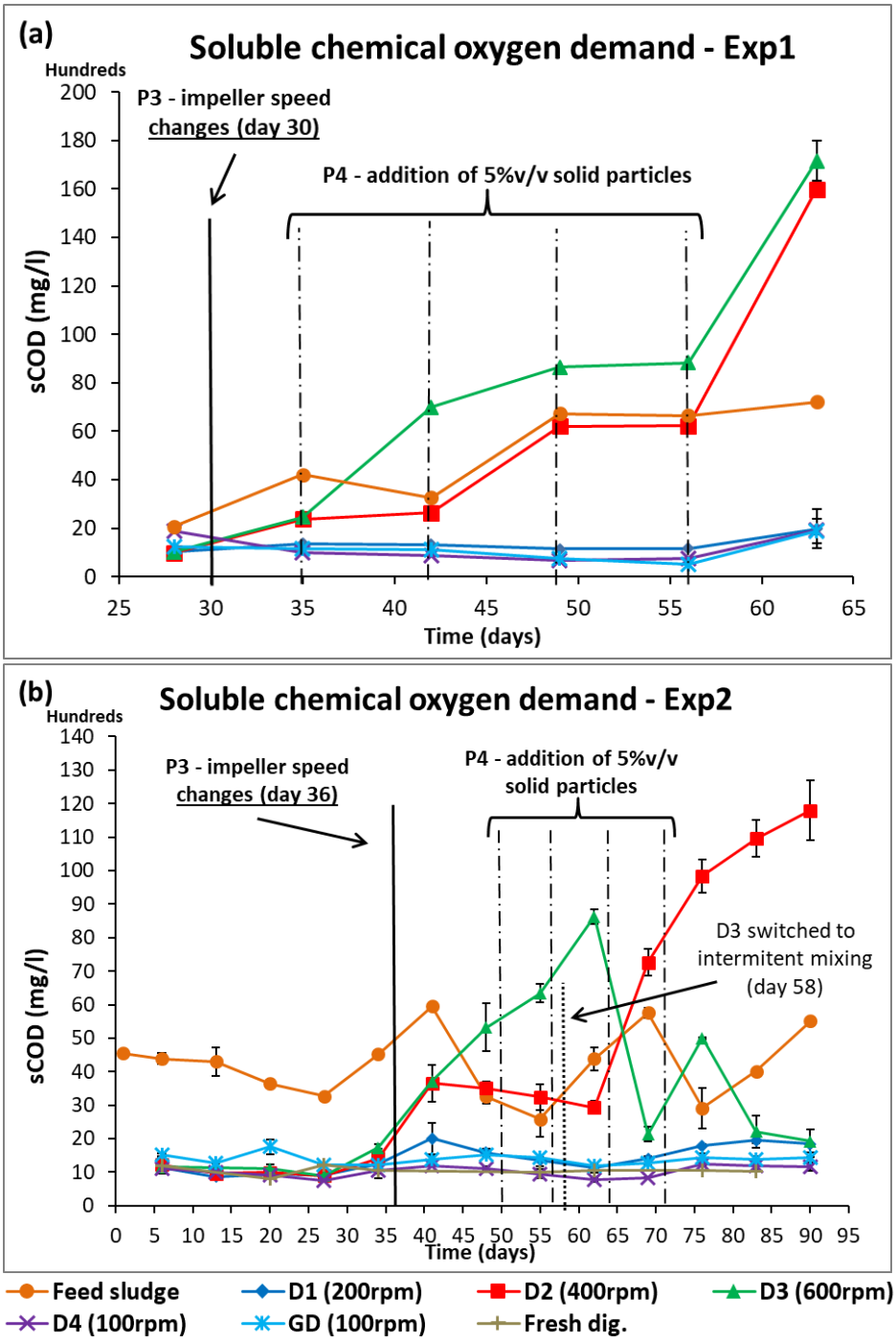

Figure 6.20: sCOD concentration of all 5 digesters for Exp1 (a) and Exp2 (b). Plot (b) also contains fresh digestate values from Finham's WWTP AD tank. Error bars are not visible in all samples because of their small value. Note that measurements for Exp1 started on day 28, whilst Exp2 covers the entire experimental time. In Exp2, intermittent mixing consisted of a maximum of 15 minutes high-intensity mixing (600-rpm) prior and during the feeding process, but a continuous, low-intensity mixing regime (100-rpm) during the rest of the day.

6.3 Sewage Sludge Feed and Digestate rheology

Figure 6.31 shows a summary of the rheological behaviour of the AD feed sewage sludge and digestate across the entire experimental periods of Exp1 and Exp2. The curves show the averaged values of shear stress versus shear rate for a) all weekly-collected feed

samples and b) the averaged digestate values from across all tanks (D1-D4). For comparison, the rheological curves for two carboxymethyl cellulose (CMC) solutions at concentrations of 2 and 4 g/l are also shown (as CMC2 and CMC4, respectively). The overall TS concentration averages for the feed sludge and digestate (throughout Exp1 and Exp2) are also shown for reference as bar graphs. The rheological behaviour of sewage sludge depends mainly on the total solids (TS) concentration (Achkari-Begdouri and Goodrich, 1992) and, as would be expected, the sludge's rheological behaviour is more prominent in Exp1 than in Exp2 due to the increased levels of TS (i.e., more viscous). Similar behaviour is exhibited by the feed sludge (higher TS) when compared to the average value obtained from the digestate in each tank.

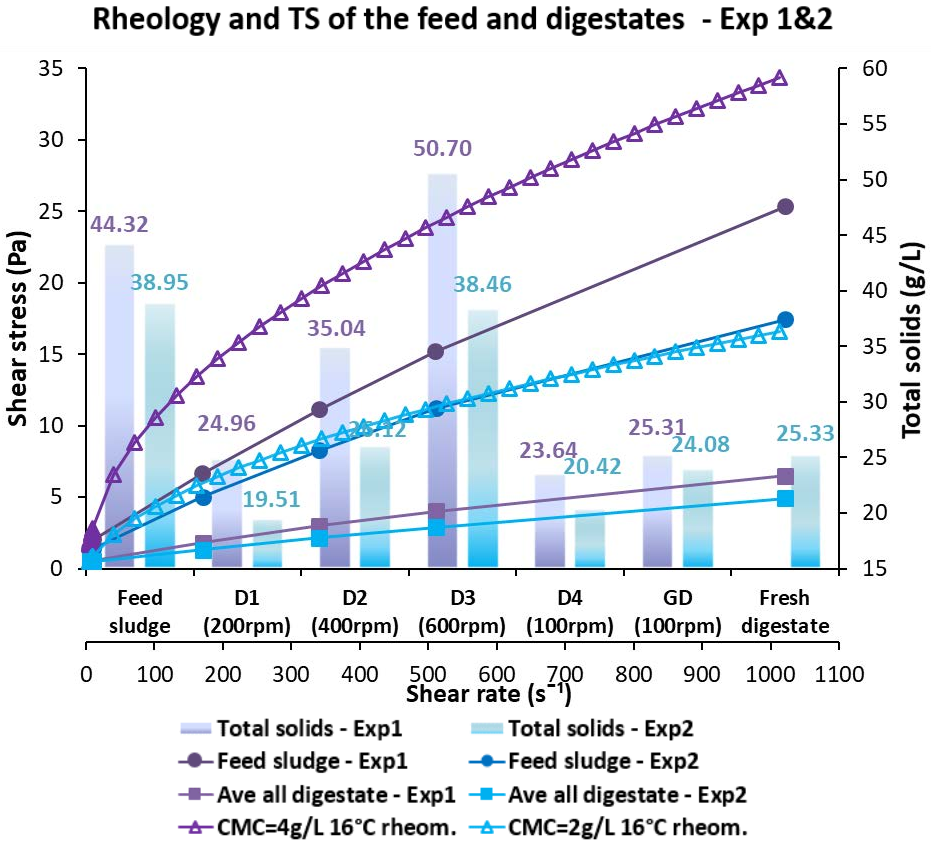

Figure 6.21: Rheological behaviour of CMC4 and CMC2 solutions compared to the average rheological behaviour of the feed sludge and digestate for all tanks throughout Exp1 and Exp2. For reference, the total solids (TS) concentrations for each tank are also shown. Error bars were omitted for clarity.

Note that despite the CMC2 solution accurately representing the rheology of the average feed sludge in Exp2, the rheological behaviour of the feed sludge used in the computational fluid dynamics (CFD) simulations (Chapter 7) was actually mimicked by the rheology of the CMC4 solution. This was based on the assumption that the feed sludge would have a TS concentration varying between 50 to 65 g/l, which clearly did not happen in the experiments. This is discussed in more detail in Chapter 8. Nevertheless, the results

indicate that researchers might have been over-predicting the rheological behaviour of feed sludge which may lead to errors when designing and operating industrial AD tanks.

6.4 Summary

This chapter presents the results of the laboratory work divided in two main parts: (i) the characterisation of inert sediment particles and feed sludge from industrial AD tanks and (ii) the semi-continuous lab-scale anaerobic digestion of sewage sludge. The results of (i) present, for the first time, the particle size distribution (PSD) and density details of inherently non-biodegradable (also referred as inert) particles contained in the sludge that accumulates in AD tanks due to inefficient mixing systems and designs. These novel data are used to build the CFD model (chapter 7) and for the preparation of the experimental work of part (ii). In addition, an analysis of feed sludge variations throughout the experimental period is given in order to better understand the role of the OLRs and their relationship with the effects of mixing regimes, suspension and/or accumulation of inert particles on the digestion performance.

The aim of the lab-scale AD experiments in part (ii) was to investigate the energy-efficiency mixing regime required to avoid inert particle accumulation in AD tanks and, in which, mixing energy and biogas yield are balanced such that energy input is minimised without detrimental impact on biogas production or sludge treatment quality. The results of all parameters used to measure digestion performance were presented and discussed. The results show that a) high-intensity mixing, thus constant inert solid suspension, inhibits the biogas and methane production and leads to poorer sludge treatment quality, whilst b) low-intensity mixing regimes do not seem to have a negative impact on treatment quality and biogas production over a short period of time. Despite the accumulation of 20% v/v of inert particles in the bottom of the low-intensity mixed tanks, the low OLRs seemed to counterbalance the loss of working volume and avoid the system's overload, leading to stable digestion. Intermittent mixing was found to be the most energy-efficient solution for a well-stabilised AD operation.

CHAPTER 7 COMPUTATIONAL FLUID DYNAMICS (CFD) SIMULATION AND EXPERIMENTAL RESULTS

This chapter presents the methods and results of the computational fluid dynamics (CFD) simulations used to investigate the fluid-solid interaction in the mechanically-mixed laboratory-scale anaerobic digesters. Section 7.1 explains the numerical methods and simulation strategy, which includes the description of multi-phase modelling, geometry and mesh generation, verification and validation methods, fluid rheology, initial and boundary conditions, discretisation schemes, turbulence, initialisation and convergence monitoring. Section 7.2 presents the results of the velocity field, solid suspension and cloud height (defined as the height from the bottom of homogenous suspension), including the analysis of the viscosity behaviour of the non-Newtonian shear-thinning sludge mixed under different particle loadings. Finally, in the last section, the results of mixing energy from the CFD and laboratory experiments are given, followed by a summary.

All CFD simulations were submitted to the University of Birmingham's High-Performance Computing (HPC) cluster, BlueBEAR. Each computational node consisted of on one dual-processor 8-core 64-bit 2.2 GHz Intel Sandy Bridge E5-2660 worker with 32 GB of memory. A total of 15 nodes was deployed and an average run time of 720 hours for each simulation case. The commercial CFD package ANSYS Fluent 18.2 was used for all simulations. The geometry and the mesh were generated using the integrated software in ANSYS workbench, DesignModeler and ANSYS Meshing, respectively.

7.1. Numerical Method and Simulation Strategy

To perform reliable CFD simulations that closely represent the real fluid flow phenomena, a set of steps must be determined, such as model choice, mesh generation and grid independence test, initial and boundary conditions, discretisation schemes and turbulence models. In addition, the drag force model, which is the most influential interaction force between the liquid and solid phases, must be determined as well as the rheological properties of sewage sludge. The latter plays an important role in the velocity field, particle distribution and cloud height. These are all discussed in the following sections.

7.1.1. Multi-phase model choice

The choice of model is very important and depends on the nature of the multi-phase flow as well as the expected results to be achieved. As shown in the literature review (chapter 3), the Eulerian-Eulerian (Eu-Eu) multi-phase model is the most common model used to simulate the solid suspension in stirred tanks. In short, Eu-Eu is composed of two or more phases, where the governing equations are solved separately for each phase, but mathematically treated as interpenetrating continua using exchange terms to account for

the transfer of mass, heat and/or momentum through continuity, energy and momentum equations, respectively. The phases can be liquid, gas or solid, in any combination and number, and the model is only limited by the memory capacity of the computer and the convergence criteria of the model. Each phase cannot occupy the same volume as any other phase, thus the concept of volume fraction must be introduced (see section 7.1.4.1). This model is recommended when more than two phases are present, being general enough to accommodate any volume fraction of any phases (ANSYS Inc., 2013). The most essential criteria for Eu-Eu model closure is that the sum of the volume fraction of each phase must be equal to 1 in all cells at all times. Given the nature of this study, the Eu-Eu model has demonstrated to be the most suitable multi-phase model and was used for all simulations to produce the results presented here.

The results from the rheological study of the feed sludge and the properties of the sediment particles found in industrial tanks were used to build the CFD model (see Chapter 6, sections 6.1.3). For the liquid phase, also named as the primary or carrier phase, the rheological behaviour of the feed sludge was mimicked by carboxymethyl cellulose (CMC) at a concentration of 4 g/l. The behaviour is described by a power-law model (see equation 3.12 in chapter 3). Section 7.1.5 explained that 4 g/l of CMC solution was able to represent the rheological behaviour of sewage sludge at a total solid concentration of 5.53%. CMC is a common chemical used in several industrial processes, mostly in the food industry, to “thicken” a liquid solution. It is broadly used to mimic the rheological properties of slurries and validate CFD models (Sindall, 2014, Dapelo et al., 2015).

Note that for the purposes of modelling non-Newtonian fluid flow, it is of crucial importance that a correct definition is provided for the limit when the viscosity is independent of shear rate (see section 7.1.5 for a complete discussion). A wrong choice/measurement of the lower and upper plateau limits of this parameter will strongly affect the velocity field (eq. 3.28) and therefore the turbulent kinetic energy, dissipation rates of the model (eq. 3.29), fluid-particle interaction forces and momentum exchange terms (eqs. 7.6 and 7.8). All of these terms are directly or indirectly dependent on the instantaneous dynamic viscosity of the liquid phase which, in case of non-Newtonian fluids, depends on the instantaneous local shear rate (see section 3.2.2).

The four solid phases’ volume fractions were based on the simplified particle size distribution of table 6.3. They were used to determine the solid distribution and cloud height for the four investigated solid loadings under four different impeller speeds in the AD experiments (chapter 6).

7.1.2. Model geometry and mesh generation

The domain of the model is based on the four identical anaerobic digestion D tanks used in the AD laboratory experiments. The tank, shown in detail in figure 7.1, has a cylindrical geometry that contains four, equally-spaced baffles equipped with one symmetrical, 4-pitched-blade turbine (PBT) centred within the tank and positioned at a fractional height of 1/3 off the flat-bottom of the tank (figure 7.1). The design of the tanks followed well-established rules for solid suspension in stirred tanks (Kresta, 2016, Machado et al., 2012, Ayranci and Kresta, 2011). The dimensions of the D tank are shown in table 7.1 and represented in figure 7.1.

Table 7.1: Dimensions of the D tanks, impeller and baffles.

Geometry	Parameters	dimension in mm
Tank	high	255.00
	diameter (T)	200.00
	liquid high (H)	200.00
Impeller	diameter (D = T/2.5)	80.00
	clarence (C = T/3)	66.67
	width (h = T/10)	20.00
	thickness (t_i = D/28)	2.00
	pitched angle (α)	45°
	number of blades	4
Baffle	width (b = T/10)	20.00
	high (h_b = H)	196.00
	gap from wall (g_w = 0.015*T)	3.00
	gap from bottom (c_b = b/5)	4.00
	thickness (t_b =0.015*T)	3.00

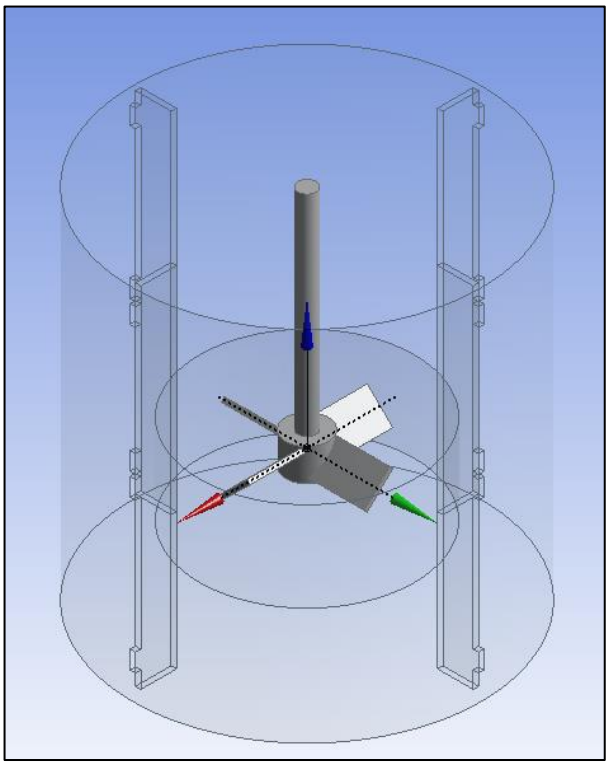

Figure 7.1: CFD model geometry. The impeller is contained in the rotating frame shown in the central region of the domain.

The use of a structured mesh (over unstructured grids), is usually preferred due to the smaller computational costs associated with the reduced number of ordered cells in which the governing equations will be resolved. For simple geometries, generating structured grids is straightforward. However, it becomes more difficult for complex geometries. On the other hand, unstructured meshes can accommodate geometries of any size and complexity. Although the tank has a simple geometry, the addition of baffles with gaps in the bottom/walls, plus the inclusion of the impeller geometry, makes the use of structured grids more difficult. In addition, the ANSYS meshing tool has a vast range of local functions that can be used to revise the mesh at regions with high refinement requirements, such as in the vicinity of the impeller wall, interfaces and baffles. These functions can be applied to single or a set of points, lines, faces or to entire regions. In this way, it allows the user to optimise the mesh in regions where it is important to capture rapid changes in key quantities such as velocity and pressure gradients. In this way, it is possible to keep a coarser grid in low-gradient regions of the domain yet still achieve a high-quality solution for the flow field.

An unstructured mesh composed of tetrahedral elements with refinement in several parts of the domain including the baffles, rod and impeller walls and the interface between the stationary and rotating frames, was used in this work. Figure 7.2 shows a cross-sectional view of the whole mesh, whilst details of the region close to the impeller's wall and 'rotational frame region' are shown in figure 7.3. The index (GCI) method was applied to test for mesh independence and is presented in section 7.1.10.1.

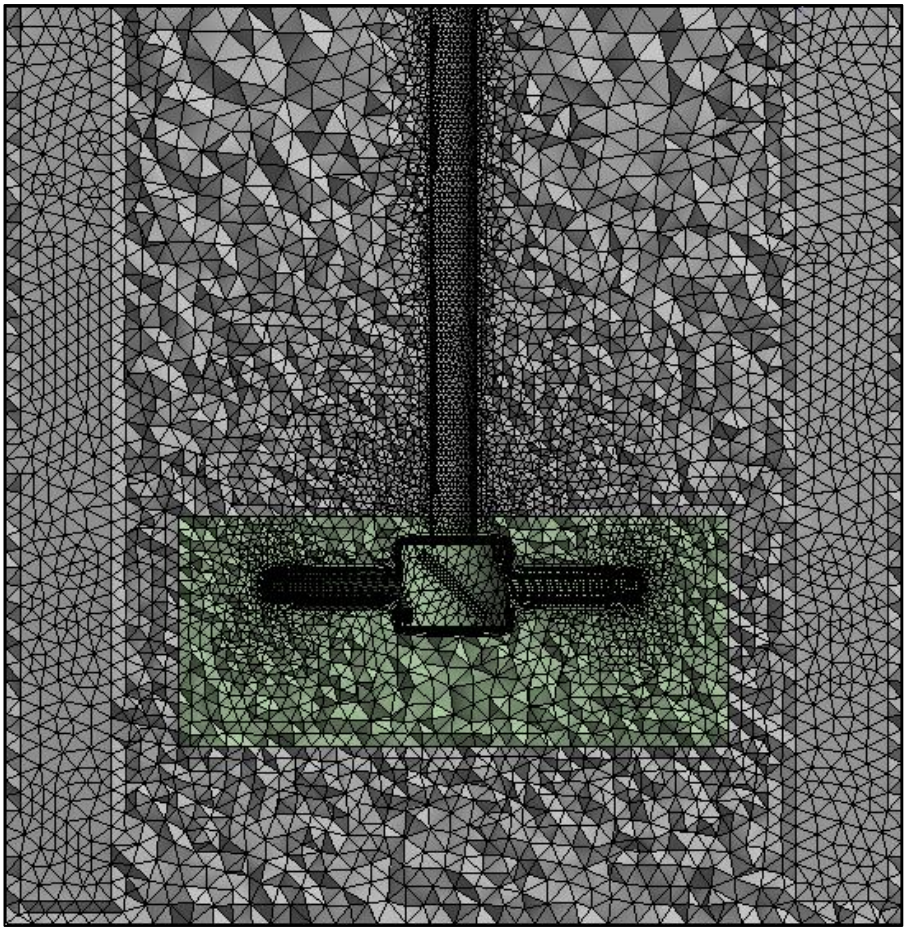

Figure 7.2: cross-section of the models' domain unstructured mesh. The region shown in grey represents the stationary frame whilst the green region represents the rotational frame.

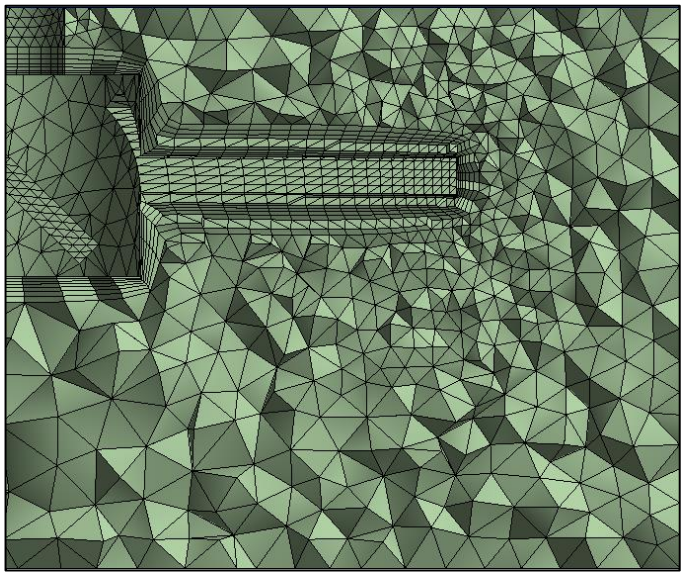

Figure 7.3: detail of the impeller's region mesh**.**

Figure 7.3 shows details of the mesh close to the impeller in the rotational frame region, where the two main control methods were used, i.e., sizing and inflation. The sizing function allows the user to set specific mesh elements and a local minimum size to a given point, line or surface, plus a growth rate up to the bulk region of the domain (where velocity

or pressure gradients are less significant and do not require fine grids). Inflation allows the creation of specifically oriented cells close to the walls experiencing high parameter gradients. The refinement of cell size and type in the boundary layer region, where the flow experience rapid changes in crucial variables' gradients, is closely related to the choice of the turbulence model (see section 3.2.3). Table 7.2 shows the parameter definitions applied to the mesh used in all simulations.

The impeller (PBT) is considered symmetrical in the vertical and horizontal planes, and the origin of the Cartesian coordinate system is located in the centre of its mass, which was the reference point to build the rest of the geometrical parts. The rotational frame region is concentric with the coordinate system's origin and its boundary walls are located at 12.62 mm above and 37.48 mm below the origin. It has a radius of 60 mm and a total volume of 5.52E-0.4 m³ (~10% of the tank's volume).

Table 7.2: details of the grid refinement functions and dimensions.

Function	Region	Parameter and value		
		Element size	Growth rate	# of layers
Sizing (faces and bulk domain)	Rotationary	5.00 mm	1.30	-
	Stationary	15.00 mm	1.30	-
	Interface	3.50 mm	1.05	-
	Baffles	1.20 mm	1.30	-
	Impeller	4.50 mm	1.20	-
Inflation	Impeller	0.20 mm	1.20	7

7.1.3. Periodic rotating flow

The baffled, mechanically-mixed vessel is equipped with one centrally-positioned, symmetric 4-blade pitched-blade turbine (PBT) that generates a periodic rotating flow. The flow patterns of the fluid and solid phases in the tank are influenced by the vessel's geometry and its components (i.e. the tanks' dimensions and shape, impeller type, position and rotating direction, the presence of baffles and its geometry and position within the tank, and so on). There are two commonly used models capable of predicting the imposed forces from the impeller to the liquid/solid/gas in CFD models: sliding grid (SG) and multiple reference frame (MRF). The SG model consists of two non-overlapping regions in the domain, forming inner and outer sub-mesh regions. The inner region contains the moving parts, i.e. the PBT, which rotates relative to the stationary outer region allowing it to shear and slide. After each time step the grid is reconnected to its closest stationary cell and all variable values are updated accordingly. Despite the more realistic reproduction of the real phenomenon, the SG method incurs greater computational cost in order to achieve a full solution and it is still computationally prohibitive in most practical cases.

The multiple reference frame (MRF) approach has been applied in the vast majority of the published scientific works on stirred tanks in both single-phase and multi-phase

models (Wadnerkar et al., 2016, Ansys Inc., 2015, Azargoshasb et al., 2015, Bridgeman, 2012, Wadnerkar et al., 2012, Wu, 2011). This method consists of two distinct mesh regions within the model's domain clearly defined by shared stationary boundary surfaces. This is where the information of neighbourhood cells are consistently interpolated between the same nodes of the grid. The outer region contains stationary walls as well as the baffles whilst the inner part contains the moving impeller. The rationale for using this method is to transform the unsteady nature of the problem in the inertial stationary frame with regard to the moving region. This is to impose the momentum transfer from the impeller to the fluid without moving it. This allows the information of the cells to be shared by the stationary, but virtually moving, neighbourhood cells through the non-overlapping interface. This way, the MRF model's computational power demand is less intense than that of the SG. The MRF was therefore chosen for this work.

7.1.4. Multi-phase modelling

The Eulerian granular multi-phase model, based on the interpenetrate continua theory, is used in this work to numerically simulate the behaviour of the sand-solid particles. These are mixed in the stirred anaerobic digestion tanks containing a CMC solution to mimic the non-Newtonian behaviour of the sewage sludge (section 7.1.1). This model introduces the concept of volume fraction, here named as α_q (ANSYS Inc., 2013). The volume fraction of the q^{th} phase, V_q, is defined by:

$$V_q = \int_V \alpha_q dV \tag{7.1}$$

where the condition of

$$\sum_{q=1}^{n} \alpha_q = 1 \tag{7.2}$$

must be met for the closure of the conservation equations.

The properties of the CMC carrier or primary phase solution are given in the next section (7.1.5) whilst the secondary phases (i.e., four solid phases) were modelled as a multi-fluid granular model to describe the fluid-solid interaction, as suggested in Fluent manuals (ANSYS Inc., 2013) and research literature (Wadnerkar et al., 2016, Liu and Barigou, 2013, Tamburini et al., 2011). The density of the solid material was set of that for sand (2650 kg/m³). The volume fraction formulation was computed by the implicit method, i.e. a scalar transport equation is solved each time step for all secondary phases. In the implicit method, the volume fraction is dependent on other quantities at the current time

step, rather than the update from the previous time step, as in the explicit method (ANSYS Inc., 2013).

The governing equations introduced in chapter 3 must be numerically resolved for each phase so that the flow fields can be drawn for any combination of phases. The equation of conservation of mass for the q^{th} phase is given by:

$$\frac{\partial}{\partial t}(\alpha_q \rho_q) + \nabla \cdot (\alpha_q \rho_q \vec{v}_q) = \sum_{p=1}^{n} (\dot{m}_{pq} - \dot{m}_{qp}) + S_q \tag{7.3}$$

where $\vec{v}_q$ is the velocity of the q^{th} phase, $\dot{m}_{pq}$ and $\dot{m}_{qp}$ account for the mass transfer from the p^{th} to q^{th} phase and vice versa. S_q is a source term that accounts for any other component of mass exchange within the system. To avoid confusion, it is important to reiterate that the fluid dynamic computational model adopted here is only concerned with understanding the fluid-solid interaction of the non-Newtonian fluid, sewage sludge and the inert solids, represented by the sand particles. The natural total solids contained in the sludge, fixed or volatile, are not modelled and only contribute to the rheological behaviour of the fluid phase in the CFD model. Therefore, there are no mass transfers between the phases and, as such, all terms of the right-hand side of eq. 7.3 are zero. The mass transfer terms will not be shown in subsequent equations and, therefore, the conservation of mass equation becomes:

$$\frac{\partial}{\partial t}(\alpha_q \rho_q) + \nabla \cdot (\alpha_q \rho_q \vec{v}_q) = 0 \tag{7.4}$$

The conservation of momentum equation of the q^{th} phase is given by:

$$\begin{aligned} \frac{\partial}{\partial t}(\alpha_q \rho_q \vec{v}_q) + \nabla \cdot (\alpha_q \rho_q \vec{v}_q \vec{v}_q) \\ = -\alpha_q \nabla \mathrm{p} + \nabla \cdot \bar{\bar{\tau}}_q + \alpha_q \rho_q \vec{g} + (\vec{F}_q + \vec{F}_{lift,q} + \vec{F}_{vm,q} + \vec{F}_{td,q}) \\ + \vec{F}_{ls} \end{aligned} \tag{7.5}$$

where *l* and *s* refers to the liquid and solid phases, respectively, $\vec{g}$ is the acceleration force due to gravity and $\bar{\bar{\tau}}_q$, $\vec{F}_q, \vec{F}_{lift,q}, \vec{F}_{vm,q}, \vec{F}_{td,q}$ and $\vec{F}_{ls}$ are, respectively, the q^{th} phase stress-strain tensor, external body forces, lift and virtual mass forces, turbulent dispersion force and lastly, the interaction force between the fluid and solid phases. The stress-strain tensor is given by:

$$\bar{\bar{\tau}}_q = \alpha_q \mu_q (\nabla \vec{v}_q + \nabla \vec{v}_q^T) + \alpha_q (\lambda_q - {}^2/_3 \mu_q) \nabla \vec{v}_q \bar{\bar{I}} \tag{7.6}$$

where μ_q and λ_q are the shear and bulk viscosity of the q^{th} phase, respectively.

Forces $\vec{F}_s, \vec{F}_{lift,s}, \vec{F}_{vm,s}$, and $\vec{F}_{td,s}$ are considered negligible when compared to the drag force in the system where $\frac{\rho_s}{\rho_l} > 2$, which is the case for this work (Fletcher and Brown, 2009, Ljungqvist and Rasmuson, 2001, ANSYS Inc., 2013). Therefore, they are neglected.

The turbulent dissipation force is the term that accounts for turbulent diffusion through momentum transfer between the fluid and solid phases. While Ljungqvist and Rasmuson (2001) and Wadnerkar et al. (2012) found this force to be negligible, more recent works of Gohel et al. (2012) and Wadnerkar et al. (2016) showed that turbulent dispersion influences the final prediction of the flow field. All authors used the same turbulent dissipation force model, whilst Wadnerkar et al. (2016) tested all three models available in Ansys Fluent and compared them. In both works, the authors reported a better prediction of the solid dispersion and cloud height compared to experimental results. Note that these studies did not include either non-Newtonian fluid behaviour or more than one solid phase, as is the case in this work. The computational costs reported are much higher and for transient simulations, experience shows that the time step size must be decreased up to 50 times to achieve convergence. Therefore, the turbulent dissipation force is also neglected in this work.

The term F_{ls} in equation 7.5 accounts for the interphase momentum exchange coefficient between the liquid and solid phases, represented by K_{ls}. The F_{ls} force is described as:

$$\vec{F}_{ls} = K_{ls}(\vec{v}_l - \vec{v}_s) \tag{7.7}$$

For granular flows $K_{ls} = K_{sl}$ and is a function of the drag force (C_D), which is given as:

$$K_{sl} = \begin{cases} \frac{3}{4} C_D \frac{\alpha_s \alpha_l \rho_l |\vec{v}_s - \vec{v}_l|}{d_s} \alpha_l^{-2.65} & for\ \alpha_l > 0.8 \\ 150 \frac{\alpha_s (1-\alpha_l)\mu_l}{\alpha_l d_s^2} + 1.75 \frac{\alpha_s \rho_l |\vec{v}_s - \vec{v}_l|}{d_s} & for\ \alpha_l \leq 0.8 \end{cases} \tag{7.8}$$

This model was proposed by Gidaspow et al. (1992) and used by Wadnerkar et al. (2016) and Liu and Barigou (2013) in very similar systems, but using mono-disperse solid phase. Note that even for the lowest solid particle loading of 5% v/v, the four solid phases in this model have different diameters and can together, occupy the cells up to α_s≈0.8, which is normally limited by the maximum packing factor of ~0.6 to 0.63. The use of the volume fraction to calculate the drag force makes the Gidaspow model the most suitable for this work, as suggested by (Liu, 2014). This concept will be detailed further in the coming sections. C_D is defined as:

$$C_D = \frac{24}{\alpha_l Re_s}[1 + 0.15(\alpha_l Re_s)^{0.687}] \tag{7.9}$$

and Re_s represents the relative Reynolds number and can be calculated from:

$$Re_s = \frac{\rho_l d_s |\vec{v}_s - \vec{v}_l|}{\mu_l} \quad 7.10$$

where d_s is the s^{th} solid phase particle's diameter and μ_l is the fluid molecular viscosity, which in the case of non-Newtonian fluids is referred to as the apparent viscosity (μ_{la}). μ_{la} is defined as the specific viscosity of a fluid under a given shear rate. The relative Reynolds Number can be rewritten as:

$$Re_s = \frac{\rho_l d_s |\vec{v}_s - \vec{v}_l|}{\mu_{la}} \quad 7.11$$

The drag force (F_{ls}), is the most important term that contributes to liquid-solid momentum exchange. It is directly (eq. 7.8) and indirectly (eq.7.11) influenced by the viscosity of the liquid phase. This fact reiterates the arguments presented in section 7.1.1. in that the correct definition/measurement of the viscosity plateau limits for the non-Newtonian fluid component is of crucial importance in order to reliably determine the flow field of a solid suspension in stirred tanks.

7.1.5. Fluid rheology modelling

For the non-Newtonian fluid models presented in chapter 3, the power-law model, given by eq. 3.12 (Kresta, 2016, Chhabra, 2007) and repeated here for clarity (eq. 7.12), was the most suitable model to represent the apparent viscosity-dependent behaviour of the shear rate according to experimental measurements;

$$\mu_a = K\dot{\gamma}^{n-1} \quad 7.12$$

where $\dot{\gamma}$ is the shear rate, K is the consistency index and *n* is the power-law index. K is a measure of the average viscosity of the fluid, whilst *n* is a measure of the deviation from Newtonian fluids. In Ansys Fluent, the shear rate is written in terms of the second invariant of the deformation tensor, $\overline{\overline{S_{ij}}}$, derived from the partial derivatives of the Eulerian velocity field, given by:

$$\overline{\overline{S_{ij}}} = \frac{1}{2}\left(\frac{\partial u_j}{\partial x_i} + \frac{\partial u_i}{\partial x_j}\right) \quad 7.13$$

$$\dot{\gamma} = \sqrt{\overline{\overline{S_{ij}}} : \overline{\overline{S_{ij}}}} \quad 7.14$$

The power-law model was used to represent the properties of the primary phase. A comparison study was carried out between carboxymethyl cellulose (CMC) concentrations at 2, 4 and 8g/l and fresh sewage sludge rheological characteristics (Fig. 7.4). A solution of

CMC of 4 g/l at 16°C reproduced the rheological behaviour of fresh AD feed sludge at TS=5.53% at 37°C (see figure 7.4). It turned out that one power-law function was unable to provide a full and precise description of the viscosity in the range where it is dependent on shear rate (SR), especially in the lower plateau limit. Errors up to one order of magnitude arise close to the plateau limits when a single equation is applied, which in turn propagates viscosity prediction errors in these regions. Therefore, an interpolation between two equations was used in order to better describe the rheological behaviour of the CMC at 4 g/l, (referred to as CMC4 hereafter).

Table 7.3 shows the shear rate and respective viscosity limits of CMC4, the consistency index *k* and power-law index *n* for each equation used. A user-defined function (UDF) was developed and compiled in the Fluent source code (appendix A) so that the viscosity in each cell is calculated in accordance with the current shear rate.

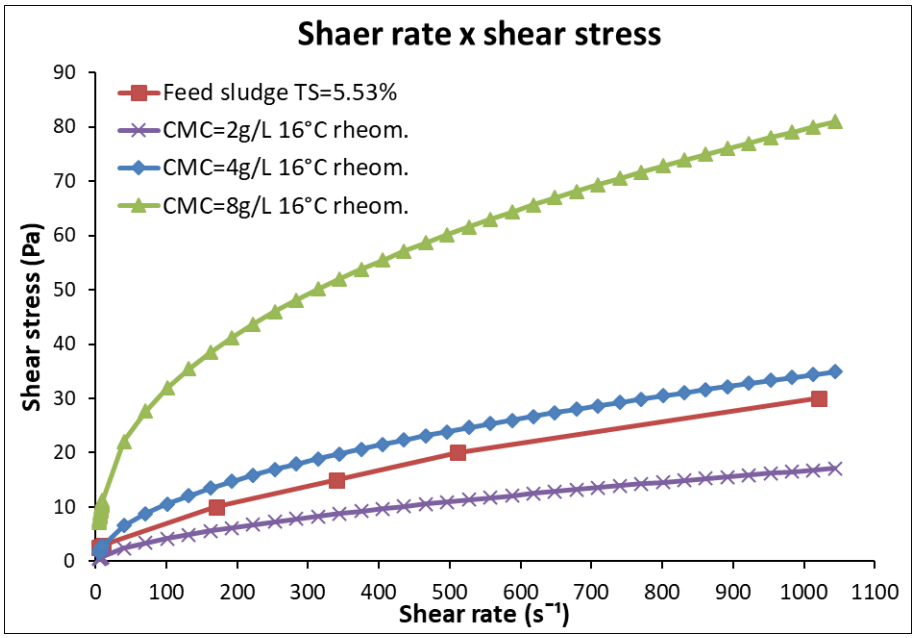

Figure 7.4: Characteristic rheological curves for CMC at 2, 4 and 8 g/l measured using the rheometer and feed sewage sludge at TS=5.53% measured in the viscometer.

Table 7.3: Characteristic of the fluid phase properties (CMC4) used to build and compile the UDF.

Power law for CMC4	Shear rate (1/s)	Viscosity (Pa.s)	k	n
Low SR limit	0.70	0.479	0.4462	0.803
Interpolation point	15.76	0.259	-	-
Upper SR limit	1500	0.026	0.9965	0.5166

7.1.6. Initial and boundary conditions

All simulations were solved using the transient solver, a built-in algorithm in Ansys Fluent that solves the governing integral equations for the conservation of mass and

momentum, plus other scalars such as turbulence. In the first stage of the model, a time step size of 0.01 seconds with a maximum of 30 iterations for each time step was used for the first 200 seconds. The convergence criteria for this first stage was $1x10^{-3}$ for the normalised residuals of the governing equations' variables. In a second stage, the time-step-size was changed to 0.005 seconds and a maximum number of 20 iterations was allowed. At this point in the model, second-order discretisation schemes were selected, and the residuals were changed to $1x10^{-5}$. In all cases, the under-relaxation factors (URFs) were halved from the default values. More details on the adopted convergence strategy are provided in section 7.1.9.

A non-slip condition defined the walls of the digester meaning that the first liquid layer assumes the velocity of the wall and increases relative to its adjacent layers until the bulk flow is reached. This creates a velocity profile called the boundary layer (Pope, 2000). In this work, the near-wall treatment was modelled by the standard wall functions included in the Ansys package (ANSYS Inc., 2013). The top surface was assumed to be 'open' or as a wall of zero-shear. As the impeller speed increases, vortexing is likely to happen on the top surface although this effect is suppressed under the zero-shear wall condition. To resolve this problem, a sixth phase could be added to model the interface between the liquid and the air using the volume of fluids model (VOF). The VOF model solves a single set of momentum equations for two or more immiscible fluids assuming the conditions for the volume fraction of each phase to be either present or not and the volume fraction of each phase is tracked throughout the domain, differently from the interpenetrating continua theory, where the momentum equation is solved by each phase. (ANSYS Inc., 2013). Several works on stirred tanks have neglected this effect due to the extra computational demand it imparts but with little increase in accuracy (Wadnerkar et al., 2016, Tamburini et al., 2014, Liu and Barigou, 2013, Bridgeman, 2012). The same approach was adopted for this work and no further investigation of the impact of this approach was carried out.

7.1.7. Turbulence model

As seen in chapter 3, there are a number of options available to account for turbulent fluctuations of the velocity field and other scalar quantities for single-phase CFD simulations. Modelling multi-phase flows, however, adds several terms to the momentum equations, making the turbulence modelling much more complex. Additionally, Ansys Fluent has a limited number of turbulent models for the Eu-Eu multi-phase model. As the literature review shows, variants of the k-ε turbulence model have been extensively used to model mechanically-mixed anaerobic digesters (Meister et al., 2018, Azargoshasb et al., 2015, Sindall, 2014, Shen et al., 2013, Bridgeman, 2012, Wu, 2011), and solid suspension in stirred tanks (Wadnerkar et al., 2016, Tamburini et al., 2014, Wadnerkar et al., 2012,

Fletcher and Brown, 2009). The standard, RNG and realisable k-ε turbulence methods, plus the SST k-ω, were considered in this work for single-phase analysis. The realisable k-ε model showed to be the most suitable for this work because of its convergence capability for the poly-disperse multi-phase model. The results and discussion of other turbulence models are given in appendix B. All simulated cases fall in the transient regime (see section 3.2.3) as shown in the table below.

Table 7.4: Details of turbulent regimes of the simulated cases (CMC4).

RPM	Impeller tip speed (m/s)	*Re* (Eq. 3.18)	*Re* (Eq. 3.21)
100	0.42	36	35
200	0.84	89	88
400	1.68	234	222
600	2.51	427	380

Three k-ε turbulence multi-phase models are available in Ansys: mixture, per-phase and dispersed models. The mixture (or homogeneous model) is applicable when the density ratio between the phases is nearly one. It is also assumed that the k and ε quantities share the same values. The per-phase model solves a set of transport equations for each phase and is appropriate when the turbulence transfer among the phases is of high importance. It is clear that neither of these models fits the exact requirements of this work where a) the density rate among the primary and secondary phases are greater than 2, b) the turbulence transfer from primary to secondary phases are neglected and c) the computational cost for using the per-phase model in a 5-phase multi-phase problem is prohibitive. The dispersed model is recommended when using a granular model and, as such, was chosen for the present work. In the dispersed model, the fluctuating quantities of the secondary phases are expressed in terms of the properties of the fluid phase and the ratio of the particle relaxation time and eddy-particle interaction time (ANSYS Inc., 2013, Feng et al., 2012, Wadnerkar et al., 2016).

7.1.8. Discretisation schemes

In first-order discretisation schemes, the governing equations are resolved in the discretised domain and the values averaged for each cell and then stored in the cells' centroid. In this case, all quantities are at the same in the point of the cell. This scheme provides reasonable solutions for unidirectional and low Reynolds number flows. However, in high-turbulence systems with large, instantaneous changes in the velocity gradients, higher-order discretisation schemes are advisable. The main difference between first and higher-order discretisation schemes is the use of upstream cell quantities to account for the cells' face values; therefore, the greater number of computational points used in higher-

order discretisation schemes. The computational cost of resolving the governing equations within higher-order discretisation schemes is much higher when compared to first-order schemes. Consequently, it is a common strategy to start solving the governing equations with first-order schemes until the solution is partially converged and then change to higher-order discretisation schemes to improve the accuracy of the solution.

The phase-coupled SIMPLE (PC-SIMPLE) discretisation scheme together with the N-phase volume fraction equations were used for the pressure-velocity coupling at all times (ANSYS Inc., 2013). The PC-SIMPLE method uses the same principle of the SIMPLE method for single-phase models but includes coupling terms, such as drag, among the phases. The N-phase volume fraction equations solve all volume fraction equations for each phase so that they satisfy the assumption of summing to a value of 1.

The first-order-upwind discretisation scheme was applied to the diffusive and convective terms for the first 200 seconds of all cases. After that, the discretisation schemes were changed to a second-order-upwind discretisation scheme until convergence was achieved. The final URFs were kept smaller than the default values so that convergence could be achieved. These are multiplying factors used to dampen the solution from previous time steps so to avoid great variations. URF leads, however, to a greater number of iterations for the solution to achieve convergence. The implicit first-order transient formulation was used for the first 200 seconds of simulation time and was then changed to the second-order implicit method.

7.1.9. Initialisation and convergence monitoring

For all modelling cases, the hybrid initialisation method was used (see ANSYS Inc. (2013) for further details). The patch function was used to “insert” the solid phases on the lower part of the domain according to the simplified PSD (particle size distribution) presented in section 6.1.3. The patched region was applied at different heights for each solid particle loading, such that all particles started at rest in the bottom of the tank. Bigger particle groups were patched first and were homogeneously distributed in the bulk-bottom region of the digester, such that solid phases occupied 5, 10, 15 and 20% by volume (v/v) of the whole domain. Note that the sum of all phases’ volume fractions must be equal 1 at all times in order to close the mass balance of the system (eq. 7.2).

In stirred tanks, the default governing equation’s convergence criteria (i.e., residuals of the equations for continuity, velocity components, turbulent kinetic energy and dissipation rate, plus the volume fraction for the multi-phase cases) are not enough to correctly predict the complete development the flow field. Therefore, further convergence parameters should be created (Ansys Inc., 2015). For the single-phase validation model, two monitoring parameters were created: an area-weighted-average (AWA) of the velocity magnitude at

the top surface and a volume-weighted-average (VWA) of the kinetic energy (KE) in the bulk region of the tank, far from the impeller. ke converges much faster in the impeller region because of the stronger velocity gradients, lower viscosity (due to high shear rates in case of non-Newtonian fluids) and faster energy dissipation rates. For the multi-phase model, four additional monitoring parameters were created; Two AWA and two VWA values of the volume fraction (vf) of the smaller and bigger particles (i.e., diameters of 0.15 and 1.18 mm, respectively). These were monitored at the first surface layer of grid cells on the bottom of the tank (for AWA) and in the entire rotational frame region (for VWA).

Convergence was considered as achieved only after the standard governing equation residuals, plus all additional convergence monitoring parameter residuals, were below $1x10^{-5}$ for all cases unless otherwise stated. For most cases, full convergence took approximately twice the actual simulation time.

A *macro* script was created to monitor the impeller torque every 20 time-steps. The torque is defined by the sum of the "dot product of a unit vector in the direction of the specified axis and the individual and net values of the pressure, viscous, and total moments and coefficients" of the impeller surface cells (ANSYS Inc., 2013). The CFD-based torque was later compared with the physical torque measured in the laboratory.

7.1.10. Model verification and validation

Verification of the discretised domain is crucial in order to minimise the errors of the resolved governing equations and ensure that the solution will be within a certain accuracy. The finite volume method (FVM) consists of discretising the physical domain into a finite number of control volumes (called cells or elements). The governing equations are then resolved in each cell and interpolated with its neighbouring cells over a number of iterations to achieve the expected solution. For time-dependent problems, the solution is given after the normalised residuals decrease to three or four orders of magnitude for all cells in the domain every time step. It became clear that the final results were dependent on the number of cells. Verification of the grid density was, therefore, necessary to avoid a low or excessive number of cells.

Validation, on the other hand, is a methodology applied to ensure that the results of the model are capable of reproducing the flow field behaviour of real-world phenomenon. This is normally achieved via experimental studies and comparing them with the CFD models results.

Roache (1998) summarised these two concepts very well by describing verification as "solving the equations right," and of validation as "solving the right equations" In this work, the universally accepted Grid Convergence Index (GCI) method is used to verify the grid density (Celik et al., 2008). Particle Image Velocimetry (PIV), another commonly used

experimental method, was applied to validate the model. For the multi-phase model, a simple visualisation technique was used to assess the cloud height at each mixing speed at all particle loads and compared to the CFD results. A brief description of the method and the results are presented next.

7.1.10.1. Grid convergence index (GCI) method

To complete a GCI test, a few steps must be followed. A summary of the methodology is provided here but for further details refer to Celik et al. (2008). Firstly, it is necessary to build at least three grids with similar grid structures (sizing functions, tetrahedral or hexahedral elements, and so on) but different densities, define as h:

$$h = \sqrt[3]{\frac{1}{N}\sum_{i=1}^{N}(\Delta V_i)} \quad 7.15$$

where N is the number of cells in each domain and ΔV_i is the volume of the i^{th} cell. The grid refinement factor is given as $r_{coarse/fine} = h_{coarse}/h_{fine}$, and according to Celik et al. (2008), should be ideally greater than 1.3. A variable of interest, and critical to the problem, φ, must be chosen for assessment of the grid. In this work, the impeller torque was chosen because it represents the momentum exchange to the fluid that is going to be dissipated and induce the mixing. Then the error $\varepsilon_{32} = \varphi_3 - \varphi_2$ and $\varepsilon_{21} = \varphi_2 - \varphi_1$ is calculated so that the apparent order p can be iteratively found. p is a function of $r_{coarse/fine}$, and is defined by the following equations:

$$p = \frac{1}{\ln(r_{21})}|ln|\varepsilon_{32}/\varepsilon_{21}| + q(p)| \quad 7.16$$

$$q(p) = \ln\left(\frac{r_{21}^p - s}{r_{32}^p - s}\right) \quad 7.17$$

$$s = 1 \cdot sgn(\varepsilon_{32}/\varepsilon_{21}) \quad 7.18$$

GCI is then calculated using a safety factor of 1.25 and is given as:

$$GCI_{fine}^{21} = \frac{1.25 e_a^{21}}{r_{21}^p - 1} \quad 7.19$$

where

$$e_a^{21} = \left|\frac{\varphi_1 - \varphi_2}{\varphi_1}\right| \quad 7.20$$

The grid independence is considered in the asymptotic range when:

$$\frac{GCI_{fine}^{21}}{r_{21}^{p} GCI_{coarse}^{32}} \cong 1 \qquad 7.21$$

The whole geometry was used to build the grid and the GCI method used to assess their independence for four cell densities: 614,075; 730,449; 1,969,788 and 3,336,841 cells, namely G1, G2, G3 and G4, respectively. The rate (given by eq. 7.20) between grids for G2, G3 and G4 was 0.83, whilst for G1, G2 and G3 it was 2121.44.

In addition to the GCI method, the velocity magnitude of the x and y velocity components along a vertical line with 100 points positioned at r/R=0.6 and 1° anti-clockwise before the baffles (see 7.1.10.2) was compared for all four girds. The result is plotted in figure 7.5. Similarly, the turbulent kinetic energy (TKE) for each grid density, and accounting for all components, was plotted in figure 7.6 for comparison.

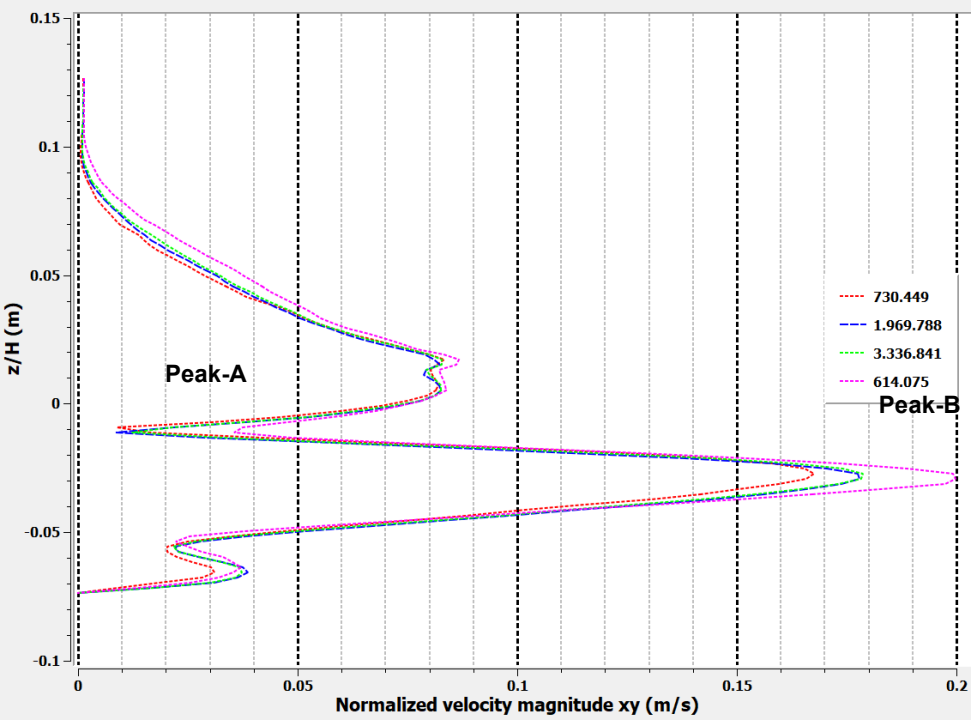

Figure 7.5: Normalised velocity magnitude along a vertical line at r/R= 0.6 and azimuthally turned 1° anti-clockwise (approximately behind the baffle, positioned as the PIV laser beam). The velocity magnitude normalised by the impeller tip's linear velocity.

Figure 7.5 shows the shape of the normalised velocity magnitude curves for all four grids, which follow the same pattern and give very similar values in the region above the impeller. Two velocity peaks appear just below the height of the impeller, the first of low velocity (peak-A) followed by the second, with the highest velocity magnitudes (peak-B), along the vertical line at r/R=0.6. The lowest point in the first peak shows a velocity

magnitude that is close to 0.01 m/s for the three finest grids whilst the value is 0.035 m/s for the coarse grid. The coarsest grid (614075 cells) shows the highest velocity value for peak-B (at ~0.20 m/s) and the second coarsest grid (730449 cells) the lowest at ~0.17 m/s. The two densest grids show an intermediate normalised velocity magnitude of ~0.18 m/s when compared to the two, less dense grids. The particle image velocimetry (PIV) results (presented in the next section) shows similar results for the grid with 730499 cells for the second peak.

Figure 7.6 shows the turbulent kinetic energy (TKE) for the same line shown in figure 7.5. The TKE is computed using the three velocity components v_x, v_y, v_z, (refer to ANSYS Inc. (2013) for a complete description). Although the normalised velocity magnitude profile along the line r/R=0.6 does not show any significant variation within the four grids tested, it is clear in figure 7.6 that the coarsest grid gives outliers in the stationary/rotational interface region. The analysed line is positioned in the vicinity of the interface border but within the rotational region. The first peak on the upper region shows an abrupt and unrealistic nine-fold increase of the TKE compared to the other three grids. The lower region below the impeller shows a less intense, but still significant, increase in the TKE compared to the other three grids. This behaviour is related to the low number of cells in the shared surfaces, where interpolation of all values occurs. The three finest grids show a good agreement in terms of both shape and values for TKE.

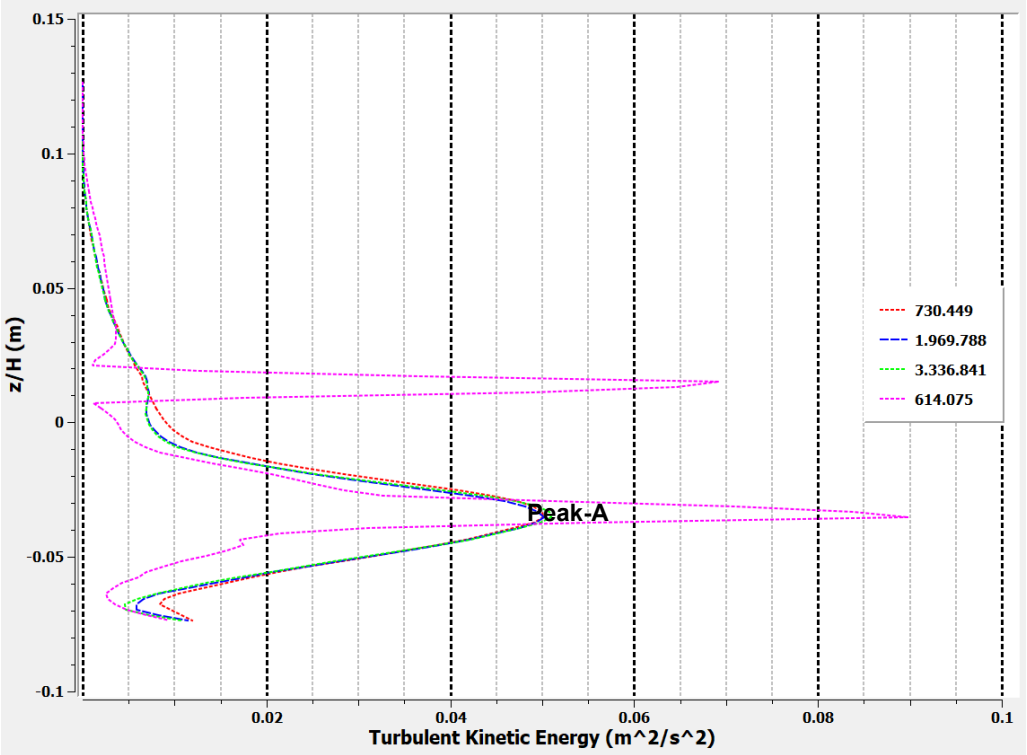

Figure 7.6: Turbulent kinetic energy along a vertical line at r/R= 0.6 and azimuthally turned 1° anti-clockwise (approximately behind the baffle, positioned in the plane created by the PIV laser beam, see next section for details).

From this analysis, the coarsest grid was rejected whilst the other three grids showed similar results with no significant difference in the GCI test. Given the higher computational cost of the two finest girds, the one with 730449 cells was selected to run all further single-, and multi-phase simulations.

7.1.10.2. Particle imaging velocimetry method and results

Of the several techniques used to obtain measurements of the flow field, the PIV method has become the common method for representing the complex flow in stirred tanks (Kresta, 2016, Sindall, 2014, Liu and Barigou, 2013, Guida, 2010). PIV is a non-intrusive technique that provides the Eulerian velocity field through consecutive images of trace particles in a transparent liquid and vessel. A pulsing laser beam highlights the diluted tracers in a plane whilst a synchronised camera, positioned perpendicular to the direction of the laser lights, captures the images of the particle in a specific time interval. The data is then analysed in a central processor and the velocity field extracted by the distance travelled by the set of tracers in the given time interval. A schematic view of the PIV experimental setup is shown in figure 7.7

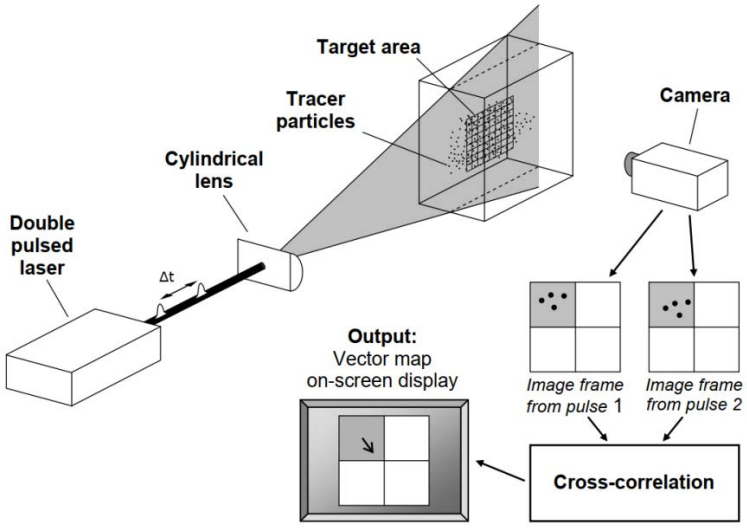

Figure 7.7: Schematic experimental set-up view of the Particle Image Velocimetry method (Guida, 2010).

The setup of the PIV experiment for the validation of the CFD model presented in this work consisted of a baffled, transparent acrylic tank with the same geometrical dimensions as the D-tanks used in the anaerobic digestion experiments. The cylindrical tank was placed, and centrally fixed, inside a squared tank with a minimum gap of 1.0 cm between the vessels. This method helps to minimise the refraction from the laser beam in the curved surface of the acrylic tank. The trace particles must be small and neutrally buoyant so that they follow the fluid flow without interfering in the flow process. Tracers must

also reflect the laser light so that it is captured by the camera. In this work, 10 μm silvered glass spheres (specific density of 1.2-1.3 kg/m3) were used. The TSI PIV system (TSI Inc) comprised of a Nd:YAG (neodymium-yttrium aluminium garnet) laser, a TSI Power view (2048 x 2048 pixels) charged coupled device (CCD) camera and a synchronizer (TSI 610035). The TSI Insight 4G software (TSI Inc) was used to control the whole system from an attached computer. The Insight software processes the set of images, converting each pair in an nx4 matrix, where n represents the number of cells (of size 64x64 pixels) whilst the columns store information of the x and y positions and velocities, respectively. 500 paired images were captured and used to determine the time-average flow field, allowing a comparison with the CFD simulation result.

Figure 7.8 shows the results of the PIV normalised velocity magnitude in the xy plane compared with the results for a single-phase CFD simulation using only the xy velocity components, both using a 4-PBT rotating at 400-rpm. The velocity magnitude is normalised by the impeller's tip linear velocity. The CFD model is able to reproduce the shape of the velocity distribution along a vertical line positioned at r/R=0.6 and at a 1° angle azimuthally behind the baffle. This position was used to place the vertical plane highlighted by the PIV laser beam.

In the upper region above the impeller, the CFD result under-predicts the normalised velocity magnitude from the open surface until the first measured point below the impeller. Nevertheless, the rapid velocity changes just before the impeller horizontal region are accurately reproduced. The greatest velocity gradients occur in the impeller region, where the highest velocity magnitude can be noted (marked as peak-B in figure 7.8). The PIV and CFD results show the high flow discharge produced below the impeller. In this region (peak-B), the normalised velocity magnitudes for the PIV and CFD results are very close (~0.16 and ~0.17 m/s, respectively). A more drastic drop after the peak-B can be noted in the measured velocity from the PIV. The CFD model also over-predicts the velocity in the region close to the tank's bottom, despite having a consistent shape to the velocity profile when compared to the PIV results.

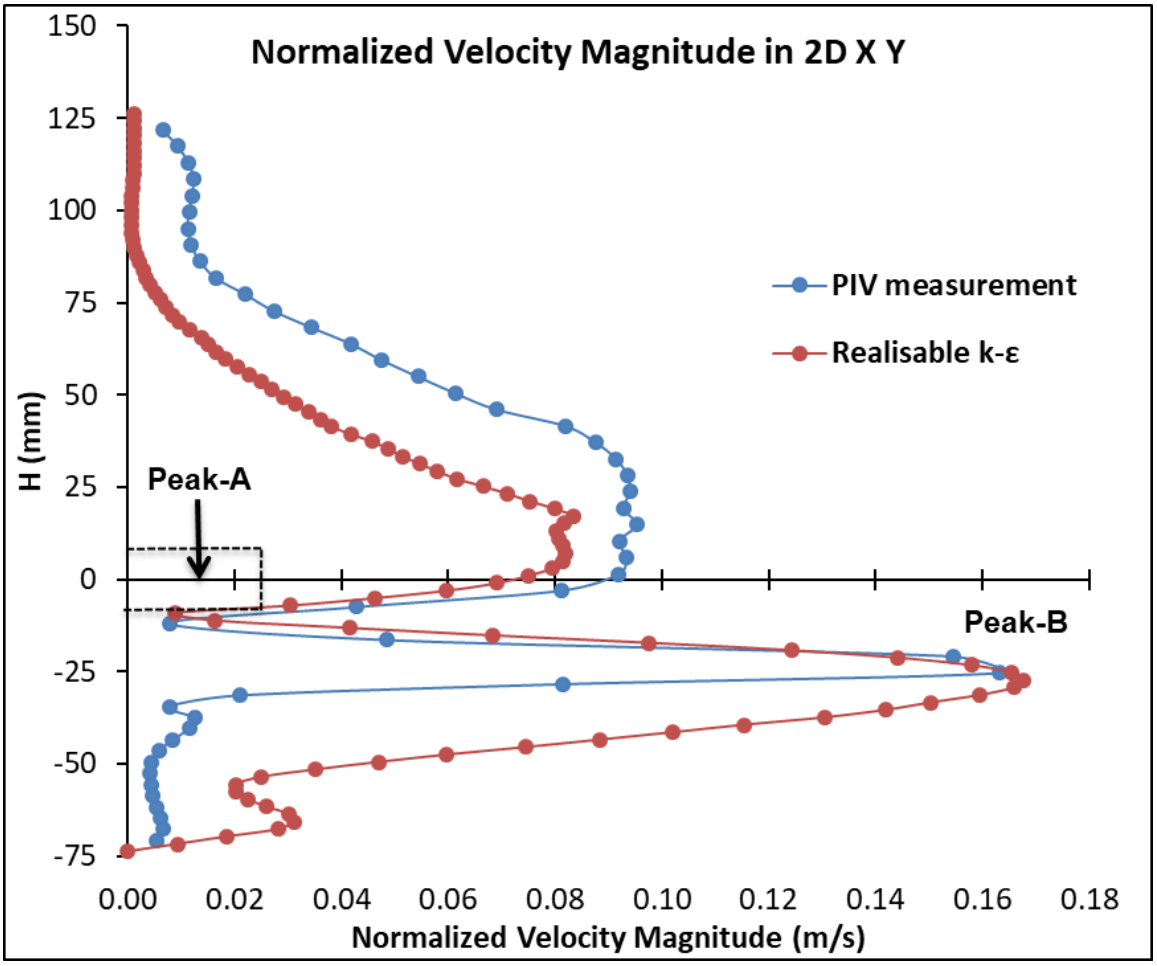

Figure 7.8: Normalised velocity magnitude by the impeller tip's linear velocity along a line at r/R= 0.6 and 1.0° anti-clockwise (approximately behind the baffle, positioned as the PIV laser bean). The impeller position is represented by the dashed lines.

Guida et al. (2010) showed that the PIV analysis of 17 azimuthally positioned vertical planes along ¼ of a complete, baffled tank (that was mixing water with a 6-pitched-blade-turbine) exhibited considerable variations in the velocity distribution and the turbulent kinetic energy distribution within planes. The fact that this work deals with a shear-thinning fluid instead of water, it is even more challenging and novel the attempt to reproduce the exact solution of the velocity field, using both experimental techniques and CFD models. Nevertheless, the CFD model was considered capable of reproducing the complex real-life phenomena of the mixing system within acceptable levels of errors. The results for the multi-phase liquid-solid CFD using the realisable k-ε turbulence model are presented in the next section.

7.2. CFD Results

This section presents the results of the CFD simulations for five different scenarios, i.e., single-phase fluid and mixtures with four different particle loadings (5, 10, 15 and 20% v/v). All scenarios consist of 4 different impeller speeds: 100, 200, 400 and 600-rpm, which

are the same as those used in the laboratory investigations presented in chapter 6. Section 7.2.1 compares the velocity magnitude and flow patterns of each system. Section 7.2.2 shows the results of the solid particle distribution and particle cloud high and compares them to the experimental visualisations. An energy analysis of the mixing power consumption between laboratory data and the CFD simulations is given in section 7.2.3. Finally, a summary of the work is provided in the last section.

7.2.1. Velocity fields

7.2.1.1. Axial, radial and tangential velocity profiles for multi-phase simulations

Figure 7.9, 7.10 and 7.11 show the axial, radial and tangential velocity components of the liquid phase (CMC4) along a vertical line positioned at r/R=0.6 between the baffle and impeller. Note that the red dashed line represents the impeller position in the normalised vertical axis. The axial distance is normalised by the liquid's height (i.e., 200 mm). All velocities are normalised by the linear velocity at the impeller's tip (Utip). The convention adopted throughout the text assumes a positive sign for the 'upwards' axial direction, 'outwards' from the vertical centre line of the shaft for the radial direction, and 'anticlockwise' (same as the impeller rotational direction) for the tangential direction of the velocity vector.

Figure 7.9 shows that the fluid flow follows similar patterns along the vertical line at r/R=0.6. It starts with very low axial velocities (close to zero) on the top surface for all impeller speeds and particle loadings studied. The axial fluid velocity starts to increase at around 0.8 of the normalised height, reaching a maximum magnitude (moving upwards - i.e., a positive sign) just above the impeller region (~0.4), shown as peak-A. Beneath the impeller region and towards the bottom of the vessel, the axial velocities in all cases start to decrease. For the two lowest impeller speeds (100 and 200-rpm), the velocities reduce from the maximum of 0.06Utip (20% v/v) to zero in the bottom of the tank. For the two highest speeds (400 and 600-rpm), the effect is reversed with increasing velocity towards the bottom, forming a second peak, peak-B, of maximum velocity -0.018Utip (20% v/v). These patterns will be further discussed later in the chapter. For now, it is interesting to note that the highest normalised axial velocities (peak-A) are produced by the lowest impeller speed for each particle loading. Peak-A increases as particle loading increases, with a maximum of (~0.06Utip) for 100-rpm at 20% v/v particle loading. This is not surprising as, with the increase of particle loading, the momentum transferred by the impeller to the liquid phase at 100-rpm is not enough to suspend the particles and/or keep them in suspension. Therefore, the energy is dissipated mostly in the liquid phase, which decreases in volume as particle loading increases. The distance between the impeller and the bottom of the moving fluid zone (i.e., the clearance ~64 mm, see figure 7.24) decreases as particles build

up forming a new quasi-static 'bottom' wall. As impeller speeds increase, the liquid phase gains more energy and is able to transfer enough momentum to the solid particles, so they are partially kept in suspension. As can be noted in figure 7.9, an increase in the impeller speed leads to a decrease in peak-A whilst peak-B increases. The flow patterns start to spread away from the impeller region and the velocities on the top and bottom regions increase.

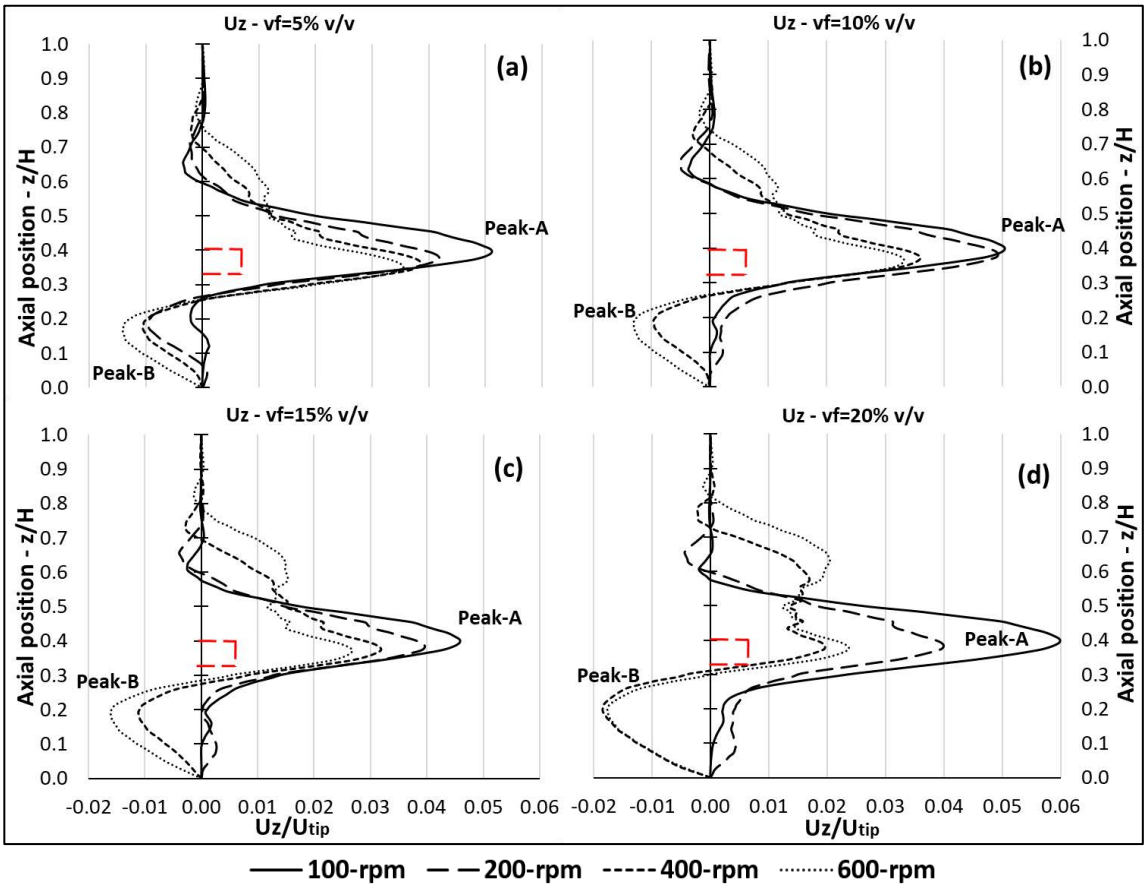

Figure 7.9: Liquid phase (CMC4) normalised axial velocity along a line at r/R=0.6 between the impeller and the baffle for the four impeller speeds investigated and four particle loadings: 5, 10, 15 and 20% v/v. The red rectangle shows the position of the impeller.

Figure 7.10 shows that the radial velocity follows the opposite behaviour: as impeller speeds increase, radial velocity increases. Two maximum velocities can be noted on opposite directions, shown as peak-A in the region above the impeller and peak-B in the region below the impeller. Here, the liquid-phase velocities for impeller speeds at 100-rpm are again concentrated in the region close to the mixing device whilst almost-zero velocities can be noted in the top and bottom surfaces. Also note that the velocity magnitude (peaks-A and -B) decreases with increasing particle loading for the 100-rpm speed, but with no significant changes noted at the other impeller speeds (for any particle loading). However, as impeller speed increases, velocity profiles spread away from the impeller region towards the upper and lower limits of the domain. It is interesting to note that the upper region has

a negative sign, meaning that the fluid is radially moving away from the tank wall towards the centre of the volume and, after passing through the impeller region, it moves towards the lateral walls. This behaviour is characteristic of pitched-blade turbines (PBT) down-pumping and is further discussed later in this chapter.

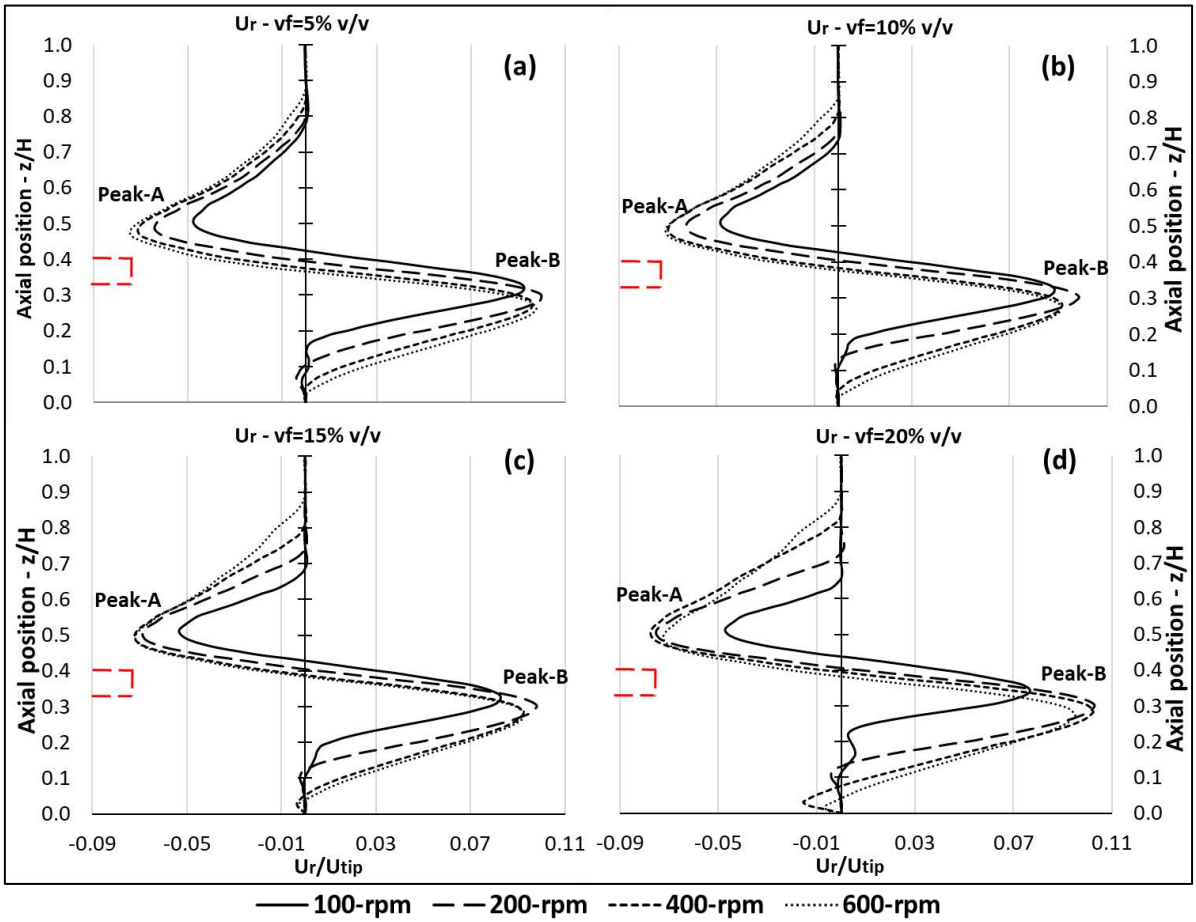

Figure 7.10: Liquid phase (CMC4) normalised radial velocity along a line at r/R=0.6 between the impeller and the baffle for the for impeller speeds investigated and four particle loadings: 5, 10, 15 and 20% v/v. The red rectangle shows the position of the impeller.

Figure 7.11 shows the normalised tangential velocity. It is clear that the rotation of the flow along the vertical line, r/R=0.6, is in the same direction of the impeller. Very similar patterns can be noted 1) high U_t close to the impeller region and smaller U_t away from this region for low impeller speeds and 2) smaller U_t close to the impeller and higher velocities on the top and bottom surfaces for high impeller speeds. As particle loading increases, the peaks are slightly shifted up due to the presence of solid particles, mainly in the lower part of the vessel.

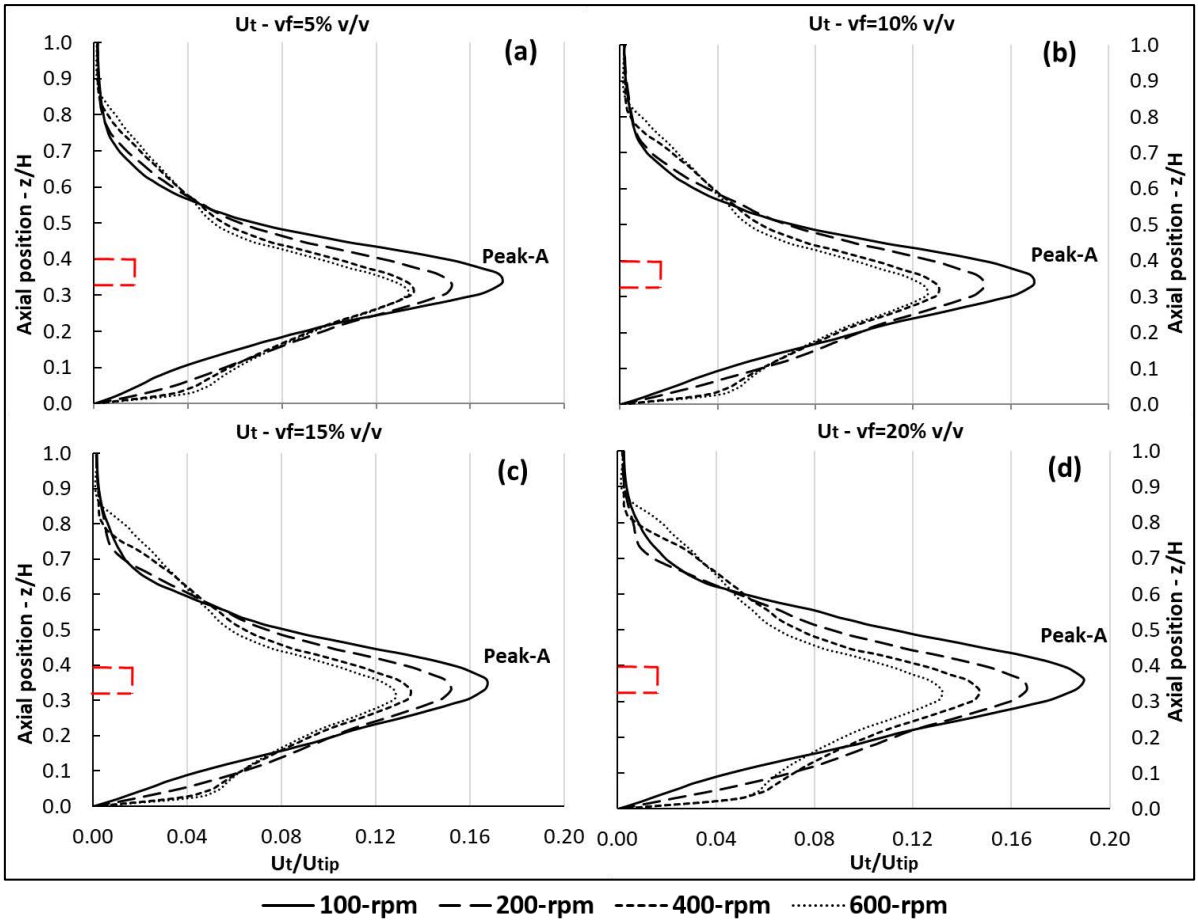

Figure 7.11: Liquid phase (CMC4) normalised tangential velocity along a line at r/R=0.6 between the impeller and the baffle for the for impeller speeds investigated and four particle loadings: 5, 10, 15 and 20% v/v. The red rectangle shows the position of the impeller.

7.2.1.2. Velocity field - contour and vector plots

The next four figures, 7.12, 7.13, 7.14 and 7.15, show contour and vector plots of the normalised velocity magnitude on a vertical plane through the centre of the impeller and the lateral walls of the tank aligned with the baffle. Each figure refers to an impeller speed and contains images (a), (b), (c) and (d), representing the four studied particle loadings of 5, 10, 15 and 20% v/v, respectively. Note that the vector plots represent the local velocity magnitude and their size does correspond to its intensity or magnitude. The vectors are plotted tangential to the vertical plane to represent the direction of the flow using the three velocity components. More details of the 3D velocity field between two consecutive baffles along the height of the tank are given later in this section. The white area on the right-hand side of each image in figure 7.12 (a) represents the location of the baffle. An illustrative scale representing the liquid height (in cm) is located on the right-hand side of each image.

In the vicinity of the impeller, indicated as region-C (i.e. the region above, below and in-between the impeller and the baffle - the so-called main recirculation zone,) normalised velocities as high as 1.0 can be observed, decreasing to ~0.10 with distance away from the

impeller. The vector plot shows the trajectory of the fluid entering from above the impeller and axially/radially discharged below. The fluid then moves towards the lateral wall and rises towards the surface before being dragged in again by the recirculation flow. Above region C, there are two other regions labelled B and A. These have very low velocities and as the particle load increases, the recirculation pattern seen in figure 7.12 (a) and (b) starts to become more chaotic (figure 7.12 (c) and (d)). This is likely to be a consequence of the accumulation of solids in the bottom of the tank, which changes the flow patterns in the main recirculation zone. The dimension of the recirculation zone extends from nearly 30 to 170 mm above the tanks' bottom in the 5% v/v particle loading case, whilst it shrinks from nearly 40 to 130 mm in the 20% v/v particle loading example. As discussed in the previous section, the axial, radial and tangential velocity components increase in the impeller region but decrease in the regions far from the impeller, as can be seen here. Region D is at the bottom of the tank, below the main recirculation zone. For low impeller speeds, the velocity vectors in this region show no clear pattern. This is because the transfer of momentum from the fluid to the solid phase is insufficient to suspend the particles in the bulk flow. As particle loading increases, the accumulation of solids in the bottom grows, which forces the low-velocity fluid to change direction. The behaviour of solid suspension phases is going to be discussed in more details in section 7.2.2 later in this chapter.

Figure 7.13 shows the contour and vector plots for all particle loadings at 200-rpm, with 7.13 (a) indicting a clear fluid flow pattern in region D. Figures 7.13 (b), (c) and (d) still show a more chaotic flow in this region as at 200-rpm the momentum transferred from the impeller to the fluid is still insufficient to provide enough energy for the fluid to carry most of the particles in suspension. At 5 % v/v particle load, some of the smallest particles are carried by the liquid phase whilst the biggest particles remain at rest in the bottom of the tank. As the particle load increases, increasing accumulations of big particles build up in the bottom of the tank, therefore, altering the liquid flow pattern. Regions A and B are affected by the additional accumulation of the settled particles as can be seen in figure 7.13 (c) and (d).

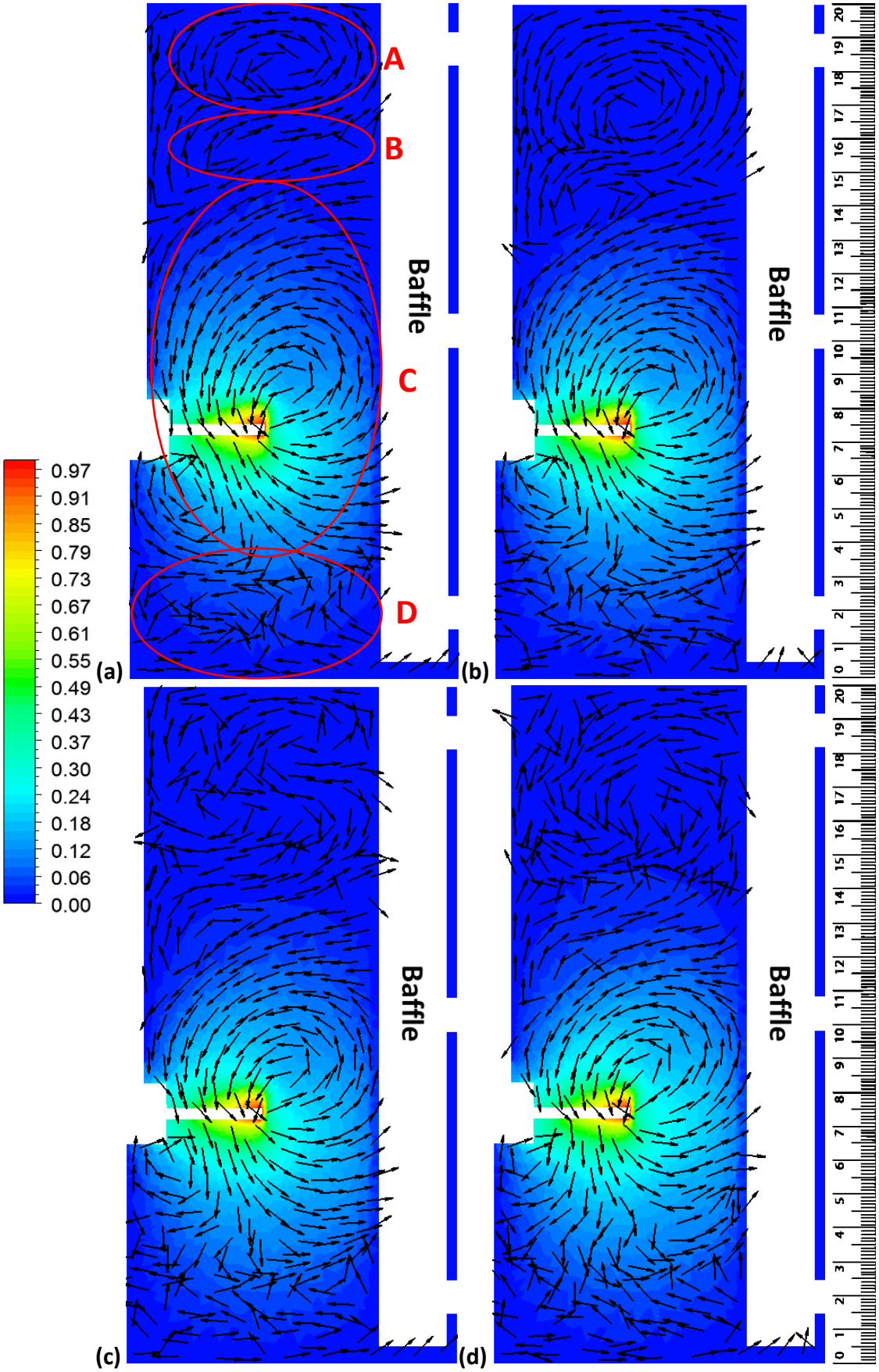

Figure 7.12: Normalised velocity magnitude contour plot and velocity magnitude vectorial plot for the liquid phase at **N=100-rpm** for different particle loadings: (a) 5, (b) 10, (c) 15 and (d) 20% v/v.

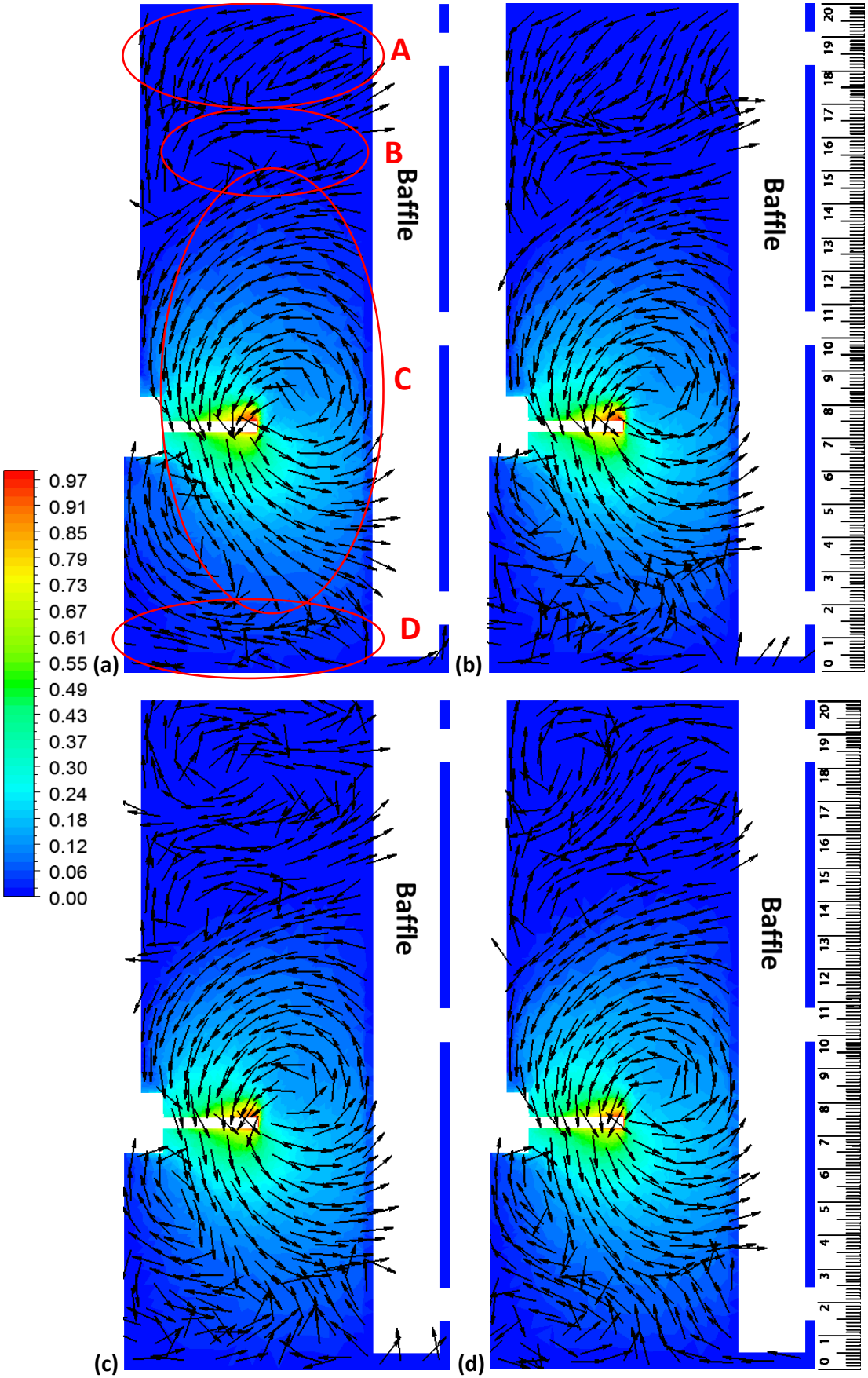

Figure 7.13: Normalised velocity magnitude contour plot and velocity magnitude vectorial plot for the liquid phase at **N=200-rpm** for different particle loadings: (a) 5, (b) 10, (c) 15 and (d) 20% v/v.

Figure 7.14 shows the normalised velocity magnitude for all particle loadings at 400-rpm where the vector flow patterns in the four regions are more well-defined for all cases. The discharge of the impeller is now reaching the bottom of the vessel, where the axial velocity increases in the negative direction. The higher velocities near the bottom induce the recirculation shown in region-D where the fluid returns to the impeller region via the central zone of the vessel. The size of region-D increases as particle load increases, which means that the impeller discharge is being pushed away from the bottom of the tank by the presence of more solid particles (see figure 7.14 (a), (b), (c) and (d)). For impeller speed at 600-rpm, the recirculation zones become more evident and the velocity magnitude distribution becomes ordered. This is because at 600-rpm the fluid contains enough energy to carry most of the particles leaving less quasi-zero flow velocity regions in the lower part of the vessel and is energy dissipated throughout the tank.

Figures 7.16, 7.17, 7.18 and 7.19 show the contour plot of the normalised velocity magnitude with 70% transparency so that the 3D vector plots of the velocity magnitude can be seen. Note that the vectors express purely the direction of the flow, not its magnitude. These plots are located in six vertical planes across the height of the vessel (named P1-P6), starting at 0.7 mm above the bottom of the tank and then equally spaced with 36.5 mm intervals in height. Note that the two previous velocity visualisations (figures 7.9-10 and 7.11-15) were plotted along a line and in a plane, both in the region between the tank's central vertical axis and the lateral wall that is aligned with the baffle. The subsequent figures show the region between two consecutive baffles where its limits are represented by the previous plots.

From figure 7.16, the positive tangential velocity (anticlockwise and with the same direction as the impeller rotation) is predominant for all velocity components, as previously shown in figure 7.11. Planes P1, P2, P5 and P6 represent the lower and upper regions of the tank away from the impeller and experience predominantly tangential velocities. From figure 7.16 (a) to (d), it can be noted that the axial and radial velocity components decrease as more solid particles are added to the system and accumulate in the bottom part of the tank at low impeller speeds, i.e. 100 and 200-rpm. In the middle planes, P3 and P4, a decrease in the radial and axial velocity components can be noted. For 20% v/v particle loading, the velocity vectors in P3, become mainly tangential (as apposed to axial) and a recirculation loop can be observed in 7.16 (d). Similar fluid dynamic behaviour can be observed at 200-rpm but with a notable difference being the gain of axial velocity in P2, close to the lateral walls between baffles.

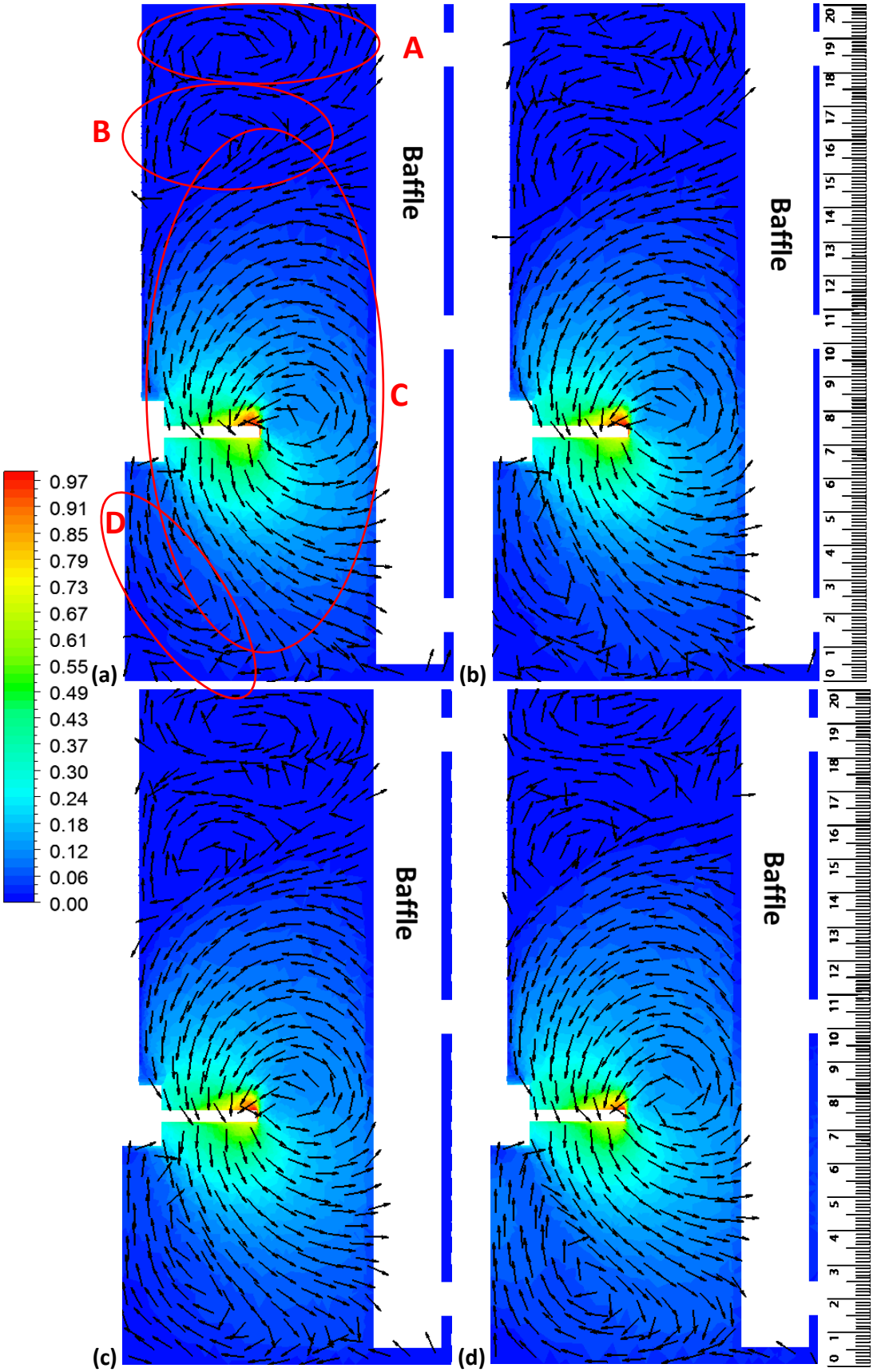

Figure 7.14: Normalised velocity magnitude contour plot and velocity magnitude vectorial plot for the liquid phase at **N=400-rpm** for different particle loadings: (a) 5, (b) 10, (c) 15 and (d) 20% v/v.

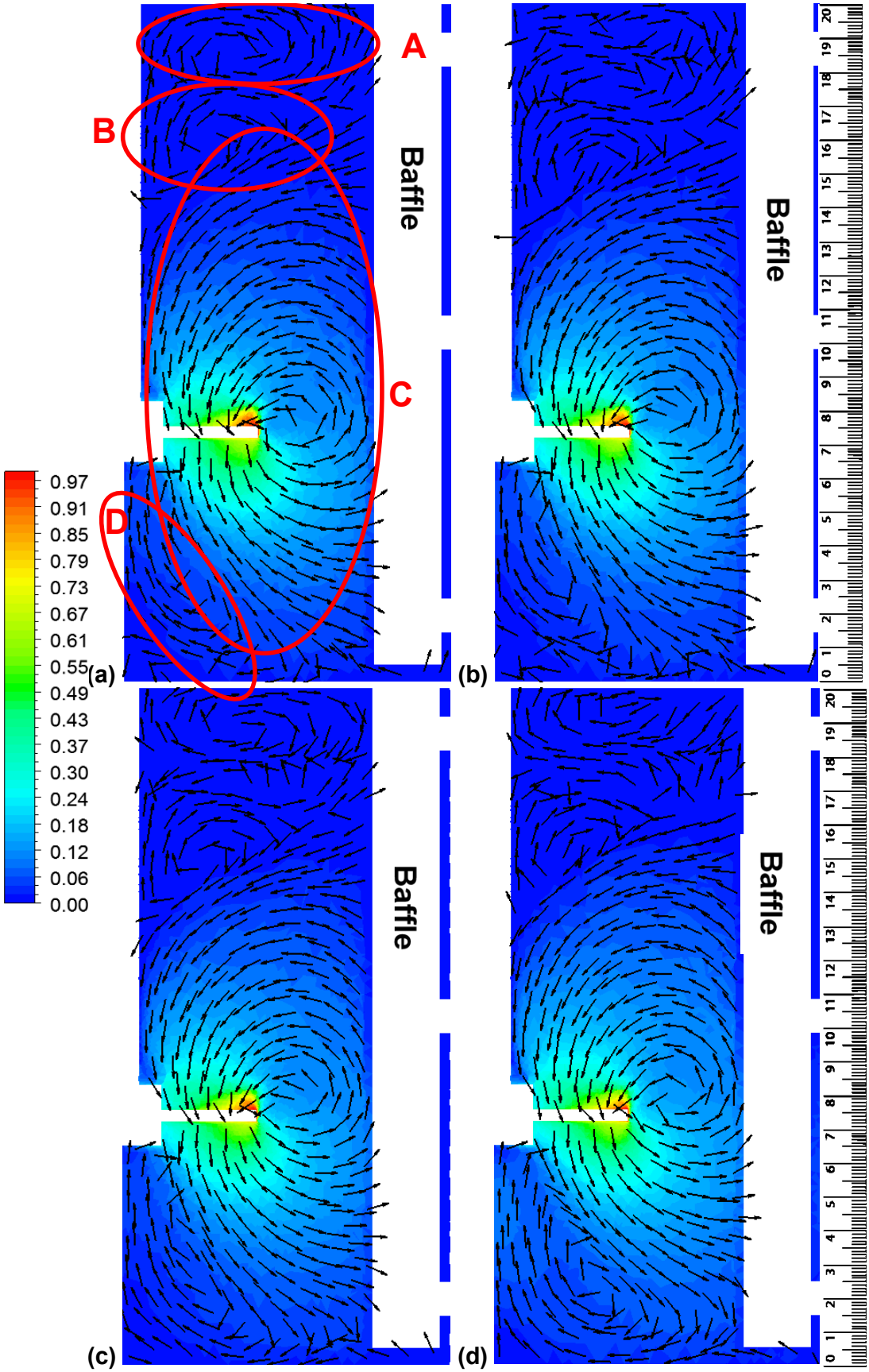

Figure 7.15: Normalised velocity magnitude contour plot and velocity magnitude vectorial plot for the liquid phase at **N=600-rpm** for different particle loadings: (a) 5, (b) 10, (c) 15 and (d) 20% v/v.

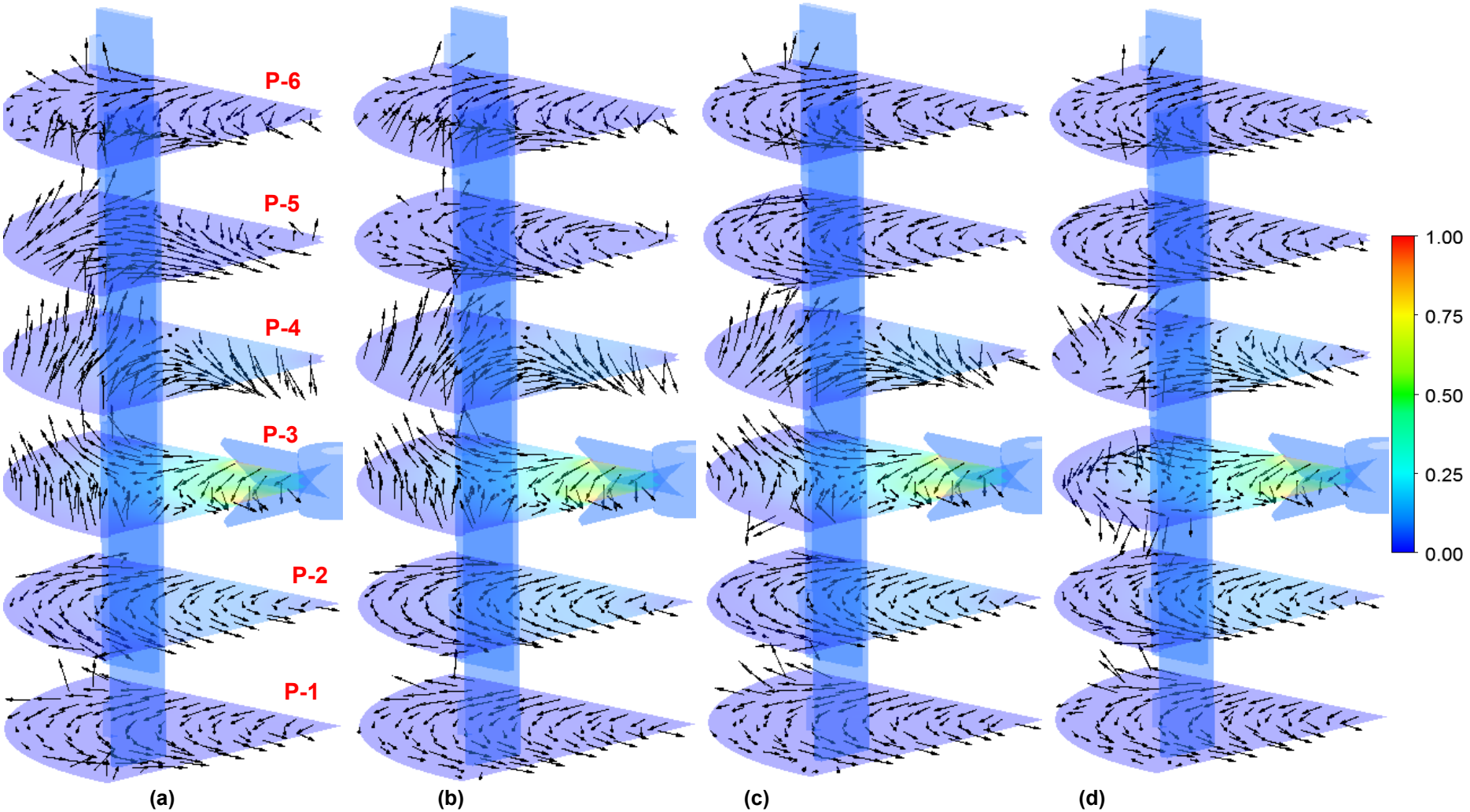

Figure 7.16: Normalised velocity magnitude contour and 3D vectorial plots in ¼, horizontal plane segments that are vertically distributed in the vessel. The image is for the liquid phase at **N=100-rpm** for 4 different particle loadings: (a) 5, (b) 10, (c) 15 and (d) 20% v/v. The first plane is positioned at 0.7 mm above the bottom of the tank whilst the other planes are equally spaced with 36.5 mm intervals. The third plane (P3) is positioned exactly in the mid-region of the impeller.

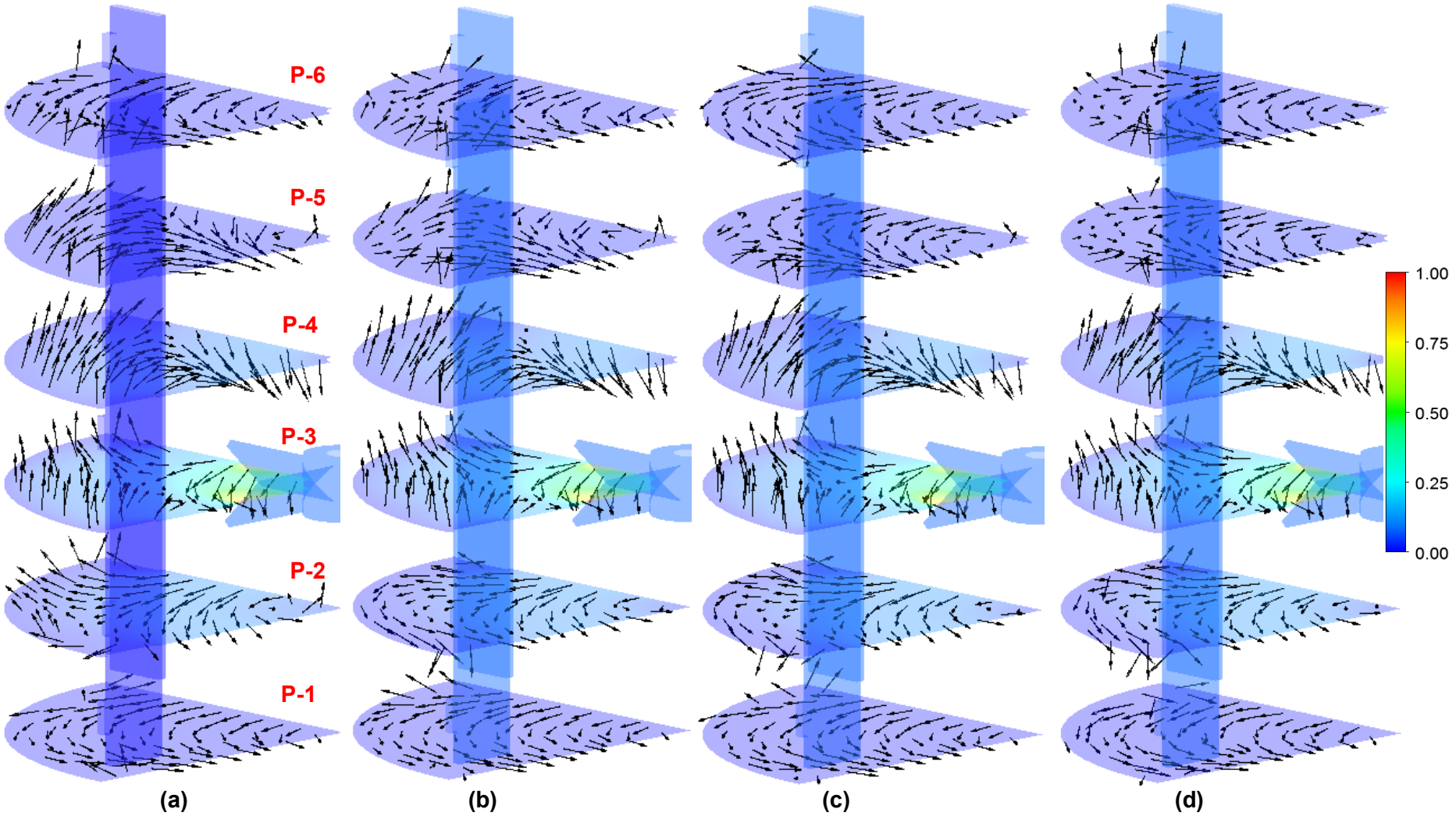

Figure 7.17: Normalised velocity magnitude contour and 3D vectorial plots in ¼, horizontal plane segments that are vertically distributed in the vessel. The image is for the liquid phase at **N=200-rpm** for 4 different particle loadings: (a) 5, (b) 10, (c) 15 and (d) 20% v/v. The first plane is positioned at 0.7 mm above the bottom of the tank whilst the other planes are equally spaced with 36.5 mm intervals. The third plane (P3) is positioned exactly in the mid-region of the impeller.

Figure 7.18 (400-rpm impeller speed model) shows no significant change in velocity pattern for planes P1 and P6 at any particle loading. However, the axial velocity close to the walls in P2 is maintained for all particle loadings (i.e., in contrast to the 200-rpm model where this is only the case for the 5% v/v particle loading case). The axial velocity profile induced by the higher impeller speed in plane P5 is less affected by increases of the particle loading, This is again, in contrast to the effect seen in the low-speed models of figure 7.16.

At 600-rpm (Figure 7.19) an increase in the radial and axial velocities close do the walls can be noted in plane P1 as a result of the strong discharge created by the impeller at high mixing speed. Flow patterns in P1 are similar for all particle loadings, indicating that the increase of solids in the system does not affect flows in the bottom of the tank as much as for the other mixing speeds. As discussed later, the impeller speed of 600-rpm is capable of providing enough inertia so that the particles are kept in homogenous suspension throughout most of the vessel. For P2, P3 and P4, the flow patterns are very similar to the ones experienced by the 400-rpm impeller speed. In P5, the upward trajectory of the flow close to the lateral wall creates a tangential recirculation zone behind the baffle, with small negative axial velocities. This means that the fluid in this region is flowing back to the impeller region. This same flow pattern has been seen in the experimental work with CMC4 and indicates that the cloud height might be around this point in the vessel. The bulk flow pattern of the fluid is very similar in all tanks and can be described in three parts: (i) downflow at the impeller discharge region, (ii) upwards flow between the baffles and near lateral walls and (iii) fluid return from the lateral walls towards the vessel axes and down back to the impeller region. This flow field is characteristic of down-pumping PBT impellers with clearance distances of less or equal to 1/3 of the liquid hight (H) (Paul et al., 2004).

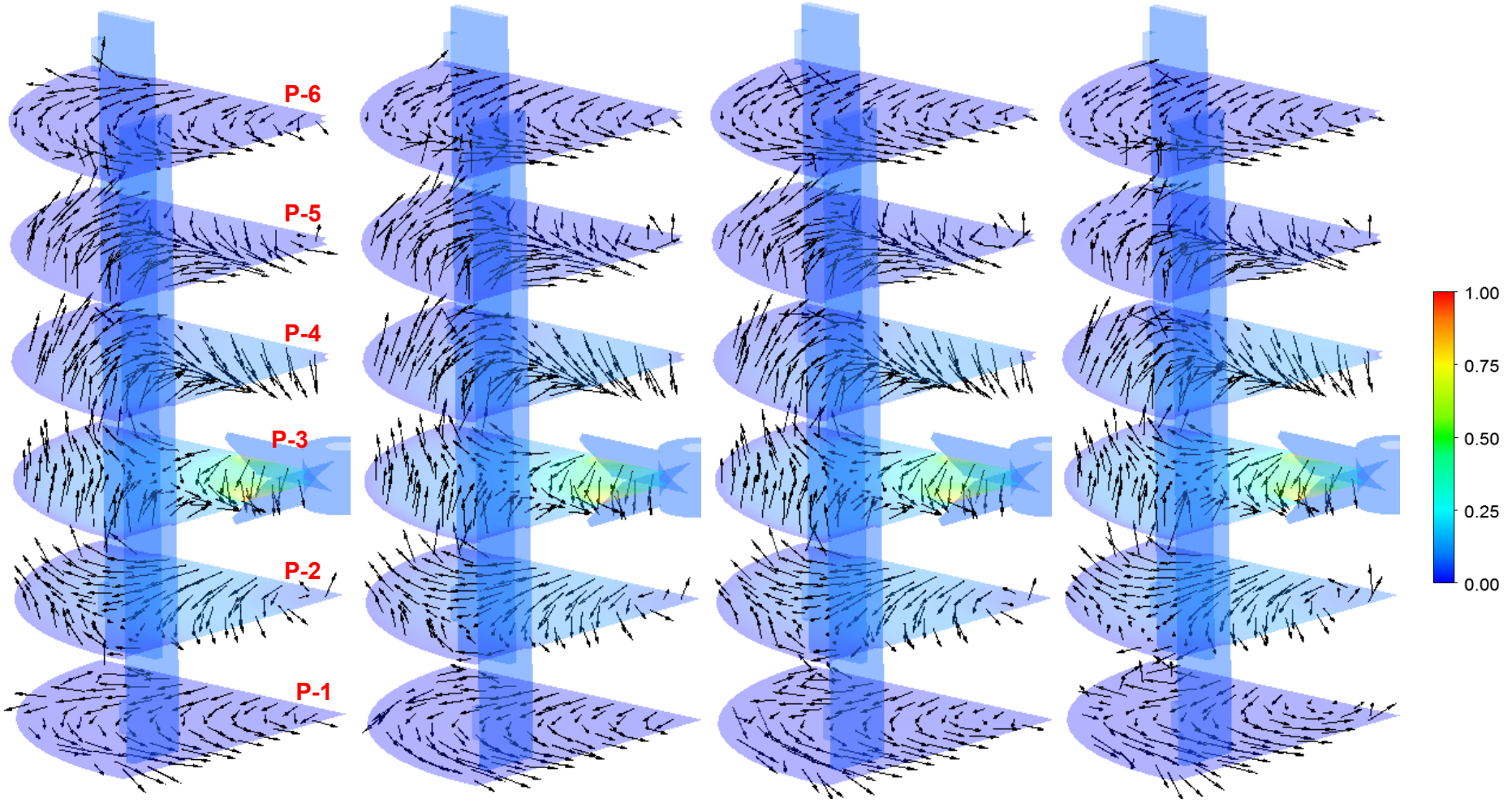

Figure 7.18: Normalised velocity magnitude contour and 3D vectorial plots in ¼, horizontal plane segments that are vertically distributed in the vessel. The image is for the liquid phase at **N=400-rpm** for 4 different particle loadings: (a) 5, (b) 10, (c) 15 and (d) 20% v/v. The first plane is positioned at 0.7 mm above the bottom of the tank whilst the other planes are equally spaced with 36.5 mm intervals. The third plane (P3) is positioned exactly in the mid-region of the impeller.

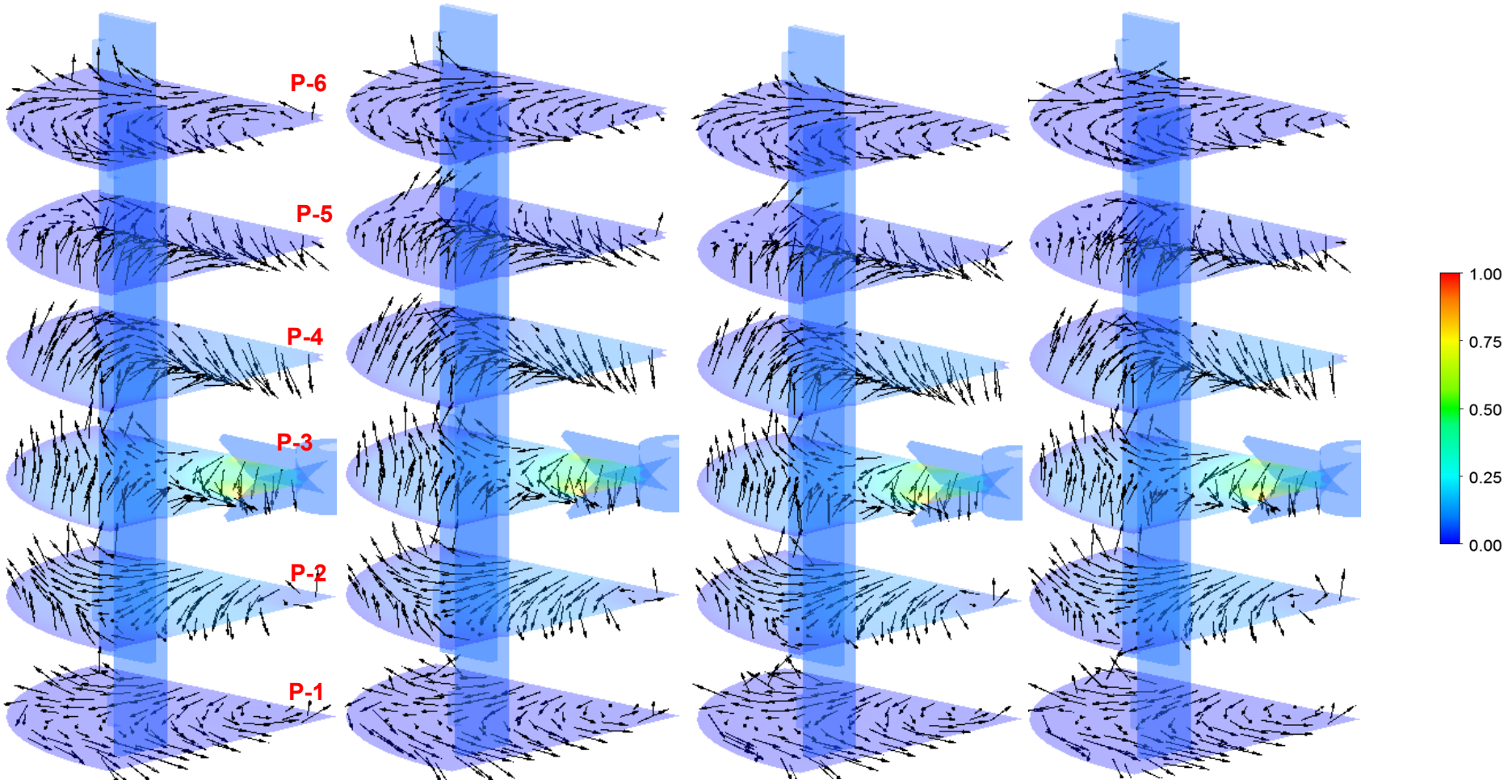

Figure 7.19: Normalised velocity magnitude contour and 3D vectorial plots in ¼, horizontal plane segments that are vertically distributed in the vessel. The image is for the liquid phase at **N=600-rpm** for 4 different particle loadings: (a) 5, (b) 10, (c) 15 and (d) 20% v/v. The first plane is positioned at 0.7 mm above the bottom of the tank whilst the other planes are equally spaced with 36.5 mm intervals. The third plane (P3) is positioned exactly in the mid-region of the impeller.

7.2.1.3. Dynamic viscosity – rheological analysis

This section presents the modelling results of the local dynamic viscosity change for different regions of a vertical plane positioned between the impeller and the baffle. For non-Newtonian shear-thinning fluids, the higher the shear rate, the lower the viscosity and therefore, less resistance to flow. As previously discussed in sections 3.2.2 and 7.1.5, the limits at which the viscosity depends on the shear rate must be defined for modelling purposes. The decision on the limits must be as accurate and realistic as possible as a wrong choice and/or measurement has a significant impact on the velocity profiles and energy dissipation, especially in regions where the shear rate is very small - thus high viscosity (Cortada-Garcia et al., 2018). A preliminary sensitivity study on the impact of shear rate limit choice on the flow field (and solid particle suspension behaviour) has been undertaken and the results show that a significant part of the non-Newtonian behaviour could be missed if the limits are poorly set and, as such, the chosen segment of the power-law model could actually represent almost linear behaviour between shear rate and viscosity. This means that instead of modelling a non-Newtonian fluid, an “almost-Newtonian” fluid with higher viscosity is represented. Further analysis is to be carried out in order to fully understand the impact of this issue on the solid suspension.

Figures 7.20, 7.21, 7.22 and 7.23 show the dynamic viscosity contour plots for all particle loadings ((a) to (d)) and impeller speeds. From all figures, it is not a surprise that in the vicinity of the impeller the highest shear rates (thus the lowest viscosities) are produced.

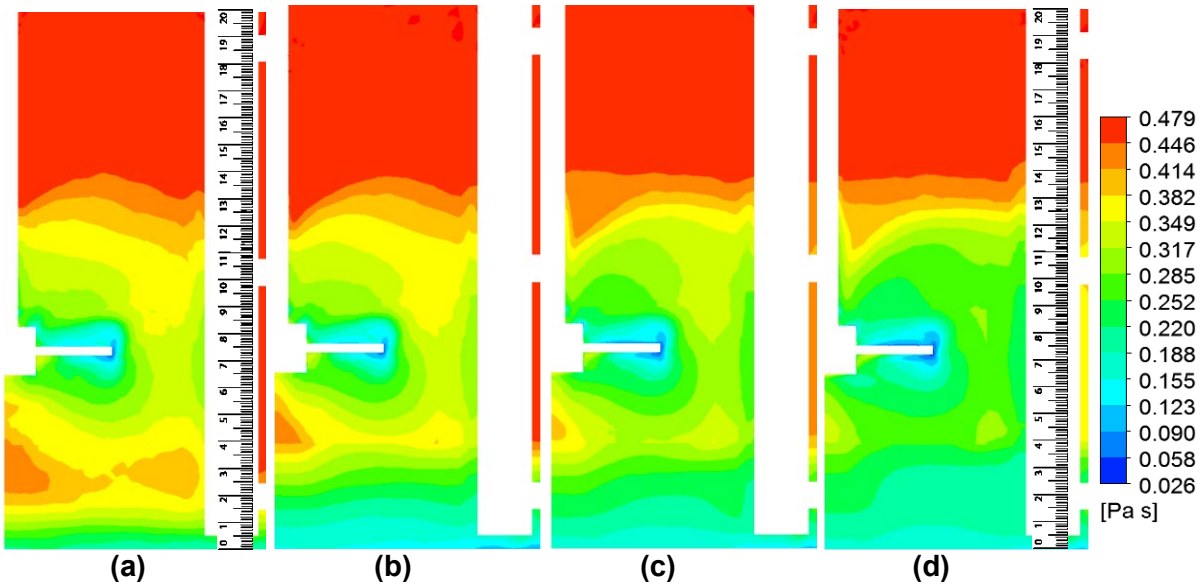

Figure 7.20: Dynamic viscosity contour plot for the liquid phase at **N=100-rpm** for different particle loadings: (a) 5, (b) 10, (c) 15 and (d) 20% v/v.

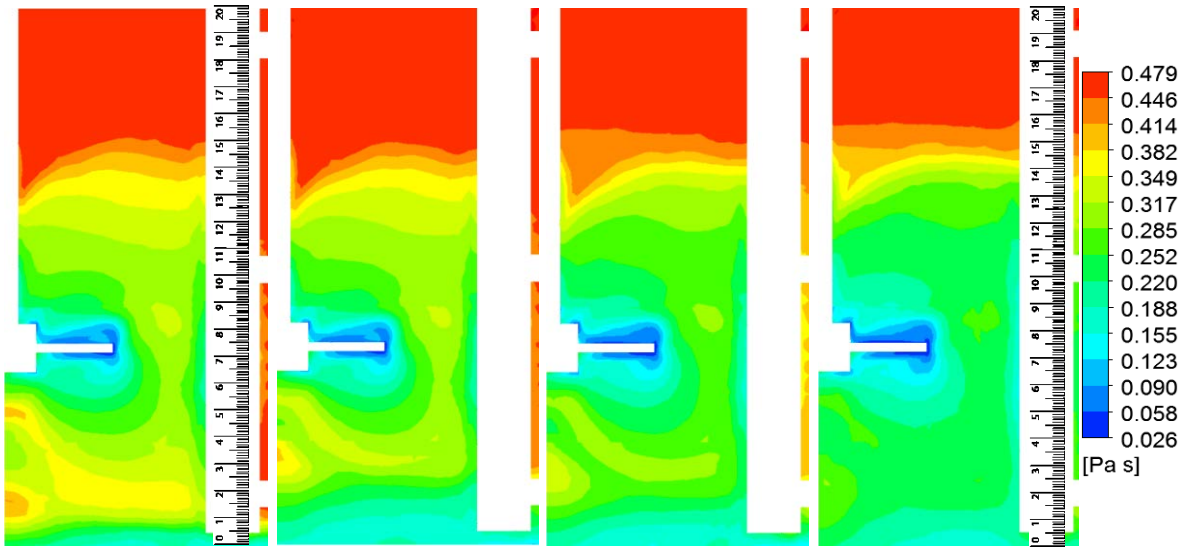

Figure 7. 21: Dynamic viscosity contour plot for the liquid phase at **N=200-rpm** for different particle loadings: (a) 5, (b) 10, (c) 15 and (d) 20% v/v.

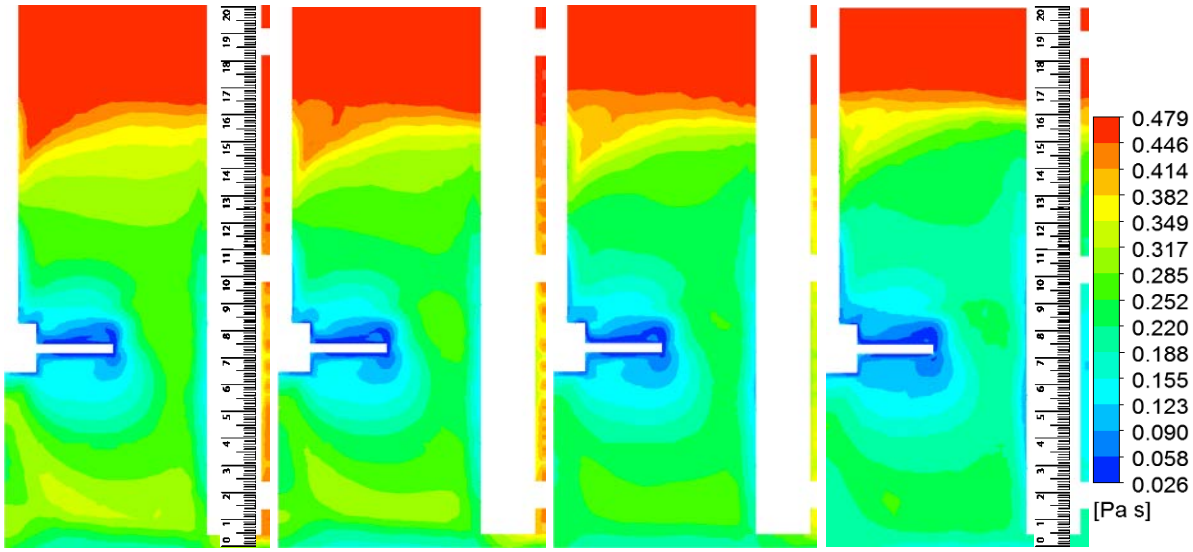

Figure 7.22: Dynamic viscosity contour plot for the liquid phase at **N=400-rpm** for different particle loadings: (a) 5, (b) 10, (c) 15 and (d) 20% v/v.

At 100-rpm, the viscosity increases homogeneously around the impeller and towards the baffle. As seen in the previous section, the regions away from the impeller have low velocity magnitudes as the fluid become more resistant to the flow. The shear rate in these regions is below 0.7 s^{-1} and the viscosity reaches the upper plateau limit at about 135 mm above the bottom of the tank (see section 3.2.2). The increase in particle loading leads to lower and more homogeneous viscosities around the impeller region but no significant change in the low shear-rate region can be noted. Interestingly, the viscosity at the bottom of the tank remains relatively constant at a value of ~0.160 Pa.s, indicating that the shear rate in this region is approximately 10 s^{-1} despite the high volumetric solid fraction (see next section for details). This is due to the small, but constant motion of the solid particles.

Similarly to the 100-rpm model, the viscosity in the high-speed impeller models reaches a minimum value around the impeller for all cases, indicating that the shear rate in this region is equal or greater than the upper plateau limit of 1500 s^{-1}. As impeller speeds increase (figures 7.21, 7.22 and 7.23), the region with low viscosities also increases in size. As a consequence, the upper zone of the tank, which experiences low shear rates, decreases in size accordingly. The lower limit of the shear rate lies at a distance of approximately 160, 170 and 185 mm above the bottom of the tank, for 200, 400 and 600-rpm models, respectively. In all cases, the viscosity becomes more homogeneous around the impeller and between the baffles whilst little impact on its vertical change can be noted.

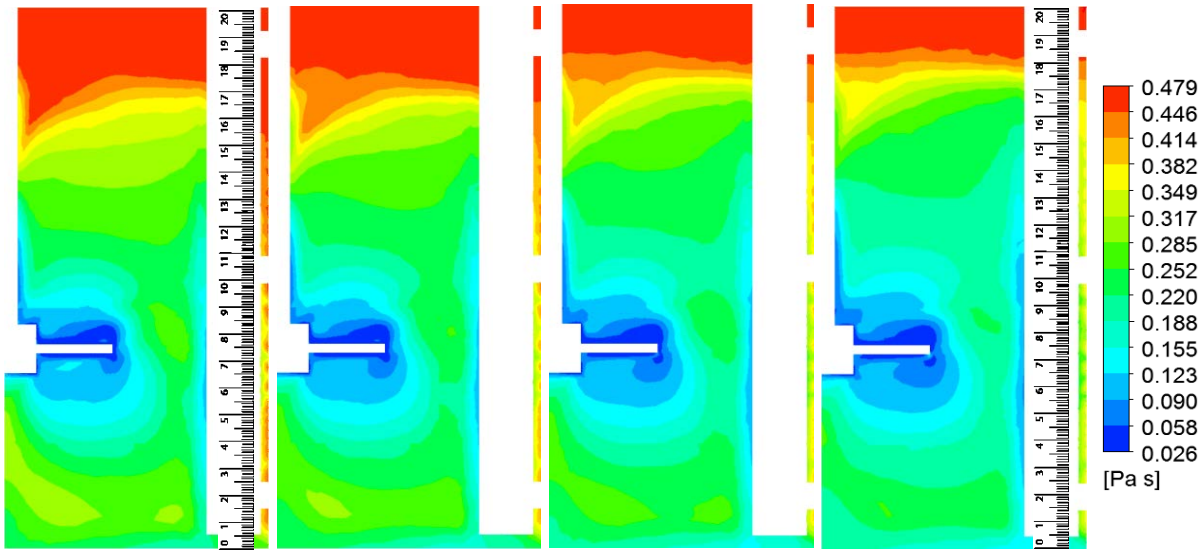

Figure 7.23: Dynamic viscosity contour plot for the liquid phase at **N=600-rpm** for different particle loadings: (a) 5, (b) 10, (c) 15 and (d) 20% v/v.

7.2.2. Particle suspension and cloud height

This section presents the results from the laboratory and CFD investigation of a sand particle suspension in the non-Newtonian shear-thinning CMC solution at 4 g/l for four different impeller speeds and four particle loadings (i.e., 100, 200, 400 and 600-rpm and volumetric fractions (v/v) of 5, 10, 15 and 20%). The ultimate objective of this investigation is to find a mixing regime capable of (re-)suspending and keeping inert dense solid particles in suspension, such that they could exit the AD tank used for the experimental work presented in chapter 6 without affecting digestion stability or biogas yields. Figure 6.5 shows a sample of the sediment found in the bottom of an industrial AD tank treating sewage sludge with the simplified particle size distribution (PSD) of these samples shown in table 6.3. This data was used to build the CFD model and with the laboratory investigations, sand particles with sizes following the simplified PSD profile were used at different volumetric concentrations to investigate the suspension of the particles under the 100, 200, 400 and

600-rpm impeller speeds. The volumetric fraction (v/v) was calculated using Archimedes' principle for 5, 10, 15 and 20% mixtures:

$$\rho_s = \frac{m}{V_s} \tag{7.22}$$

where $\rho_s, m \text{ and } V_s$ are the solid density, mass and volume. The mass for each solid phase was then calculated and the simplified PSD used to sort the particles' size before adding them to the CMC4 solution for stirring. The height occupied by the solid fraction in a quiescent CMC4 solution is shown in figure 7.24. It is important to note that although particles have different sizes, and therefore able to fill the void between two bigger particles, their densities are the same. Bigger particles tend to accumulate faster in the bottom of the AD tank, forming layers with distinct particle sizes as can be seen in figure 7.24. The dynamics of motion for non-spherical particles in turbulent non-Newtonian fluid flow is far from trivial. For modelling purposes, however, even for reasonably spherical shapes on a macroscopic level, there are many imperfections that can influence in the solid-liquid momentum exchanges (Ochieng and Lewis, 2006). In this work, errors might have arisen from the assumption of spherical shapes for the sand particles. Nevertheless, the results show a good agreement between the experimental and CFD works.

In the CFD model, all particles were assumed to be spherical using the granular model and a maximum packing limit factor of 0.6 was used. In poly-disperse multi-phase systems, however, the volume fraction in a single cell can be higher than the defined maximum because particles with different diameters can fit into the voids between multiple spheres. This is not always the case (as seen in figure 7.24) where bigger particles accumulate first and the smallest particles settle on top. Note that Ansys Fluent does attempt to calculate an appropriate maximum packing fraction based on the particle size and concentration in each cell (see section 17.5.12 ANSYS Inc. (2013) for the mathematical modelling) and, as shown later in this section, the local maximum volume fraction is as great as ~0.8. For particle settling in a tank of quiescent fluid, the free-falling Stokes law (eq. 7.23) for spherical particles holds true for non-Newtonian fluids of Reynolds number less than 0.1, where particle-particle interaction is neglected (Chhabra, 2007). The pressure and friction drag forces (F_D) are expressed in terms of the drag correction factor (Y) for a sphere falling in a power law medium and is given by:

$$F_D = 3\pi\mu dvY \tag{7.23}$$

$$Y = \frac{C_D Re_{PL}}{24} \tag{7.24}$$

$$Re_{PL} = \frac{\rho_l {v_s}^{(2-n)} d^n}{K} \tag{7.25}$$

where Re_{PL} is the particle Reynolds number, *d* is the particle diameter, v_s is the free-fall velocity of the sphere and μ is the fluid viscosity assuming the characteristic shear rate around a sphere to be equal to (v_s/d) (Chhabra, 2007). All other terms have been previously given. The free-fall velocity of a spherical particle in a stationary power-law fluid can be written as:

$$v_s = \left(\frac{g d^{n+1}(\rho_s - \rho_l)}{18KY}\right)^{\frac{1}{n}} \qquad 7.26$$

Equation 7.26 describes the settling behaviour of the solid phase and reduces to the familiar Stokes equation for n=1 (Newtonian fluids). In turbulent agitated tanks, the settling velocity will always be less than the free-settling velocity. The turbulent Newton's law will determine whether the particle will lift-off or remain stationary, swirl and/or roll in the bottom of the tank according to the drag force (mainly). This is then balanced by the gravitational and buoyant forces acting on the particles for the case of negligible particle-particle interaction forces (eq. 7.5 and 7.7) (Kresta, 2016, Chhabra, 2007). It again becomes clear that a realistic rheological characterisation for the non-Newtonian carrier phase is an important consideration, given that the main forces acting on liquid-solid momentum exchange are dependent on the fluid viscosity.

For a liquid-solid stirred AD tank, the level within the liquid at which most particles are kept in suspension determines the cloud height (CH), which is given by the distance to this level to the bottom of the tank (Paul et al., 2004). Above this level, few particles will enter the liquid zone whilst below it there is a solid-rich fluid mixture. The cloud height determination is important so that the inert dense particles can achieve a certain level in the AD tank and exit from top-mounted outlets. Bittorf and Kresta (2003) proposed a method to predict the cloud height based on the assumption that the dominant driving force for solid distribution is the upwardly moving flow along the lateral walls and baffles. They related the maximum local velocity of the flow at the wall to the impeller tip speed at the 'just-suspension' condition in order to determine the cloud height. This method is not suitable for this work as the impeller behaviour for just suspension speeds is not the subject of this research. Alternatively, Ochieng and Lewis (2006) used a CFD method to predict cloud height that has been extensively used in the literature (Liu and Barigou, 2013, Tamburini et al., 2012, Hosseini et al., 2010). This method is based on the axial profile of the normalised solids concentration. The points of inflection in the profile give the regions where particle concentration changes more readily, whilst a relatively constant vertical line means a homogenous solid concentration (see figure 7.25).

(a) (b) (c) (d)

Figure 7.24: Settled particles at the bottom of the tank for (a) 5, (b) 10, (c) 15, and (d) 20% v/v particle loadings. The red arrow indicates the height of the particles.

All simulated cases were initiated with particles resting at the bottom of the tank, as suggested by Tamburini et al. (2011). Figure 7.25 shows the results of the normalised volume fraction (or solid concentration) along a line positioned at r/R=0.6 between the baffle and the impeller. The local volume fraction (α_{ls}) is normalised by the average volume fraction in the tank (α_{s_ave}) (eq. 7.27). The inflection points (indicated by the red arrow) are shown in figures 7.31-34 as iso-surfaces for the total solid volume fraction.

$$\alpha_{Ns} = \frac{\alpha_{ls}}{\alpha_{s\_ave}} \qquad 7.27$$

where α_{Ns} is the normalised volume fraction. In figure 7.25 (a)-(d), the maximum normalised volume fraction (horizontal axis) is always given by the lower impeller speed for all solid loadings. This occurs because, at lower speeds, the impeller does not provide enough energy to either cause suspension or keep most of the particles in suspension, thus particles stay resting at the bottom. Therefore, α_{ls} is much greater than α_{s_ave} at the bottom of the tank, leading to larger values of α_{Ns} (eq. 7.27).

To determine the degree of solid accumulation or suspension in the tank, the method proposed by Ochieng and Lewis (2006) was used. Two inflection points were determined: lower and upper. The lower inflection point indicates the accumulation of particles where $\alpha_{ls} > \alpha_{s\_ave}$. This region contains quasi-static particles and is referred to as the solid "bed" where it is possible to determine the bed height (BH) through the α_{Ns} lower inflection point. The upper inflection point indicates the cloud height (CH) where above this point, $\alpha_{ls} < \alpha_{s\_ave}$, and the solid concentration decreases to zero, meaning that this portion of the tank has little or no solids in suspension. In fact, it is well-established that the cloud height almost never reaches the total liquid height, even for impeller speeds as high as three times more than the "just suspension" speed (Paul et al., 2004).

The bed height is always at a higher normalised axial position for lower mixing speeds, as illustrated in figure 7.25 (b). Here, the lower inflection point for 100-rpm is at ~0.20 units of the normalised axial position above the bottom of the tank whereas it is at

~0.07 for 400 and 600-rpm speeds. On the other hand, the upper inflection point (CH) for low mixing speeds generally occurs at around 0.6 units of the normalised axial position and increases to ~0.85 as impeller speed increases. This phenomenon becomes more apparent in figure 7.25 (c) and (d), where the $\alpha_{ls}/\alpha_{s\_ave}$ ratio is smaller. Not only does the cloud height increase with impeller speed, but the lower inflection point tends to disappear, meaning that the solid distribution is becoming more homogeneous throughout the entire vertical axis of the tank, or $\alpha_{ls} \cong \alpha_{s\_ave}$.

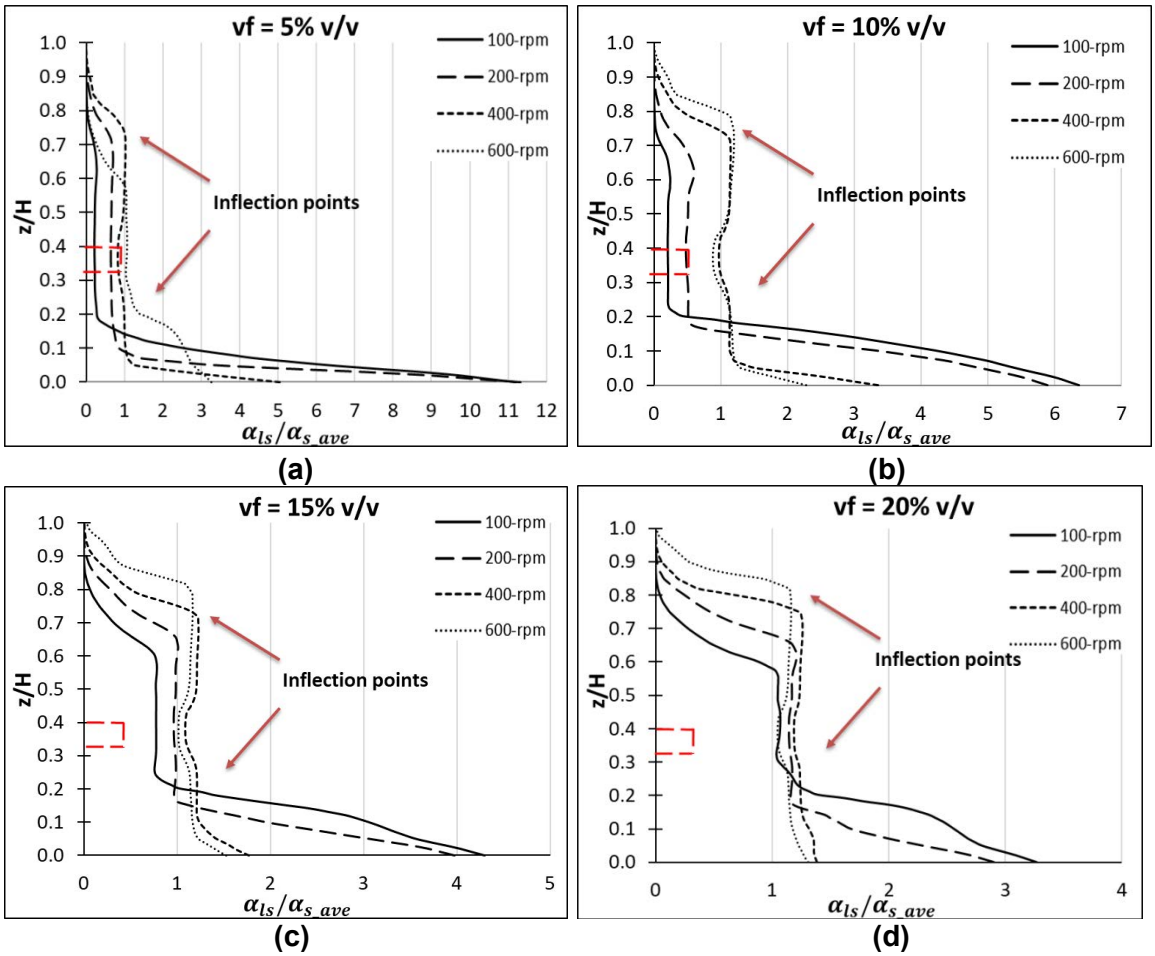

Figure 7.25: Local total solid particles concentration normalised by the volumetric average in the tank plotted along a line at r/R=0.6 between the impeller and the baffle for the four impeller speeds investigated and four particle loadings: 5, 10, 15 and 20% v/v. The red rectangle shows the position of the impeller.

It is worth noting that for any given particle loading, there is always a small portion of solids in suspension for the lowest impeller speeds. Figure 7.25 and figures 7.27-30 show the normalised solid concentration (α_{Ns}), which accounts for the sum contribution of all four particle phases (or sizes). As previously discussed, all particles were considered as spheres with the same density but different diameters. Due to hydrodynamic forces, bigger particles tend to stay in the bottom region when suspended, thus reach the bottom first and are less likely to be re-suspended once trapped at the bottom of the tank. To illustrate this, figure

7.26 presents the individual solid particle distribution along the same vertical line as in figure 7.25, for the smallest ($d_p = 0.15$ mm) and biggest particles ($d_p = 1.18$ mm) for all impeller speeds and two particle loadings, 5% ((a) and (b)) and 20% v/v ((c) and (d)), respectively. According to the PSD, they contribute similarly to the total solid volume fraction with approximately 30% by volume for each size (see table 6.3). As can be seen figure 7.26 (a) and (b), most of the 0.15 mm particles are in suspension at all the impeller speeds, except for the lowest speed of 100-rpm. In contrast, most of the 1.18 mm sized particles are found in the bottom of the tank. For 20% v/v particle loading, most of the 0.15 mm particles are in suspension whilst most of 1.18 mm particles rest at the bottom of the tank for low impeller speeds and in suspension for high impeller speeds.

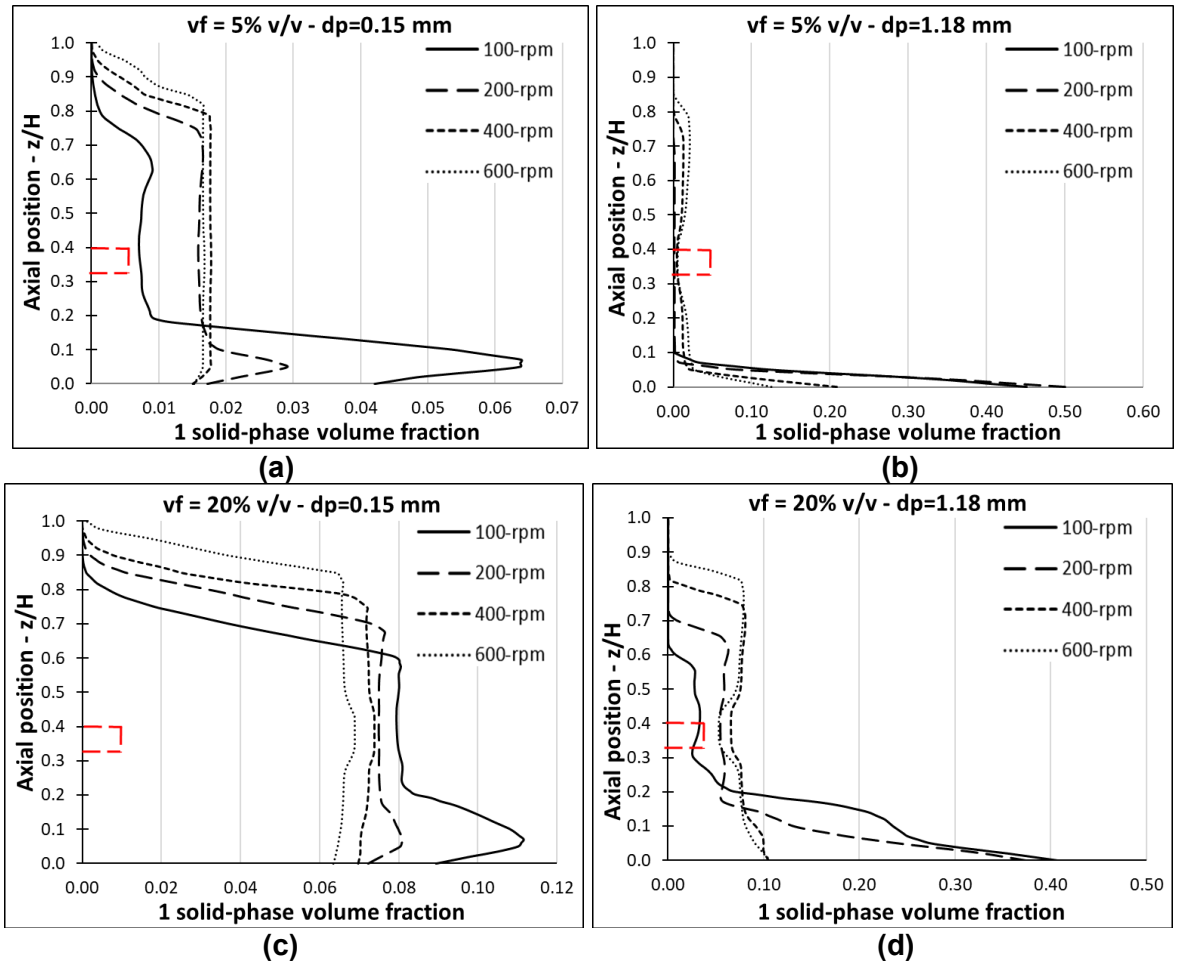

Figure 7.26: Local individual solid particles concentration plotted along a line at r/R=0.6 between the impeller and the baffle for all four impeller speeds investigated. (a) and (b) shows the solid concentration for particle loading of 5% v/v for particles with diameter of 0.15 and 1.18 mm, respectively. (c) and (d) shows the solid concentration for particle loading of 20% v/v for particles with diameter 0.15 and 1.18 mm, respectively. The red rectangle shows the position of the impeller.

Figures 7.27-30 show the iso-surface and rendered, normalised volume fraction plots for each impeller speed across all of the particle concentrations. Note that the solid

concentration accounts for all of the four solid phases present with images (a), (b), (c) and (d) always referring to the 5, 10, 15 and 20% particle loadings. The CFD simulation results are presented on the left side of each image (a, b, c and d) whilst on the right side, the experimental results using sand particles in the CMC4 solution are shown. All pictures from the experimental work were taken perpendicular to the same vertical plane shared by the impeller shaft and the baffle (only ¼ of the tank is shown). A schematic scale is placed close to baffle to give an estimation of the length, although the depth of the pictures gives a distorted impression of the actual height.

The solid suspension experiments start with all particles resting on the bottom of the tank for each particle loading. The impeller speed began at 100-rpm and was incrementally increased to 200, 400 and 600-rpm. The stirrer was turned off to leave the particles to settle completely and another 5% v/v of sand particles were added before the stirrer was turned on again. The process was repeated until all particle loadings were tested for all impeller speeds. The torque was measured for each experimental setup and compared with the CFD-derived torque for an energy balance evaluation, presented in the next section.

Figure 7.27 (a) shows that for 100-rpm, α_{ls} the local solid concentration is up to 12 times higher than for α_{s_ave} (tank averaged solid concentration), decreasing to approximately 4 times, as particle load increases from 5% to 20% v/v. It is clear from figures 7.25 and 7.27 that most particles are resting in the bottom of the tank for all particle loadings. At 5 and 10% v/v particle loadings, α_{Ns} normalised solid concentration in the bulk flow is less than 0.5 and it increases to approximately 1.0 for 15 and 20% loadings. As more particles are added to the system at lower mixing speeds, the distance between the settled particles and the impeller decreases, increasing their exposure to the region of the tank experiencing the highest energy dissipation from the impeller. As previously discussed, and shown in figure 7.24, smaller particles tend to lie on top of the settled bigger particles after a period of intensive mixing.

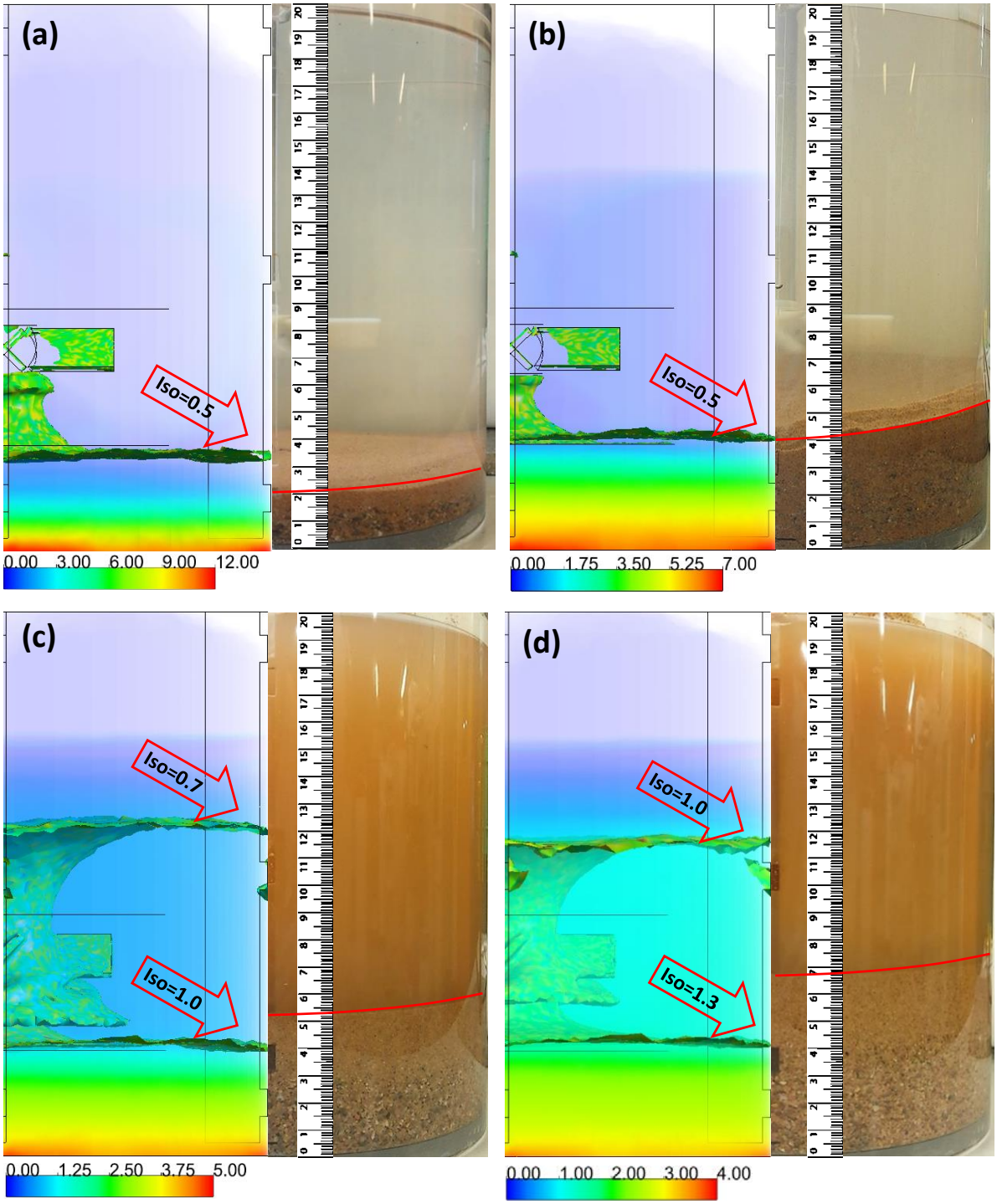

Figure 7.27: Iso-surface (value indicated inside the red arrow) and volume rendering (coloured bar) plots of the normalised total volume fraction at **N=100-rpm** for different particle loadings: (a) 5, (b) 10, (c) 15 and (d) 20% v/v. Note that the coloured bars representing the normalised solid concentration (α_{Ns}) are different for each particle loading, as discussed in the text.

With an increase in particle loading and the settled particles getting closer to the impeller, small particles are re-suspended and kept in suspension, as can be seen in figures 7.26 and 7.27 (c) and (d). The bed height (BH) formed by the settled particles on the bottom of the tank is indicated by the red line on the right-hand side image in figure 7.27. For the

CFD results, the inflection points showed in figure 7.25, are drawn as iso-surfaces, and their values are indicated inside the red arrow. Figures 7.27-30 also show the coloured rendering based on the α_{Ns} value and give a better visualisation of the solid particle distribution throughout the tank. The relatively uniform volume fractions observed above, below and in the impeller regions seen in figure 7.25 (~0.2 and 0.65 for low impeller speeds and ~0.05 and 0.85 for the high impeller speeds, respectively) are represented in figures 7.27-7.30 by constant colours. These are low-gradient regions where no subtle changes in solid concentration occur, indicating homogeneous solid particle distribution. Although the images are shown in 2D, the rendering tool produces images with transparency and represents the 3D projection of the solid concentration. Comparing the iso-surfaces with the experimental results in figure 7.27 (a-d), it can be seen that the inflection point method predicts the BH accurately for 10 and 15% v/v particle loadings, whilst over-, and under-predicting BH for 5 and 20% v/v particle loadings, respectively. As seen in figure 7.25, the solid concentration has a constant value from approximately 0.2 units of the normalised axial position (~40 mm) up to ~0.7 (140 mm). This is where the upper inflection point, i.e. the cloud height (CH), is defined. From ~0.7 to ~0.8 (~140 to 160 mm), the concentration decreases to zero at around 0.9 (180 mm). Note that no common threshold value is found in the literature for CH. Kasat et al. (2008) used the average solid volume fraction of the system to define the iso-surface value, whilst Tamburini et al. (2009) adopted a threshold of α_{ls}=0.1. The inflection point method gives an indication of the location of the CH, but it still sensitive to the threshold choice. Furthermore, a precise definition of the cloud height is often subjective, even when more advanced techniques such as positron-emission particle-tracking (PEPT) and laser Doppler velocimetry (LDV) are used. This is because of the unsteady nature of the fluid flow in stirred tanks. PEPT, LDV and CFD can determine the averaged solid concentration values over time, but in reality, CH might vary considerably within seconds, as seen in the laboratory experiments and reported by several authors (Kresta, 2016, Tamburini et al., 2012, Tamburini et al., 2011, Hosseini et al., 2010, Bittorf and Kresta, 2003). To date, there has been no published CFD work that considers multiple secondary solid phases mixed in a non-Newtonian fluid, therefore the threshold points determined here were a case of visually identifying the inflection point. In future work, further investigation should be carried out for validating the CFD model using more advanced techniques such as particle tracking or PEPT. A more accurate definition of the cloud height for poly-dispersed solid mixing can be then be defined.

Despite the transparency of the CMC solution, it was difficult to see the CH phenomena occurring in the pictures from the laboratory experiments and particularly so for low solid concentrations. This is because of the small particles in suspension and therefore the high turbidity of the solution. That said, the fluid becomes visually clearer for more

homogeneous suspensions at higher mixing speeds, as shown in the analysis for 400 and 600-rpm.

Figure 7.28 shows that the lower inflection point used to plot the iso-surfaces from (a) to (d) shows close agreement for the 200-rpm impeller speed. Figure 7.28 (a) shows a horizontal flat iso-surface, illustrating that the flow discharge of the impeller is barely affecting the shape of the “bed”. However, in figure 7.28 (b) to (d), a curved iso-surface can be noted where the “bed” region below the impeller discharge is at a lower level than that near the walls and baffles. In fact, the height of the solid “bed” for 5, 10, 15 and 20% v/v particle loadings is approximately 17, 29, 48 and 64 mm in the still solution (figure 7.24) and approximately 25, 39, 55 and 71 mm for the measured height at 200-rpm. This represents an increase of approximately 8, 10, 7 and 7 mm in the BH, respectively. The visualisation technique does not allow a precise measurement of the suspended fraction or the curvature effect below the impeller discharge region, but the increase of the “bed” height near the walls must be justified. The PEPT technique would only give a precise measurement of the curvature if the PEPT’s seed particle does not get stuck in the bed. The LDV technique will not capture the curvature, as the particles on the wall would hinder the signal reception of the sensor. As a consequence, CFD-based evaluations of BH shape, curvature and 3D, time changing form are the most accurate way to fully understand solid bed formation and morphology in an AD chamber.

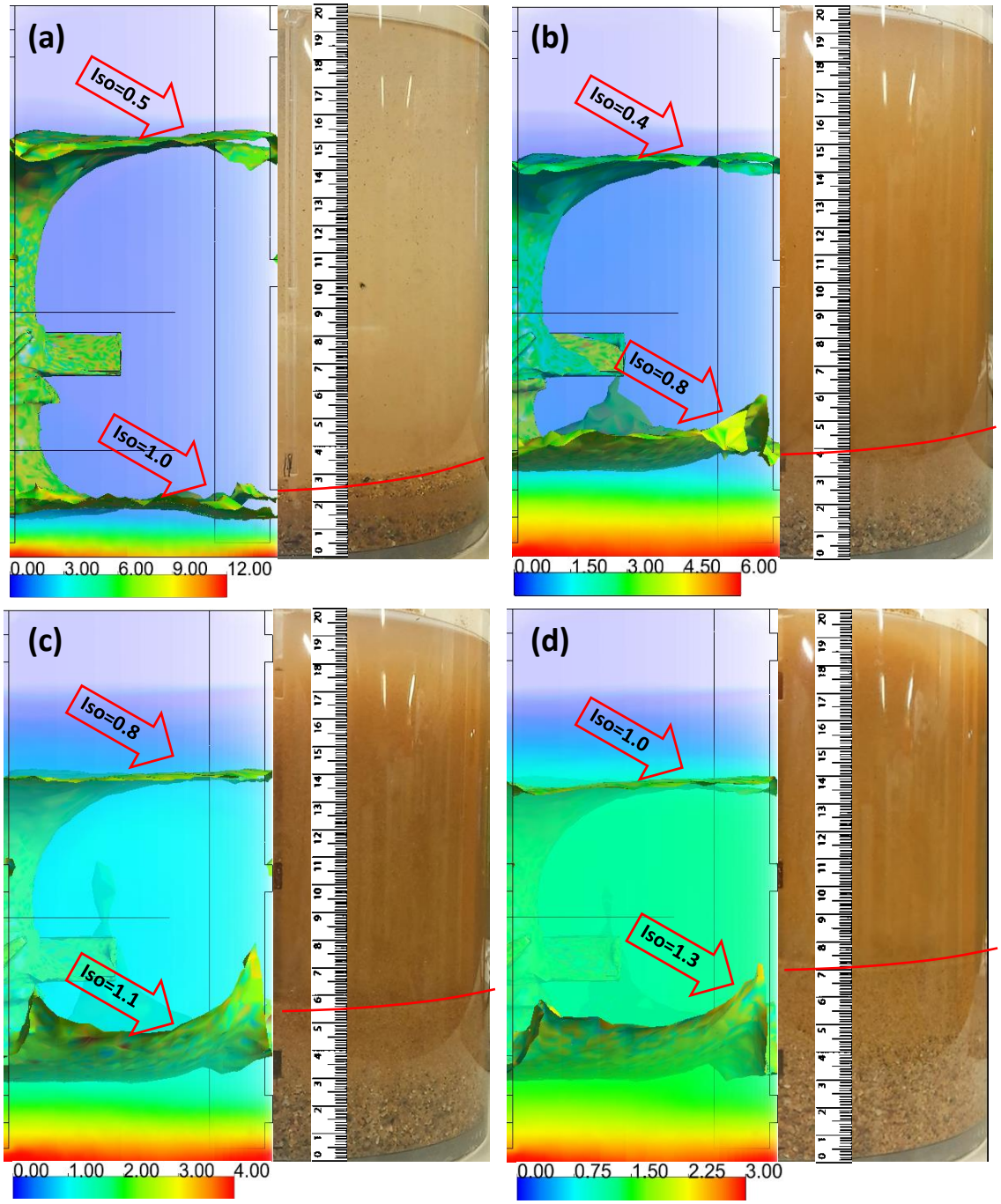

Figure 7.28: Iso-surfaces (value indicated inside the red arrow) and volume rendering (coloured bar) plots of the normalised total volume fraction at **N=200-rpm** for different particle loadings: (a) 5, (b) 10, (c) 15 and (d) 20% v/v. Note that the coloured bars representing the normalised solid concentration (α_{Ns}) are different for each particle loading, as discussed in the text.

The boundary between the solid-rich suspension and the free-solid solution is unclear from the experimental images. From the CFD results, however, the region lies between 140 and 175 mm, where the solid concentration drops from a constant value to zero. The CH has a flat surface close to the walls and curved towards the centre of the tank in figure 7.28 (a) and (b), which is in contrast to the CH seen in the 400 and 600-rpm results (discussed later).

The results also show that an increase in impeller speed from 100 to 200-rpm has little effect on the suspension behaviour of the solid fractions present in the system. It can be seen that a component of the smaller-sized particle fraction tends to stay in suspension whilst the rest stays trapped within the intra-particle void space left by bigger particles, forming a quasi-static solid bed where the velocity field is almost zero (see figures 7.9 to 7.23).

Figure 7.29 shows the results for all particle loadings mixed at 400-rpm. The CH represented by the iso-surface plot now appears in the upper region of the tank and extends downwards into the impeller region. By definition, the iso-surface is based on the inflection point where α_{Ns} starts to decrease from a relatively constant value down towards zero. The region close to the impeller experiences considerable drops in α_{Ns}, hence the presence of the iso-surface at this point in the tank. These drops become increasingly apparent in figure 7.25 (b), (c) and (d), between 0.25 and 0.45 units of the normalised axial distance. The CH iso-surface is also not flat in its overall form as previously observed in the 100 and 200-rpm cases (figures 7.27 and 7.28).

Taking the anti-clockwise rotation of the impeller as a reference frame in terms of the liquid-solid flux rotation, the CH is lower in the tank in the volume after the baffles and higher before them (i.e., there is a drop in CH of about 30 mm across the baffle in the direction of flow rotation). This effect is the primary functional design intention of the baffle for solid suspensions in a stirred tank (Paul et al., 2004). Considering the uneven shape of the CH and the unsteady nature of the experimental mixing system, the CFD model predicts the CH well for all particle loadings with an error ±10 mm (5%).

From the experimental images showed in figure 7.25 (c) and 7.29, it is notable that the impeller speed of 400-rpm is still unable to keep all particles suspended for any of the particle loadings tested (the red line drawn on the experimental images marks the BH). The CFD results show a higher α_{Ns} in the central region, where particles have tended to accumulate behind the baffles and close to the walls. The iso-surface shows a good agreement with the BH of the experimental results.

Finally, figure 7.30 shows the normalised solid concentration for all particle loadings mixed at 600-rpm. As for 400-rpm results, the CFD-based CH is uneven, but well defined for all particle loadings. In all cases, CH is established at around 160 mm for both the CFD model and the experimental results. The inflection points given in figure 7.25 showed consistent similarities for all particle loadings at 600-rpm. The considerably lower maximum $\alpha_{ls}/\alpha_{s\_ave}$ ratio indicates a much more even distribution of the solids for all cases. Interestingly, the inflection point method indicates that only complete suspension is achieved for 20% v/v particle loading at 400 and 600-rpm, where α_{Ns} is constant from the

bottom of the tank up to the upper inflection point, i.e. CH. In contrast, the experimental results show no visible solid accumulation in the bottom of the tank for 600-rpm. This could not be entirely confirmed because the zone directly below the impeller was not fully visible in the experiment. Additionally, α_{ls} is extracted from the line at r/R=0.6 between the baffle and the impeller and represents the solid distribution only in this region. The rendering plots show regions where the $\alpha_{ls}/\alpha_{s_{ave}}$ rate is 2.0 at the bottom between baffles, indicating solid accumulation in these areas.

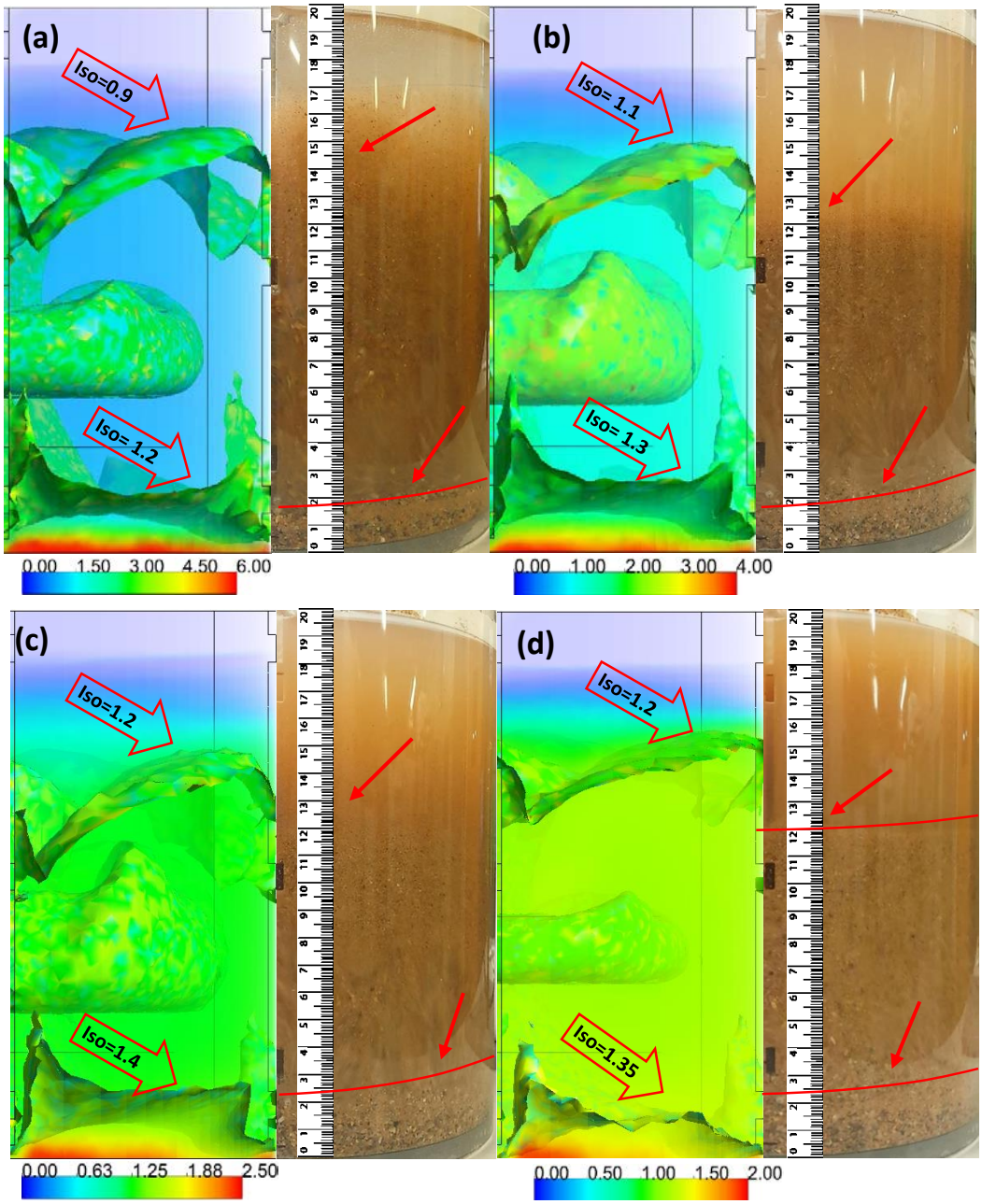

Figure 7.29: Iso-surfaces (value indicated inside the red arrow) and volume rendering (coloured bar) plots of the normalised total volume fraction at **N=400-rpm** for different particle loadings: (a) 5, (b) 10, (c) 15 and (d) 20% v/v. Note that the coloured bars representing the normalised solid concentration ($\boldsymbol{\alpha_{Ns}}$) are different for each particle loading, as discussed in the text.

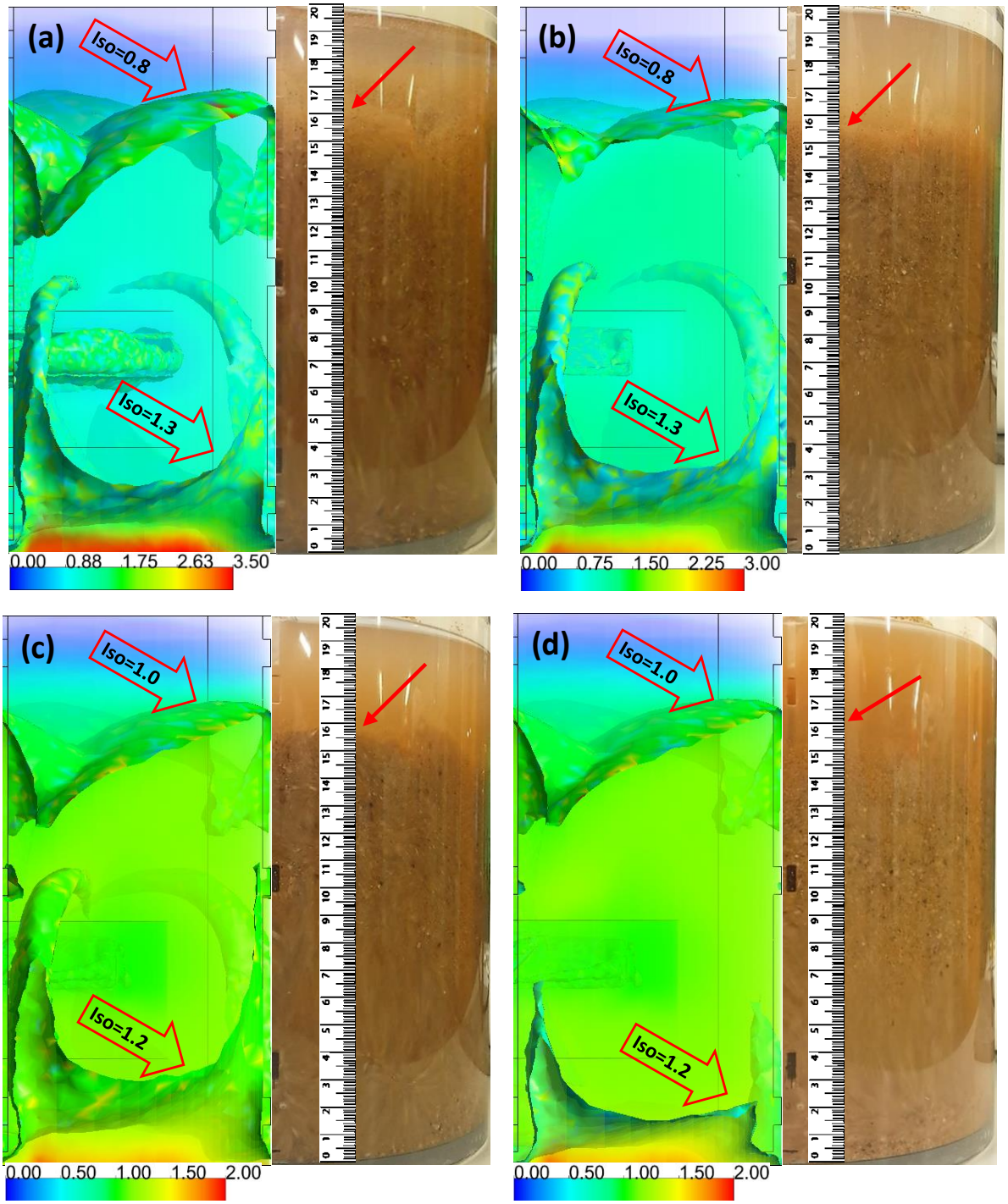

Figure 7.30: Iso-surfaces (value indicated inside the red arrow) and volume rendering (coloured bar) plots of the normalised total volume fraction at **N=600-rpm** for different particle loadings: (a) 5, (b) 10, (c) 15 and (d) 20% v/v. Note that the coloured bars representing the normalised solid concentration (α_{Ns}) are different for each particle loading, as discussed in the text.

7.3. Mixing Energy

This section presents an analysis of the energy used for mixing the fluids within the AD tanks and compares, directly, the experimental and computational results. The quality of mixing in industrial processes must be balanced with the mixing energy, such that the process' functional aims are achieved whilst being economically viable. As discussed in

chapter 2 and 3, several works have looked at different mixing systems and regimes and assessed their effects on AD. However, only one paper has been identified amongst the peer-reviewed literature available via Web of Science that looks at the industrial problem of inert particle sedimentation and accumulation in AD tanks (Klimento et al., 2004). The impact of inert particle sedimentation on the overall efficiency of the AD process are straightforward; loss of effective working volume, dead zone(s) formation, frequent tank cleaning, short residence times, poor sludge treatment quality and organics reduction, and, ultimately, less biogas and methane yield. Klimento et al. (2004) research, however, is limited to characterising the physical, chemical and mineralogical composition of the sediment.

Figure 7.31 shows the impeller torque results determined from the experimental investigation of solid suspensions, under all impeller speeds and particle loadings. These are compared to the equivalent computational (CFD) torque results. The results also include data and models from a single-phase system for comparison. The experimental torque was registered from the stirrer's digital display (Radleys' scientific stirrers model RZR 2102 – instrument precision 0.001 N.m), whilst the torque from the CFD model was computed from the pressure fields over the surface of the impeller blades. From figure 7.31, it can be noted that the torque increases with impeller speed, as would be expected. At 100-rpm, the average torque for both the experiment and CFD model is approximately 0.002 N.m. whilst at 600-rpm, the differences between the measured and computed torque are 0.02 N.m for the single phase system and 0.017 N.m for 20% v/v particle loading. Both methods showed a torque increase with particle loading, which is consistent with other works (Brucato et al., 2010, Micheletti et al., 2003). These authors agree that the power increase with higher solid concentrations is due to the energy dissipation resulting from the frictional forces of liquid-solid and solid-solid interaction, especially if large particles are present.

Despite the fact that similar trends exist for all the experimental conditions, it is clear that the measured torque diverges from the CFD results as impeller speed increases. Several authors have successfully validated CFD simulations for stirred tanks using measured values of torque (Cortada-Garcia et al., 2017, Bridgeman, 2012, Wu, 2010b, Paul et al., 2004). In this case, the torque measurements are taken from the stirring equipment is determined from the power consumption of the stirring device (Heildolph, 2011). Despite using a scientific-quality the manufacturer could not fully guarantee the degree of accuracy and precision of the torque measurements. To investigate this, an analysis of the repeatability and variance of the torque measurements was undertaken in the laboratory. Three different stirrers were used to mix a known volume and consistency of a batch of CMC4 solution across the full range of impeller speed and particle loadings. In total, this equated to over 50 individual measurements of torque with the results being consistent

across all three stirrers (less than 5% variance). This indicates that the relative precision of the torque measurements is acceptable but that there may be a small systematic error in the absolute value for all stirrers. This would explain the discrepancies between the measured and CFD results and, as such, the CFD results are accepted for reference to the power-related evaluations that follow.

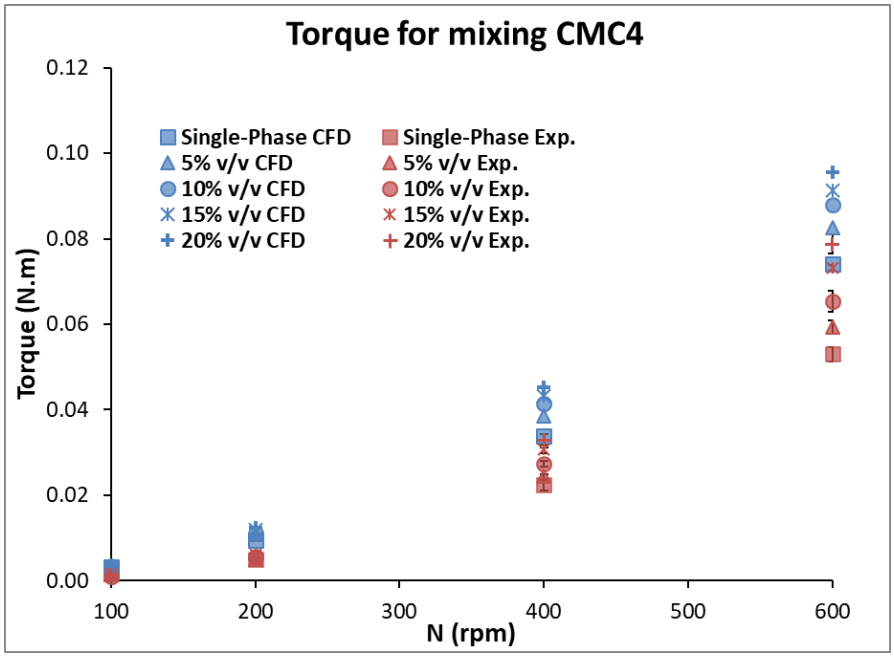

Figure 7.31: Measured and CFD computed torque for the four impeller speeds and the single- and multi-phase particle systems.

The power consumption can be computed from the torque using the following expression:

$$P = 2\pi NT \qquad 7.28$$

where N is the impeller speed and T is the torque. Figure 7.32 gives the power consumption for each of the conditions studied. As with the torque, the power consumption increases with increasing impeller speed and particle loading. It is clear from the results that solid suspension is only achieved during high-power mixing. Figure 7.33 compares the daily average energy produced in the digesters after the impeller speeds are changed (phases 3 and 4) along the mixing power. As discussed in chapter 6, biogas production at higher mixing speeds (400 and 600-rpm) dropped a few days after the inert particles were inserted. This was followed by a drop in methane content, thus decreasing the biogas' 'energy' value. Despite the accumulation of inert particles in the bottom of the tank, the lower mixing speeds (100 and 200-rpm) produced more biogas and therefore more energy can be extracted from the AD system. The difference in biogas yields between AD experiments 1 and 2 (Exp1 and Exp2) have been discussed in chapter 6 and are most likely to be because of the lower

organic loading rates (OLR) over the course of Exp2. Nevertheless, a trend can be noted in both experiments: energy production drops with an increase in the mixing power. Interestingly, the two lowest mixing powers produce similar amounts of energy whilst the higher mixing powers also produces similar amounts of energy.

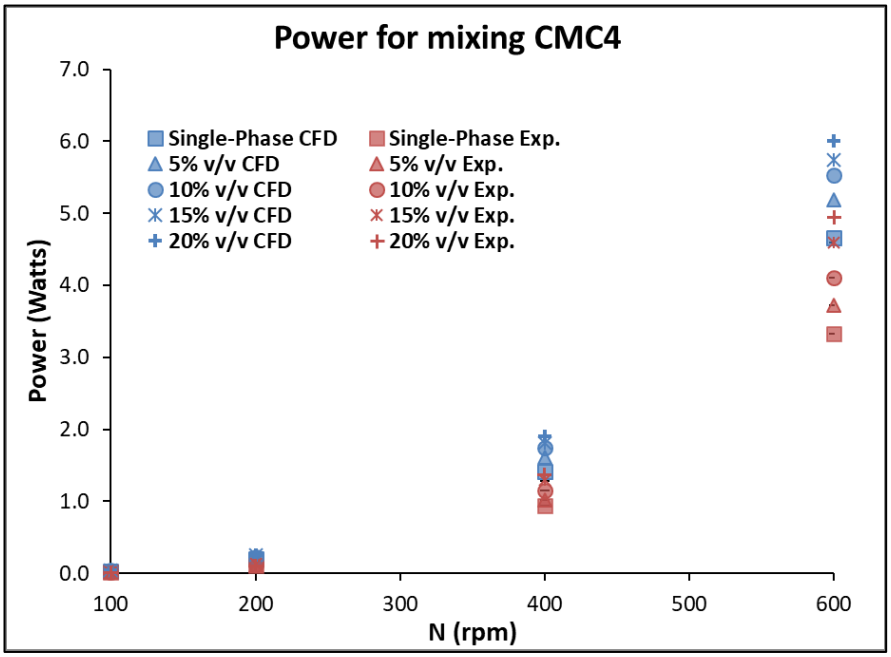

Figure 7.32: Mixing power calculated using eq. 7.28 for the measured and CFD computed torque for the four impeller speeds and the single- and multi-phase systems.

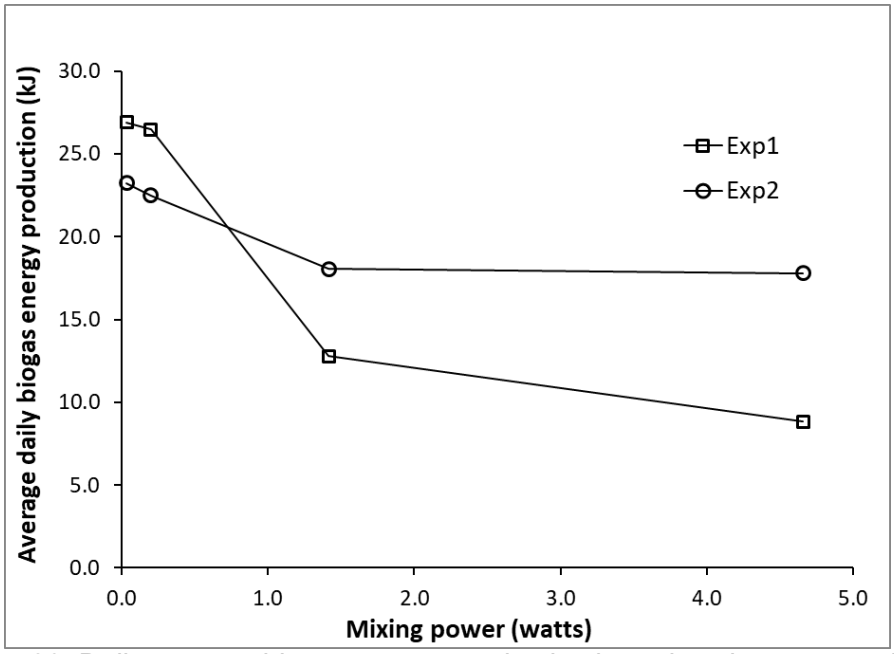

Figure 7.33: Daily average biogas energy production based on the average daily biogas volume during phases 3 and 4, after impeller speed was changed. Biogas heating value is approximately 25 MJ/m³ for ~65% CH4 (Appels et al., 2008).

7.4. Summary

This chapter presents the results of the CFD and experimental investigation of solid suspensions immersed in a non-Newtonian shear-thinning fluid. The model was intended to mimic the real-life sedimentation and suspension phenomena of inert solid particles in an anaerobic sewage sludge digestion tank. The rheological characteristics of sewage sludge at a total solid concentration of 5.53% was mimicked using a CMC solution of 4 g/l. Sediment particles found in industrial tanks were mimicked using sand particles because of their similar physical and geometrical nature and potential effects on the AD process. Four particle loadings and four impeller speeds were investigated, totalling sixteen different mixing scenarios.

The multiphase CFD model represented the fluid flow and solid behaviour of the particles in the stirred tank in question to a high degree of equivalence. The velocity profiles corresponded well to those found in the experimental PIV measurements and, within acceptable error margins, agree with the literature. Despite the limited scientific research on stirred tanks with solid suspensions in non-Newtonian fluids (and their complex fluid dynamics), the experimental work corroborated the CFD results in most of the conditions investigated.

The inflection point method for solid concentrations was used to accurately locate the bed height (BH) and cloud height (CH). The solid concentration curves were derived from the CFD results, but more advanced techniques are required for the validation of the CFD model. CFD-based iso-surfaces (defined from on the inflection point method) provided a computationally-based assessment of BH and CH and showed good agreement with the experimental visualisation of the CH/BH.

Finally, the mixing energy produced from the anaerobic digestion process (energy out) was compared to against the mixing power of the stirrer (energy in). It was shown that a higher mixing power detrimentally affects biogas production, thus energy output, despite being essential for avoiding inert particle sedimentation. A further discussion on the practical impact of inert particles in AD systems, plus the findings of both the CFD and experimental, is provided in the next chapter.

CHAPTER 8 DISCUSSION AND IMPLICATIONS FOR WWTP AD SYSTEMS

The primary aim of this research was to develop and test experimental and CFD-based methods that can identify energy-efficient mixing regimes in mechanically-mixed anaerobic digesters that are impacted by the sedimentation of inert solid particles. From a practical perspective, improving AD system performance is important for the wastewater treatment industry as their goal is to minimise digester energy input without having detrimental effects on biogas production and sludge stabilisation. The importance of mixing for solid suspensions in AD reactors, and its impact on process efficiency, is evident from the literature and the detailed results provided in chapters 6 (AD Results) and 7 (CFD Results) of this thesis. In these chapters, the results have been presented, interpreted and discussed in some detail, particularly with regard to the scientific objectives of the project. In this final chapter, the key findings are summarised and discussed in terms of the benefits and limitations associated with investigating AD systems both physically and computationally. The implications of this work on the design and operation of 'real-world' WWTP digesters are also considered along with insights gained from developing the unique CFD models of digester performance. It is important to note that this work represents the first investigation of sedimentation in laboratory-scale anaerobic digesters carried out by incorporating the presence of inert particles inside the tanks both experimentally (chapter 6) and computationally (chapter 7).

The key AD process-related findings of this work can be summarised as follows;

- The constant suspension of inert particles in highly intensive mixing regimes has a detrimental effect on biogas production, sludge treatment quality and high power consumption.
- Low mixing regimes do not contribute to the solid suspension of inert particles but ensure stable digestion, biogas production and good sludge stabilisation.
- Intermittent mixing could provide a solution for minimising mixer power consumption without negatively affecting biogas yields and sludge stabilisation.
- Multi-phase CFD models can be used successfully to visualise the complex, fluid-solid interactions in an AD system and help improve the understanding of mechanisms for solid suspension in AD tanks.

In what follows, the practical aspects of this research are discussed with specific relevance to the understanding of anaerobic digestion process in industrial applications and the validity of using CFD models and laboratory based experiments as representative analogues.

8.1. Sewage Sludge, Feed Sludge, Digestate and Sediment Properties

The experiments were designed on the assumption that feed sludge samples would have a TS concentration varying between 5 and 6.5% and VS representing 70 to 80% of the TS concentration (IWA Publishing, 2007). This assumption was based on few preliminary measurements and information from the operating plant manager at Finham Wastewater Treatment Works (WTW), where all samples were collected. At these concentrations, an average organic loading rate (OLR) of 2.5 kgVS/m^3/day could be achieved with a daily feeding volume (DFV) of 400 ml of fresh sludge, with tanks being fed six times a week. Noutsopoulos et al. (2013) investigated several combinations of greasy domestic sludge and primary sewage and concluded that 3-litre anaerobic digesters operating at mesophilic temperatures produced the highest amounts of biogas at OLR=2.4 kgVS/m^3/day. According to Severn Trent guidelines, they aim to operate their AD tanks at an OLR of 2.5 kgVS/m^3/day.

Throughout the experiments, it became evident that TS was often below the expected range (5-6.5%), which would result in considerably lower biogas production at the industrial scale. As a result, lower OLRs occurred and daily feed volumes (DFV) could have been increased to compensate for this. This is actually the current practice of many WWTPs operating AD tanks. As discussed in chapter 2, acetoclastic methanogens are responsible for about 70% of the methane production but are slow-growing microorganisms that need considerable amounts of time to double its population (several days) (Gerardi, 2003). The practice of increasing DFV to compensate for lower VS in the feed sludge is based on a 'rule of thumb' and may lead to shorter retention times, which in turn can result in methanogen wash out, accumulation of VFAs and eventually process failure. In the laboratory, however, adjusting the DFV would have added another variable to the already complex experimental setup. There does not appear to be any research in the literature that makes use of such practice for long periods of time. For all the reasons described above, a constant DFV and a variable OLR, was the preferred option.

Alternatively, synthetic sludge could have been used to provide constant VS feed throughout the entire experimental period, but as Sindall (2014) pointed out, synthetic sludge does not represent real sludge properties in terms of either nutrients or flow characteristics. Additionally, the four digesters investigated by Sindall (2014) failed sooner or later, regardless of the mixing regime. This was attributed to the long-term exposure of the microbial population to trace elements inhibitors. If that was the case, it becomes difficult to judge the real impact of different mixing regimes on the digestion performance. Another alternative is to freeze the necessary amount of sludge for the entire experimental period as in (Hoffmann et al., 2008). The drawbacks of this practice are the need of significant

(costly) storage capacity to keep the sludge at -20°C plus the structural changes that happen in the substrate during the process of freezing and unfreezing, which may result in changes in the VS availability as well as rheological characteristics of the slurry (Eaton et al., 2005). It is evident that the variation of TS concentrations adds complications to the experimental work. However, this is the same reason why real sludge AD experiments should be encouraged. Otherwise the real-life challenges could not be fully comprehended. For this research, the challenges of dealing with mid-term anaerobic digestion of real sewage sludge samples were overcome with successful and reliable results.

The sludge and digestate rheological properties were successfully monitored for a considerable period (weekly for 20 weeks) in this work. It is clear that the rheological properties vary considerably with changes in feed sludge and TS over time. Therefore it is important that measurements of 'real' AD materials are used for building reliable and representative CFD models. CFD models using external (or proxy) rheological data to simulate different substrates (e.g., cow manure (Achkari-Begdouri and Goodrich, 1992)) have previously been used to investigate sewage sludge digesters (Bridgeman, 2012, Meister et al., 2018). Such investigations may miss-lead mixing optimisation attempts because the rheological behaviour of these slurries depends not only on the TS concentration (which might be similar for many different kinds of feedstock) but also on shape and size of the particles, and particularly, its origin (Seyssiecq et al., 2003). It is, of course, impractical to model the fluid flow for each sludge variation but it is important to understand the dynamics of each system more carefully in order to achieve the highest level of design and operational optimisation. As such, the rheological data collected within this research adds a significant contribution to the broader understanding of laboratory-scale, mechanically-mixed sewage sludge AD tanks and its relevance to industrial-scale tanks.

Sediment samples from out-of-service AD tanks were collected randomly in the sediment pile on-site and brought to the laboratory for characterisation. The results show that particle size is in the range of approximately 0.063 to 2.000 mm diameter, which is consistent with the results of Klimento et al. (2004). Interestingly, bigger particles were less dense than the smaller ones. Although the shape of the particles was not analysed in detail, from visual observation the presence of snail shells, gravel, hair, seeds, stones and sand was notable. Similar results were found by Klimento et al. (2004). This indicates that the mixing system of the industrial scale tank was able to suspend all particles up to a threshold point at which a balance between the size, density and shape exists for a range of particle shapes. To build a CFD model that could model these particle-related factors, and run it in a reasonable amount of time, is currently impractical and therefore simplifications have to be made. Nevertheless, this work has provided evidence (for the first time) that CFD can be used to successfully simulate the fluid dynamics of inert solid particle suspensions in

sewage sludge AD tanks and that the results can be experimentally validated, using real sediment data, albeit at the laboratory scale.

8.2. AD Performance

The experimental results showed that low mixing speeds (100 and 200-rpm or D4 and D1, respectively) had no significant detrimental effect on the digestion performance and biogas production when inert particles were either absent or present for a broad range of particle loadings (5 to 20% v/v) On the other hand, biogas production and digestion performance have been considerably affected by the increased mixing intensity (400-rpm and 600-rpm or D2 and D3, respectively), but only after inert particles were added into the tanks (P4). These results are in agreement with most of the literature (Kaparaju et al., 2008, Hoffmann et al., 2008, Bridgeman, 2012, Sindall, 2014, Kress et al., 2018, Kariyama et al., 2018) although these studies have not fully considered the phenomena of inert dense particles sedimentation. Interestingly, the control tank (GD) produced slightly more biogas on average than tanks D1 and D4 during both experiments (note that biogas production was normalised by the total volume of each tank). This was an unexpected result, based on the assumption that all digesters were consistently operating under capacity. A reasonable explanation is that the differences were caused by biogas measurement errors by the inverted 'bucket' chamber mechanism immersed in the liquid receptacle or sampling discrepancies (discussed in section 5.4.2). Alternatively, the fact that all D tanks were connected to one measurement device (4 chambers) whilst GD was connected to a second device of the same type could account for the systematic variance. These are, of course, technical issues but it is evident from the findings that increasing the impeller speed from 100 to 200-rpm, and adding inert particles up to 20% v/v, is unlikely to have affected either digestion performance or biogas production. Looking at this another way, reducing the impeller speed by half seems to have a limited effect on overall AD performance, even with some degree of inert particle sedimentation. This is consistent with the findings of Bridgeman (2012) and Sindall (2014) who conclude that lower mixing speeds are preferable in order to save energy and that low mixing intensities, independent of how they are defined for each system, have beneficial or neutral effects on the digestion process and biogas production (Kariyama et al., 2018). In contrast to the performance of AD at low mixing intensities, the negative effects of the highest mixing speeds on biogas production and digestion performance were evident by the end of each experiment. This is contrary to the results of Hoffmann et al. (2008) and Kaparaju et al. (2008) but in agreement with Sindall (2014). It is worth mentioning again that these studies did not include the effect of inert particle suspensions on AD performance. All real-world slurries inherently have inert particles in suspension, including sewage sludge and cow manure. As this is the first study

to comprehensively assess the impact of such particles at high mixing speeds, there is no corroborating evidence to confirm this effect is scalable to the industrial scale. However, the combined CFD and experimental results here strongly suggest that the constant suspension of such inert particles in mechanically-mixed digesters has a detrimental effect on digestion stability, biogas production and quality of sludge treatment. Therefore, there should be careful consideration whether inert particles, if present and settled, should be (re)suspended in industrial scale AD plants in order optimise the net energy of the plant. Intermittent mixing with short-time intensive mixing could be an alternative solution for industrial AD plants (as indicated in Chapter 6). The best practice, however, seems to be to avoid inert particle sedimentation by applying intensive mixing for short periods of time, but maintaining mixing modes at the minimum level required by each specific system.

Ultimately, more needs to be done in order to create a wide and diverse resource in which AD designers and operators can access validated and reliable data to optimise the performance of their plant. From the outcomes of this research, this would include the investigation of;

- Intermittent, intensive mixing regimes that alternate between on and off modes instead of running at continuous low and/or high mixing intensities. Several operational modes could be investigated, such as different mixing intervals/cycles, variable impeller speeds, dynamic OLRs and inert particle loadings based on energy and biogas production cycles.
- Different tank designs (e.g., curve-bottomed, egg-shaped) and mixing types (e.g., combined biogas and slurry recirculation).
- Reconfigurations of the inlet and outlet interfaces to optimise fluid recirculation, sediment suspension and re-suspension plus the extraction of sediment during mixing.

8.3. AD and CFD Coupling

The CFD model presented in chapter 7 has proven to reliably replicate the fluid flow patterns of the AD system and has been validated by experimental results. This unique, multi-phase, liquid-solid CFD model has been used to investigate the sedimentation/suspension phenomena of inert dense solid particles in AD systems for the first time. As such, it can help design more efficient digesters and create strategic operational plans for WWTP operators to optimise the overall energy efficiency of their AD plant by reducing mixing-related energy costs whilst assuring steady biogas yields. The model was used to assess four process-related parameters: (i) flow velocity, (ii) solid particle distribution, (iii) bed and cloud height, and (iv) the viscosity behaviour of the non-Newtonian sludge. Particle imaging velocimetry (PIV) was used to ensure the model could predict the

velocity fields with reasonable accuracy with the experimental data validating the solid suspension and cloud/bed height findings. From the CFD results, it can be seen that for low mixing speeds, most solid particles accumulate in the bottom of the tank and only a fraction of the small particles remain suspended. In these circumstances, it is reasonable to assume that these particles did not influence the AD process. It is also important to note that the velocity and dynamic behaviour of the particles in suspension (e.g., at low concentration) appear to be more detrimental and impacting on the AD processes than the amount of particles in suspension. These insights would not have been gained without the use of CFD models, illustrating the importance of the numerical simulations. The ability to visualise the 3D, time-varying flow fields within the AD vessel is key for understanding the complex dynamic interactions between liquid and solid phases that can occur in industrial scale AD systems.

The CFD results, supported by the experiments, highlight some very interesting practical aspects of the AD mixing process. At low impeller mixing speeds, smaller particles tend to be partially suspended whilst bigger particles stay at rest in the bottom. At higher speeds, all (or most) particles are in suspension and are 'active' within the recirculation zones of the digester. In the laboratory experiments physical damage occurred to the impellers at constant high mixing speeds. This is very likely to be a result of abrasion from the constant and high energetic collisions between the impeller and suspended particles over long periods of time. Damage to the particles might have also occurred at certain levels within the tank which might have resulted in breakdown of the bigger particles which, in turn, increases the relative number of smaller particles. If that was the case, the solid distribution and cloud heights could vary considerably over the duration of a tank's operational cycle, further supporting the need for more sophisticated approaches to designing and operating AD plant.

The research also showed the importance of correctly determining the viscosity of the fluid system, particularly where it depends on shear rate. An incorrect viscosity range might result in unrealistic flow patterns, energy dissipation, solid suspension and increased power consumption. This can mislead the design of mixing systems and result in the under or over-estimation of the power requirement needed for proper mixing.

Finally, a comparison between the PIV and CFD results showed some levels of discrepancy in the magnitude of the velocity field near the liquid column surface, despite describing the shape very well. This difference is likely to be caused by a simplification within the CFD model at the upper surface, which is treated as a shear-free flat surface wall. In reality, a vortex is created in this surface as a result of the pressure differences between the downwards flow near the centre of the tank and upwards flow near the walls. This phenomena is neglected in the CFD model and is likely to be the source of the velocity

differences in this region. Care must then be taken when investigating and interpreting CFD models of industrial-scale AD tanks as the exit of the sewage sludge digesters are often located in the very upper part of the tank, this is also where the inert particles in suspension could escape in the flow. Incorporating more appropriate boundary conditions at top of the current CFD model would be possible but this is not a trivial task. In practice, it would require knowledge of the tank's internal pressure gradients and possibly the development of dynamically changing interface condition to represent the uppermost surface of the fluid column. This is work that is envisaged for the next phase of the research.

CHAPTER 9 CONCLUSIONS AND RECOMMENDATIONS

In chapter 4, the aims and objectives of this research were described as follows;

Aims

To investigate an energy-efficient AD mixing regime designed to avoid the sedimentation of inert solids in a mechanically-mixed anaerobic sludge digester in order to find a balance between AD mixing energy and digestion performance such that the energy input is minimised without imposing a negative impact on biogas production.

Objectives

- Characterise sewage sludge and sediment particle distribution of samples from full-scale anaerobic digestion tanks.
- Quantify the impact of inert particle loadings, sedimentation and/or suspension on sludge treatment quality and biogas yields in laboratory-scale, mechanically-mixed digesters.
- Assess the flow fields and sedimentation/suspension of sewage sludge solid particles inside a laboratory-scale anaerobic digester under different mixing scenarios through CFD simulations and physical experiments.
- Determine the minimum mixing intensity required to keep organic and inorganic particulates in homogeneous suspension throughout the digester.
- Monitor biogas yields and methane content during a range of mixing conditions and assess the parameters that increase biogas yield with the highest calorific value.

The findings of the work have fully met the aims and objectives using a combination of CFD-based numerical modelling and laboratory scale physical experiments. The key outcomes of the research were;

- Low mixing speeds (<200-rpm) do not have a negative impact on AD performance for all inert particle loadings and in the absence of inert particles.

- For impeller speeds above 400-rpm, and in the absence of inert particles, digestion performance is not affected.

- For continuous mixing at impeller speeds above 400-rpm, in the presence of inert particles, digestion performance, biogas production and methane yields were negatively affected.

- The accumulation of particles at low mixing speeds changes the velocity fields inside the digesters under increased particle loadings.

- Mixing the digester at 600-rpm for ~10 minutes/day and then decreasing the impeller speed to lower mixing speeds (100-rpm), allows suspended particles to exit the system without impacting AD performance and reduces particle sedimentation/accumulation.

- Energy efficiency of the AD plant can be optimised by developing appropriate mixing regimes through the use of the CFD modelling approach.

- Multi-phase CFD models have successfully simulated the fluid dynamics and physical characteristics of mechanically-mixed digesters under a range of different particle loadings and impeller speeds, as verified laboratory experiments and PIV.

- It is important to use real sludge properties in the CFD models and laboratory experiments in order to replicate AD processes accurately and realistically.

9.1. Recommendations for Future Work

From the findings of this work, it is recommended that the following research is conducted in order to fully realise the potential of the combined CFD-experimental evaluation approach in real-world industrial AD applications.

- Use a constant OLR for optimal anaerobic digestion operation to investigate the impact of inert solid particles under different mixing regimes and particle loadings on biogas production and digestion performance.
- Use more advanced particle tracking technologies to physically validate the CFD models using experimental analogues – i.e., Positron-Emission Particle Tracking (PEPT).
- Develop up-scaled CFD models that can simulate industrial AD plant with a higher degree of realism and sophistication.
- Evolve the current CFD models to incorporate; different rheological behaviours, particle sizes, shapes and densities; a range of mixer types and mixing regimes.

- Apply CFD modelling to gas-mixed digesters under a variety of particle loadings at laboratory, pilot and industrial scale, as it is the most common sewage sludge AD mixing system in WWTP in the UK. This work serves as a first step into liquid-solid, multi-phase modelling of anaerobic digesters and provides novel data that can facilitate the implementation of a third phase (gas) in the CFD model.

REFERENCES

ACHKARI-BEGDOURI, A. & GOODRICH, P. R. 1992. Rheological properties of Moroccan dairy cattle manure. *Bioresource Technology,* 40**,** 149-156.

ADEKUNLE, K. F. & OKOLIE, J. A. 2015. A Review of Biochemical Process of Anaerobic Digestion. *Advances in Bioscience and Biotechnology,* Vol.06No.03**,** 8.

ANSYS INC. 2013. ANSYS Fluent Theory Guide.

ANSYS INC., F. T. 2015. Modeling Turbulent Flow in a Mixing Tank.

APPELS, L., BAEYENS, J., DEGREVE, J. & DEWIL, R. 2008. Principles and potential of the anaerobic digestion of waste-activated sludge. *Progress in Energy and Combustion Science,* 34**,** 755-781.

AUBIN, J., FLETCHER, D. F. & XUEREB, C. 2004. Modeling turbulent flow in stirred tanks with CFD: the influence of the modeling approach, turbulence model and numerical scheme. *Experimental Thermal and Fluid Science,* 28**,** 431-445.

AYRANCI, I. & KRESTA, S. M. 2011. Design rules for suspending concentrated mixtures of solids in stirred tanks. *Chemical Engineering Research & Design,* 89**,** 1961-1971.

AYRANCI, I. & KRESTA, S. M. 2014. Critical analysis of Zwietering correlation for solids suspension in stirred tanks. *Chemical Engineering Research & Design,* 92**,** 413-422.

AYRANCI, I., MACHADO, M. B., MADEJ, A. M., DERKSEN, J. J., NOBES, D. S. & KRESTA, S. M. 2012. Effect of geometry on the mechanisms for off-bottom solids suspension in a stirred tank. *Chemical Engineering Science,* 79**,** 163-176.

AZARGOSHASB, H., MOUSAVI, S. M., AMANI, T., JAFARI, A. & NOSRATI, M. 2015. Three-phase CFD simulation coupled with population balance equations of anaerobic syntrophic acidogenesis and methanogenesis reactions in a continuous stirred bioreactor. *Journal of Industrial and Engineering Chemistry,* 27**,** 207-217.

BANKS, C. J., CHESSHIRE, M. & STRINGFELLOW, A. 2008. A pilot-scale comparison of mesophilic and thermophilic digestion of source segregated domestic food waste. *Water Sci Technol,* 58**,** 1475-81.

BANKS, C. J. & HEAVEN, S. 2013. Optimisation of biogas yields from anaerobic digestion by feedstock type. *Biogas Handbook: Science, Production and Applications***,** 131-165.

BAROUTIAN, S., ESHTIAGHI, N. & GAPES, D. J. 2013. Rheology of a primary and secondary sewage sludge mixture: dependency on temperature and solid concentration. *Bioresour Technol,* 140**,** 227-33.

BAUDEZ, J. C., MARKIS, F., ESHTIAGHI, N. & SLATTER, P. 2011. The rheological behaviour of anaerobic digested sludge. *Water Res,* 45**,** 5675-80.

BENBELKACEM, H., GARCIA-BERNET, D., BOLLON, J., LOISEL, D., BAYARD, R., STEYER, J. P., GOURDON, R., BUFFIERE, P. & ESCUDIE, R. 2013. Liquid mixing and solid segregation in high-solid anaerobic digesters. *Bioresour Technol,* 147**,** 387-94.

BIOENERGY EUROPE 2018. Statistical Report. 2018 ed. Brussels.

BITTORF, K. J. & KRESTA, S. M. 2003. Prediction of cloud height for solid suspensions in stirred tanks. *Chemical Engineering Research & Design,* 81**,** 568-577.

BOLZONELLA, D., INNOCENTI, L. & CECCHI, F. 2002. Biological nutrient removal wastewater treatments and sewage sludge anaerobic mesophilic digestion performances. *Water Sci Technol,* 46**,** 199-208.

BRIDGEMAN, J. 2012. Computational fluid dynamics modelling of sewage sludge mixing in an anaerobic digester. *Advances in Engineering Software,* 44**,** 54-62.

BRIDGEMAN, J., JEFFERSON, B. & PARSONS, S. A. 2010. The development and application of CFD models for water treatment flocculators. *Advances in Engineering Software,* 41**,** 99-109.

BRUCATO, A., CIPOLLINA, A., MICALE, G., SCARGIALI, F. & TAMBURINI, A. 2010. Particle suspension in top-covered unbaffled tanks. *Chemical Engineering Science,* 65**,** 3001-3008.

CALDERBANK, P. H. & MOO-YOUNG, M. B. 1959. The prediction of power consumption in the agitation of non-Newtonian fluids. *Chem Eng Res Des,* 37**,** 26–33.

CAMPESI, A., CERRI, M. O., HOKKA, C. O. & BADINO, A. C. 2009. Determination of the average shear rate in a stirred and aerated tank bioreactor. *Bioprocess Biosyst Eng,* 32**,** 241-8.
CELIK, I. B., GHIA, U., ROACHE, P. J., FREITAS, C. J., COLEMAN, H. & RAAD, P. E. 2008. Procedure for Estimation and Reporting of Uncertainty Due to Discretization in CFD Applications. *Journal of Fluids Engineering,* 130**,** 078001-078001-4.
CHHABRA, R. P. 2007. *Bubbles, drops, and particles in non-Newtonian fluids*.
CORTADA-GARCIA, M., DORE, V., MAZZEI, L. & ANGELI, P. 2017. Experimental and CFD studies of power consumption in the agitation of highly viscous shear thinning fluids. *Chemical Engineering Research & Design,* 119**,** 171-182.
CORTADA-GARCIA, M., WEHELIYE, W. H., DORE, V., MAZZEI, L. & ANGELI, P. 2018. Computational fluid dynamic studies of mixers for highly viscous shear thinning fluids and PIV validation. *Chemical Engineering Science,* 179**,** 133-149.
COUGHTRIE, A. R., BORMAN, D. J. & SLEIGH, P. A. 2013. Effects of turbulence modelling on prediction of flow characteristics in a bench-scale anaerobic gas-lift digester. *Bioresour Technol,* 138**,** 297-306.
CRAIG, K. J., NIEUWOUDT, M. N. & NIEMAND, L. J. 2013. CFD simulation of anaerobic digester with variable sewage sludge rheology. *Water Res,* 47**,** 4485-97.
DACHS, G. & REHM, W. 2006. Der Eigenstromverbrauch von Biogasanlagen und Potenziale zu dessen Reduzierung. *Hg. v. Solarenergieförderverein Bayern e.V. München*.
DAPELO, D., ALBERINI, F. & BRIDGEMAN, J. 2015. Euler-Lagrange CFD modelling of unconfined gas mixing in anaerobic digestion. *Water Res,* 85**,** 497-511.
EATON, A. D., CLESCERI, L. S., GREENBERG, A. E. & FRANSON, M. A. H. 2005. *Standard methods for the examination of water and wastewater*, American Public Health Association.
ESHTIAGHI, N., MARKIS, F., YAP, S. D., BAUDEZ, J. C. & SLATTER, P. 2013. Rheological characterisation of municipal sludge: a review. *Water Res,* 47**,** 5493-510.
FANGARY, Y. S., BARIGOU, M., SEVILLE, J. P. K. & PARKER, D. J. 2002. A Langrangian study of solids suspension in a stirred vessel by Positron Emission Particle Tracking (PEPT). *Chemical Engineering & Technology,* 25**,** 521-528.
FANN INSTRUMENT, C. 2016. Viscometer Instruction Manual Model 35 Houston, Texas, USA: .
FENG, X., LI, X., CHENG, J., YANG, C. & MAO, Z.-S. 2012. Numerical simulation of solid–liquid turbulent flow in a stirred tank with a two-phase explicit algebraic stress model. *Chemical Engineering Science,* 82**,** 272-284.
FLETCHER, D. & BROWN, G. 2009. Numerical simulation of solid suspension via mechanical agitation: effect of the modelling approach, turbulence model and hindered settling drag law. *International Journal of Computational Fluid Dynamics,* 23**,** 173-187.
FORSTER, C. F. 2002. The rheological and physico-chemical characteristics of sewage sludge. *Enzyme and Microbial Technology,* 30**,** 6.
GANIDI, N., TYRREL, S. & CARTMELL, E. 2009. Anaerobic digestion foaming causes--a review. *Bioresour Technol,* 100**,** 5546-54.
GEERDINK, R. B., SEBASTIAAN VAN DEN HURK, R. & EPEMA, O. J. 2017. Chemical oxygen demand: Historical perspectives and future challenges. *Anal Chim Acta,* 961**,** 1-11.
GERARDI, M. H. 2003. *The Microbiology of Anaerobic Digesters,* New York, United States, John Wiley & Sons.
GIBSON, M. M. & LAUNDER, B. E. 2006. Ground effects on pressure fluctuations in the atmospheric boundary layer. *Journal of Fluid Mechanics,* 86**,** 491-511.
GIDASPOW, D. 1994. *Multiphase flow and fluidization : continuum and kinetic theory descriptions,* Boston, Mass.; Harcourt, Boston, Mass. : Academic Press ;.
GIDASPOW, D., BEZBARUAH, R. & DING, J. 1992. Hydrodynamics of Circulating Fluidized Beds: Kinetic Theory Approach. *7th engineering foundation conference.* EF.
GMI LTD 2016. GT Series User Handbook. Inchinnan Business Park, Inchinnan, Renfrew PA4 9RG: Gas Measurement Intruments

GOHEL, S., JOSHI, S., AZHAR, M., HORNER, M. & PADRON, G. 2012. CFD Modeling of Solid Suspension in a Stirred Tank: Effect of Drag Models and Turbulent Dispersion on Cloud Height. *International Journal of Chemical Engineering,* 2012**,** 1-9.

GOMEZ, X., CUETOS, M. J., CARA, J., MORAN, A. & GARCIA, A. I. 2006. Anaerobic co-digestion of primary sludge and the fruit and vegetable fraction of the municipal solid wastes - Conditions for mixing and evaluation of the organic loading rate. *Renewable Energy,* 31**,** 2017-2024.

GUIDA, A. 2010. *Positron emission particle tracking applied to solid-liquid mixing in mechanically agitated vessels*.

GUIDA, A., NIENOW, A. W. & BARIGOU, M. 2010. The effects of the azimuthal position of the measurement plane on the flow parameters determined by PIV within a stirred vessel. *Chemical Engineering Science,* 65**,** 2454-2463.

HACH 2015. Method 8000 - Chemical Oxygen Demand standard test for Water, Wastewater and Seawater. PO Box 389, Loveland, Colorado 80539 - USA: Hach.

HEAD, K. H. 2006. *Manual of soil laboratory testing. Vol. 1: soil classification and compaction tests. 3rd ed*.

HEILDOLPH 2011. Instruction Manual - Instruction Manual.

HOFFMANN, R. A., GARCIA, M. L., VESKIVAR, M., KARIM, K., AL-DAHHAN, M. H. & ANGENENT, L. T. 2008. Effect of shear on performance and microbial ecology of continuously stirred anaerobic digesters treating animal manure. *Biotechnol Bioeng,* 100**,** 38-48.

HOSSEINI, S., PATEL, D., EIN-MOZAFFARI, F. & MEHRVAR, M. 2010. Study of Solid-Liquid Mixing in Agitated Tanks through Computational Fluid Dynamics Modeling. *Industrial & Engineering Chemistry Research,* 49**,** 4426-4435.

IWA PUBLISHING 2007. Sludge Treatment and Disposal. *In:* ANDREOLI, C. V., VON SPERLING, M. & FERNANDES, F. (eds.) *Biological Wastewater Treatment.* London - New York: IWA Publishing.

KAPARAJU, P., BUENDIA, I., ELLEGAARD, L. & ANGELIDAKIA, I. 2008. Effects of mixing on methane production during thermophilic anaerobic digestion of manure: lab-scale and pilot-scale studies. *Bioresour Technol,* 99**,** 4919-28.

KARIYAMA, I. D., ZHAI, X. & WU, B. 2018. Influence of mixing on anaerobic digestion efficiency in stirred tank digesters: A review. *Water Res,* 143**,** 503-517.

KARPINSKA, A. M. & BRIDGEMAN, J. 2018. CFD as a Tool to Optimize Aeration Tank Design and Operation. *Journal of Environmental Engineering,* 144.

KASAT, G. R., KHOPKAR, A. R., RANADE, V. V. & PANDIT, A. B. 2008. CFD simulation of liquid-phase mixing in solid–liquid stirred reactor. *Chemical Engineering Science,* 63**,** 3877-3885.

KATOH, S. & YOSHIDA, F. 2009. *Biochemical Engineering*, Wiley-VCH Verlag GmbH & Co. KGaA.

KELLY, W. & GIGAS, B. 2003. Using CFD to predict the behavior of power law fluids near axial-flow impellers operating in the transitional flow regime. *Chemical Engineering Science,* 58**,** 2141-2152.

KIM, J. K., OH, B. R., CHUN, Y. N. & KIM, S. W. 2006. Effects of temperature and hydraulic retention time on anaerobic digestion of food waste. *J Biosci Bioeng,* 102**,** 328-32.

KLIMENTO, I., PARKER, W., LEBEAU, B. & HALL, S. 2004. An Evaluation of Sediment Formation in the Anaerobic Digesters at ROPEC. *WEFTEC 2004.* Water Environment Federation.

KOMEMOTO, K., LIM, Y. G., NAGAO, N., ONOUE, Y., NIWA, C. & TODA, T. 2009. Effect of temperature on VFA's and biogas production in anaerobic solubilization of food waste. *Waste Manag,* 29**,** 2950-5.

KOWALCZYK, A., HARNISCH, E., SCHWEDE, S., GERBER, M. & SPAN, R. 2013. Different mixing modes for biogas plants using energy crops. *Applied Energy,* 112**,** 465-472.

KRESS, P., NAGELE, H. J., OECHSNER, H. & RUILE, S. 2018. Effect of agitation time on nutrient distribution in full-scale CSTR biogas digesters. *Bioresour Technol,* 247**,** 1-6.

KRESTA, S. M. E., A. W.; DICKEY, D. S,; ATIEMO-OBENG, V. A. 2016. *Advances in Industrial Mixing*, wiley.

LABATUT, R. & GOOCH, C. A. 2012. *Monitoring of Anaerobic Digestion Process to Optimize Performanceand Prevent System Failure*.

LANT, P. & HARTLEY, K. 2007. Solids characterisation in an anaerobic migrating bed reactor (AMBR) sewage treatment system. *Water Res,* 41**,** 2437-48.

LEMMER, A., NAEGELE, H.-J. & SONDERMANN, J. 2013. How Efficient are Agitators in Biogas Digesters? Determination of the Efficiency of Submersible Motor Mixers and Incline Agitators by Measuring Nutrient Distribution in Full-Scale Agricultural Biogas Digesters. *Energies,* 6**,** 6255-6273.

LI, H., SI, D., LIU, C., FENG, K. & LIU, C. 2018. Performance of direct anaerobic digestion of dewatered sludge in long-term operation. *Bioresource Technology,* 250**,** 355-364.

LI, L. H., LI, D., SUN, Y. M., MA, L. L., YUAN, Z. H. & KONG, X. Y. 2010. Effect of temperature and solid concentration on anaerobic digestion of rice straw in South China. *International Journal of Hydrogen Energy,* 35**,** 7261-7266.

LINDMARK, J., ERIKSSON, P. & THORIN, E. 2014a. The effects of different mixing intensities during anaerobic digestion of the organic fraction of municipal solid waste. *Waste Manag,* 34**,** 1391-7.

LINDMARK, J., THORIN, E., FDHILA, R. B. & DAHLQUIST, E. 2014b. Effects of mixing on the result of anaerobic digestion: Review. *Renewable & Sustainable Energy Reviews,* 40**,** 1030-1047.

LIU, J., GAO, Y., PEARCE, P., SHANA, A. & SMITH, S. R. 2017. *Statistical modelling anaerobic digestion for process optimisation and bench-marking: a case study of E. coli inactivation across all Thames Water conventional sewage sludge treatment sites*.

LIU, L. 2014. *Computational fluid dynamics modelling of complex fluid flow in stirred vessels.* PhD, University of Birmingham.

LIU, L. & BARIGOU, M. 2013. Numerical modelling of velocity field and phase distribution in dense monodisperse solid-liquid suspensions under different regimes of agitation: CFD and PEPT experiments. *Chemical Engineering Science,* 101**,** 837-850.

LIU, M. B. & LIU, G. R. 2010. Smoothed Particle Hydrodynamics (SPH): an Overview and Recent Developments. *Archives of Computational Methods in Engineering,* 17**,** 25-76.

LJUNGQVIST, M. & RASMUSON, A. 2001. Numerical simulation of the two-phase flow in an axially stirred vessel. *Chemical Engineering Research & Design,* 79**,** 533-546.

MACHADO, M. B., NUNHEZ, J. R., NOBES, D. & KRESTA, S. M. 2012. Impeller characterization and selection: Balancing efficient hydrodynamics with process mixing requirements. *Aiche Journal,* 58**,** 2573-2588.

MALCZEWSKA, B. 2009. Variability of rheological parameters in function of gravimetric concentration of sludge. *Electronic Journal of Polish Agricultural Universities,* 12.

MEISTER, M., REZAVAND, M., EBNER, C., PUMPEL, T. & RAUCH, W. 2018. Mixing non-Newtonian flows in anaerobic digesters by impellers and pumped recirculation. *Advances in Engineering Software,* 115**,** 194-203.

METZNER, A. B. & OTTO, R. E. 1957. Agitation of Non-Newtonian Fluids. *Aiche Journal,* 3**,** 3-10.

MICHELETTI, M., NIKIFORAKI, L., LEE, K. C. & YIANNESKIS, M. 2003. Particle concentration and mixing characteristics of moderate-to-dense solid-liquid suspensions. *Industrial & Engineering Chemistry Research,* 42**,** 6236-6249.

MONTEITH, H. & & STEPHENSON, J. 1981. Mixing Efficiencies in Full-Scale Anaerobic Digesters by Tracer Methods. *Water Pollution Control Federation,* 53**,** 78-84.

MORRISON, F. A. 2001. *Understanding rheology*.

MYINT, M., NIRMALAKHANDAN, N. & SPEECE, R. E. 2007. Anaerobic fermentation of cattle manure: modeling of hydrolysis and acidogenesis. *Water Res,* 41**,** 323-32.

NIKOLIC, D. D. & FRAWLEY, P. J. 2016. Application of the Lagrangian meshfree approach to modelling of batch crystallisation: Part I-Modelling of stirred tank hydrodynamics. *Chemical Engineering Science,* 145**,** 317-328.

NOUTSOPOULOS, C., MAMAIS, D., ANTONIOU, K., AVRAMIDES, C., OIKONOMOPOULOS, P. & FOUNTOULAKIS, I. 2013. Anaerobic co-digestion of grease sludge and sewage sludge: the effect of organic loading and grease sludge content. *Bioresour Technol,* 131**,** 452-9.

OCHIENG, A. & LEWIS, A. E. 2006. CFD simulation of solids off-bottom suspension and cloud height. *Hydrometallurgy,* 82**,** 1-12.

OLATUNJI, O. 2016. *Natural Polymers : Industry Techniques and Applications,* Cham, Springer International Publishing : Imprint: Springer.

ONG, H. K., GREENFIELD, P. F. & PULLAMMANAPPALLIL, P. C. 2002. Effect of mixing on biomethanation of cattle-manure slurry. *Environ Technol,* 23**,** 1081-90.

PARK, C., LEE, C., KIM, S., CHEN, Y. & CHASE, H. A. 2005. Upgrading of anaerobic digestion by incorporating two different hydrolysis processes. *J Biosci Bioeng,* 100**,** 164-7.

PAUL, E. L., KRESTA, S. M., ATIEMO-OBENG, V. A. & NORTH AMERICAN MIXING, F. 2004. *Handbook of industrial mixing: science and practice*.

PEARCE, D. 1975. *Equipment for measurement of gas production at low rates of flow. Technical memorandum TM104*, Water Research Centre.

PEVERE, A., GUIBAUD, G., VAN HULLEBUSCH, E., LENS, R. & BAUDU, M. 2006. Viscosity evolution of anaerobic granular sludge. *Biochemical Engineering Journal,* 27**,** 315-322.

POPE, S. B. 2000. *Turbulent Flows,* Cambridge, Cambridge University Press.

RAJESHWARI, K. V., BALAKRISHNAN, M., KANSAL, A., LATA, K. & KISHORE, V. V. N. 2000. State-of-the-art of anaerobic digestion technology for industrial wastewater treatment. *Renewable and Sustainable Energy Reviews,* 4**,** 135-156.

ROACHE, P. J. 1998. Verification of codes and calculations. *Aiaa Journal,* 36**,** 696-702.

RUBAL, J. S., TORRE, J. A. C. & GONZALEZ, I. D. C. 2012. Influence of Temperature, Agitation, Sludge Concentration and Solids Retention Time on Primary Sludge Fermentation. *International Journal of Chemical Engineering,* 2012**,** 8.

SANIN , F. D. 2002. Effect of solution physical chemistry on the rheological properties of activated sludge. *Water SA,* 28.

SEYSSIECQ, I., FERRASSE, J.-H. & ROCHE, N. 2003. State-of-the-art: rheological characterisation of wastewater treatment sludge. *Biochemical Engineering Journal,* 16**,** 41-56.

SHEN, F., TIAN, L., YUAN, H., PANG, Y., CHEN, S., ZOU, D., ZHU, B., LIU, Y. & LI, X. 2013. Improving the mixing performances of rice straw anaerobic digestion for higher biogas production by computational fluid dynamics (CFD) simulation. *Appl Biochem Biotechnol,* 171**,** 626-42.

SHI, X. C., LIN, J., ZUO, J. N., LI, P., LI, X. X. & GUO, X. L. 2017. Effects of free ammonia on volatile fatty acid accumulation and process performance in the anaerobic digestion of two typical bio-wastes. *Journal of Environmental Sciences,* 55**,** 49-57.

SINDALL, R. C. 2014. *Increasing the efficiency of anaerobic waste digesters by optimising flow patterns to enhance biogas production / by Rebecca Clare Sindall.* Thesis (PhD)--University of Birmingham, College of Engineering and Physical Sciences, 2015.

SINDALL, R. C. 2015. *Increasing the efficiency of anaerobic waste digesters by optimising flow patterns to enhance biogas production.* PhD, University of Birmingham.

SKELLAND, A. H. P. 1967. Non-Newtonian flow and heat transfer. *Journal of Polymer Science Part A-2: Polymer Physics,* 5**,** 1327-1328.

SPINOSA, L. & LOTITO, V. 2003. A simple method for evaluating sludge yield stress. *Advances in Environmental Research,* 7**,** 655-659.

STANLEY, S. J. & SMITH, D. W. 1995. Measurement of Turbulent-Flow in Standard Jar Test Apparatus. *Journal of Environmental Engineering-Asce,* 121**,** 902-910.

TAMBURINI, A., CIPOLLINA, A., MICALE, G., BRUCATO, A. & CIOFALO, M. 2011. CFD simulations of dense solid–liquid suspensions in baffled stirred tanks: Prediction of suspension curves. *Chemical Engineering Journal,* 178**,** 324-341.

TAMBURINI, A., CIPOLLINA, A., MICALE, G., BRUCATO, A. & CIOFALO, M. 2012. CFD simulations of dense solid–liquid suspensions in baffled stirred tanks: Prediction of the minimum impeller speed for complete suspension. *Chemical Engineering Journal,* 193-194**,** 234-255.

TAMBURINI, A., CIPOLLINA, A., MICALE, G., BRUCATO, A. & CIOFALO, M. 2013. CFD simulations of dense solid–liquid suspensions in baffled stirred tanks: Prediction of solid particle distribution. *Chemical Engineering Journal,* 223**,** 875-890.

TAMBURINI, A., CIPOLLINA, A., MICALE, G., BRUCATO, A. & CIOFALO, M. 2014. Influence of drag and turbulence modelling on CFD predictions of solid liquid suspensions in stirred vessels. *Chemical Engineering Research & Design,* 92**,** 1045-1063.

TAMBURINI, A., CIPOLLINA, A., MICALE, G., CIOFALO, M. & BRUCATO, A. 2009. Dense solid–liquid off-bottom suspension dynamics: Simulation and experiment. *Chemical Engineering Research and Design,* 87**,** 587-597.

TIAN, Z., CHAULIAC, D. & PULLAMMANAPPALLIL, P. 2013. Comparison of non-agitated and agitated batch, thermophilic anaerobic digestion of sugarbeet tailings. *Bioresour Technol,* 129**,** 411-20.

TSI INC. *PIV SYSTEM 2D MEASUREMENT* [Online]. USA. Available: https://www.tsi.com/products/fluid-mechanics-systems/piv-systems/piv-system-2d-measurement/ [Accessed 23/10/2019 2019].

UN-HABITAT 2008. Global Atlas of Excreta, Wastewater Sludge, and Biosolids Management. UN-Habitat.

USEPA 1976. Anaerobic Sludge Digestion Operation Manual.

USER GUIDE 2016. Fann Model 35 - Instruction Manual. Fann Instrument Company.

VAN LIER, J. B., MAHMOUD, N. & ZEEMAN, G. 2008. Anaerobic Wastewater Treatment. *Biological Wastewater Treatment, Principles, Modelling and Design.* London - UK: IWA Publishing

VENNEKER, B. C. H., DERKSEN, J. J. & VAN DEN AKKER, H. E. A. 2010. Turbulent flow of shear-thinning liquids in stirred tanks—The effects of Reynolds number and flow index. *Chemical Engineering Research and Design,* 88**,** 827-843.

VERSTEEG, H. K. & MALALASEKERA, W. 2007. *An introduction to computational fluid dynamics : the finite volume method*.

VESVIKAR, M. S. 2006. *Understanding the Hydrodynamics and Performance of Anaerobic Digesters.* PhD, Washington University.

VESVIKAR, M. S. & AL-DAHHAN, M. 2005. Flow pattern visualization in a mimic anaerobic digester using CFD. *Biotechnol Bioeng,* 89**,** 719-32.

VON SPERLING, M., ANDREOLI, C. V., SPERLING, M. V., FERNANDES, F. P. D. & UNIVERSIDADE FEDERAL DE MINAS GERAIS. DEPARTAMENTO DE ENGENHARIA SANITÁRIA E, A. 2007. *Sludge treatment and disposal*.

WADNERKAR, D., TADE, M. O., PAREEK, V. K. & UTIKAR, R. P. 2016. CFD simulation of solid-liquid stirred tanks for low to dense solid loading systems. *Particuology,* 29**,** 16-33.

WADNERKAR, D., UTIKAR, R. P., TADE, M. O. & PAREEK, V. K. 2012. CFD simulation of solid–liquid stirred tanks. *Advanced Powder Technology,* 23**,** 445-453.

WANG, Y. Y., ZHANG, Y. L., WANG, J. B. & MENG, L. 2009. Effects of volatile fatty acid concentrations on methane yield and methanogenic bacteria. *Biomass & Bioenergy,* 33**,** 848-853.

WARD, A. J., HOBBS, P. J., HOLLIMAN, P. J. & JONES, D. L. 2008. Optimisation of the anaerobic digestion of agricultural resources. *Bioresour Technol,* 99**,** 7928-40.

WATERUK 2012. Sustainability Indicators 2010-2011. Technical report. London: Water UK.

WOOD, D. K. & TCHOBANOGLOUS, G. 1975. Trace Elements in Biological Waste Treatment. *Water Pollution Control Federation,* 47**,** 1933-1945.

WU, B. 2010a. CFD simulation of gas and non-Newtonian fluid two-phase flow in anaerobic digesters. *Water Res,* 44**,** 3861-74.
WU, B. 2010b. CFD simulation of mixing in egg-shaped anaerobic digesters. *Water Res,* 44**,** 1507-19.
WU, B. 2011. CFD investigation of turbulence models for mechanical agitation of non-Newtonian fluids in anaerobic digesters. *Water Res,* 45**,** 2082-94.
WU, B. 2012. CFD simulation of mixing for high-solids anaerobic digestion. *Biotechnol Bioeng,* 109**,** 2116-26.
WU, B. & CHEN, S. 2008. CFD simulation of non-Newtonian fluid flow in anaerobic digesters. *Biotechnol Bioeng,* 99**,** 700-11.
XIAO, K. K., GUO, C. H., ZHOU, Y., MASPOLIM, Y. & NG, W. J. 2016. Acetic acid effects on methanogens in the second stage of a two-stage anaerobic system. *Chemosphere,* 144**,** 1498-1504.
XIAO, K. K., GUO, C. H., ZHOU, Y., MASPOLIM, Y., WANG, J. Y. & NG, W. J. 2013. Acetic acid inhibition on methanogens in a two-phase anaerobic process. *Biochemical Engineering Journal,* 75**,** 1-7.
XU, Z., ZHAO, M., MIAO, H., HUANG, Z., GAO, S. & RUAN, W. 2014. In situ volatile fatty acids influence biogas generation from kitchen wastes by anaerobic digestion. *Bioresour Technol,* 163**,** 186-92.
YANG, G., ZHANG, P., ZHANG, G., WANG, Y. & YANG, A. 2015. Degradation properties of protein and carbohydrate during sludge anaerobic digestion. *Bioresour Technol,* 192**,** 126-30.
YU, L., MA, J. & CHEN, S. 2011. Numerical simulation of mechanical mixing in high solid anaerobic digester. *Bioresour Technol,* 102**,** 1012-8.
YU, L., MA, J. W., FREAR, C., ZHAO, Q. B., DILLON, R., LI, X. J. & CHEN, S. L. 2013. Multiphase modeling of settling and suspension in anaerobic digester. *Applied Energy,* 111**,** 28-39.
ZEALAND, A. M., ROSKILLY, A. P. & GRAHAM, D. W. 2017. Effect of feeding frequency and organic loading rate on biomethane production in the anaerobic digestion of rice straw. *Applied Energy,* 207**,** 156-165.
ZWIETERING, T. N. 1958. Suspending of Solid Particles in Liquid by Agitators. *Chemical Engineering Science,* 8**,** 244-253.

APPENDIX A

Modification of Viscosity via UDF

A user-defined function (UDF) was developed and compiled in the Fluent source code so that the viscosity in each cell is calculated in accordance with the current shear rate. The code specifies two shear rate ranges (0.699 to 15.7574 and 15.7574 to 1500 s^{-1}, as described in section 7.1.5, table 7.3) where the consistency index K and the power-law index *n* are chosen to better describe the full range of the non-Newtonian behaviour. As such, errors associated with the deviation of the fitting curve, especially at low shear rate ($\dot{\gamma} < 100\ s^{-1}$) were minimised at the same time as the lower and upper viscosity plateau were well-defined.

```
/* File name: non_new_parallel_cmc4.c */

/*****************************************************************
UDF that modifies the power-law model for CMC solution at 4 g/l
*****************************************************************/

#include "udf.h"
#include "math.h"
#include "mem.h"

/** Includes the library that contains the Cell Flow Variables
such as:

C_MU_L(c,t)     cell_t c, Thread *t   laminar viscosity
C_MU_T(c,t)     cell_t c, Thread *t   turbulent viscosity
C_MU_EFF(c,t)   cell_t c, Thread *t   effective viscosity  **/


DEFINE_PROPERTY(cell_viscosity,c,t)

{
#if !PARELLEL

real SR=C_STRAIN_RATE_MAG(c,t); /* ShearRate second invariant of
the rate of strain*/
real mu_eff;

real n1=0.803;              /* power law index 1 */
real k1=0.4462;             /* consistency index 1 */
real lsrl1=0.699;           /* low shear rate limit 1*/
real hsrl1=15.7574;         /* high shear rate limit 1*/


real n2=0.5116;             /* power law index 2 */
real k2=0.9965;             /* consistency index 2 */
real lsrl2=15.7574;         /* low shear rate limit 2*/
real hsrl2=1500;            /* high shear rate limit 2*/
```

```
if (SR<lsrl1) {
         mu_eff=0.4788;
     }
      else if (SR<=hsrl1) {
         mu_eff=k1*pow(SR,(n1-1));
     }
      else if (SR<=hsrl2) {
         mu_eff=k2*pow(SR,(n2-1));
     }
      else {
         mu_eff=0.0280;
     }
      return mu_eff;
#endif
}
```

APPENDIX B

Turbulence Models

As part of the CFD model validation (section 7.1.10), the realisable k-ε, standard k-ε, RNG k-ε and SST k-ω turbulence models were investigated. In order to find the best model able to reproduce the velocity fields of the PIV measurement results, three aspects were analysed: (i) normalised velocity magnitude along a vertical line positioned between the baffles and the impeller's tip (Figure B.1); (ii) Reynolds number (Table B.1), and (iii) normalised velocity magnitude contour and vectorial plots (Figure B.2). The velocity magnitude was calculated from *u* and *v* velocities only, and it was normalised by the impeller's tip speed.

For time-dependent problems, the solution is given after the normalised residuals decrease to four or more orders of magnitude for all cells in the domain every time step. Small residuals of the monitoring parameters indicate, amongst other factors, that the Navier-Stokes equations are converging to a solution. The SST k-ω turbulence model did not converge bellow $5x10^{-4}$, convergence similar to Craig et al. (2013). All k-ε models converged bellow $1x10^{-5}$ for all monitoring parameters. This includes the extra two parameters for the single-phase fluid flow: the area-weighted-average (AWA) of the velocity magnitude on the tank's top surface, and the volume-weighted-average (VWA) of the kinetic energy (KE) of the tank's bulk flow region (stationary frame, see figures 7.1 and 7.2 in Chapter 7).

Figure B.1 shows the normalised velocity magnitude for the PIV and the four turbulence models along a vertical line positioned at r/R=0.6 and at a 1° azimuthally rotated anticlockwise behind the baffle. It can be noted in the region above the impeller that all turbulence models well reproduce the shape of the curve, but underpredict the normalised velocity magnitude up to a maximum of ~0.04 m/s at around 40 mm above the impeller. The regions indicated in figure B.1 by peak-A and peak-B correspond to the high intensity mixing regions, located in the vicinity of the impeller. Peak-A is located in a small recirculating zone, as shown in figure B.2 by a red circle, whilst peak-B is located in the impeller discharge. The k-ε turbulence models were able to recreate the location and general shape of the two peaks. However, the standard k-ε and the RNG k-ε models over predict the normalised velocity magnitude of peak-A and peak-B by around 0.01 m/s and 0.04 m/s, respectively, whilst the realisable k-ε model accurately predicts both peaks. The SST k-ω turbulence model overestimates the normalised velocity magnitude of both peaks by more than double the maximum velocity of the PIV results for peak-B (~0.18 m/s difference).

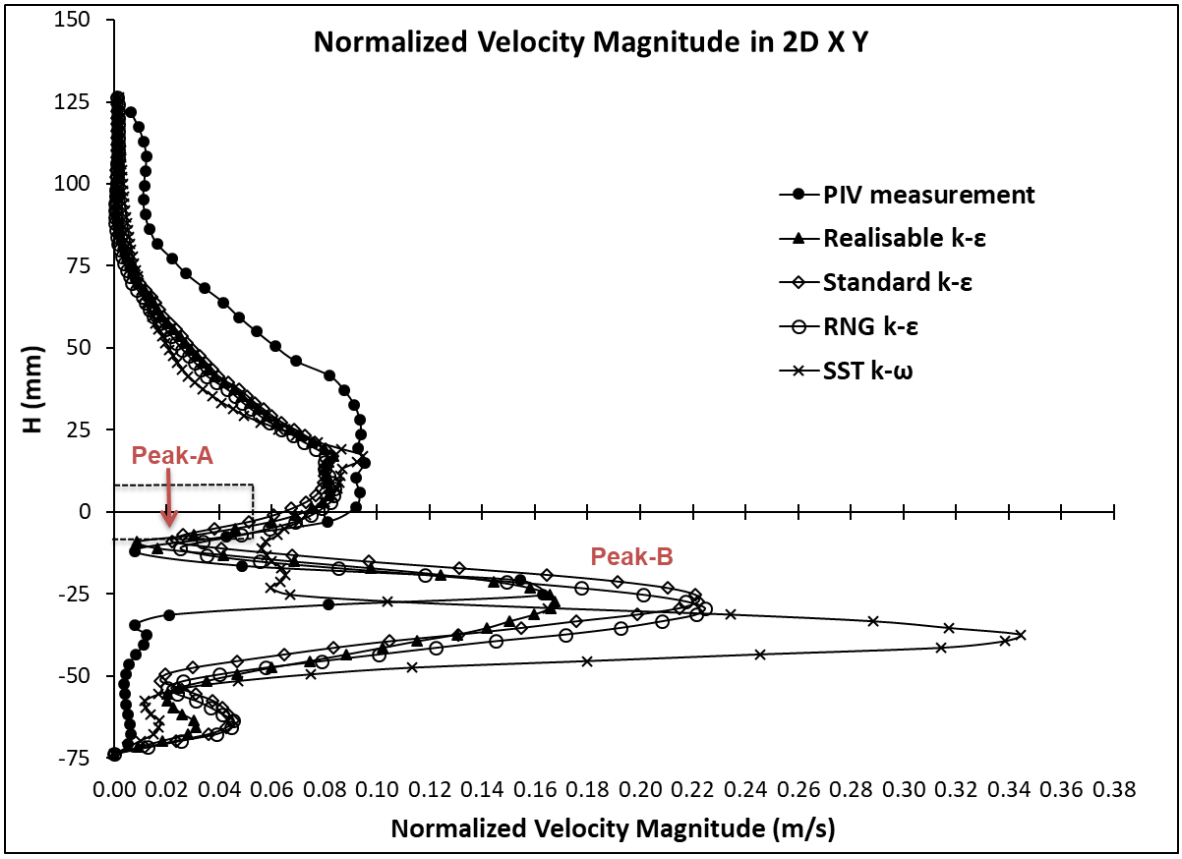

Figure B.1: Normalised velocity magnitude along a vertical line at r/R= 0.6 and azimuthally turned 1° anti-clockwise (approximately behind the baffle, positioned as the PIV laser beam) for all four turbulence models and the PIV measurement at **N=400-rpm**. The velocity magnitude is normalised by the impeller tip's linear velocity. The dashed rectangle indicates the position of the impeller (not scaled).

Table B.1 shows a comparison between a reference Reynolds number (Re) (eq. 3.21, Chapter 3) and all four turbulence models studied. The Re calculated using equation 3.21 does not require the viscosity properties explicitly, only through the consistency index (K) and power-law number (n), and is based on the average shear rate ($\mathrm{k_s}$) proposed by Metzner and Otto (1957). In order to compare the different turbulence models, the Re was calculated using equation 3.19 and the VWA viscosity, directly extracted from the CFD model in the rotating frame (see figures 7.1 and 7.2 in Chapter 7), region of high intensive mixing. The results shown in table B.1 indicate that the k-ε models estimate the Re reasonably well, being the realisable k-ε the closest to the reference value. The SST k-ω model overestimates the Re with approximately 20% error, being the worst prediction investigated. Similar results were found by Wu (2011), where the realisable k-ε model presented the lowest errors for different impeller speeds and several non-Newtonian viscosities.

Table B.1: Reynolds number (Re) calculated from the VWA viscosity in the rotating zone for all investigated turbulence models at **N=400-rpm**.

	Eq. 3.21	Realisable k-ε	Standard k-ε	RNG k-ε	SST k-ω
Re	222	234	235	238	265
error %	-	5.19	5.90	7.41	19.35

Figure B.2 shows the u-v normalised velocity magnitude contour and vectorial plots for the PIV (a) and CFD (b-e) results. The length of the vectors in figure B.2 (a) accounts for the u-v velocity components whilst the CFD results also include the third velocity component (w). Nevertheless, this does not affect the direction of the flow indicated by the arrow, only its length, i.e. magnitude. It can be noted that all CFD results reproduce reasonably well the fluid flow patterns seen in figure B.2 (a). There are two distinguished recirculating zones in the bulk flow, one above and one below the impeller. The regions immediately above and below the impeller present the highest velocities, characteristic flow of pitched-blade turbines (Gohel et al., 2012, Guida et al., 2010, Liu and Barigou, 2013). The three k-ε models tested were able to recreate the velocity magnitude field and location with considerable accuracy throughout the whole domain, whilst the SST k-ω model overestimates both, magnitude and shape of the velocity field. In agreement with Sindall (2014), who showed that the SST k-ω was only able to predict one parameter correctly (the maximum radial velocity at the discharge of the Rushton impeller), the SST k-ω model performed the worst in all other parameters analysed. This can be confirmed by the peaks shown in figure B.1, which can be better visualised in figure B.2 (e), where the length, shape and velocity magnitude of the fluid in the impeller discharge region are the most discrepant from the PIV measurements. These results might be due to the convergence difficulty, a problem also faced by Craig et al. (2013), who despite the symmetry of their tank, found that the velocity fields were not symmetrical when using the same turbulence model. In fact, the residuals they used did not converge bellow $5x10^{-3}$, going against best CFD practices.

The analysis of the four turbulence models available in Fluent for Eulerian-Eulerian multi-phase modelling indicates that the realisable k-ε model appears to be the best fit to the experimental data, both in terms of predicting the velocity distribution and magnitudes throughout the tank. As shown in the literature review in Chapters 2 and 3, realisable k-ε is the most common and accepted turbulence model used to simulate stirred tanks and solid suspension. Therefore. it was chosen as the model to perform all further single-phase and multi-phase simulations of this work.

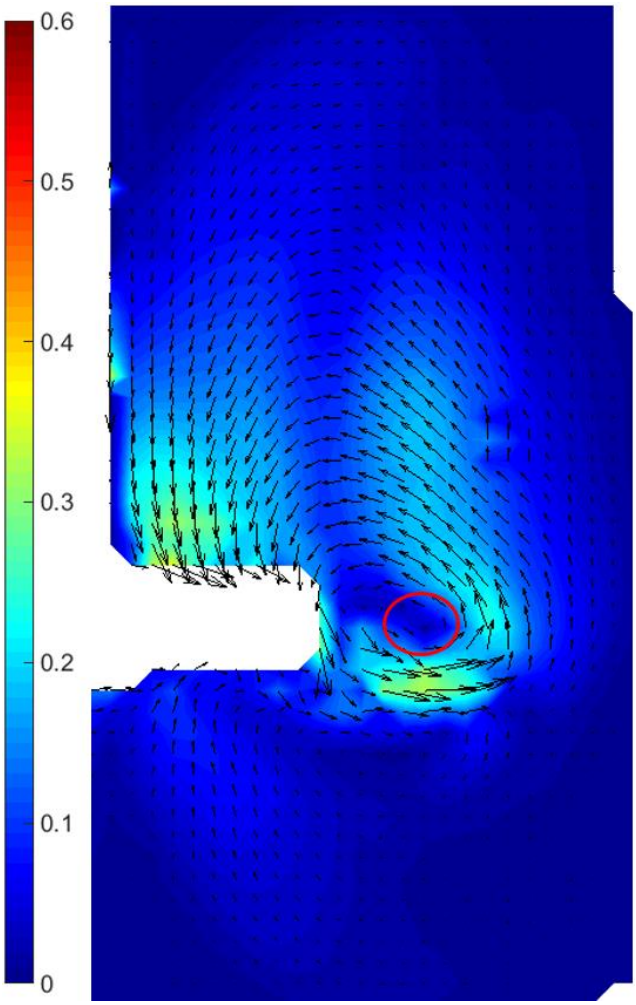

(a)

Figure B.2: Normalised velocity magnitude contour plot and velocity magnitude vectorial plot for the liquid phase at **N=400 rpm** for the PIV measurement and different turbulence models: (a) PIV, (b) realisable $\boldsymbol{k}$-$\boldsymbol{\varepsilon}$, (c) standard $\boldsymbol{k}$-$\boldsymbol{\varepsilon}$, (d) RNG $\boldsymbol{k}$-$\boldsymbol{\varepsilon}$ and (e) SST $\boldsymbol{k}$-$\boldsymbol{\omega}$. Figure continue in the next page. Continue in the next page.

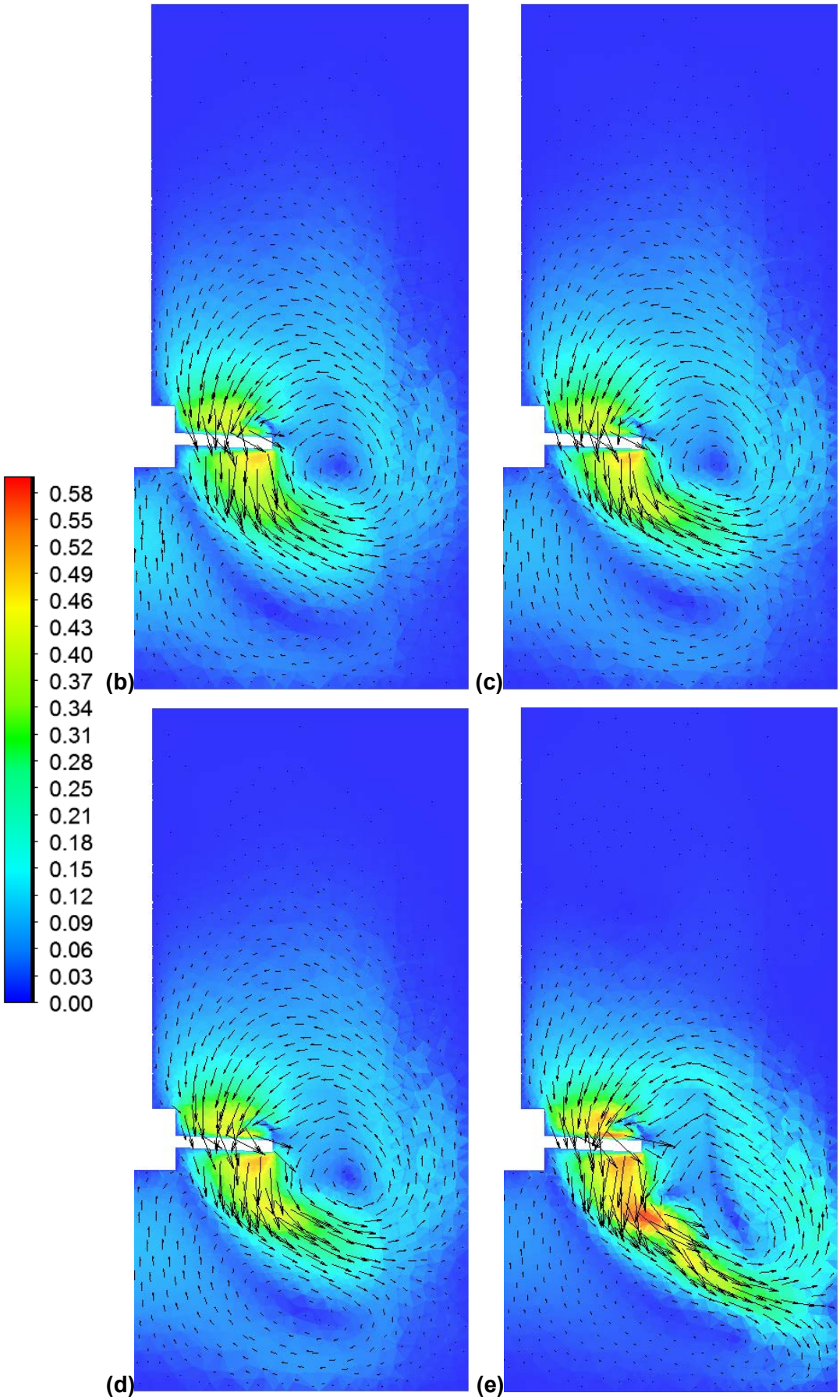

Figure B.2: continuation.